IN-26
117606
P-289

NASA Contractor Report 189211

Improving the Low Temperature Ductility of NiAl

Sumit Guha
Dartmouth College
Hanover, New Hampshire

(NASA-CR-189211) IMPROVING THE LOW TEMPERATURE DUCTILITY OF NiAl Ph.D. Thesis (Dartmouth Coll.) 289 p
N92-33951
Unclas
G3/26 0117606

July 1992

Prepared for
Lewis Research Center
Under Grant NAG3-775

National Aeronautics and
Space Administration

ABSTRACT

The intermetallic NiAl, by virtue of its high melting point, relatively low density (compared to the Ni-base superalloys) and excellent high temperature oxidation resistance, exhibits excellent potential as a structural material for application in air-breathing and single-stage-to-orbit engines. Unfortunately, like most intermetallics, NiAl is brittle at ambient temperatures. This brittleness has been partly attributed to the lack of five independent slip systems as required by von Mises criterion for uniform, volume conserving deformation since the opeartive <100> slip offers only three independent slip systems. Isostructural FeAl, however, deforms by <111> slip at room temperature which provides five independent slip systems. Thus, it was decided to macroalloy NiAl with Fe to promote <111> slip therby possibly improving the ductility. An alternative approach was multi-phase alloys based on NiAl. The results indicated that up to 6% tensile elongation combined with high yield strength (~800 MPa) could be obtained for an alloy Ni-30at.%Al-20at.%Fe with an essentially ordered b.c.c microstructure. These results compare favorably with those of stoichiometric (Ni-50at.%Al) where 2% tensile elongation and ~250 MPa yield stength is observed. Interestingly, like Ni-50Al, this alloy also deforms by <100> slip at room temperature. The multi-phase alloy approach proved even more successful with ductilities of ~20%, yield strength of 760-850 MPa (depending upon heat treatment) and high fracture strength (1200-1400 MPa) being observed for an alloy Ni-20at.%Al-30at.%Fe. The room temperature and elevated temperature microstructure, mechanical properties and deformation behavior of the multi-phase alloy Ni-20Al-30Fe and alloys similar to its constituent phases has been examined here. The high room temperature ductility of the multi-phase alloy was attributed to deformation transfer across interphase boundaries and the crack stopping action of the constituent γ/γ' phase. At elevated temperatures, it was observed that while the constituent γ/γ' phase became increasingly brittle with increasing temperatures, the β' phase became more ductile. Thus,

the multi-phase alloy did not exhibit any elevated temperature embrittlement. Similarly, while the β' phase became weak at high temperatures, the γ/γ' phase exhibited better strength retention leading to the improved elebvated temperature strength of the multi-phase alloy. Thus, the multi-phase alloy benefits from both its constituent phases, with each phase alleviating the disadvantages associated with the other phase over any temperature range. The multi-phase alloy approach is suggested as a possible apporach to designing intermetallic-based alloys.

ACKNOWLEDGEMENTS

I would like to express my appreciation and gratitude to a number of people for their assistance in completing this work. The assistance and guidance of my advisor, Dr. I. Baker is gratefully acknowledged; working in close association with him has been a real pleasure. I am also grateful to Dr. M.V. Nathal, my mentor at NASA Lewis Research Center, for the guidance and assistance in various stages of this work and to Dr. P. Munroe for teaching me 'hands-on' electron microscopy and would like to acknowledge the use of some of his work (micrographs) on room temperature microstructure and dislocation analysis in β' and γ/γ' alloys in this thesis. Also, I would like to thank Dr. E.M. Schulson, my masters program advisor, for the training in graduate-level materials work I received during my masters program and Prof. F.E. Kennedy for serving on my thesis committee and the various useful comments I have received from him from time to time. I am also grateful to the following personnel at NASA Lewis Research Center for the assistance I have received during the course of this work: Dr. J.D. Whittenberger, Dr. R.D. Noebe, Dr. I. Locci, Dr. S.V. Raj, Dr. R.A. Mackay, Mr. D.J. Gaydosh, Mr. D. Deadmore and Mr. R. Davies. And finally, I would like to thank Dr. R.O. Loutfy and Dr. J.C. Withers for the understanding and encouragement I have received in finishing this thesis while being employed at MER Corp and Dr. D. Chakroborty for granting me access to a word processing system at the University of Arizona. The financial assistance of NASA Lewis Research Center for three years is gratefully acknowledged (contract no. NAG3-775).

TABLE OF CONTENTS

1. INTRODUCTION

1.1 General Background 1

1.2 The Present Study 4

1.3 Approaches to Improving Ductility of NiAl 5

1.4 Proposed Approaches 8

1.5 Alloy Compositions Chosen for Investigation 10

2. LITERATURE SURVEY

2.1 Introduction 11

2.2 Properties of Nickel Aluminides

2.2.1 Ni-Al Phase Diagram 11

2.2.2 Mechanical Behavior of Nickel Aluminides 15

2.3 Ni-Fe-Al Alloys Literature Survey

2.3.1 Ni-Fe-Al Phase Diagrams 22

2.3.2 Lattice Spacing Constants and Defect Structures 31

2.3.3 Mechanical Behavior of Ni-Fe-Al Alloys 32

2.4 Alloy Selection 37

3. MATERIALS AND EXPERIMENTAL TECHNIQUES

3.1 Materials 39

3.2 Materials Processing 39

3.3 Mechanical Testing 42

3.4 Metallography 45

3.5 Electron Microscopy 45

3.6 X-ray Diffraction 46

4. MULTI-PHASE Ni-20Al-30Fe AND ITS CONSTITUENT PHASES

4.1 Introduction 49

4.2 Microstructures

4.2.1 Room Temperature 49

4.2.2 Elevated Temperature 65

4.3 Mechanical Properties

4.3.1 Room Temperature 83

4.3.2 Elevated Temperature 89

4.4 Deformation Mechanisms

4.4.1 Room Temperature 119

4.4.2 Room Temperature TEM In-situ Straining Experiments 128

4.4.3 Elevated Temperature 143

4.5 Creep Behavior 149

4.6 Summary 158

5. ANNEALING EFFECTS ON ROOM TEMPERATURE MICROSTRUCTURE AND MECHANICAL PROPERTIES

5.1 Microstructures 160

5.2 Mechanical Behavior 173

5.3 Summary 202

6. ROOM TEMPERATURE MECHANICAL BEHAVIOR OF Ni-40Al-30Fe

6.1 Microstructure 204

6.2 Mechanical Properties 207

7. MULTI-PHASE ALLOY Ni-36Al

7.1 Microstructure 218

7.2 Mechanical Properties 226

8. FURTHER DISCUSSION 234

9. SUMMARY OF MAJOR RESULTS 245

10. CONCLUSION 248

10. SUGGESTIONS FOR FUTURE WORK 249

11. REFERENCES 251

APPENDIX I.

APPENDIX II.

LIST OF TABLES

Table. 3.1 Summary of alloy compositions and expected microstructures 40

Table. 3.2 Compositions, Solidus and Liquidus temperatures of alloys investigated. 41

Table 4.2.1 Compositions of phases of multi-phase Ni-20Al-30Fe,β' Ni-30Al-20Fe, γ/γ Ni-12Al-40Fe at elevated temperatures 68

Table 4.3.1 Room temperature tensile properties of as-extruded Ni-20Al-30Fe, Ni-30Al-20Fe and Ni-12Al-40Fe. 84

Table 4.3.2 Summary of elevated temperature tensile behavior of Ni-20Al-30Fe, Ni-12Al-40Fe and Ni-30Al-20Fe. 96

Table 5.1 Summary of room temperature tensile properties in as-extruded and annealed state 188

LIST OF FIGURES

Figure 1. The operating engine temperatures for various jet engines. 3

Figure 2.1 The binary Ni-Al phase diagram 12

Figure 2.2 The ordered-bcc (B2) crystal structure. 13

Figure 2.3 Ni-Fe-Al solidus and liquidus projections and various isotherms 24-29

Figure 2.4 Contours of constant lattice spacing (only last three decimal places shown) in Ni-Fe-Al system 31

Figure 2.5a-b Dependence of creep strength of Ni-Fe-Al β' alloys on (a) Fe content (b) Al content 33

Figure 2.6a-b Dependence of (a) yield strength (b) elongation of γ' Ni-Fe-Al alloys on Fe concentration at different temperatures 35

Figure. 3.1 The standard tensile specimen used for mechanical testing. 43

Figure. 3.2 Relationship between primary slit size and specimen dimensions. 47

Fig 4.2.1a-d Optical and TEM micrographs of single-extruded Ni-20Al-30Fe 50-51

Fig 4.2.2a-f Optical and TEM micrographs of double-extruded Ni-20Al-30Fe 53-55

Fig 4.2.3a-b Optical and TEM micrographs of single-extruded Ni-12Al-40Fe 58

Fig 4.2.4a-b Optical and TEM micrograph of double-extruded Ni-30Al-20Fe 60

Fig 4.2.5a-c X-ray diffraction patterns from Ni-30Al-20Fe 61-63

Fig 4.2.6 STEM micrograph of double-extruded Ni-30Al-20Fe 64

Fig 4.2.7a-b Composition of matrix and grain boundary in Ni-30Al-20Fe using STEM 64

Fig 4.2.8 Optical micrograph of Ni-20Al-30Fe-0.17B 66

Fig 4.2.9a-d TEM micrographs of 627°C and 827°C annealed Ni-20Al-30Fe 69-70

Fig 4.2.10a-d TEM micrographs of 627°C and 827°C annealed Ni-12Al-40Fe 72-73

Fig 4.2.11a-f TEM micrographs of 627°C and 827°C annealed Ni-30Al-20Fe 75-77
Fig 4.2.12a-d Optical micrographs of isochronally annealed Ni-20Al-30Fe 79-80
Fig 4.2.13a-d Optical micrographs of isochronally annealed Ni-20Al-30Fe-0.17B 81-82
Fig 4.3.1 Room temperature stress-strain curves of as-extruded Ni-20Al-30Fe, Ni-30Al-20Fe and Ni-12Al-40Fe 85
Fig 4.3.2a-d Fractographs of RT tensile-tested Ni-20Al-30Fe, Ni-30Al-20Fe and Ni-12Al-40Fe 87-88
Fig 4.3.3 Polished longitudinal section of tensile-tested Ni-20Al-30Fe 90
Fig 4.3.4a-e Vickers hot hardness tests for Ni-20Al-30Fe, Ni-30Al-20Fe, Ni-12Al-40Fe and Ni-20Al-30Fe-0.17B 91-95
Fig 4.3.5 Stress-strain curves for Ni-20Al-30Fe at 27, 427, 627 and 827°C 99
Fig 4.3.6 Stress-strain curves for Ni-12Al-40Fe at 27, 427, 627 and 827°C 100
Fig 4.3.7 Stress-strain curves for Ni-30Al-20Fe at 27, 627 and 827°C 101
Fig 4.3.8 Stress-strain curves for Ni-30Al-20Fe-0.17B at 27, 427, 627 and 827°C 102
Fig 4.3.9a-b Temperature dependence of yield strength and elongation of Ni-20Al-30Fe, Ni-30Al-20Fe and Ni-12Al-40Fe 103-104
Fig 4.3.10a-c Fractographs of 427, 627 and 827°C tensile-tested Ni-20Al-30Fe 107-108
Fig 4.3.11a-b Fractographs of 427 and 627°C tensile-tested Ni-12Al-40Fe 109
Fig 4.3.12a-b Fractographs of 627 and 827°C tensile-tested Ni-30Al-20Fe 110
Fig 4.3.13a-d Analysis of polished longitudinal sections of Ni-20Al-30Fe tested at 427°C-827°C 111-112
Fig 4.3.14 Polished longitudinal section of 627°C-tested Ni-12Al-40Fe 115
Fig 4.3.15a-b Polished longitudinal sections of 627 and 827°C tested Ni-30Al-20Fe 116
Fig 4.3.16a-c Polished longitudinal sections of 627 and 827°C tested Ni-20Al-30Fe-0.17B 117-118
Fig 4.4.1a-d Dislocation analysis in β' phase in Ni-20Al-30Fe 120-121
Fig 4.4.2a-d Dislocation analysis in γ/γ' phase in Ni-20Al-30Fe 122-123
Fig 4.4.3a-d Dislocation analysis in β' alloy Ni-30Al-20Fe 125-126
Fig 4.4.4 TEM micrograph of β'-γ/γ' interface in Ni-20Al-30Fe 127

Fig 4.4.5 Geometry of in-situ specimens and their relation to the extrusion axis 129

Fig 4.4.6-4.4.25 TEM in-situ straining micrographs 131-140

Fig 4.4.26a-c Comparison of dislocation densities in 27, 627 and 827°C deformed Ni-30Al-20Fe 145-146

Fig 4.4.27a-c Dislocation analysis in β' phase of Ni-20Al-30Fe deformed ~5% at 827°C 147-148

Fig 4.4.28a-c Dislocation analysis in γ phase of Ni-20Al-30Fe deformed ~5% at 827°C 150-151

Fig 4.5.1 Comparison of creep rates of as-extruded and coarsened Ni-20Al-30Fe, Ni-12Al-40Fe and Ni-30Al-20Fe 152

Fig 4.5.2a-b Polished longitudinal section of as-extruded and coarsened Ni-20Al-30Fe 155

Fig 4.5.3a-b Creep deformation substructures in β' and γ phase in Ni-20Al-30Fe samples deformed at 827°C 156

Fig 5.1a-b SDF micrographs of β' and γ/γ' phases in 500°C-annealed Ni-20Al-30Fe 162

Fig 5.2a-b SDF micrographs of β' and γ/γ' phases in 750°C-annealed Ni-20Al-30Fe 163

Fig 5.3a-c TEM micrographs of Ni-20Al-30Fe annealed at 750°C 164-165

Fig 5.4a-c TEM micrographs for the γ/γ' Ni-12Al-40Fe annealed at 500°C 167-168

Fig 5.5a-b TEM micrographs for the γ/γ' Ni-12Al-40Fe annealed at 750°C 169

Fig 5.6a-b TEM micrographs for the β' Ni-30Al-20Fe annealed at 500°C 171

Fig 5.7a-b TEM micrographs for the β' Ni-30Al-20Fe annealed at 750°C 172

Fig 5.8 RT hardness of isochronally annealed Ni-20Al-30Fe 174

Fig 5.9 RT hardness of isochronally annealed Ni-30Al-20Fe 175

Fig 5.10 RT hardness of isochronally annealed Ni-12Al-40Fe 176

Fig 5.11 RT hardness of isothermally (500 & 750°C) annealed Ni-30Al-20Fe 179

Fig 5.12 RT hardness of isothermally (500 & 750°C) annealed Ni-12Al-40Fe 180

Fig 5.13 RT hardness of isochronally annealed Ni-20Al-30Fe-0.17B 181

Fig 5.14	Stress-strain curves of annealed Ni-20Al-30Fe	184
Fig 5.15	Stress-strain curves of annealed Ni-30Al-20Fe	185
Fig 5.16	Stress-strain curves of annealed Ni-12Al-40Fe	186
Fig 5.17	Stress-strain curves of annealed Ni-20Al-30Fe-0.17B	187
Fig 5.18a-c	Effect of isochronal annealing on yield, fracture strength and ductility of Ni-20Al-30Fe, Ni-12Al-40Fe and Ni-30Al-20Fe	191-193
Fig 5.19a-c	Fractographs of annealed Ni-20Al-30Fe	195-196
Fig 5.20a-b	Fractographs of annealed Ni-30Al-20Fe	197
Fig 5.21a-b	Fractographs of annealed Ni-12Al-40Fe	198
Fig 5.22a-d	Fractographs of annealed Ni-20Al-30Fe-0.17B	199-200
Fig 5.23a-b	Polished longitudinal sections of Ni-20Al-30Fe-0.17B	201
Fig 6.1a-d	Optical and TEM micrographs of as-extruded Ni-40Al-30Fe	205-206
Fig 6.2	Deformation substructure of 750°C-annealed Ni-40Al-30Fe (strained ~.5%)	208
Fig 6.3a-b	TEM SDF micrographs of 750°C-annealed Ni-40Al-30Fe	209
Fig 6.4a-b	TEM SDF micrographs of as-extruded 750°C-annealed Ni-40Al-30Fe	210
Fig 6.5	RT hardness of isochronally annealed Ni-40Al-30Fe	211
Fig 6.6	Stress-strain curves of as-extruded and 750°C-annealed Ni-40Al-30Fe	213
Fig 6.7	Fractograph of as-extruded Ni-40Al-30Fe	214
Fig 6.8	Vickers hot hardness tests on Ni-40Al-30Fe	216
Fig 7.1	Casting defect in as-extruded Ni-36Al	2199
Fig 7.2	Optical micrograph of as-extruded Ni-36Al	218
Fig 7.3a-b	Optical micrographs of heat treated (solution annealed at 1200°C, quenched to 430°C and aged at 700°C)Ni-36Al	221
Fig 7.4a-b	Optical micrographs of heat treated (solution annealed at 1200°C, quenched to 430°C and aged at 800°C) Ni-36Al	223
Fig 7.5a-b	Optical micrographs of heat treated (solution annealed at 1200°C, water	

	quenched and aged at 700°C) Ni-36Al	224
Fig 7.6a-b	Optical micrographs of heat treated (solution annealed at 1200°C, water quenched and aged at 800°C) Ni-36Al	225
Fig 7.7a-d	Hot hardness tests for as-extruded Ni-36Al and Ni-36Al-0.17B; and heat treated (aged at 700°C and 800°C) Ni-36Al	228-231
Fig 7.8a-b	Fractographs of as-extruded and heat treated Ni-36Al	232

CHAPTER 1

INTRODUCTION

1.1 GENERAL BACKGROUND

In early 1987, the US Office of Science and Technology (OST) established goals for subsonic, supersonic and transatmospheric flight vehicles[1]. With the aim of maintaining the dominant position of the US in the expanding international market for civil aviation, OST envisions an entirely new generation of civil aircraft for subsonic flights, noteworthy for fuel efficiency and attractive price. On the other hand, the goals for supersonic flight call for long distance efficiency, i.e. vehicles that will cruise for thousands of miles at supersonic speeds. Such aircraft will link the US directly with the farthest of the pacific rim countries, and expand the ability of military aircraft to be widely based and, thus, carry out missions over greater distances. The OST goal for transatmospheric flight vehicles calls for aircraft that can take off from and land on conventional runways, and fly not only in the upper atmosphere but also in space. The National Aerospace Plane (NASP), a program for the development of manned, single-stage-to-orbit transfer, transatmospheric flight vehicles, can also be envisioned for military and commercial missions.

The first of such transatmospheric flight vehicles, the experimental X-30, is scheduled for tryout in the mid-90's. After take off, it will gradually accelerate as it shifts through three increasingly powerful air-breathing engines like a race car changing gears. As it approaches top speed, with a last kick from a booster rocket, it will sprint past 24,000 kmph and soar out of atmosphere into orbit around the earth[2]. These goals place formidable demands on engine and airframe materials. Although current designs for NASP call for active cooling with the hydrogen fuel, thereby improving the thrust-to-weight ratio, meeting performance and weight requirements will necessitate the use of many nontraditional materials like ordered alloys (e.g. titanium aluminides or nickel aluminides) and metal matrix and ceramic matrix composites etc.[1,3].

CURRENT ENGINE MATERIALS

An indication of what materials technology has already achieved in improving aerospace vehicles can be seen in its application to jet engines. Over the last three decades, the thrust delivered by a big jet engine has increased almost sixfold, to the current ~33000 Newtons [1]. At the same time, the weight of the engine has only doubled. The thrust -to-weight ratio for the next generation engines is expected to be 10:1, and may approach 15:1 by the end of the century. Current jet engines use nickel-base superalloys in the hot sections (turbine and combustor) and nickel-base alloys, steels, and titanium alloys (e.g. Ti-6Al-4V) in the cooler parts of the engine (compressor). A typical propulsion system consists of 38% (by weight) nickel, 28% steel, 22% titanium, and 8% aluminum, along with small amounts of composites[1]. Superalloys incorporate large fractions of heavy elements like tungsten, molybdenum etc. in their composition and are designed for application in the most demanding part of the engine i.e. the turbine blades and vanes, which are exposed to very high temperatures and stresses. As performance requirements have increased, the microstructures of superalloys have evolved from equiaxed, polycrystalline forms to columnar grains produced by directional solidification, which eliminate boundaries transverse to the stress axis and enhance creep resistance, to single-crystals where grain boundaries are completely eliminated[4]. Currently, single-crystal superalloys are used extensively in jet engines.

Figure 1 shows the engine temperatures of various jet engines [1]. The NASP is likely to employ a Scramjet for its final stage [2], thereby placing severe demands on materials technology. Current requirements demand use of materials under constant and cyclic stresses at temperatures up to 1150°C in highly oxidizing environments. Even the best single-crystal superalloys, however, require thermal-barrier protection in the highly oxidizing environment of the jet engines [4]. Furthermore, nickel-base superalloys are limited by their melting temperatures (current applications like high bypass engines use superalloys very close to their melting points). Thus, advanced engine requirements would be impossible to meet with the current superalloys. And finally, the superalloys have high density. The continuing emphasis on higher thrust-to-weight ratio necessitates developments of engine materials with higher specific strength (i.e. strength to density ratio).

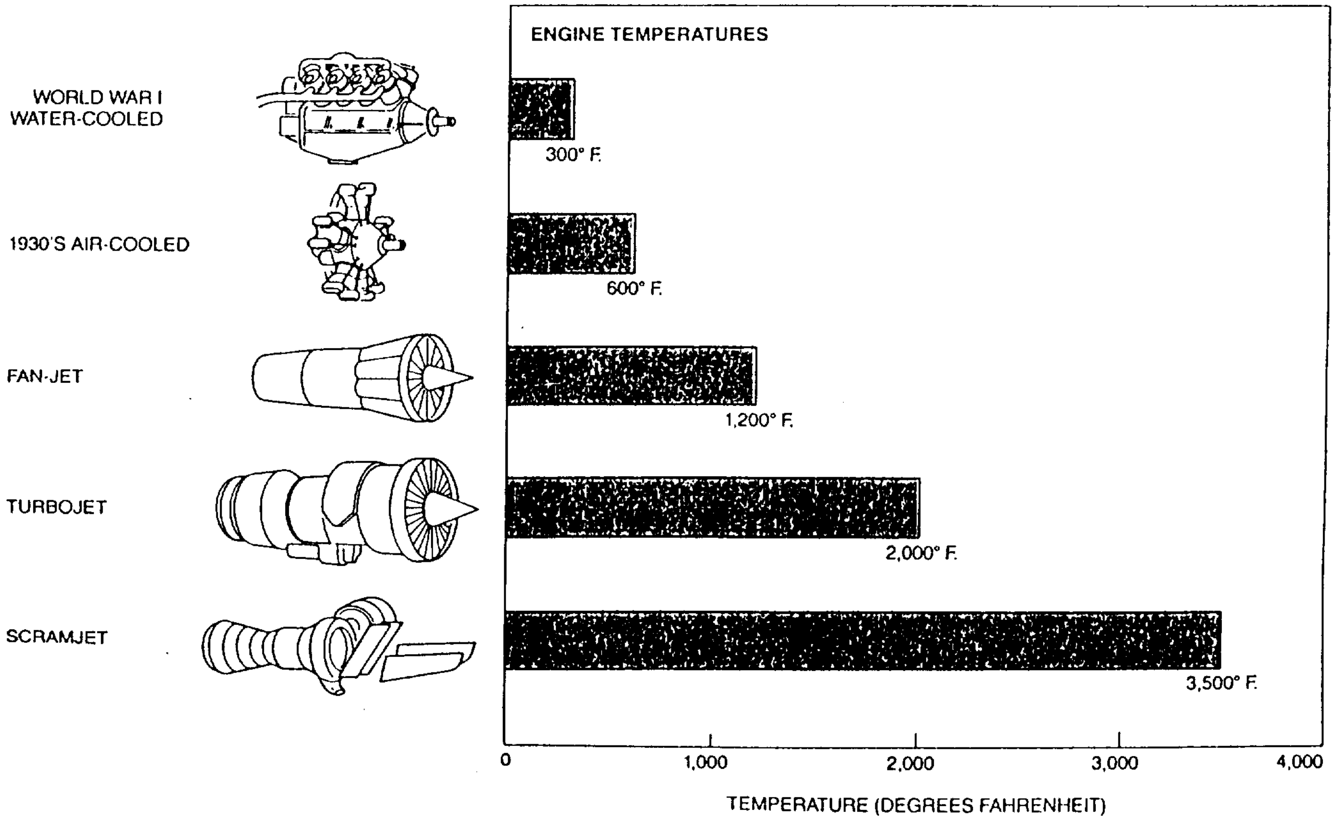

Figure 1. The operating engine temperatures for various jet engines [1].

FUTURE ENGINE MATERIALS

Materials demands for the newer engines, with their emphasis on higher operating temperatures and improved thrust-to-weight ratio, are unlikely to be met by the superalloys for reasons mentioned above. Increasing the pressure ratio inside engines to 70:1 and rotor inlet temperature to 1500°C would result in almost 25% fuel savings [5]. New research, with the goal of developing materials lighter than superalloys and capable of withstanding higher operating temperatures, is underway. Several engine manufacturers are involved in materials development programs. Ordered alloys (primarily aluminides), refractory metal alloys and composites hold promise for operating temperatures up to 1500°C. It is estimated that by the year 2000, a typical propulsion system would consist of about 20% each of composites, steel, nickel and aluminum, 15% titanium, 2% ordered alloys and 1% ceramics[1].

1.2 THE PRESENT STUDY

The intermetallic NiAl is a potential candidate as a structural material for the next generation of advanced aircraft engines because of its high melting point (1638°C [6]), oxidation resistance [7] and low density (5.9 Mg/m^3). Two problems exist which compromise its potential. First, the high temperature strength of NiAl is poor; viz. the yield strength of the intermetallic decreases sharply beyond ~500°C [8]. Second, like most strongly-ordered alloys, polycrystalline NiAl exhibits brittleness at low temperatures (<500°C) [9]. While the former problem may be overcome by reinforcing NiAl-based alloys by some suitable continuous ceramic fibers, the attendant difference in coefficients of thermal expansion between a metal matrix and a ceramic fiber would require a matrix capable of some ambient temperature ductility. The ambient temperature brittleness of NiAl would probably preclude the use of NiAl-based matrices in metal matrix / ceramic fiber composites.

The purpose of the present investigation is to attempt to alleviate, based on scientific principles, the ambient temperature brittle behavior of NiAl and examine ductile NiAl-based alloys which could be suitable as a matrix for Intermetallic Matrix Composites (IMCs).

1.3 APPROACHES TO IMPROVING THE DUCTILITY OF NiAl

The fundamental problem of room temperature brittleness of NiAl is attributed to its <100> slip vector [10], which provides only three independent slip systems [11] instead of the five deformation modes required for uniform, volume conserving deformation [12]. (Note that the <111> slip vector commonly observed in b.c.c alloys provides five independent slip systems [11]). Of the several possible approaches to alleviating the ambient brittleness of NiAl, a few with greatest promise are discussed in this section.

Grain Size Refinement

Schulson [13] proposed to improve the ductility of NiAl through grain size refinement, where below a critical grain size d_c, the stress to nucleate cracks (of the order of grain size) was less than the stress to propagate them. And indeed, Schulson and Barker [14] found that at 400°C and for grain sizes less than 20μm, up to 40% elongation could be obtained for Ni-49 at.% Al. Unfortunately, the critical grain size d_c decreases rapidly with decreasing temperature so that at 295°C d_c was measured to be ~5μm [15]. At room temperature, the d_c is expected to be even lower. Such grain sizes are difficult to obtain through conventional processing routes. Furthermore, the very fine grained microstructure may not be stable at the service temperatures. Although a fine dispersion could be added to prevent grain size coarsening, it could decrease d_c further since the critical grain size has been hypothesized to be sensitive to impurity content [13]. Also, the creep resistance of such fine-grained polycrystalline aggregate is expected to be poor. Several investigators, however, have noted a reverse dependence of creep properties on grain size for NiAl. For example, Whittenberger [16] reported that fine grained alloys (grain size below 15μm) were more creep resistant than coarse grained alloys.

Fine particle Additions

In addition to stabilising fine grains, fine dispersoids may homogenize slip (that is reduce the planarity of slip) and reduce local stress concentrations thereby delaying crack nucleation. Seybolt [17] added fine oxide dispersions of Al_2O_3, Y_2O_3 and ThO_2 to NiAl and whilst improved creep rupture properties resulted, the low temperature ductility problem was exacerbated. Note that, besides ThO_2 which was dispersed on a scale comparable to a modern dispersion strengthened alloy, the remaining additives were dispersed as coarse particles (~0.5μm). Although, one could argue, that the homogenization of slip will be affected by the particle size and arrangment and that appropriate thermo-mechanical processing could help produce a more uniformly dispersed microstructure, this approach appears to have little promise for NiAl since the fundamental problem of the lack of five independent slip systems cannot be changed through dispersoid additions.

Microalloying

Small additions of boron (~500 ppm) to nickel-rich Ni_3Al can increase the room temperature elongation from 0 to 50% [18]. Ni_3Al has the five independent slip systems required for general plastic flow [19] but suffers from intrinsic grain boundary brittleness. Boron microadditions segregate to the grain boundaries and help in alleviating the brittleness. Microalloying with boron has been tried for NiAl [15] without any success. Although, like Ni_3Al, boron segregated to the grain boundaries, no improvement in ductility was observed, presumably because the fundamental problem of an inadequate number of slip systems remained unchanged. However, this approach still deserves limited further examination.

Second Phase/Fiber Additions

Instead of trying to improve ductility, an alternative approach would be to improve the toughness of NiAl. Discontinuous fibers of Al_2O_3 and SiC could be added to NiAl to suppress crack propagation. Alternately, a second phase may be added to increase fracture toughness. The investigations by Russell and Edington [20] and Moskovic [21] in binary (Ni-Al) and ternary (Ni-Al-Cr) multi-phase alloys respectively indicated that addition of second phase precipitates to the microstructure to form *in-situ* composites holds promise for improving the room temperature mechanical properties like damage tolerance and ductility.

Based on the previous work, the addition of a second phase to NiAl seems worthy of examination.

Macroalloying

In general, macroalloying can be used to change the crystal structure or to produce a second phase. Liu and Inouye [22] used macroalloying to change the crystal structure of Co_3V from DO_{19} (ordered hexagonal based on two $L1_2$ (ordered f.c.c) unit cells) to the higher symmetry $L1_2$-structured $(Co,Fe)_3V$, which was ductile. The space group of NiAl is Pm3m which is a highly symmetric structure. Macroalloying to produce a second phase is likely to improve ductility, as discussed earlier.

An alternate macroalloying approach would be the addition of a third element which will make bonding more metallic and thus promote <111> slip, thereby providing five independent slip systems. Since B2-structured iron-rich FeAl deforms by <111> slip at low temperature [23,24], iron additions to NiAl may promote <111> slip. Additionally, iron-rich FeAl is ductile [24,25]. It should be noted that <111> slip has been reported by

Law and Blackburn [26] for nickel-rich NiAl, macroalloyed with transition metals (~5 at.% Cr or Mn).

1.4 PROPOSED APPROACHES

Based on previous work which showed some promise, the approaches selected for this study are:

i) macroalloying NiAl with iron to make the bonding more metallic and promote <111> slip at low temperatures

ii) additional phases added to NiAl to improve the ductility / toughness.

iii) furthermore, the two approaches may be combined i.e. iron added to NiAl may promote <111> slip and also form a multi-phase microstructure.

iv) microalloying the multi-phase alloys with boron since any improvement in ductility in either/both phases may result in improved ductility for the aggregate.

Multi-phase Microstructure

Russell and Edington [20] first reported improved ductility / toughness of off-stoichiometric NiAl with the addition of a $L1_2$-structured second phase. The microstructure and mechanical behavior will be described in Chapter 2. The binary NiAl-Ni_3Al system was also examined by Khadkikar et al.[27] who reported limited (~0.5%) tensile elongation for Ni-29 at.%Al after suitable heat treatment. Similarly, Moskovic [21] reported a ten-fold increase in room temperature fracture toughness in Ni-30at.%Al-7at.%Cr after suitable heat treatment. The most encouraging results, however, were due to Inoue et al.[28] who reported ~600 MPa yield strength and 17% elongation for rapidly solidified Ni-20at.%Al-30at.%Fe wires made by an 'in-rotating-water' rapid solidification technique. The tensile tested wires exhibited dimple fracture. The microstructure of the melt-spun ribbons consisted of both B2 and $L1_2$ grains of 0.2μm size (a duplex microstructure). The ductility was attributed to three factors: grain size refinement, suppression of ordering and suppression of grain boundary segregation. No experimental evidence was produced in support of the latter two suggestions, although in a separate study [29], a high density of anti-phase boundaries (APBs) were reported in rapidly solidified Ni-Fe-Al alloys of $L1_2$ crystal structure but different compositions. The deformation modes for the constituent phases were not examined for this alloy, thus the reasons behind the large elongation obtained were not clear.

Macroalloying

It should be noted that Inoue et al.[28] also reported that melt-spun wires of B2-structured Ni-30at.%Al-20at.%Fe of 4μm grain size exhibited 5% plastic strain, a yield strength of 400 MPa and a mixture of dimple and intergranular fracture, when deformed in tension at room temperature. Again, the ductility was attributed to three factors: grain size refinement (although unalloyed NiAl of 4μm grain size is not ductile at room temperature [15]), suppression of ordering and suppression of grain boundary segregation, although no experimental evidence was produced in support of the latter two suggestions. Also, since the deformation modes were not examined for this alloy, a further possibility was that the B2 phase exhibited <111> slip.

Microalloying

Furukawa et al.[30] have recently demonstrated a remarkable improvement in tensile elongation resulting from microalloying additions. The alloy Ni-27at.%Al-14at.%Fe, which is located in the multi-phase field at room temperature (see fig. 2.3b), exhibited a B2 + martensite microstructure when processed through a rapid solidification route, and exhibited a 2.8% tensile elongation and 394 MPa fracture stress in the undoped state. However, when microalloyed with boron, an almost sixfold improvement in ductility was possible. The fracture stress and elongation were observed to be sensitive to the level of boron doping, increasing up to 1100 MPa and 18% elongation for 0.17at.% boron, and then decreasing to 880 MPa and 9.5% elongation for 0.45at.% boron. The tensile fracture surface of the boron-doped alloy showed dimple fracture in contrast to the intergranular fracture for the conventionally solidified Ni-27Al-14Fe. Thus, boron doping may prove a viable option for improving ductility for NiAl-based multi-phase alloys.

Thus, the Ni-Fe-Al B2 and multi-phase alloys warrant further examination. Particularly relevant is whether they would exhibit ductility when processed through more conventional processing routes.

1.5 ALLOY COMPOSITIONS CHOSEN FOR INVESTIGATION

Based on the approaches outlined above, seven alloy compositions (all compositions in atomic percent) were chosen for investigation, the choice of alloys will be descibed in detail in the next chapter (see section 2.4). Three of these alloys, Ni-30Al-20Fe, Ni-40Al-30Fe and Ni-50Al-25Fe were from the B2 single phase field in the room temperature section of the Ni-Fe-Al phase diagram, while the two multiphase alloys, Ni-20Al-30Fe and Ni-36Al were examined in both boron-doped and an undoped state.

CHAPTER 2

LITERATURE SURVEY

2.1 This chapter reviews the Ni-Al phase diagram, the previous studies on room temperature mechanical and deformation behavior of nickel aluminides, the various possible approaches to the ductility problem, and discusses the motivation behind the approach chosen for this study. The literature for Ni-Fe-Al alloys is reviewed and the choice of compositions chosen for investigation is discussed.

2.2 Properties of Nickel Aluminides

2.2.1 Ni-Al Phase Diagram

Figure 2.1 shows the Ni-Al phase diagram due to Singleton et al.[6]. The phase NiAl, which has an ordered bcc (B2) crystal structure of CsCl type, exists over a wide range of compositions. At 400°C, the phase field extends from 41.5 at.% Al to 55 at.% Al. At higher temperatures, the solid solubility range increases, varying from 58 at.% Al at 1133°C where the reaction NiAl + L = Ni_2Al_3 occurs, to 30.8 at.% Al at the peritectic temperature of 1395°C where the reaction NiAl + L = Ni_3Al occurs. The stoichiometric composition Ni-50Al melts congruently at 1638°C; the solidus and liquidus temperature decreases with deviations on either side of stoichiometry. The high melting temperature (higher than both its constituent elements) is indicative of the strongly ordered nature of NiAl.

The B2 crystal structure is shown in figure 2.2. It consists of two interpenetrating simple cubic lattices (i.e. two atoms per unit b.c.c cell) with Ni and Al atoms occupying one lattice site each. Deviations from stoichiometry lead to non-symmetrical defect structures[31,32]. On the Ni-rich side, excess Ni atoms sit on the Al sub-lattice. However, the Al-rich compositions are accommodated by vacancies on the Ni sub-lattice, indicating a higher bond energy for Al-Al bonds than Ni-Al bonds (which are preferred in ordered lattices) or Ni-Ni bonds. Furthermore, in aluminum-rich NiAl the vacancies may be ordered [33]. In addition to single constitutional defects, triple defects consisting of two vacancies on one sub-lattice and anti-site atom on the other sub-lattice, have been suggested [33-35] to exist even in some stoichiometric B2 compounds in order to explain the low formation energies of vacancies and their high concentrations at elevated temperatures [36,37]. For example, in isostructural FeAl at 800°C, the thermal vacancy concentration is forty times greater than a typical metal at its melting temperature, and in aluminum-rich compositions, constitutional vacancies occupy up to 10% of the lattice sites, mostly on the Fe sub-lattice [38,39]. These constitutional defects decrease the degree of long range order (LRO). Ordering, however, is maintained up to the solidus temperatures in NiAl [40].

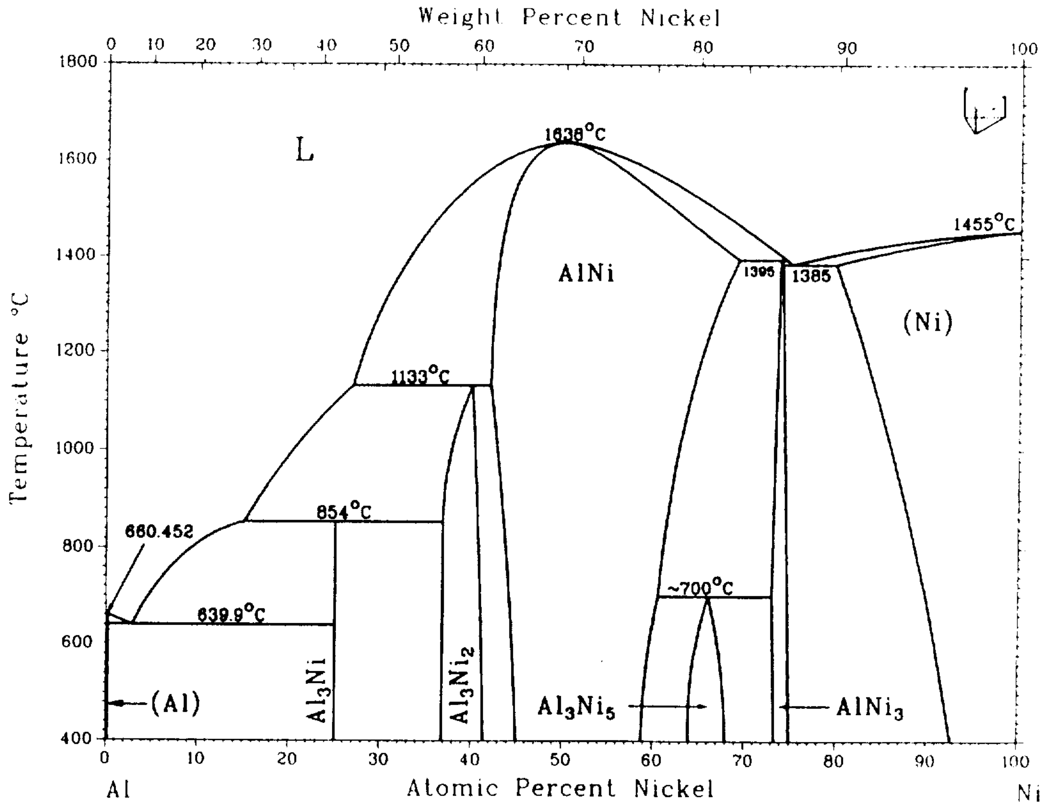

Figure 2.1 The binary Ni-Al phase diagram (from ref. 6).

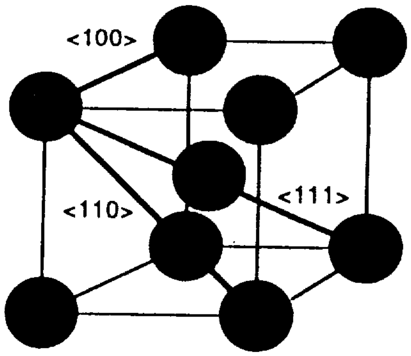

Figure 2.2 The ordered-bcc (B2) crystal structure.

A tetragonal twinned martensite of $L1_0$ crystal structure (CuAu type) can be formed by quenching Ni-rich NiAl from 1200°C[41]. The stoichiometric composition, however, has not been observed to transform martensitically[42]. Rosen and Goebel [43] reported martensitic microstructures for β' NiAl with less than 37% Al, quenched from 1000°C. Similarly, Maxwell and Grala [44] reported a martensitic reaction for a Ni-31.5Al alloy. Ball produced stress-induced martensite in Ni-43Al [45]. Enami et al.[46] determined the structure of matrensite in Ni-36.8Al consisted of {111}<112> twins. Smialek and Hehemann [45] noted that large deviations from stoichiometry (~10%) are needed before the martensite formation begins; the M_S temperature increases with increasing nickel content. Ball [45] rationalized the role of non-stoichiometry in producing martensite in NiAl in terms of phase stability and resistance to shear. Since deviations on the Ni-rich side of stoichiometry led to a decrease in electron/atom ratio from the value of 1.5 at stoichiometry, the phase stability of NiAl decreases with respect to martensite formation. Furthermore, increasing Ni-rich compositions lead to decreasing LRO which reduces the resistance to shear for martensitic transformations.

In contrast to the wide phase field of B2 NiAl, the $L1_2$-structured intermetallic Ni_3Al, exists over a relatively narrow range of composition. Figure 2.1 shows that the Ni_3Al phase field spans the composition range 25%Al-26.5%Al at 400°C. The stoichiometric composition is stable up to the peritectic temperature of 1395°C.

The two-phase region between NiAl and Ni_3Al (fig. 2.1) has not been studied extensively. Recently, a new phase Ni_5Al_3 has been identified in this two-phase region by Enami and Nenno [48] through transmission electron microscopy. The single (Ni_5Al_3) phase field extends from 32%Al to 36%Al at 400°C, with the phase stability region decreasing with increasing temperatures up to 700°C[49], above which Ni_5Al_3 is unstable. Above 700°C, the phases present in this two-phase region consist of Ni-rich NiAl and Al-rich Ni_3Al. The width of the two-phase field decreases with increasing temperature up to the peritectic temperature of 1395°C, where the reaction $Ni_3Al = NiAl + L$ occurs.

The microstructures resulting from various heat treatments in this two-phase field has been investigated by Russell and Edington [20], Khadkikar et al [27] and Locci et al.[50]. For Ni-36Al, solution-treated at 1150°C for 2 hrs, quenched into a fluidized bed at 430°C for 2 min. (to avoid complications in the ageing process from a residual defect density arising from the martensitic transformation), and up-quenched to 875°C, the ageing temperature, and aged up to 120 hrs, Russell and Edington [20] reported that the microstructure consisted of Ni_3Al needles, 1μm in diameter and 20μm long, in a matrix of NiAl. The NiAl grain boundaries were also lined with the Ni_3Al phase. Khadkikar et al.[27] studied two compositions in the two-phase field, Ni-29Al and Ni-35Al. At the homogenizing temperature of 1250°C, the former alloy consists of a two-phase microstructure, NiAl + Ni_3Al, while the latter alloy transforms completely to Ni-rich NiAl: quenching from the homogenization temperature transforms the Ni-rich alloy into a 3R martensite. Upon ageing at 850°C, the martensite is transformed back into Ni-rich NiAl. Ageing at 600°C produces the Ni_5Al_3 phase in the microstructure, with the Ni-29Al transforming into Ni_5Al_3 + Ni_3Al, while the Ni-35Al transforms into NiAl + Ni_5Al_3. The observed microstructures are consistent with the phase diagram shown in figure 2.1. Recently, Locci et al.[50] have reported the effects of heat treatment on Ni-37Al. For the alloy quenched from 1250°C, a microstructure consisting of NiAl+martensite was found. Long time ageing (30 days) of the quenched microstructure at 550°C resulted in complete transformation of the matrix to the orthorhombic Ni_5Al_3, with traces of NiAl being detected only by x-ray analysis. Long time annealing at 650°C resulted in similar microstructure, although the NiAl x-ray peaks were easier to detect. Very complex microstructures were reported for shorter ageing times. For example, ageing for 12 hrs at 550°C resulted in Ni_2Al precipitates in a 7R martensite matrix, along with needle-like plates which corresponded to new variants of 3R martensite. In addition, ~250 nm precipitates were observed, which were identified by microdiffraction to be Ni_5Al_3.

2.2.2 Mechanical Behavior of Nickel Aluminides

NiAl

Rozner and Wasilewski [51] first reported limited room temperature tensile ductility (~2.5% elongation) for polycrystalline, near-stoichiometric NiAl, processed through a casting and extrusion route, although the grain size and chemical analysis results were not reported. In the studied temperature range of -196 to 1100°C the tensile ductility was observed to be essentially constant from room temperature to ~400°C. The results are in sharp contrast to those reported by Grala [52], where no elongation was observed below 600°C. The room temperature ductility was recently reproduced by Hahn and Vedula [53], who reported the grain size to be 11-16μm and the wet chemical analysis results as Ni-50.3Al. Ball and Smallman [54] studied the mechanical behavior of cast, polycrystalline stoichiometric and off-stoichiometric NiAl in compression in the temperature range 200-1000°C. For both the stoichiometric and off-stoichiometric alloys (Ni-rich as well as Al-rich), a brittle-to-ductile transition behavior was noted at a homologous temperature of

~0.45Tm. At the lowest test temperature (200°C), the stoichiometric alloy exhibited higher strain to fracture than either off-stoichiometric alloy. By contrast, Pascoe and Newey [9] reported significantly higher room temperature compressive ductility in polycrystalline, Ni-rich alloy of similar composition as Ball and Smallman [54], but processed through a casting and hot extrusion route. The fracture mode was noted by Pascoe and Newey [9] to be generally intergranular for fine grained polycrystals (~50μm grain size), with an increased tendency for transgranular cleavage with increasing grain size. Single crystals were observed to fail by cleavage on {110} planes.

The yield strength of nominally stoichiometric NiAl was noted by Rozner and Wasilewski [51]to be essentially independent of temperature up to 600°C, beyond which the strength was markedly dependent upon temperature. Pascoe and Newey [9] have shown the yield strength (actually the 0.2% proof stress) of NiAl to be sensitive to composition; at 327°C, the yield strength was observed to have a minimum for the stoichiometric alloy, increasing with increasing deviations from stoichiometry, with the rate of increase being higher on the Al-rich side than the Ni-rich side. The variation of yield strength with temperature for off-stoichiometric (both Ni-rich and Al-rich) alloys was similar to the stoichiometric alloy, although the 'critical temperature' beyond which the strength decreased sharply was highest for the stoichiometric alloy (600°C).

The usual slip system for NiAl was identified to be {110}<100> by Ball and Smallman [10]. Wasilewski, Butler and Hanlon [55] have observed the operation of both {110}<100> and {100}<100> slip systems in single crystal NiAl. Uniform, volume conserving deformation requires the operation of at least five independent deformation modes [12], often referred to as von Mises criterion for polycrystalline deformation. A <100> slip vector, by contrast, provides only three independent slip systems [11, 56], regardless of the number of planes on which slip occurs. Thus, the brittle behavior of NiAl (in tension) has often been ascribed to the lack of sufficient slip systems to satisfy von Mises criterion. Additional slip systems can be activated at higher stress levels. For example, Pascoe and Newey [9] have observed the operation of <111> slip in NiAl single crystals compressed in the <100> direction, often referred to as the 'hard' orientation since the resolved shear stress for <100> slip is zero. While the activation of the <111> slip vector would certainly alleviate the problem of lack of sufficient number of slip systems [11,12], such an activation prior to fracture initiation and propagation is unlikely due to the random grain arrangement (lack of a <100> wire-texture along strain axis) in polycrystalline samples. The observed ductility in compression may be ascribed to the delayed fracture initiation and propagation under compressive stresses.

Ni_3Al

In contrast to NiAl, the $L1_2$-structured intermetallic Ni_3Al exhibits tensile ductility in single crystal form[57]. Polycrystals of stoichiometric, Ni-rich and Al-rich compositions are, however, brittle and fail by intergranular fracture[58-60]. The slip systems of Ni_3Al have been determined to be {111}<110>[61,19], which provides five independent slip systems for deformation[11]. Thus, unlike NiAl, the brittleness of the stoichiometric alloy is unrelated to any lack of sufficient number of independent slip systems. Rather, Ni_3Al suffers from intrinsic grain boundary weakness. The beneficial effect of boron additions on the mechanical behavior of Ni_3Al was first reported by Aoki and Izumi [18]. The tensile ductility of the stoichiometric alloy was improved from zero to ~35% elongation by the addition of a few hundred ppm of boron, and the fracture mode changed from intergranular to a mixture of intergranular and transgranular fracture. The effectiveness of boron additions was confirmed by Koch et al.[62] who further optimized the boron concentration for good ductility. Liu et al.[59] further determined that boron was an effective ductilizer only in Ni-rich alloys; the ductility decreased steadily as the Al concentration of boron-doped alloys was increased from 24%Al to 25%Al. The fracture mode became increasingly intergranular with increased Al content, such that at 25%Al, the fracture mode for the boron-doped alloy was mostly intergranular. It should be noted, however, that even the stoichiometric alloy benefitted from boron doping[60]. Boron doping is, however, ineffective for Al-rich alloys[59]. Boron helps in alleviating the intrinsic grain boundary brittleness by segregating to grain boundaries; quenching of boron-doped Ni-24Al reduces ductility, presumably due to insufficient segregation of boron to the grain boundaries[63]. The segregation as measured by the B/Ni ratio, decreased with increasing Al content, while the Al/Ni ratio increased. By contrast, Briant and Taub [64] have noted that when processed through a rapid solidification route, boron-doped Ni_3Al attains high ambient temperature ductility in addition to increased strength, the latter presumably being a result of boron solid solution strengthening. Baker et al.[65] have suggested that grain boundaries for Ni-rich alloys are partially disordered due to the co-segregation of Ni and B, while for Al-rich compositions, long range order is restored at the grain boundaries, thus the alloy becomes brittle.

There are two theories regarding the role of boron at grain boundaries: (a) boron simply increases the cohesive strength of the boundary[59]; (b) boron eases slip transmittal across the boundary by disordering the boundary[66]. The latter suggestion was based upon experimental results which indicate that boron reduces the effectiveness of grain size strengthening in stoichiometric Ni_3Al (a reduced slope for yield strength vs. grain size measurements), presumably due to reduced barrier to slip transmittal across grain boundaries. Interestingly, a reduced dependence of yield strength on grain size is also observed for boron-doped Ni-rich Ni_3Al but not for boron-doped Al-rich Ni_3Al [67]. Since the Ni-rich and stoichiometric alloy exhibit improved ductility with boron doping, while the Al-rich alloy is unaffected, these results do indicate a correlation between the reduced yield strength vs. grain size slope in boron-doped alloys and ductility. MacKenzie and Sass [68] presented the first direct experimental evidence of a thin disordered grain boundary film in boron doped alloys using high resolution electron microscopy. Similarly, Baker et al. [69], using convergent beam diffraction, have also reported the observation of a ~20nm thick disordered grain boundary phase in alloys produced by hot-extrusion of rapidly solidified powders. A similar hypothesis of a disordered phase along grain boundaries causing enhanced ductility has been put forward by Horton and Miller [70] based on field ion microscope observations of rapidly-solidified Ni_3Al.

The ductility of Ni_3Al is also reported to be sensitive to grain size, test temperature and atmosphere. Weihs et al.[60] noted that, while the undoped stoichiometric alloy did not show any increased room temperature ductility with decreased grain size, the boron-doped alloy exhibited increased ductility, within the scatter of data, when the grain size was reduced below ~20μm. At elevated temperatures, increased ductility was attained by reducing the grain size to below a critical level. For example, at 750°C, the elongation of the undoped alloy increased from <1% for grain sizes of 40μm or more to over 40% for a 2.9μm grain size. Similar trends were observed for the boron-doped alloy. By contrast, Takeyama and Liu [71] have reported that the ductility was grain size independent for boron-doped Ni-rich Ni_3Al up to 760°C; at higher temperatures, the ductility was observed to increase with decreasing grain size. Both Weihs et al.[60] and Takeyama et al.[71] have noted a trend of decreasing ductility with increasing test temperatures for similar grain-sized specimens. In both cases, the fracture behavior of fine grained specimens changed from dimple type at room temperature to increasingly intergranular at higher temperatures [71]. The ductility minimum is much reduced in severity (and less intergranular cracking occurs) when tests are carried out in vacuum. For example, for an alloy containing 0.5% Hf and 0.07%B, the ductility at 760°C increased steadily as the air pressure was decreased from 1 to 10^{-8} torr [72]. The embrittlement in oxygen-bearing environments at elevated temperatures appears to be due to the adsorption of oxygen at grain boundaries, thereby lowering cohesion. By contrast, even cube-oriented single crystals of $Ni_3(Al,Ti)$, when tested over a range of temperatures, exhibited sharply decreased ductility from about 15% at room temperature to ~1% at 827°C, the peak flow stress temperature (see below)[57], suggesting that the embrittlement at elevated temperatures could be an intrinsic behavior of the lattice.

Ni_3Al along with some other $L1_2$-structured intermetallics like Ni_3Ge, Zr_3Al, Co_3Ti etc., exhibit anomalous yield strength behavior, where the yield strength increases with increasing temperature up to about 650°C [73]. The dislocations in $L1_2$ alloys are paired (Burgers' vector a/2<110>) with an anti-phase boundary (APB) between them. The anomalous yield behavior is postulated to arise from the anisotropy of APB energy and the lack of mobility of superlattice screw dislocations (which governs the plastic deformation behavior of Ni_3Al) on {100} planes [74]. The splitting of the screw dislocation is energetically more favorable on the {100} planes [75] due to the lower APB energy. These superlattice dislocations are, however, sessile because the cores of the partials spread outside the plane of the APB. The higher energy superlattice dislocation on {111} plane is, by contrast, glissile with the core being confined to the slip plane. The cross-slip from {111} to {100} planes requires the partials to be coalesced first into a single dislocation, hence, at low temperature, deformation is on {111}. At higher temperatures, however, such cross slip becomes possible due to thermal activation, leading to dislocation immobilization (Kear Wilsdorf mechanism); the sessile dislocations act as obstacles giving rise to increased flow stresses. The decrease in yield strength beyond the peak temperature (~700°C) is associated with the onset of cube slip where both partials glide on {100} planes[76].

The peak flow stress temperature is influenced by grain size for both the stoichiometric[60] and Ni-rich composition[71]. For the stoichiometric alloy, Weihs et al.[60] have reported that the peak temperature is shifted to lower temperatures for smaller grain sizes and the magnitude of anomalous hardening is reduced. In fact, the finest grain sized alloy (~3μm) did not exhibit any anomalous strengthening. At temperatures in excess of a critical temperature (~627°C in their data), the coarser grain-sized alloys were stronger. Furthermore, for similar grain sizes, boron-doped alloys exhibited higher flow stresses than the undoped alloy. Takeyama and Liu [71] have concluded that a similar type of behavior occurs for the boron-doped Ni-rich alloy; the peak flow stress for similar grain size (~85μm) boron-doped Ni-rich alloy was approximately similar to the undoped stoichiometric alloy [60].

NiAl + Ni_3Al

Russell and Edington [20] first reported the mechanical behavior of the cast and homogenized, two-phase NiAl+Ni_3Al alloy, Ni-36Al, aged at 875°C for 1, 3 and 24 hrs (the microstructures have been discussed earlier). Room temperature compression tests showed a smooth transition from elastic to plastic behavior. The 0.2% flow stress was measured at 705 MPa for an one hour ageing time and 765MPa for 3 and 24 hrs ageing times. Fracture strains >8% (in compression) were obtained in all cases. Room temperature impact values of 0.14-0.28 m.kgf were obtained (using cast and extruded alloys), which was significantly higher than the 0.012 m.kgf value reported for stoichiometric NiAl, the most ductile composition. Alloys of composition (Ni-38Al) similar to the matrix (NiAl) of heat treated Ni-36Al, were also tested after similar ageing treatment. The 'matrix' alloy exhibited <1% strain to fracture over the temperature range 0-600°C, although ~15% strain was recorded at 700°C. The improved room temperature compressive ductility and impact strength of the two-phase alloy were attributed to the presence of Ni_3Al precipitates, which were thought to inhibit the nucleation and propagation of microcracks.

An added benefit of two-phase alloys was the improved high temperature strength. Ni-36Al, aged at 875°C for 1 hr, when tested in the temperature range 0-700°C, exhibited essentially a temperature independent 0.2% flow stress of 700MPa[20].

Khadkikar et al.[27] have also studied the mechanical properties of two compositions in this two-phase region, Ni-29Al and Ni-35Al (with small additions of Hf-0.9% and B-0.1%). The alloys were processed through a powder extrusion route. The microstructures resulting from various heat treatments have already been discussed above. Both the as-extruded alloys failed in a brittle manner in tension. However, Ni-29Al, homogenized at 1250°C and either water quenched (phases in microstructure: Ni_3Al+martensite) or annealed at 850°C for 24 hrs (phases present: Ni_3Al+NiAl), exhibited deviations from purely elastic behavior under tensile loading. By contrast, Ni-35Al was reported to be too brittle to be fabricated into tensile specimens.

Moskovic[21] reported an almost ten-fold increase in room temperature fracture toughness of a ternary two-phase alloy, Ni-30Al-7Cr, over single phase NiAl. The fracture toughness of single phase material was 6 $MPa\sqrt{m}$, which was increased to 50 $MPa\sqrt{m}$ following heat treatment to produce a stable dispersion of rod-shaped Ni_3Al precipitates in a NiAl matrix.

2.3 Ni-Fe-Al Alloys Literature Survey:

2.3.1 Ni-Fe-Al Phase Diagrams

The pioneering investigation of the ternary Ni-Fe-Al system is due to Köster[77] who explained the relationship of the face-centred cubic and body-centred cubic phase fields. This was followed by x-ray investigations of the ternary system by Bradley and Taylor [78] who proposed a complete phase diagram, which provided a rapid survey of the distribution of solid phases at low temperatures, then unknown. The elevated temperature isotherms were subsequently proposed by Bradley [79, 80] based on his microscopical studies into the ternary system. The phase diagram literature has recently been reviewed by Rivlin and Raynor [81].

Figure 2.3a shows the liquidus and solidus projections of the ternary system [78], constructed between 1600°C and 1350°C, at intervals of 50°C, the solidus and liquidus being represented by solid and dashed lines respectively. The two liquidus surfaces intersect at a univariant line which extends from the Al-Ni eutectic ($L = \beta' + \gamma'$) at 1385°C to the Fe-Ni peritectic ($L + \delta_{Fe} = \gamma_{Fe}$) at 1513°C. From 1385°C to the point U1 (1380°C), the reaction is Al-Ni eutectic reaction. At U1, the reaction is $L + \gamma' = \gamma_{Ni} + \beta'$. From U1 to lower temperatures, the univariant peritectic reaction is $L + \gamma_{Ni} = \beta'$, i.e. the two liquidus surfaces in this range define the primary crystallization of γ_{Ni} and β', respectively [81]. This again is terminated by a second invariant point U2 (at 1350°C where the reaction is $L + \beta = \gamma_{Ni} + \beta'$, β' and β being ordered and disordered bcc), located by Bradley [79] at Ni-6.4Al-71.4Fe (wt.%). According to Bradley [79], there is a minimum at 1340°C in the liquidus and solidus, located in the $\gamma_{Ni} + \beta'$ region at approximately Ni-3Al-53Fe (wt.%).

Solid phases in the iron-rich corner have been examined extensively by Bradley [79, 80] and Kiuti [82-84] and are generally in agreement, specially with regard to the development of β'+β miscibility gap. However, while Bradley used anneals of up to nine weeks at 750°C, Kiuti's anneals were only 1 hr, hence the adopted isotherms [81] are based on work of Bradley [79, 80] and Bradley and Taylor [78]. Figure 2.3b is an isotherm based on x-ray investigations by Bradley and Taylor [78] of powders (from lumps which were homogenized at 1300°C) annealed at 900°C and cooled at 10°C per hour *in vacuo* to room temperature. At compositions up to 50 at.% Al, the solid phases involve only two cubic structures, fcc and bcc, and their ordered derivatives. The ordered-fcc phases Ni_3Fe (α') and Ni_3Al (γ'), in spite of being isomorphous, do not form a continuous solid solution, unlike the ordered-bcc structures FeAl and NiAl which are mutually soluble, presumably due to the low disordering temperature and sluggish ordering kinetics of the Ni_3Fe phase. The two-phase area β+β' constitutes a miscibility gap of ordered and disordered bcc structures identified by the investigations of both Kiuti [84] and Bradley and Taylor [78].

Figures 2.3c-i show sothermal sections from 1350°C to 750°C at 100°C intervals as reported by Bradley [79, 80]. At 1350°C (fig. 2.3c), a narrow $\gamma_{Fe}+\beta$ region connects the Fe-Al system with the invariant point ($\gamma_{Fe}+\beta+\beta'+L$), from where the $\gamma_{Ni}+\beta'$ region extends to the three-phase triangle $\gamma_{Ni}+\gamma'+\beta'$. The three-phase region borders two two-phase regions, $\gamma'+\beta'$ and $\gamma'+\gamma_{Ni}$. The $\gamma_{Ni}+\beta'$ phase field is wider at 1250°C (fig. 2.3d) than at 1350°C. Also, the $\gamma_{Fe}+\beta$ and $\gamma_{Ni}+\beta'$ phase fields are shifted towards higher aluminum contents. The $\gamma_{Ni}+\gamma'$ phase field is shifted towards the Ni side and the $\gamma_{Ni}+\beta'$ field widens on both sides. The three-phase triangle $\gamma_{Ni}+\gamma'+\beta'$ is still very narrow. The main difference, however, is the appearance of another three-phase traingle $\gamma_{Fe}+\beta+\beta'$ and a two-phase region $\beta+\beta'$ from the $\gamma_{Fe}+\beta$ region near the Fe corner.

At 1150°C (fig. 2.3e), there is further widening of all the miscibility gaps, with the $\gamma_{Ni}+\gamma'$ phase field widening out in the direction of Fe-Ni, in confirmity with the extension of the γ' phase field itself towards the Fe-Ni side. The three-phase $\gamma_{Ni}+\gamma'+\beta'$ triangle widens out as does the $\gamma_{Fe}+\beta+\beta'$ phase field.

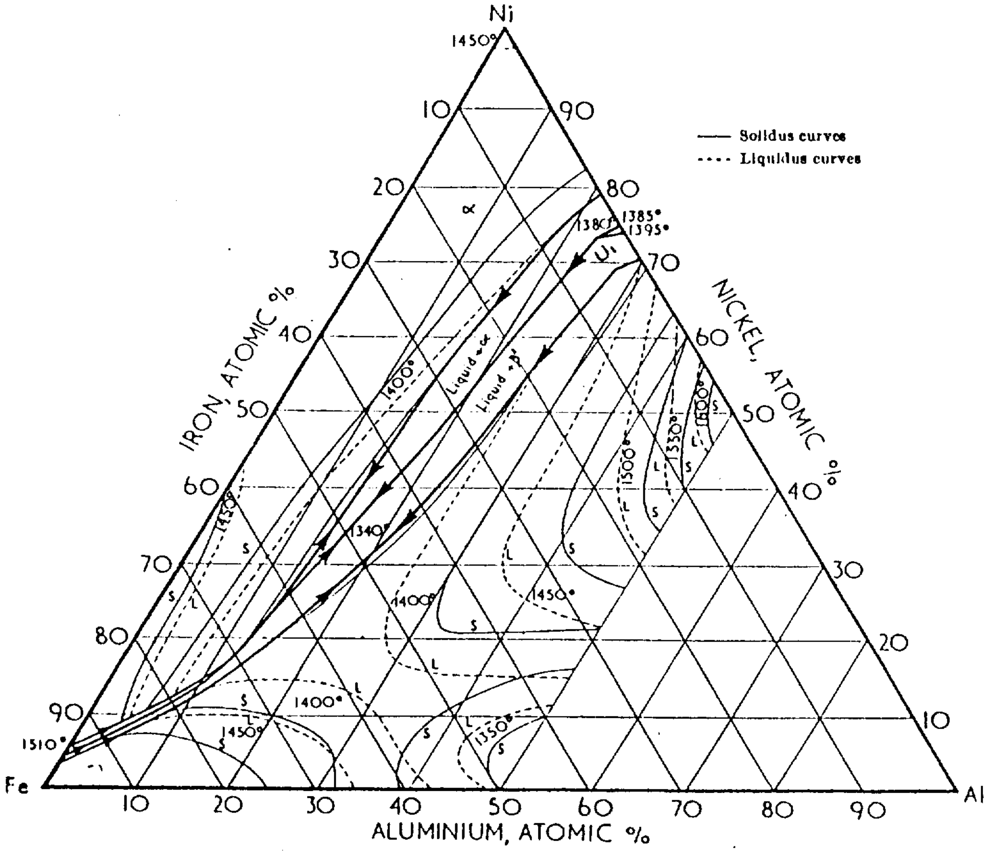
Ni
1450°
—— Solidus curves
···· Liquidus curves
1385°
1395°
1380
IRON, ATOMIC %
NICKEL, ATOMIC %
Liquid + α
Liquid + γ'
1400°
1340°
1500°
1550°
1600°
1450°
1400°
1350°
1510°
α
L
S
Fe
Al
10
20
30
40
50
60
70
80
90
ALUMINIUM, ATOMIC %

Figure 2.3a Solidus and liquidus projections of Ni-Fe-Al alloys between 1600°C and 1350°C at 50°C intervals [after 78].

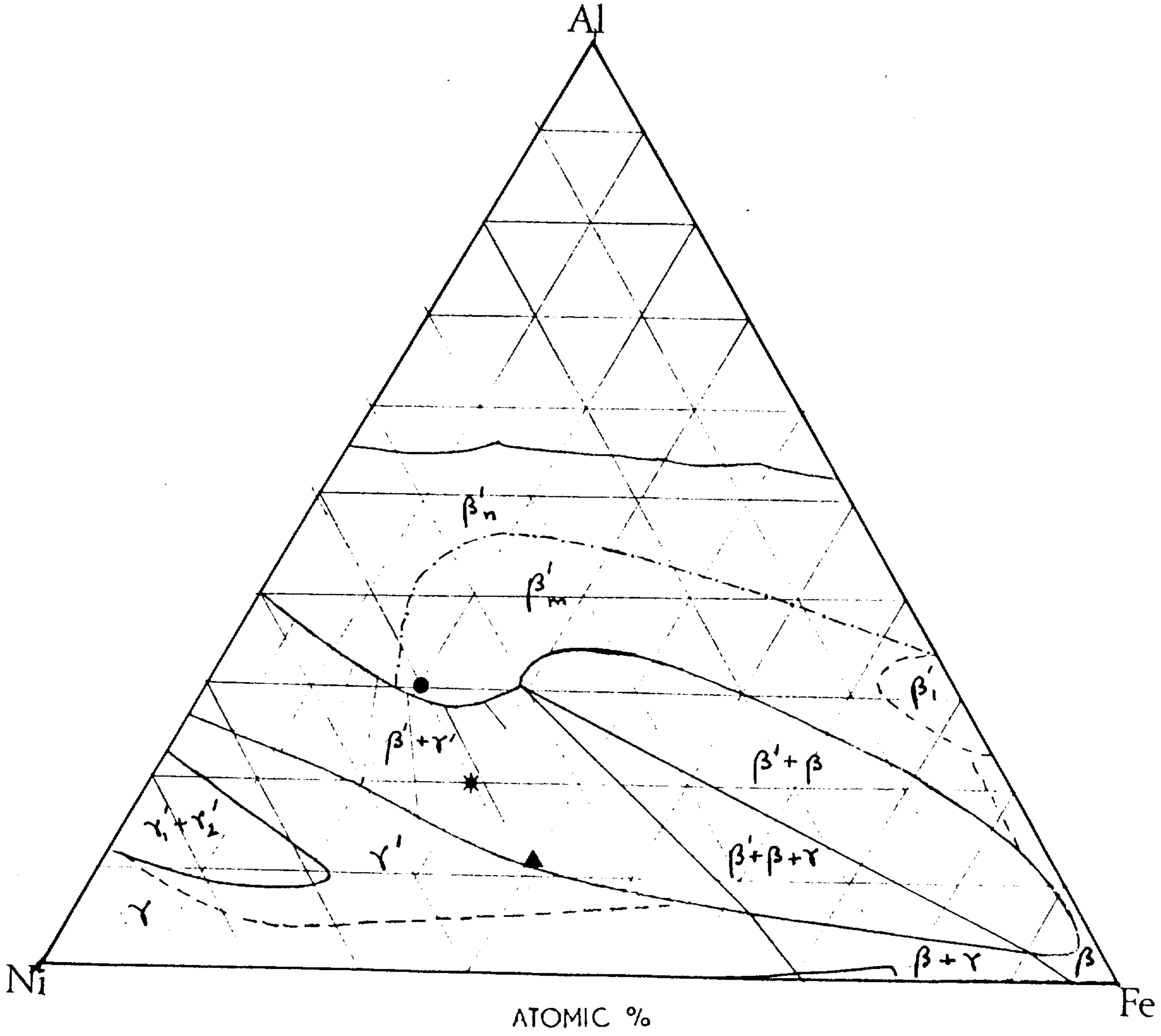

Figure 2.3b Solid phases at room temperature based on x-ray investigations of Bradley and Taylor [78] using powder annealed at 900°C and cooled at 10°C per hour. Seven tie-lines, as suggested by Bradley and Taylor [78], are shown in the $\beta'+\gamma'$ multi-phase field. The subscripts m and n, respectively, represent magnetic and non-magnetic β' alloys. The dashed (---) lines represent superlattice boundaries while the chain-dashed line (-.-.-) represents magnetic boundary. Note that the Ni-rich end of this phase diagram is considerably from the Ni-rich end in the 400°C isotherm in fig. 2.3j. The symbols (•), (Δ) and (*) represent the alloy compositions Ni-30Al-20Fe, Ni-20Al-30Fe and Ni-12Al-40Fe respectively on the isotherms (figs. 2.3b-j).

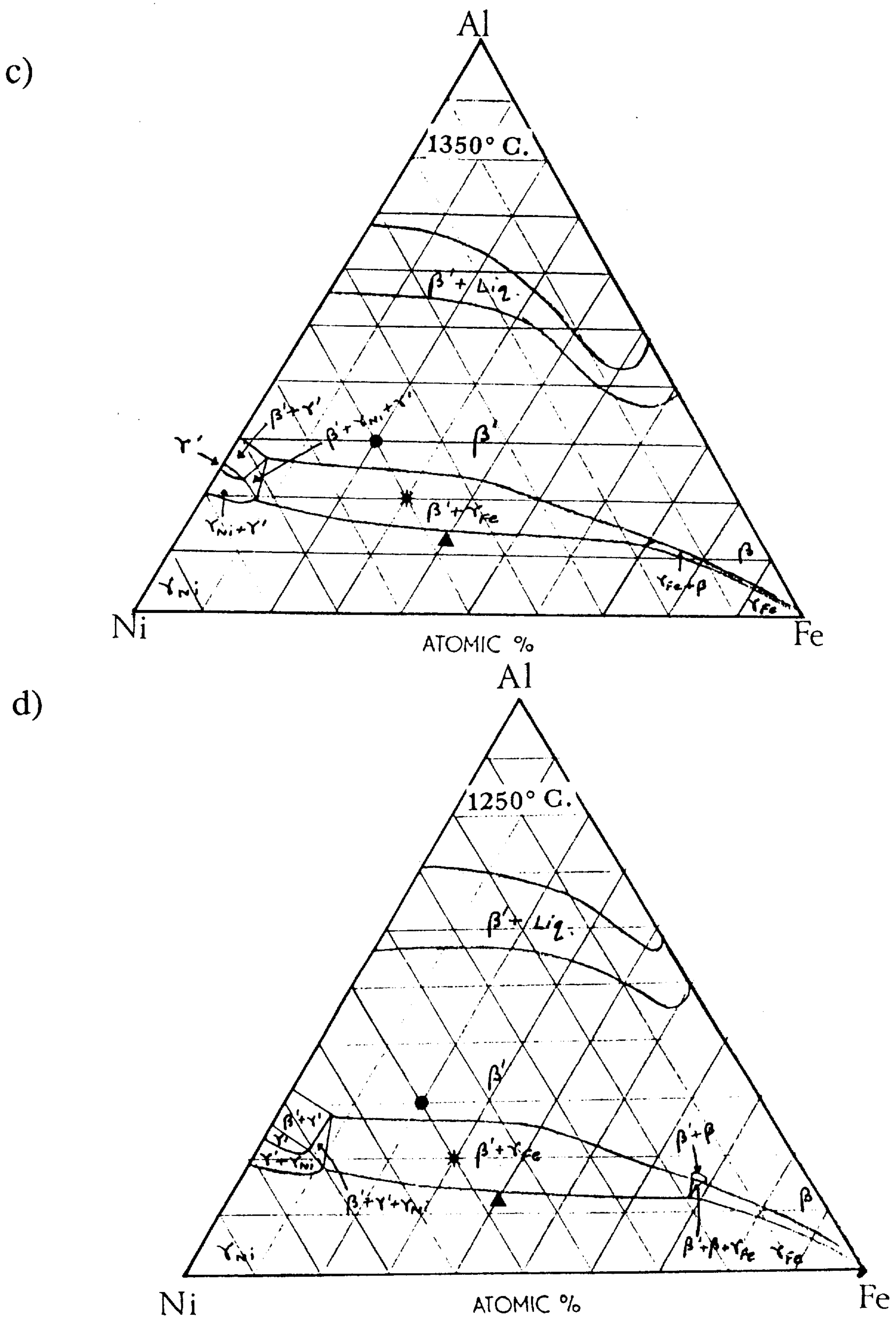

c)
Al
1350° C.
β' + Liq.
β'
β'+γ'
β'+γ_Ni+γ'
γ'
γ_Ni+γ'
β'+γ_Fe
β
γ_Fe+β
γ_Fe
γ_Ni
Ni
ATOMIC %
Fe
d)
Al
1250° C.
β'+ Liq.
β'
β'+γ'
γ'
γ'+γ_Ni
β'+γ_Fe
β'+γ'+γ_Ni
β'+β
β
β'+β+γ_Fe
γ_Fe
γ_Ni
Ni
ATOMIC %
Fe

Figure 2.3 c-d Isothermal sections of Ni-Fe-Al system: (c) 1350°C (d) 1250°C.

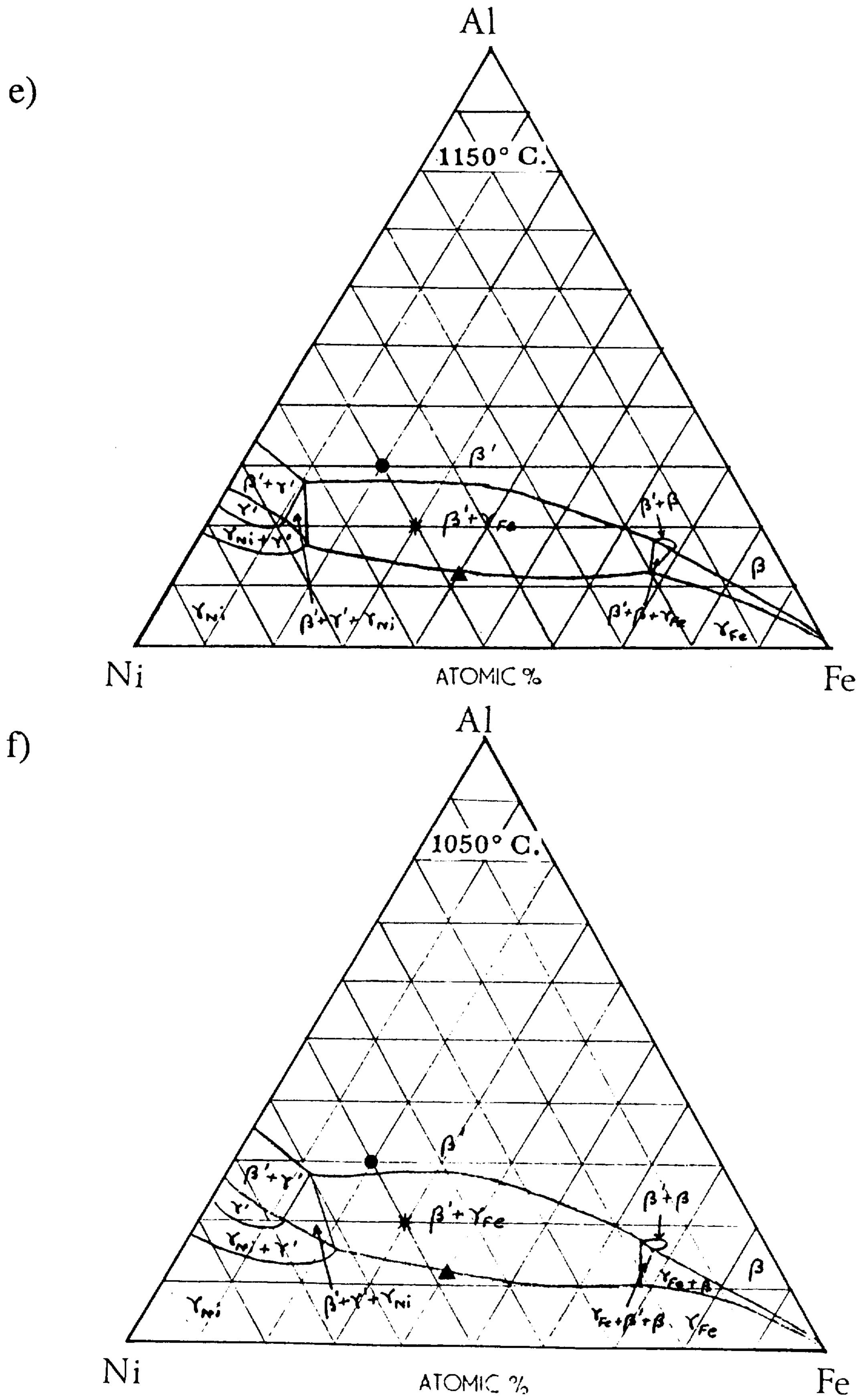
e)
Al
1150° C.
β'
β'+γ'
γ'
γNi+γ'
β'+γFe
β'+β
β
γNi
β'+γ'+γNi
β'+β+γFe
γFe
Ni
ATOMIC %
Fe
f)
Al
1050° C.
β'
β'+γ'
γ'
γNi+γ'
β'+γFe
β'+β
β
γFe+β
γNi
β'+γ'+γNi
γFe+β'+β
γFe
Ni
ATOMIC %
Fe

Figure 2.3 e-f Isothermal sections of Ni-Fe-Al system: (e) 1150°C (f) 1050°C.

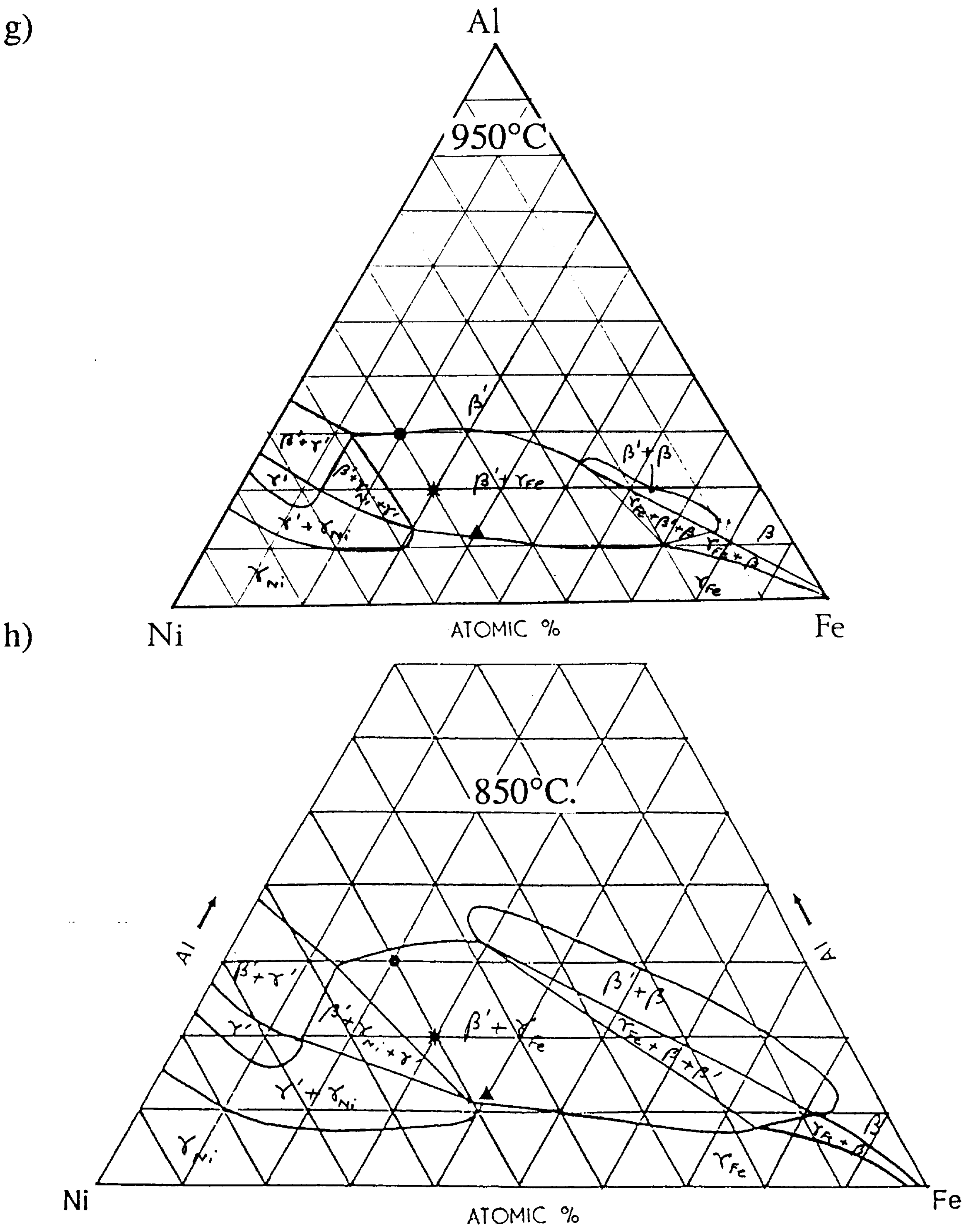
g)
Al
950°C
β'
β'+γ'
β'+β
γ'
β'+γNi+γ'
β'+γFe
γ'+γNi
γFe+β'+β
β
γFe+β
γNi
γFe
h)
Ni
ATOMIC %
Fe
850°C.
Al
Al
β'+γ'
γ'
β'+γNi+γ'
β'+γFe
β'+β
γFe+β+β'
γ'+γNi
γNi
γFe
γFe+β
β
Ni
ATOMIC %
Fe

Figure 2.3 g-h Isothermal sections of Ni-Fe-Al system: (g) 950°C (h) 850°C.

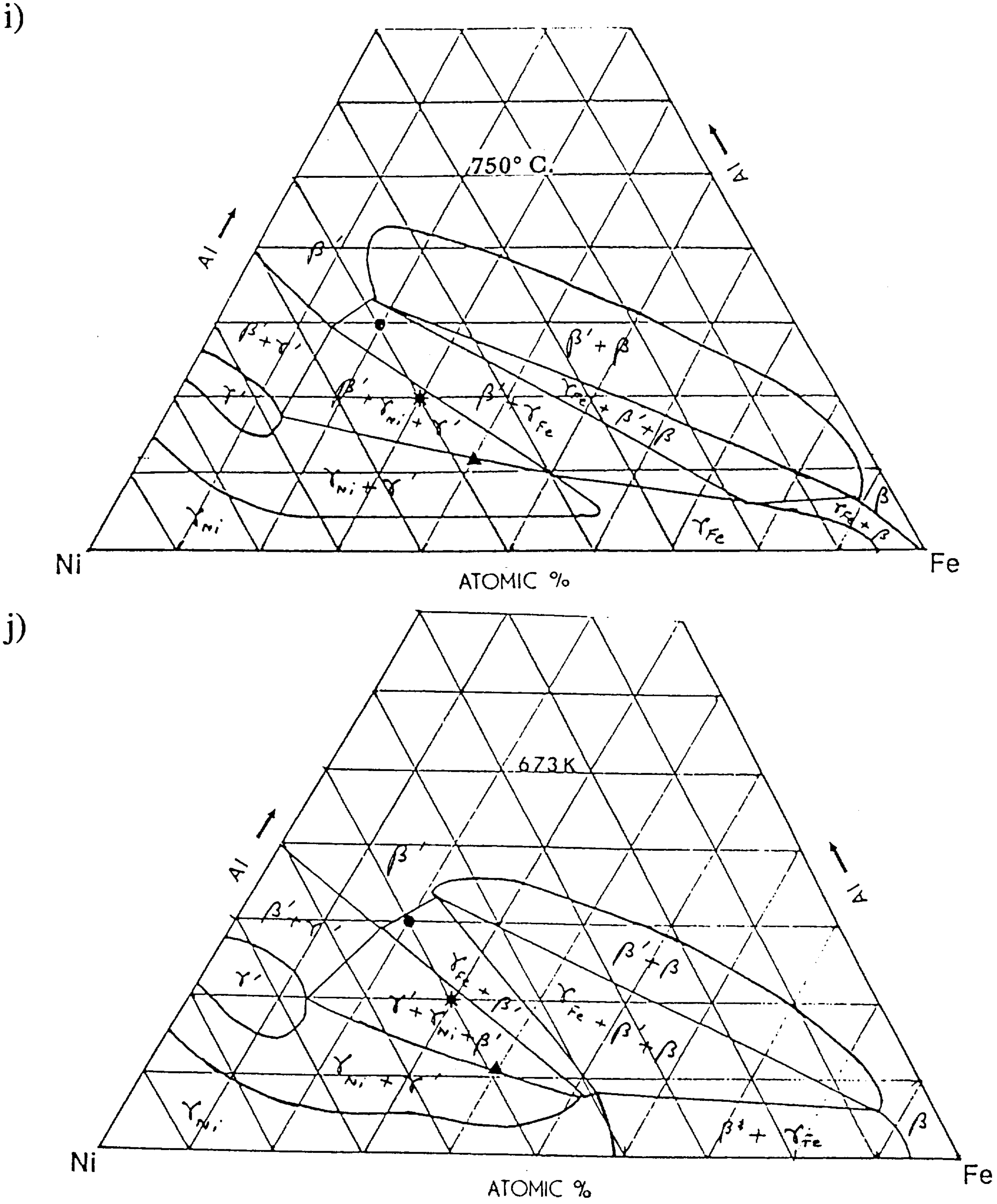

i)
750° C.
Al →
Al →
β'
β' + γ'
γ'
β' + γNi + γ'
β' + γFe
β' + β
γFe + β' + β
γNi + γ'
γNi
γFe
γFe + β
β
Ni
Fe
ATOMIC %
j)
673 K
Al →
Al →
β'
β' + γ'
γ'
γFe + β'
γ' + γNi + β'
γFe + β' + β
β' + β
γNi + γ'
γNi
β' + γFe
β
Ni
Fe
ATOMIC %

Figure 2.3 i-j Isothermal sections of Ni-Fe-Al system: (i) 750°C (j) 400°C.

Many of the tendencies shown in the 1150°C isotherm are carried over to the 1050°C isotherm (fig. 2.3f); a further widening of the miscibility gaps is found at all points. The $\gamma_{Ni}+\gamma'$ region widens on both sides; the $\gamma'+\beta'$ widens only on the Al side. The γ' region becomes more stable, and continues to encroach upon the $\gamma_{Ni}+\gamma'$ phase field, carrying with it the widening of the $\gamma_{Ni}+\gamma'+\beta'$ phase field. The $\gamma_{Fe}+\beta$ phase field is widened and displaced towards the Fe-Ni side. The $\gamma_{Fe}+\beta+\beta'$ triangle however, is displaced without being widened. The two-phase $\beta+\beta'$ phase field is still small, similar to 1150°C isotherm.

At 950°C (fig. 2.3g), the widening of the phase fields continue with the β' phases extending towards the Al corner and the γ_{Ni} region falling back towards the Fe-Ni edge of the isotherm. The enlarged $\gamma_{Ni}+\gamma'$ region gives rise to an enlarged three-phase region $\gamma_{Ni}+\gamma'+\beta'$, while the $\beta+\beta'$ region begins to expand rapidly (mainly in a direction perpendicular to NiAl), thereby leading to the establishment of a significant three-phase field $\gamma_{Fe}+\beta+\beta'$. The γ_{Fe} phase boundary falls back towards poorer Al levels leading to an expansion of the two-phase $\gamma_{Fe}+\beta$ phase field.

Isotherms at the lower temperatures of 850°C (fig. 2.3h) and 750°C (fig. 2.3i) exhibit similar trends as observed in the 950°C isotherm. The two-phase $\beta+\beta'$ field expands in all directions, but mainly perpendicular to NiAl. The second significant change is the extension of the two-phase $\gamma_{Ni}+\gamma'$ phase field towards the Fe-Ni edge and the Fe corner of the phase diagram, the extension being quite dramatic at 750°C. The extensions of the two-phase $\beta+\beta'$ and $\gamma_{Ni}+\gamma'$ phase fields lead to significantly expanded three-phase fields $\gamma_{Fe}+\beta+\beta'$ and $\gamma_{Ni}+\gamma'+\beta'$. The β' compositions of the two-phase and three-phase fields are pushed towards higher Al levels with decreasing temperature.

Figure 2.3j is an isothermal section at 400°C of the Ni-Fe-Al ternary system as reported by Sauthoff [85]. The two-phase $\beta+\beta'$ miscibility gap has narrowed in all directions compared to the 750°C isotherm, indicating that the miscibility gap is most stable only in an intermediate temperature range (around 750°C). By contrast, the three-phase $\gamma_{Fe}+\beta+\beta'$ phase field has widened considerably.

2.3.2 Lattice Spacing Constants and Defect Structures

Lipson and Taylor [86] reported contours of constant lattice spacing in the ternary Ni-Fe-Al system where a maximum in spacing at stoichiometric NiAl was observed to extend into the ternary system (see figure 2.4), but to a decreasing extent as the FeAl compositions were approached. Density measurements on the Al-deficient side (<50 at.%) suggested 2 atoms per unit cell while those on and the Al-rich side (> 50 at.%) suggested

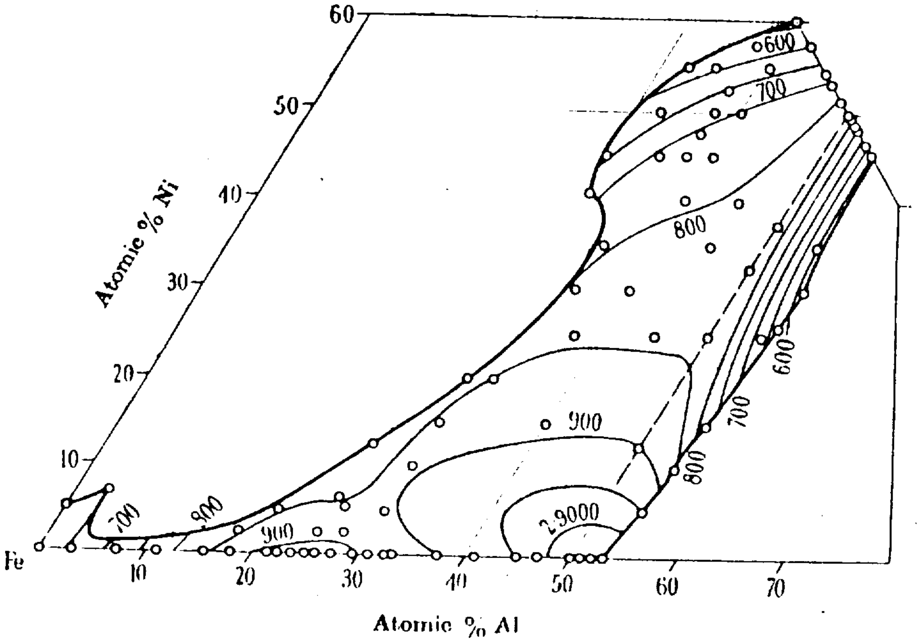

Figure 2.4 Contours of constant lattice spacing (only last three decimal places shown) in Ni-Fe-Al system (from Lipson and Taylor [86]).

less than 2 atoms per unit cell. The results suggested vacancies on the Al-rich side and anti-site defect structures on the Al-deficient side, similar to binary Ni-rich NiAl alloys [34,35]. The omission of atoms on the Al-rich side of stoichiometry and the attendant decrease in lattice spacing indicate the importance of atomic size factor; since Al atoms are larger than Ni or Fe atoms, the omission of atoms may result from the inability to squeeze in a bigger Al atom in place of a smaller Ni or Fe atom.

2.3.3 Mechanical Behavior of Ni-Fe-Al alloys

Prior to this investigation, there had been few studies on the mechanical behavior of Ni-Fe-Al β' or γ'-based alloys.

β' Alloys

Inoue et al.[28] studied the room temperature tensile behavior of wires of three β' alloys, Ni-25Al-30Fe, Ni-30Al-20Fe and Ni-30Al-30Fe, processed through an 'in-rotating-water' melt-spinning technique. The mechanical properties of Ni-30Al-20Fe (4μm grain size) have been discussed earlier (yield strength of 400 MPa and ~5% plastic strain, mixture of dimple and intergranular fracture; see section 1.4 "Macroalloying"). Both Ni-25Al-30Fe and Ni-30Al-30Fe exhibited a 2μm grain size, a high yield strength (~650 MPa and 750 MPa, respectively), and low plastic elongation (0.2%). The observed fracture mode was a mix of intergranular and transgranular cleavage fracture. The strong modulated contrast observed for β' (Ni,Fe)(Fe,Al) alloys was suggested to be related to the phase separation of β' alloys into NiAl-rich and Fe-rich phases (although no experimental evidence was presented), which in turn was suggested to be responsible for the decreasing room temperature ductility with increasing Al or Fe levels.

Investigations into the elevated temperature mechanical behavior of Ni-Fe-Al β' alloys were limited to compressive creep tests and 0.2% proof stress measurements by Rudy and Sauthoff [87, 88]. The alloy of composition Ni-50Al-10Fe exhibited a higher flow stress than stoichiometric NiAl over the range of test temperatures (RT-1000°C), presumably due to solid solution hardening by Fe on the Ni-sub-lattice. Also, at temperatures lower than 600°C, significant increases in proof stress was observed for Al-deficient alloys like Ni-40Al-10Fe. However, at temperatures in excess of 700°C, the Al-deficient alloys were weaker than the stoichiometric (50 at.% Al) alloys.

Investigations into creep behavior of Ni-Fe-Al β' alloys [88] indicated that Fe-rich stoichiometric β' alloys (e.g Fe-50Al-10Ni) exhibited worse creep resistance than Ni-rich β' alloys (e.g. Ni-50Al-10Fe) at 900°C. Furthermore, the creep resistance of Ni-50Al-10Fe β' alloy was superior to the stoichiometric binary NiAl alloys over the range of test temperatures 750°C-1027°C. The creep resistance was shown to be sensitive to iron content and to stoichiometry (see figures 2.5a-b). In particular, deviations from stoichiometry on Al-deficient side led to sharp decreases in creep strength.

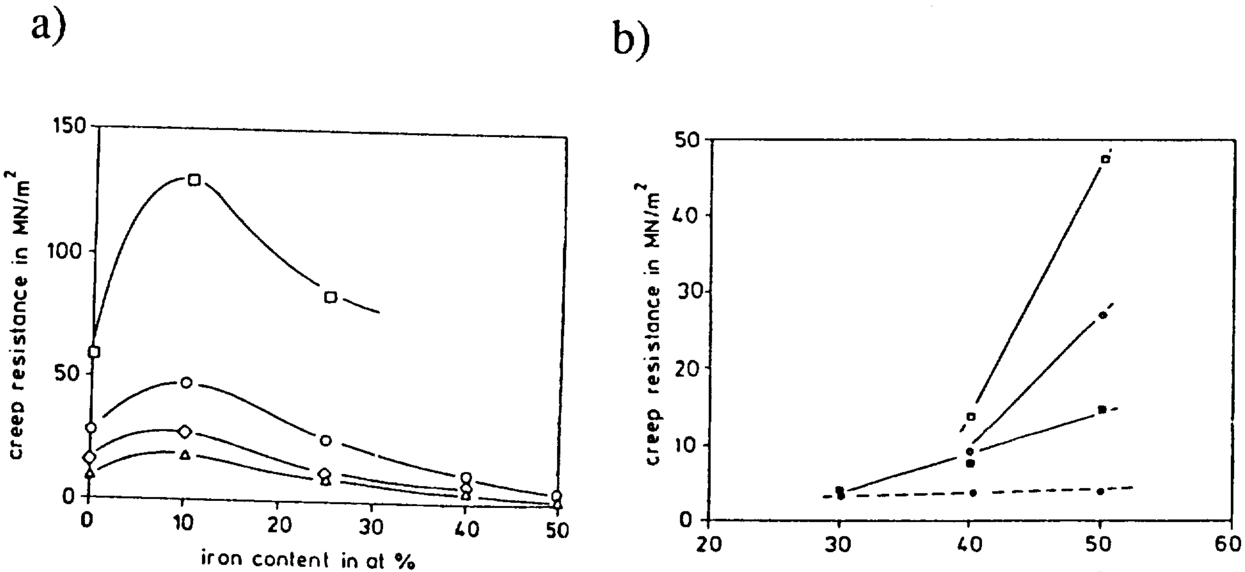

Creep resistance (at $\dot{\epsilon} = 10^{-7}\ s^{-1}$) as a function of the iron content for various temperatures (aluminium content, 50 at.%): □, $T = 750$ °C; ○, $T = 900$ °C ◇, $T = 982$ °C; △, $T = 1027$ °C.

Creep resistance as a function of the aluminium content ($\dot{\epsilon} = 10^{-7}\ s^{-1}$; $T = 900$ °C): □, $Fe_{10}Ni_{90-x}Al_x$; ○, $Ni_{100-x}Al_x$; ■, $Ni_{10}Fe_{90-x}Al_x$; ●, $Fe_{100-x}Al_x$.

Figure 2.5a-b Dependence of creep strength of Ni-Fe-Al β' alloys on (a) Fe content (b) Al content [88].

Another important difference in the creep behavior of Ni-rich and Fe-rich Ni-Fe-Al β' alloys was the deformation sub-structure. While both alloys exhibit dislocations of <100> Burgers' vector, the Fe-rich alloys exhibit a microstructure consisting of numerous tangled dislocations and loops while the Ni-rich alloys exhibit well-defined subgrain boundaries and a dislocation density lower than the Fe-rich alloys. This indicates that creep in Fe-rich alloys is dislocation glide controlled (also referred to as alloy-type creep behavior [89]) while in Ni-rich alloys is climb-controlled (referred to as pure metal-type creep behavior [89]).

γ'-based Alloys

Inoue et al.[29] have also studied the room temperature tensile behavior of wires of Ni-Fe-Al γ' alloy, Ni-20Al-10Fe, processed through an in-rotating-water melt spinning technique. The as-quenched microstructure consisted of equiaxed grains (~5μm in diameter) with a high density of anti-phase domains ~30-55 nm in diameter, inside each grain, indicating a lower degree of ordered state than the equilibrium state where no anti-phase boundaries (APB) were seen. The alloy exhibited a yield strength of 390 MPa and a plastic elongation of ~4%.

Horton et al.[90] have studied both the room temperature and elevated temperature mechanical behavior of Ni_3Al macroalloyed with Fe and microalloyed with boron. Most of the alloy compositions were chosen such that the sum of the Al level plus half the Fe added equalled 25% (i.e. assuming that Fe replaced Al and Ni equally) and the Fe concentration ranged from 0 to 20 at.%. While the microstructure of alloys containing up to 10 at.% Fe were single-phase, alloys with higher Fe concentration (e.g. Ni-17.5Al-15Fe, Ni-20Al-15Fe and Ni-15Al-20Fe) contained scattered regions of disordered web surrounding ordered precipitates (γ/γ' microstructure). Room temperature tensile tests indicated high plastic elongation for all the alloys, with the ductility decreasing (from ~55% for Ni_3Al to

~50% for Ni-20Al-10Fe to ~30% for Ni-15Al-20Fe) with increasing iron concentration while the yield strength increased (from ~250 MPa for Ni_3Al to 369 MPa for Ni-20Al-10Fe to ~600 MPa for alloy with 20 at.% Fe) with increasing iron concentration. Elevated temperature (400, 600, 850 and 1000°C) tensile tests indicated a trend of decreasing ductility with increasing temperature for all alloys until 850°C above which it rose slightly. Also, the alloys exhibited anomalous strengthening with increasing temperature, with the strength reaching a maxima around 600°C. The intermediate temperature (600 and 850°C) yield strength increased with increasing Fe concentration. However, at 1000°C, the yield strength was insensitive to the Fe concentration. Figure 2.6a-b summarizes the variation of yield strength and elongation as a function of iron content at different temperatures.

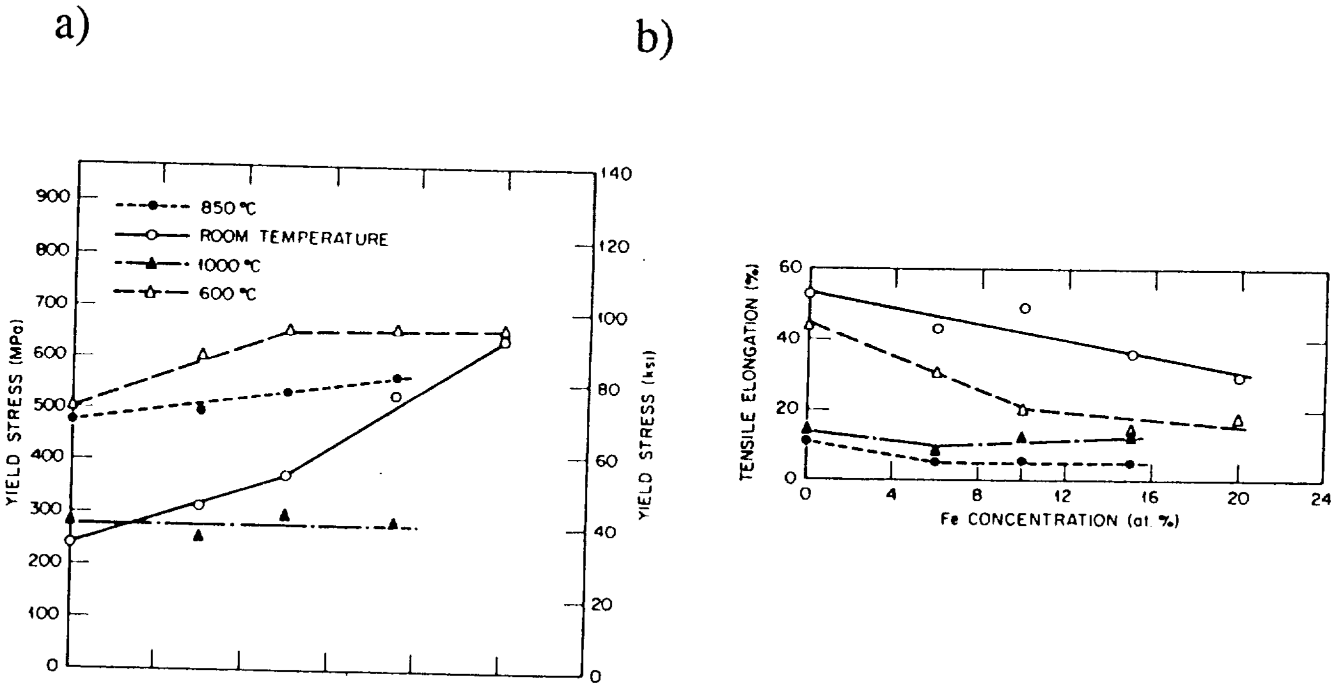

Figure 2.6 Dependence of (a) yield strength (b) elongation of γ' Ni-Fe-Al alloys on Fe concentration at different temperatures [90].

It is interesting to note that for the composition Ni-20Al-10Fe, while Inoue et al.[29] observed a high density of APB's in the rapidly solidified microstructure, Horton et al.[90] reported a single phase (no APBs) microstructure for the boron-doped conventionally processed alloy. Furthermore, while the undoped rapidly solidified alloy exhibited ~4% elongation at room temperature, the boron-doped alloy exhibited significantly increased ductility, indicating that boron-doping is effective even for Ni-Fe-Al γ' alloys. Cahn et al.[91] have suggested that ductility in Ni-Fe-Al γ' alloys is related to the anti-phase domain structure itself which exercise a "braking action" on the moving dislocations thereby reducing stress concentrations. The observations of Horton et al.[90], however, suggest that extensive ductility is possible even without anti-phase domains.

Multi-phase alloys

Inoue et al.[28] have studied the room temperature mechanical behavior of Ni-Fe-Al multi-phase alloys in wire form, processed through in-rotating-water melt spinning route. The alloys contained a fixed 20 at.% Al while the Fe concentration ranged from 20 to 32.5 at.% (balance Ni). The yield strength of the alloys varied between 400 and 600 MPa, the strength increasing with increasing Fe content. The plastic elongation of the alloys ranged from 3% for Ni-20Al-20Fe to a maximum of 17% for Ni-20Al-27.5Fe. The mechanical behavior of Ni-20Al-30Fe has already been discussed earlier (see section 1.4 "Multi-phase Microstructure").

Horton et al.[92] have also studied the microstructure and mechanical behavior (both room and elevated temperature behavior) of the multi-phase alloy Ni-20Al-40Fe, processed through an arc-drop casting and hot-rolling route. The microstructure following an anneal of 1 hr at 1050°C consisted of approximately equal amounts of β' and γ' phases. The compositions of the individual phases were reported as Ni-28Al-25Fe and Ni-11Al-54Fe, respectively. The alloy exhibited a room temperature yield strength and elongation of 700 MPa and 9% respectively. Interestingly, Inoue et al.[28] reported that the room temperature microstructure of the same alloy, processed through rapid solidification route, as β'. The yield strength and elongation were reported[28] as ~700 MPa and 0%. The elongation is in sharp contrast to that reported by Horton et al.[92] and is presumably related to differences in the microstructure, which itself is possibly related to difference in processing. At higher temperatures (600, 750 and 900°C), the strength decreased continuously (from ~260 MPa at 600°C to ~130 MPa at 900°C) while the elongation increased steadily, reaching almost 60% at 900°C.

2.4 Alloy Selection:

Based on the previous work outlined above [20,21,28-30,92], seven alloys were chosen for further investigation. Three alloys chosen from the Ni-Fe-Al β' phase field (see phase diagram in fig. 2.3b) were of composition (all compositions given here are in atomic percent) Ni-30Al-20Fe, Ni-40Al-30Fe and Ni-50Al-25Fe. The choice of the first composition was motivated by the observation of ~5% tensile ductility in the rapidly-solidified state [28]. The choice of the second alloy was motivated by the observation of limited tensile ductility in Fe-40Al [93]. The third alloy Ni-50Al-25Fe was chosen purely on the merit of its higher aluminum content; a higher aluminum content generally implies lower density and improved oxidation resistance for the alloy. Rather than rapid solidification, a more conventional processing route (casting + hot extrusion) was chosen to see if the tensile ductility could be obtained in a non-rapidly solidified state.

The fourth alloy chosen for investigation, Ni-20Al-30Fe, was from the Ni-Fe-Al multi-phase field (see fig. 2.3b). The alloy exhibited ~15% room temperature elongation and ~600 MPa yield strength [28] in a rapidly solidified state. Again, the processing route chosen was casting+hot extrusion to see if the previously observed tensile ductility was a result only of a rapidly-solidified microstructure or could also be reproduced in a non-rapidly solidified state. The emphasis was however, a better understanding of the deformation behavior of the alloy. Thus, as will be discussed later, the deformation behavior of alloys of composition (Ni-30Al-20Fe and Ni-12Al-40Fe) similar to the constituent phases of the alloy Ni-20Al-30Fe, processed through a similar (conventional) route, were studied and correlated with those of the alloy Ni-20Al-30Fe. Furthermore, based on reports of greatly increased ductility (from ~3% to 18% elongation) in a boron-doped state [30] for an alloy Ni-27Al-14Fe, it was decided to study the influence of microalloying with boron, if any, on the deformation behavior of Ni-20Al-30Fe.

The sixth alloy chosen for investigation was multi-phase binary Ni-36Al, also processed through a casting+hot extrusion route, the choice being motivated by the work of Russell and Edington[20]. The alloy was also microalloyed with boron for possible improvements in ductility.

CHAPTER 3

MATERIALS AND EXPERIMENTAL TECHNIQUES

This section describes the materials and adopted processing routes, methods of specimen preparation for mechanical testing, optical microscopy, transmission electron microscopy and experimental techniques for mechanical testing and x-ray diffraction.

3.1 Materials

As discussed in the last section (section 2.4), seven alloys were initially chosen for investigation (all compositions in atomic percent): Ni-30Al-20Fe, Ni-40Al-30Fe, Ni-50Al-25Fe, Ni-20Al-30Fe, Ni-36Al, Ni-20Al-30Fe-0.17B and Ni-36Al-0.17B. In order to understand the deformation behavior of the multi-phase alloy, Ni-20Al-30Fe, in terms of the deformation characteristics of its constituent phases, compositions of the individual constituent phases were determined, see later. These were approximately Ni-30Al-20Fe and Ni-12Al-40Fe. The former constituted the composition of one of the alloys selected for this study. Thus, an alloy of composition Ni-12Al-40Fe corresponding to the other phase was also added to the list of alloys to be investigated. Thus, eight alloys were chosen for this investigation: β' Ni-30Al-20Fe, Ni-40Al-30Fe and Ni-50Al-25Fe; undoped and boron-doped multi-phase Ni-20Al-30Fe and Ni-36Al; and Ni-12Al-40Fe. The alloy compositions and their expected microstructures are summarized in the Table 3.1.

3.2 Materials Processing

The processing route chosen for this investigation was casting followed by hot-extrusion. Ingots (Batch 1), 50 mm in diameter and 150 mm long of Ni-50Al-25Fe,

Table 3.1 Summary of alloy compositions and the expected microstructures

No.	Alloy Comp.(at.%)				Expected Microstructure
	Ni	Al	Fe		
1.	50	20	30		Multi-phase β'+γ/γ' alloy
2.	50	30	20		β' constituent of the above alloy
3.	48	12	40		γ/γ' constituent of the multi-phase alloy
4.	50	20	30	(0.17B)	boron-doped Ni-Fe-Al multi-phase alloy
5.	64	36			binary NiAl+Ni_3Al multi-phase alloy
6.	64	36		(0.17B)	boron-doped binary multi-phase alloy
7.	30	40	30		β' alloy
8.	25	50	25		β' alloy

Ni-40Al-30Fe, Ni-30Al-20Fe, Ni-36Al and Ni-20Al-30Fe were cast at United Technologies Research Center, and sections, 100 mm long, from each alloy were placed in 75mm O.D. cans of mild steel and extruded (subsequently referred to as Batch 1, single-extruded alloys) at 1100°C using a 7:1 area reduction ratio at Oak Ridge National Laboratory and sand-cooled. The extrusions for the alloys Ni-36Al and Ni-50Al-25Fe were not successful for these conditions since they were badly cracked (note: even the cast ingots of these alloys were cracked, indicating very brittle behavior). Sections, 25 mm in diameter and 100 mm long, of the remaining three extruded alloys were stripped of the steel jacket, re-canned in mild steel (50 mm O.D.) and re-extruded at 1000°C at a 6:1 area reduction ratio at NASA Lewis Research Center and air-cooled. These extrusions will be referred to as Batch1 double-extruded alloys. A second ingot of Ni-20Al-30Fe (henceforth referred to as Batch2), similar to the first ingot, was extruded at NASA Lewis at

1100°C using a 6:1 area reduction (first-extrusion), air-cooled and 100 mm sections re-canned in mild steel and re-extruded at 1000°C using the same area reduction; these alloys will be identified as Batch 2 single or double-extruded alloys.

Ingots, 37 mm in diameter and 150 mm long of Ni-12Al-40Fe, Ni-36Al, Ni-36Al-0.2B and Ni-20Al-30Fe-0.17B were cast at NASA Lewis and sections, 100 mm long, were canned in mild steel (50 mm O.D.), extruded using 16:1 area reduction ratio at 1200°C and air-cooled in their steel jackets. The higher extrusion ratio was chosen to yield extrusions of approximately 10 mm in diameter from which cylindrical bars, 6 mm in diameter, could be machined easily without much material wastage. The higher extrusion temperatures were necessitated by the higher extrusion ratios used.

The extrusion process parameters are attached in APPENDIX 1.

Table. 3.2 Compositions, Solidus and Liquidus temperatures of alloys investigated.

Composition (nominal,at.%)	Composition (analyzed, at.%)	C ppm (wt.)	O	Liquidus Temp., °C	Solidus Temp.°C
Ni-20Al-30Fe	Ni-19Al-30Fe	<100	60	1410	1370
Ni-20Al-30Fe-0.17B	Ni-20.5Al-30Fe-0.2B	68	42	-	-
Ni-30Al-20Fe	Ni-30Al-21Fe	<100	90	1490	1400
Ni-12Al-40Fe	Ni-12.5Al-38.5Fe	414	148	-	-
Ni-40Al-30Fe	Ni-37Al-27Fe	100	46	1450	1540
Ni-50Al-20Fe	Ni-53Al-20Fe	140	360	-	-
Ni-36Al	Ni-39Al	100	110	-	-

Table 3.2 shows the nominal compositions of the alloys together with the analyzed Ni, Fe, Al contents obtained by the Inductively Coupled Plasma method. Carbon and oxygen concentrations were obtained by the Leco Carbon Oxygen analysis method and are also listed in Table 3.2. Differential thermal analysis (DTA) was used to determine the solidus and liquidus temperatures of Ni-40Al-30Fe, Ni-30Al-20Fe and Ni-20Al-30Fe and are listed in Table 3.2; the solidus and liquidus temperatures for the remaining alloys could not be determined due to limited access to the DTA which was located at Lewis Research Center.

3.3 Mechanical Testing

Tensile Testing

Tensile specimens (as shown in fig. 3.1), 3.2 mm in diameter and 33.0 mm long were centerless-ground from the extruded bars with the tensile direction corresponding to the direction of extrusion. Prior to tensile testing, they were electropolished in an electrolyte consisting of 10% (by vol.) perchloric acid in methanol at -30°C and 20 volts. During polishing, the electrolyte was continuously stirred (magnetically) in a stainless steel beaker (cathode); the specimen to be polished was the anode and was itself rotated slowly during polishing. Heat treatments, if any, were carried out on polished tensile specimens.

Both room and elevated temperature tensile testing was carried out using Instron (at NASA Lewis) and MTS (at Dartmouth) testing frames. The tensile specimens were strained to fracture at a constant cross-head speed of 0.25 mm/min (initial strain rate of ~1 x 10^{-4} s^{-1}). While most room temperature tensile tests were carried out in air, a few were also performed in vacuum. The vacuum tests were carried out at ~10^{-7} torr in an Instron test frame equipped with a vacuum chamber (at NASA Lewis). The elevated temperature (427, 627 and 827°C) tensile tests were carried out in air using an Instron test frame equipped with a three-zone furnace (at NASA Lewis). The test specimens were heated to the test temperatures in less than 1.5 hrs with no overheating. The temperature was monitored using three thermocouples attached to the middle and shoulders of the specimens and any temperature differences across the specimen was minimized to ±3°C by varying the power input to the three zones of the furnace. Boron nitride was used as a parting agent to prevent bonding between the test specimen and the superalloy grips. In order to avoid buckling of the specimen due to thermal expansion, the bottom pull-rod was left free during heating to the test temperature and connected to the cross-head just before testing.

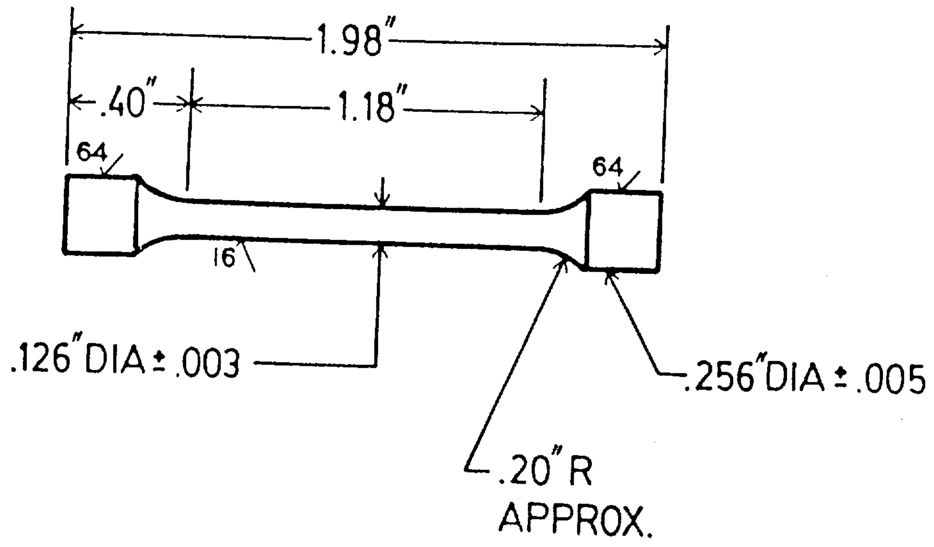

Figure. 3.1 The standard tensile specimen used for mechanical testing.

Compression testing

Cylindrical shaped specimens with a length-to-diameter ratio of (at least) 2 were used for compression tests. Specimens were machined from the extruded bars with the extrusion axis along the axis of the cylindrical specimen. The tests were carried out at room temperature in air in a MTS test frame at Dartmouth. The initial strain rate was maintained at ~1 x 10^{-4} s^{-1}. The specimens were compressed between two heat-treated high-carbon plattens to prevent any deformation of the loading train. $MoSi_2$ was used as a lubricating agent between the plattens and the specimen. Prior to commencement of test, the specimens were manually pre-loaded with a small load to maintain alignment with the loading axis.

Hot Hardness Testing

Hot hardness tests were carried out using a Nikon hot hardness tester at NASA Lewis. Cylinders, 3mm in diameter and 3 mm long, were indented with a sapphire indentor using a 500 gm load, over a range of temperatures from 27°C to ~900°C. The dwell time of the indentor was maintained at 10 sec. The specimen and the indentor were heated independently and their temperatures were monitored by thermocouples attached to the specimen and the indentor surface. The difference between the indentor and specimen temperature was always less than 5°C. Boron nitride was used as a parting agent between the cylindrical specimen and the holder. A helium atmosphere was used inside the test chamber for temperatures less than ~750°C; tests at higher temperatures were carried out in vacuum. An average of seven indentations was performed on each sample.

Compression Creep Testing

Elevated temperature creep tests were carried out in air in a constant load test frame equipped with a computer-controlled data acquisition system at NASA Lewis. Cylindrical-shaped test specimens of multi-phase Ni-20Al-30Fe and alloys similar to its constituent phases Ni-30Al-20Fe and Ni-12Al-40Fe, ~6.25mm in diameter and 12.5 mm long, were tested at 827°C at an initial stress of 60 MPa. The load was applied using a 4:1 constant load lever arm. The temperature was monitored to within ± 2°C using three thermocouples attached to the top, middle and bottom of the sample similar to high temperature tensile testing. The creep strain was measured using a super linear variable capacitor (SLVC) in conjunction with extensometers. Boron nitride was used as a parting agent between the

SiC push-bars and the test specimen to prevent welding of the specimen to the push-rod during the creep test. A small stress (~1 MPa) was applied to the specimen during heating to maintain alignment.

3.4 Metallography

Specimens for optical microscopy were prepared by grinding on SiC papers up to 600 grit, and polished successively with 1μm, 0.3μm and 0.05μm diamond paste and finally with colloidal silica. Polishing with colloidal silica resulted in a slight etching of the sample, suitable for optical microscopy on otherwise unetched samples. Polished multi-phase alloy specimens were etched with a reagent consisting of 50 gms molybdic acid dissolved in 25ml HF and 75 ml H_2O. Some specimens (e.g. the specimens of Ni-12Al-40Fe), however, required stronger etching and were etched with Marble's reagent. Also, the specimens of heat-treated β' alloys Ni-40Al-30Fe and Ni-30Al-20Fe were etched with Rosenhein's etch to compare the results with the optical microscopy work of Bradley [79, 80] on Ni-Fe-Al β' alloys. Optical microscopy work was completed using a Nikon Epiphot microscope equipped with differential interference contrast (DIC) imaging at NASA Lewis and a Reichert MeF2 metallograph at Dartmouth.

3.5 Electron Microscopy

Scanning Electron Microscopy

Specimens for fracture surface examination required little or no specimen preparation (other than a wash in methanol or acetone and mounting on the appropriate holder) and were examined in a JEOL JSM 35C (Dartmouth) or a JEOL 840F (NASA

Lewis) scanning electron microscope. Specimen preparation for examination of longitudinal sections of deformed tensile specimens (in back-scattered "compo" mode) was similar to the metallographic sample preparation described earlier.

Transmission Electron Microscopy

Thin foils from deformed or undeformed sections of the tensile specimens were prepared by grinding 3mm diameter discs from 600μm to 250μm thickness on 600 grit SiC paper and either electropolishing or ion-milling them to perforation. Samples for elevated temperature microstructural examination were prepared from the undeformed ends of the tensile-tested specimens, by re-annealing them at the respective test temperatures and water quenching. Multi-phase Ni-20Al-30Fe specimens were prepared by electropolishing 3 mm discs, about 250μm in thickness, in a Struers Tenupol using a solution of 30% (by vol.) HNO_3 in methanol at 248K and 10 volts (~0.75 Amp.). Similarly, thin foils of γ/γ' alloys were prepared by electropolishing in a solution of 10% (by vol.) H_2SO_4 in methanol at 268K and 10 volts. Thin foils of the β' alloy were ion-beam thinned to perforation using a gun current of 0.5 mA and a gun voltage of 6 kV. Specimens for examination of the deformation sub-structure in both multi-phase and β' alloys were prepared by ion-milling techniques as described above.

The thin foils were examined in a 200 kV JEOL 2000FX transmission electron microscope equipped with a Tracor Northern 5500 II energy dispersive x-ray spectroscopy (EDS) system.

3.6 X-ray Diffraction

X-ray diffraction experiments were carried out on powder and bulk samples (from extrusions) in a computer controlled SIEMENS D5000 diffractometer equipped with a

Kevex solid state detector connected to a Microvax 2000 data acquisition system. Powders of -325 mesh size were obtained in a rapidly-solidified state from Homogeneous Metals Inc.. Annealing of powder was performed at 500°C or 750°C in flowing argon; the crucibles holding the powder were wrapped in aluminum (for 500°C anneals) or tantalum foils (for 750°C anneals). Bulk samples were prepared by sectioning extrusions parallel, perpendicular and oblique (at 45°) to the extrusion direction. The transverse and oblique sections yielded round and elliptical samples which do not provide a constant area as illuminated by the beam (a necessary condition for meaningful quantitative x-ray diffraction analysis) through any chosen angular rotation range. Thus, the round and elliptical samples were cut into square and rectangular shaped samples, which provide a constant irradiated length in one direction (normal to a line drawn from source to detector). Samples were annealed in flowing argon, polished metallographically and etched to obtain a strain-free surface prior to examination in the diffractometer.

The slit sizes chosen corresponded to the dimensions of bulk samples or powder-filled areas. The lateral spread of the beam (see figure 3.2) on the sample was a function of the angle of incidence of x-rays on the sample and was derived to be of the form:

$$L = (\text{slit size in mm}) * (1+k) / \sin\theta$$

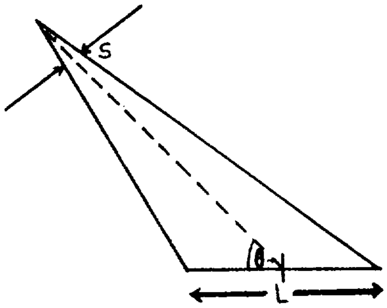

Figure. 3.2 Relationship between primary slit size and specimen dimensions.

where L is the length of irradiated area (along a line drawn from x-ray source to detector), θ the angle of x-ray incidence at the axis of diffractometer, k a constant determined experimentally to be ~0.5 using long time exposures on glass slides mounted at the reflection plane and measuring the dimensions of irradiated impression left by the x-ray beam. The step sizes used during scanning were less than 0.5° (usually 0.032°), the counting times were limited to a maximum of 50 sec for Cu k_α radiation and about 100-200 sec for Cu k_β radiation.

Bulk samples were mounted on a glass slide, placed inverted (with the sample touching the glass plate) on a flat glass plate, and attached to the sample holder with putty. This procedure ensures that the top surface of the bulk sample is in the same plane as the three reference pins (which define the focussing plane) of the diffractometer. Powders were loaded using the back-loading technique where a hollow rectangular slit is placed on a glass plate, filled with powder loaded from back, compressed (scraping of any excess) and secured firmly at the back using a glass slide and putty. The powder in contact with the glass plate (top surface) is the side exposed to x-rays and is usually free from any texture effects.

The data obtained were analyzed using the SIEMENS program DIFFRAC 500.

CHAPTER 4

Multi-phase Ni-20Al-30Fe and Its Constituent Phases

4.1 This chapter presents the room temperature and elevated temperature microstructures, mechanical properties and deformation behavior of the as-extruded multi-phase alloy, Ni-20Al-30Fe, and alloys similar to its constituent phases along with the results of in-situ straining experiments in the ternary multi-phase alloy.

4.2 Microstructures

4.2.1 Room Temperature

Multi-phase Alloy

According to figure 2.3b, which is a section of the Ni-Fe-Al phase diagram for alloys cooled slowly (10°C/hr) from the homogenization temperature of 900°C, the alloy Ni-20Al-30Fe (marked with a '*') lies in a two-phase region ($\beta' + \gamma'$) while the alloys Ni-30Al-20Fe (•) and Ni-12Al-40Fe (Δ) lie at the edge of the two-phase region in the β' and γ' phase fields, respectively. Note that β' represents the B2-structured (Ni,Fe)(Fe,Al) alloys. Similarly, γ' represents the $L1_2$-structured $(Ni,Fe)_3(Fe,Al)$ alloys. The symbols β and γ represent, respectively, the b.c.c and f.c.c phases in the Al-deficient section of the phase diagram.

Optical microscopy of the transverse sections of single-extruded (Batch 1) Ni-20Al-30Fe (see figure 4.2.1a) showed a coarse pro-eutectic phase (~50μm in diameter) distributed in a fine eutectic matrix. TEM confirmed this observation and showed that the lamellae width of both phases in the eutectic were similar (~0.5μm) (fig. 4.2.1b). The crystal structures of different phases in the extruded multi-phase alloy were identified by

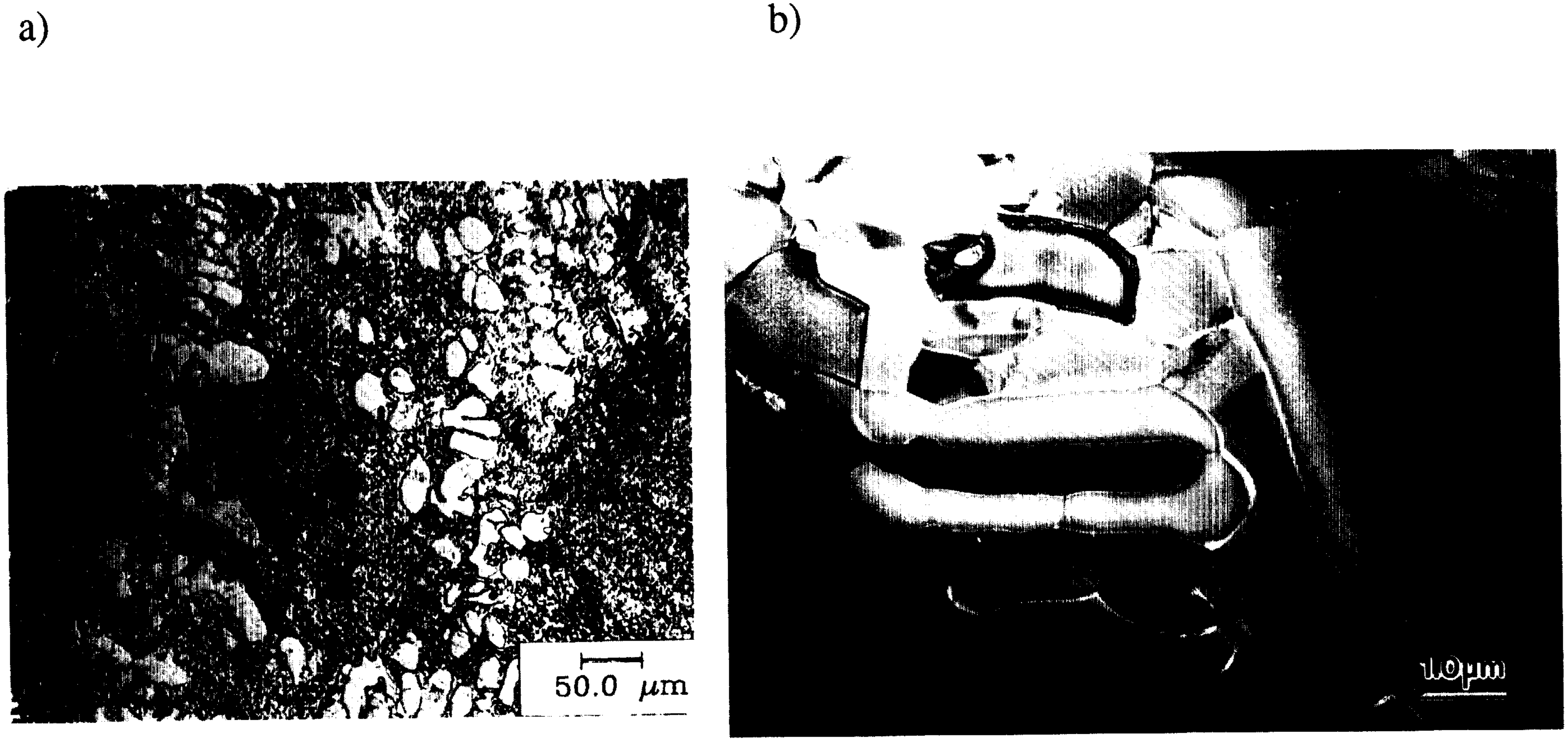

Figure 4.2.1 Single-extruded multi-phase alloy Ni-20Al-30Fe: (a) optical micrograph showing a coarse (~50μm) pro-eutectic phase in a fine-scaled eutectic (b) TEM bright field micrograph showing a eutectic lamellae width of ~0.5μm (c) SAD pattern from the coarse pro-eutectic phase showing a B2 structure (d) SAD pattern from a eutectic phase (composition Ni-12Al-40Fe) showing a $L1_2$ structure (see superlattice spots).

ORIGINAL PAGE
BLACK AND WHITE PHOTOGRAPH

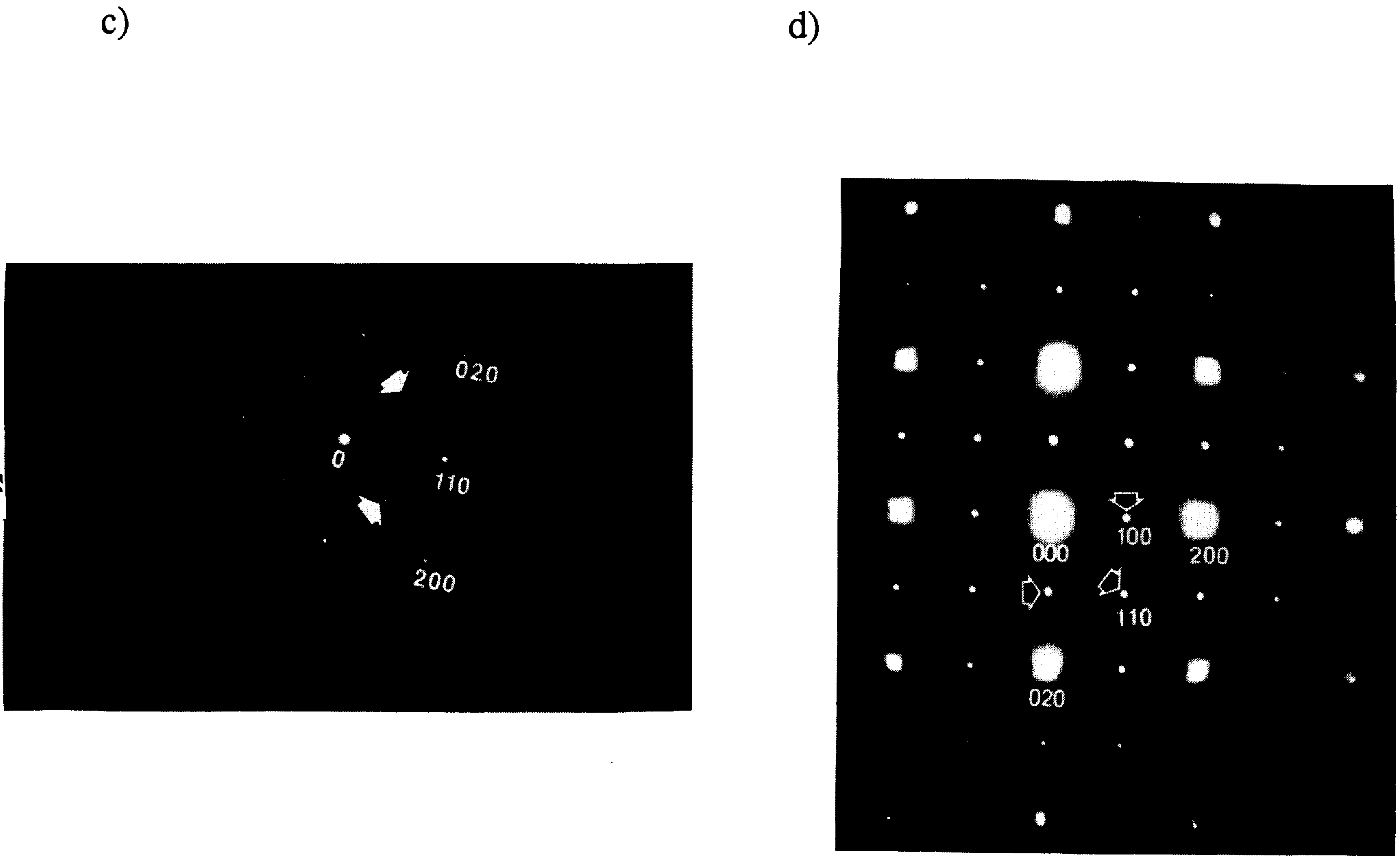
c)
020
0
110
200
d)
000
100
200
110
020

Figure 4.2.1 continued.

ORIGINAL PAGE
BLACK AND WHITE PHOTOGRAPH

Selected Area Diffraction (SAD) in the TEM. SAD patterns from the pro-eutectic and one of the eutectic phases indicated a B2 crystal structure (fig. 4.2.1c); superlattice reflections in the SAD patterns (fig. 4.2.1d) from the other eutectic phase indicated a $L1_2$ crystal structure. The compositions of pro-eutectic phase and phases in the eutectic were determined using EDS on thin foils to be approximately:

B2 pro-eutectic phase : Ni-30Al-20Fe (at.%)
B2 eutectic phase : Ni-32Al-15Fe
$L1_2$ eutectic phase : Ni-12Al-40Fe

These measurements of constituent phase compositions of the single-extruded multi-phase alloy form the basis for the selection of alloys Ni-30Al-20Fe and Ni-12Al-40Fe as representative of the individual phases of the multi-phase microstructure. Note that the composition Ni-30Al-20Fe is fairly close to those of both the pro-eutectic and eutectic B2-structured phases.

The second extrusion (Batch 1) of Ni-20Al-30Fe resulted in a refinement of the microstructure with the pro-eutectic phase measuring ~20μm in diameter (figure 4.2.2a). Figure 4.2.2b is an optical micrograph of the longitudinal section of this double-extruded multi-phase alloy, in which the eutectic can be observed to be dispersed between the elongated pro-eutectic phase (which is elongated in the direction of extrusion). The microstructure of the double-extruded multi-phase alloy was again observed using a TEM to consist of pro-eutectic and eutectic phases; the eutectic lamellae width was again ~0.5μm (fig. 4.2.2c) similar to the single-extruded alloy. The dislocations observed in various phases in fig. 4.2.2c result from a slight deformation (~2% in compression) to the sample prior to thin-foil preparation; the extruded microstructure was largely free of dislocations. Like the single-extruded alloy, the pro-eutectic phase was again identified, using SAD, to be B2-structured. Similarly, one of the eutectic phases was again identified to be β' while

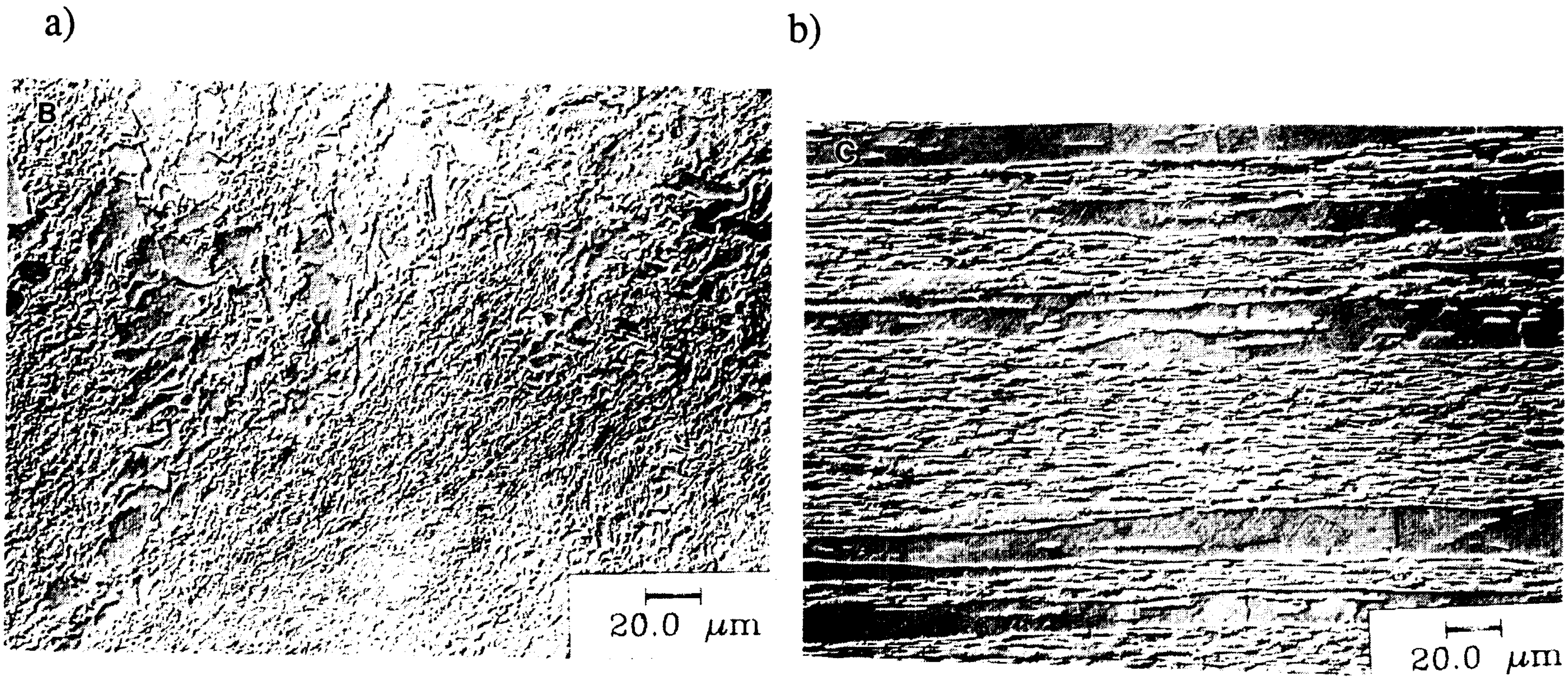

Figure 4.2.2 Double-extruded multi-phase alloy Ni-20Al-30Fe: (a) optical micrograph from transverse section (Differential Interferometry Contrast, DIC) (b) optical micrograph - longitudinal section , DIC contrast (micron marker parallel to extrusion direction) (c) TEM micrograph showing a lamellae width of ~0.5μm (d) SAD pattern from the pro-eutectic B2 phase (e) SAD pattern from the eutectic $(Ni,Fe)_3(Fe,Al)$ phase showing a $L1_2$ structure (see superlattice reflections) (f) Superlattice centered-dark-field TEM micrograph of the $(Ni,Fe)_3(Fe,Al)$ phase indicating that the microstructure is not fully ordered. Note the refinement in size of pro-eutectic phase from ~50μm in single-extruded state to ~20μm in double-extruded state. Also, note the streaking in <110> directions in both diffraction patterns.

ORIGINAL PAGE
BLACK AND WHITE PHOTOGRAPH

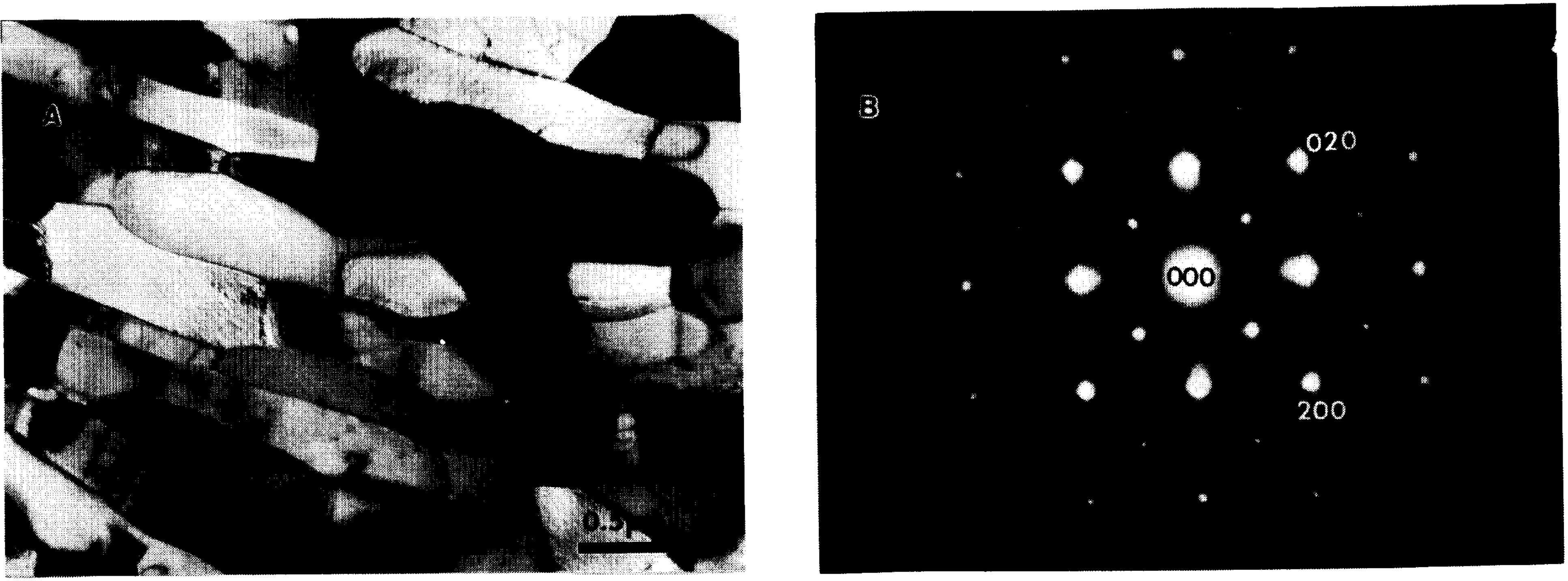
A
0.5μ
B
020
000
200

c)

d)

Figure 4.2.2 continued.

ORIGINAL PAGE
BLACK AND WHITE PHOTOGRAPH

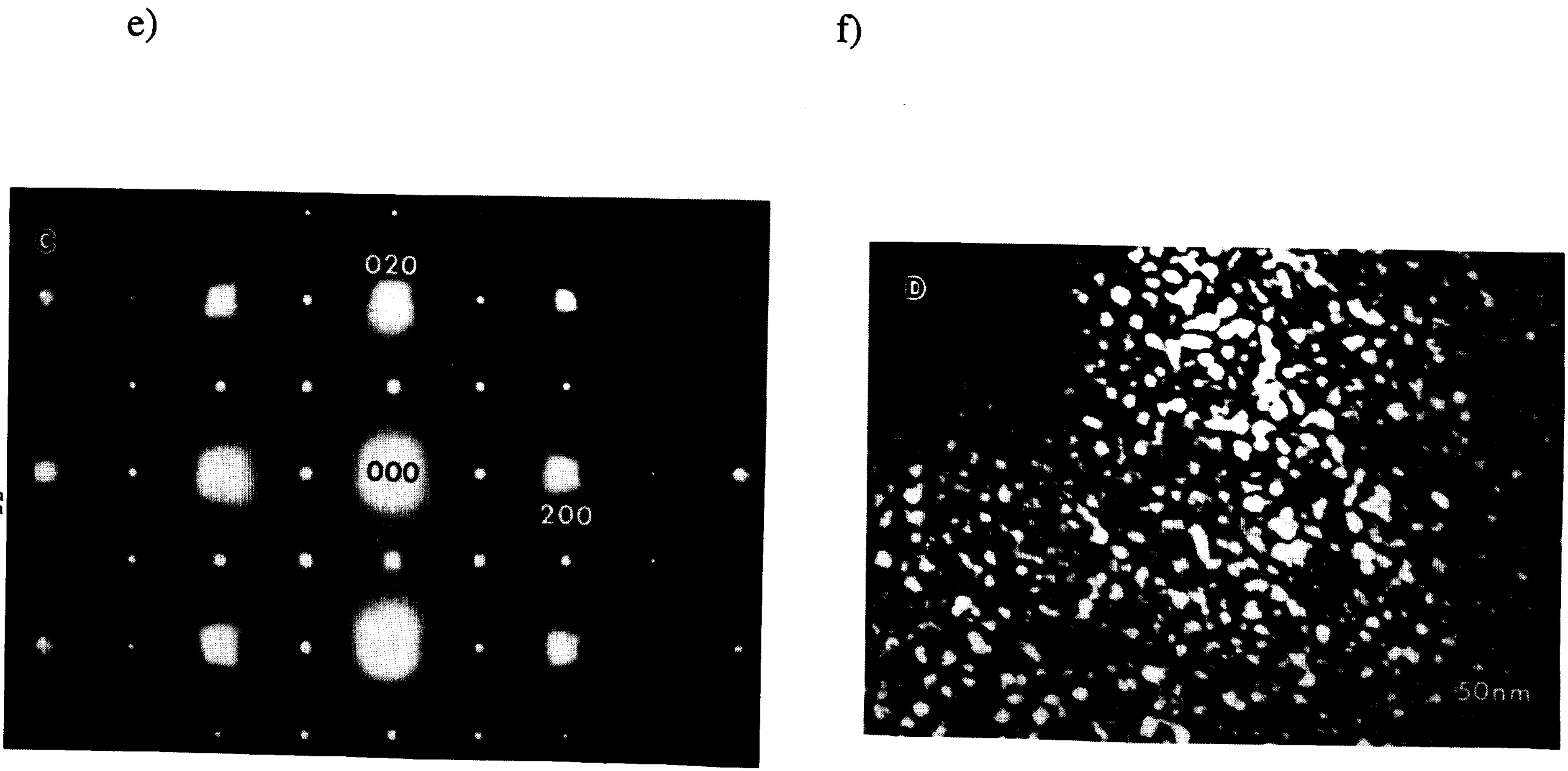
e)
f)
C
020
000
200
D
50nm

Figure 4.2.2 continued.

ORIGINAL PAGE
BLACK AND WHITE PHOTOGRAPH

the other eutectic phase (based on $(Ni,Fe)_3(Fe,Al)$) showed γ' superlattice reflections, similar to the single-extruded alloy. A mottled appearance, often referred to as a tweed microstructure, was observed in all the phases under two-beam imaging conditions [94], and streaking in <110> directions was observed in SAD patterns for both β' and γ' phases, see figures 4.2.1d-e. Both of these effects are believed to arise either from phonon interactions or from a dispersion of fine precipitates [95-96].

Based on the observation of superlattice reflections in SAD patterns of the $(Ni,Fe)_3(Fe,Al)$-based phase (of composition Ni-12Al-40Fe) in the extruded alloy, Ni-20Al-30Fe, the microstructure would appear to be ordered (γ' or $L1_2$). Inoue et al.[28] also reported that the structure of the $(Ni,Fe)_3(Fe,Al)$ phase in rapidly solidified Ni-20Al-30Fe was γ' (although the composition was not reported). However, using superlattice-dark-field imaging in TEM, Field et al.[97] observed that the microstructure consisted of bright regions in a dark matrix and suggested that the microstructure of the $(Ni,Fe)_3(Fe,Al)$-based phase (again, the composition was not reported) in rapidly solidified Ni-20Al-30Fe consisted of a dispersion of fine, ordered precipitates in a disordered matrix. By contrast, Inoue et al.[29] described a similar microstructure in rapidly solidified Ni-Fe-Al γ' alloys as a high density of APB's. Superlattice dark-field TEM micrographs (fig. 4.2.2f) of the $(Ni,Fe)_3(Fe,Al)$-based phase in the cast and extruded Ni-20Al-30Fe indicate that the microstructure is not fully ordered; the regions of darker contrast interspersed within brightly lit (ordered) regions indicate the possibility of either a high density of APB's or a γ/γ' type microstructure (ordered precipitates in disordered matrix).

Very fine, ordered precipitates in a disordered matrix usually result in a mottled appearance [98-100] under two-beam imaging conditions. However, since the mottled appearance of this $(Ni,Fe)_3(Fe,Al)$ phase has been shown to persist even when no superlattice spots are visible in the SAD pattern (after suitable heat treatment [94]), the tweed microstructure cannot be considered as proof of a γ/γ'-type microstructure. Because of the fine scale of the microstructure in fig. 4.2.2f, it was difficult to establish whether the microstructure consisted of fine APB's or fine γ' precipitates without further experiments (see below).

A predominant orientation relationship, observed between the β' and the $(Ni,Fe)_3(Fe,Al)$ phase (later confirmed to be γ/γ', see below) in the eutectic, was identified to be the Kurdjumov-Sachs relationship, i.e. $\{110\}_{\beta'} \parallel \{111\}_{\gamma/\gamma'}$ and $<111>_{\beta'} \parallel <110>_{\gamma/\gamma}$, as noted previously by Field et al.[97] in rapidly solidified material of similar composition.

$(Ni,Fe)_3(Fe,Al)$-based phase Ni-12Al-40Fe

The alloy Ni-12Al-40Fe had a composition similar to that of the $(Ni,Fe)_3(Fe,Al)$ phase in the double-extruded multi-phase Ni-20Al-30Fe. The microstructure of transverse sections of single extruded Ni-12Al-40Fe consisted mostly of equiaxed grains with a grain diameter of ~50µm, although some elongated grains (arrowed in fig. 4.2.3a), indicative of incomplete recrystallization, were also present. The longitudinal sections exhibited a similar microstructure.

Figure 4.2.3b is a superlattice (001) dark-field image of the cast and extruded Ni-12Al-40Fe which was cooled from 1000°C, where the alloy is known to be fully disordered [94], to room temperature at a rate of 12°C per hour. The bright, cuboidal precipitates of ~100nm size distributed in a dark (disordered) matrix, clearly indicate a coarsened γ/γ' microstructure and not an APB structure. (Note that for Ni-12Al-40Fe, the room temperature phase diagram in slow cooled (10°C/hr from 900°C) alloys (figure 2.3b) indicates a single-phase γ' structure). Thus, it is clear that the microstructure of $(Ni,Fe)_3(Fe,Al)$ phase in double-extruded Ni-20Al-30Fe is a γ/γ' microstructure, thereby confirming the observations by Field et al.[97]. The size of the ordered regions in the γ/γ' phase in the extruded multi-phase alloy was ~10nm. Henceforth, the microstructure of the multi-phase alloy will be referred to as a $\beta' + \gamma/\gamma'$ microstructure, while the alloys

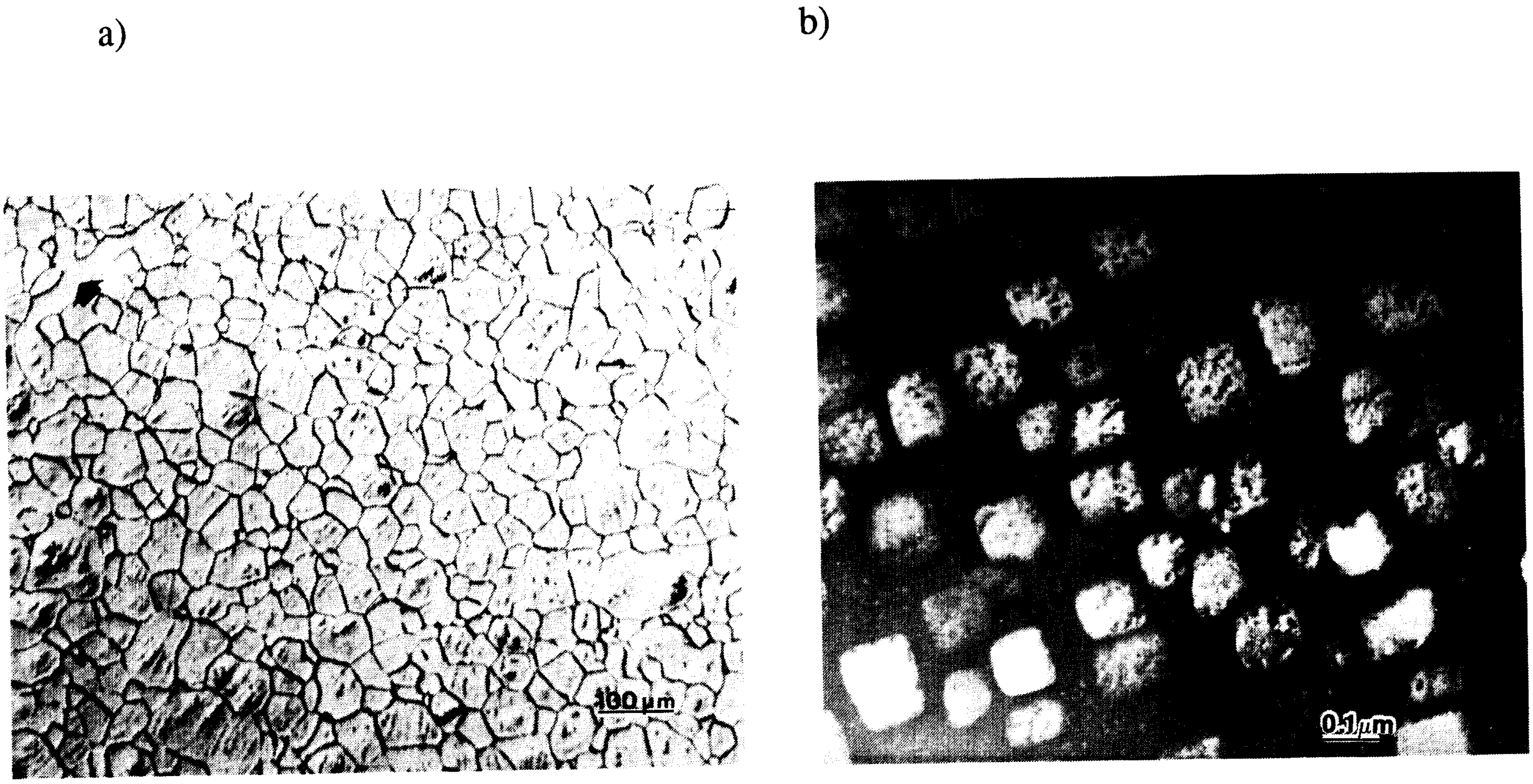

Figure 4.2.3 (a) Optical micrograph of transverse section of cast and extruded Ni-12Al-40Fe, shows mostly equiaxed grains although some elongated grains (arrowed), indicative of incomplete recrystallization, are also present (b) Superlattice dark field TEM micrograph of extruded and annealed (1000°C/3 hrs followed by furnace cool at 12°C/hr) Ni-12Al-40Fe, showing cubiodal γ precipitates of ~100 nm size in a f.c.c matrix.

ORIGINAL PAGE
BLACK AND WHITE PHOTOGRAPH

Ni-30Al-20Fe and Ni-12Al-40Fe would be considered similar to the β' and γ/γ' phases in the multi-phase alloy.

β' Ni-30Al-20Fe

The optical microstructures of the transverse section of the β' alloy, Ni-30Al-20Fe, were similar after both extrusions (Batch 1) and contained equiaxed grains of ~25μm grain size. Longitudinal sections of the double-extruded alloy exhibited a microstructure similar to the transverse sections, although some cracks were observed along the extrusion directions (fig. 4.2.4a). The microstructure was determined to be fully recrystallized in the TEM. While the grains were mostly free of dislocations, a few residual dislocations with a <001> Burgers' vector were observed (fig. 4.2.4b). X-ray diffractometry on 0° (longitudinal), 45° and 90° (transverse) sections (fig. 4.2.5a-c) indicated that while the {111} reflections could be observed only in the transverse sections, strong (compared to other orientations) {100} reflections could be observed only in the 45° sections. Note that for material with a {111} texture, {100} reflections are more likely to be observed along 45° to wire axis since the angle between {111} and {100} is 54.7°. These observations are indicative of a {111} wire texture in the material. Subsequent TEM observations on thin foils made from transverse sections of extrusions confirmed that almost all grains were near the [111] zone axis, thereby confirming that the extruded alloy was textured.

Interestingly, a discontinuous, thin (~10nm) grain boundary film (fig. 4.2.6) was also observed in the double-extruded alloy. Compositional measurements (using a VG Scanning Transmission Electron Microscope) of the grain boundary phase and grain interior regions indicated iron-enrichment at the grain boundaries [101] (see fig. 4.2.7a-b). Similar conclusions were derived from Auger Electron Spectroscopy analyses of compositions from intergranular and transgranular regions of fracture samples of the

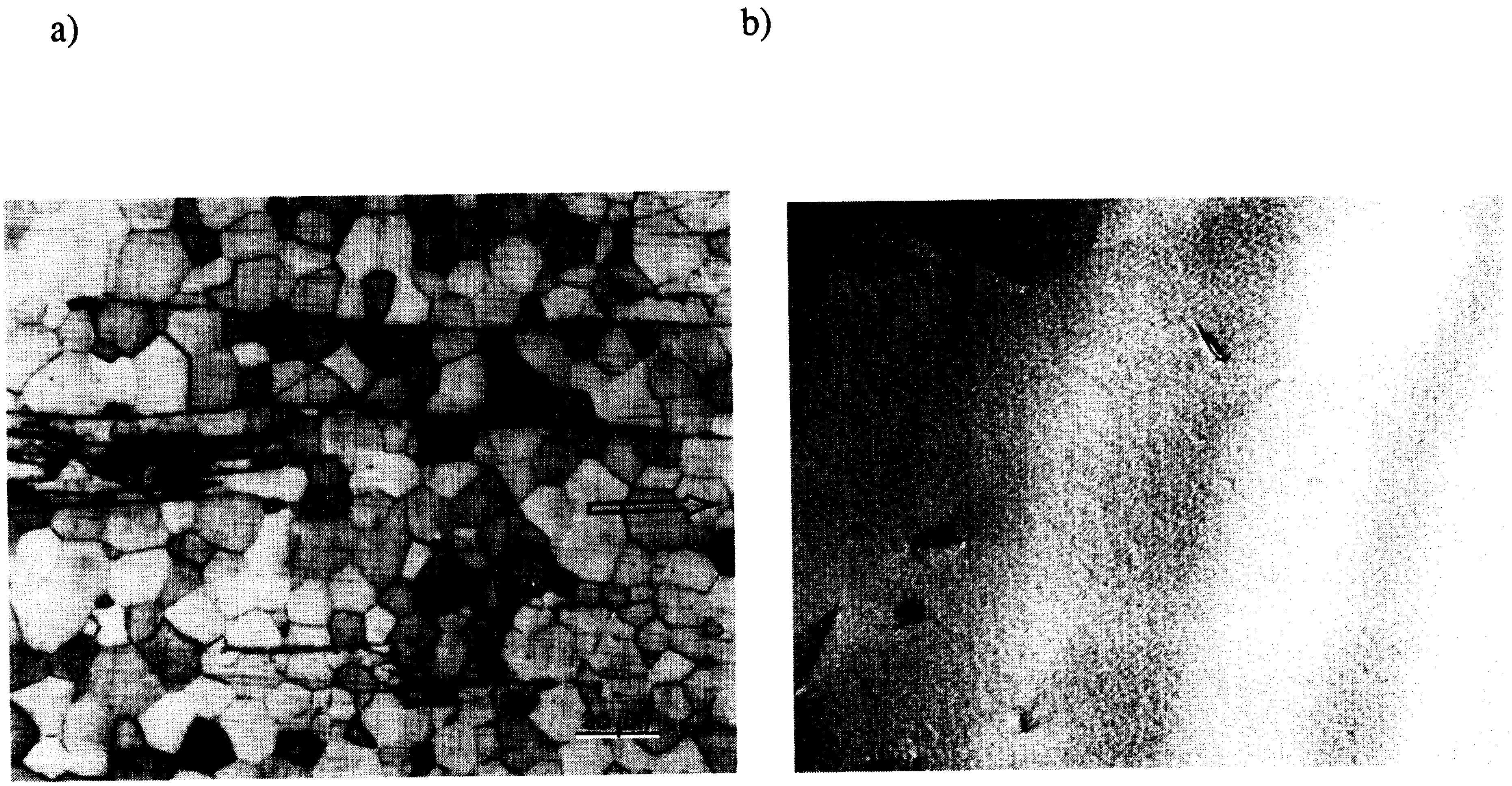

Figure 4.2.4 Double-extruded β' alloy Ni-30Al-20Fe: (a) optical micrograph of longitudinal section showing equiaxed grains ~25μm in size and a few cracks along the extrusion direction (b) TEM indicated the microstructure to be fully recrystallized; occasionally, a few residual dislocations with <100> Burgers' vector were observed.

ORIGINAL PAGE
BLACK AND WHITE PHOTOGRAPH

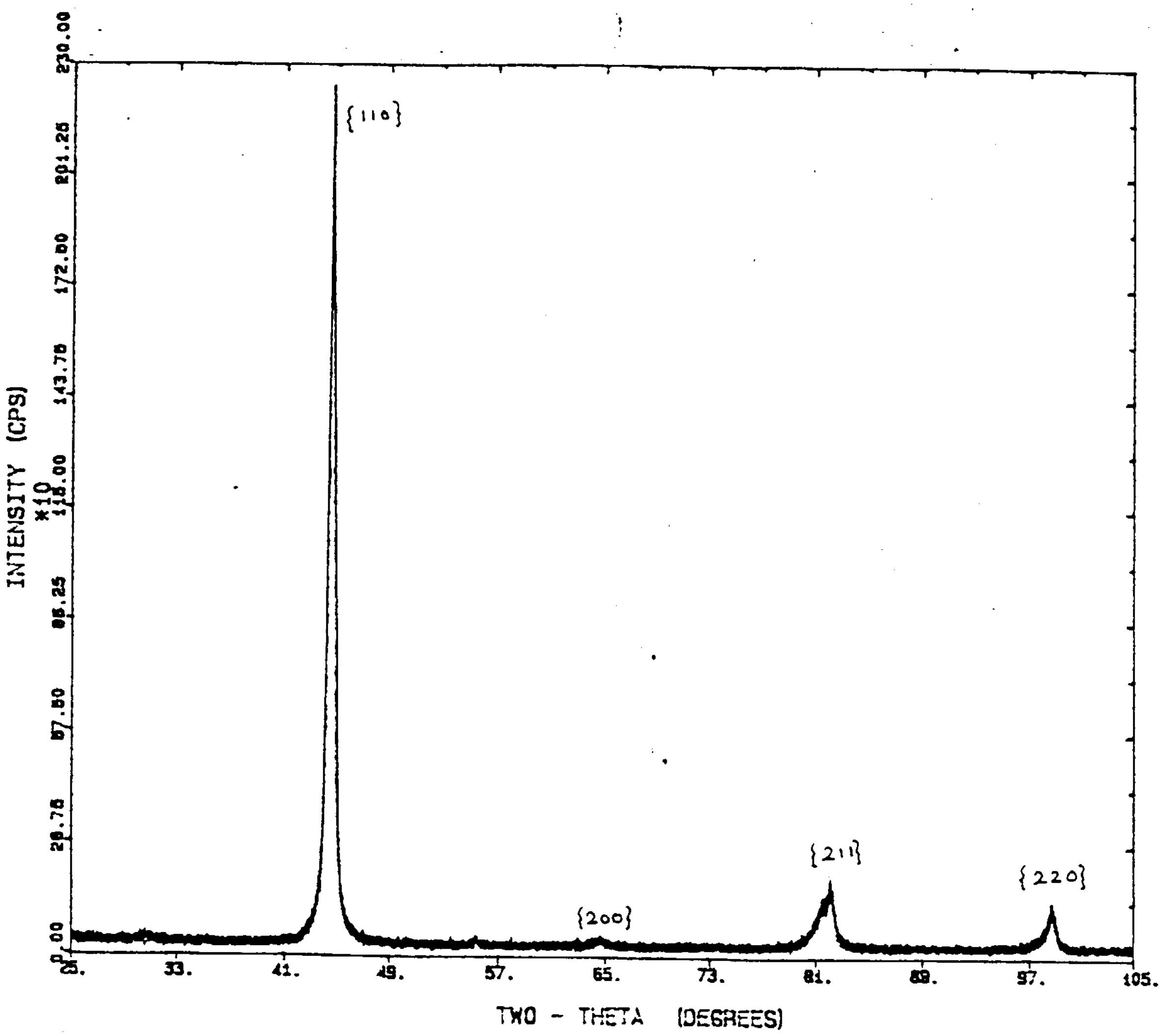

Figure 4.2.5a

Figure 4.2.5 X-ray diffraction patterns from double-extruded β' alloy Ni-30Al-20Fe taken along: (a) longitudinal (0° to extrusion direction) (b) oblique (45°) and (c) transverse (90°).

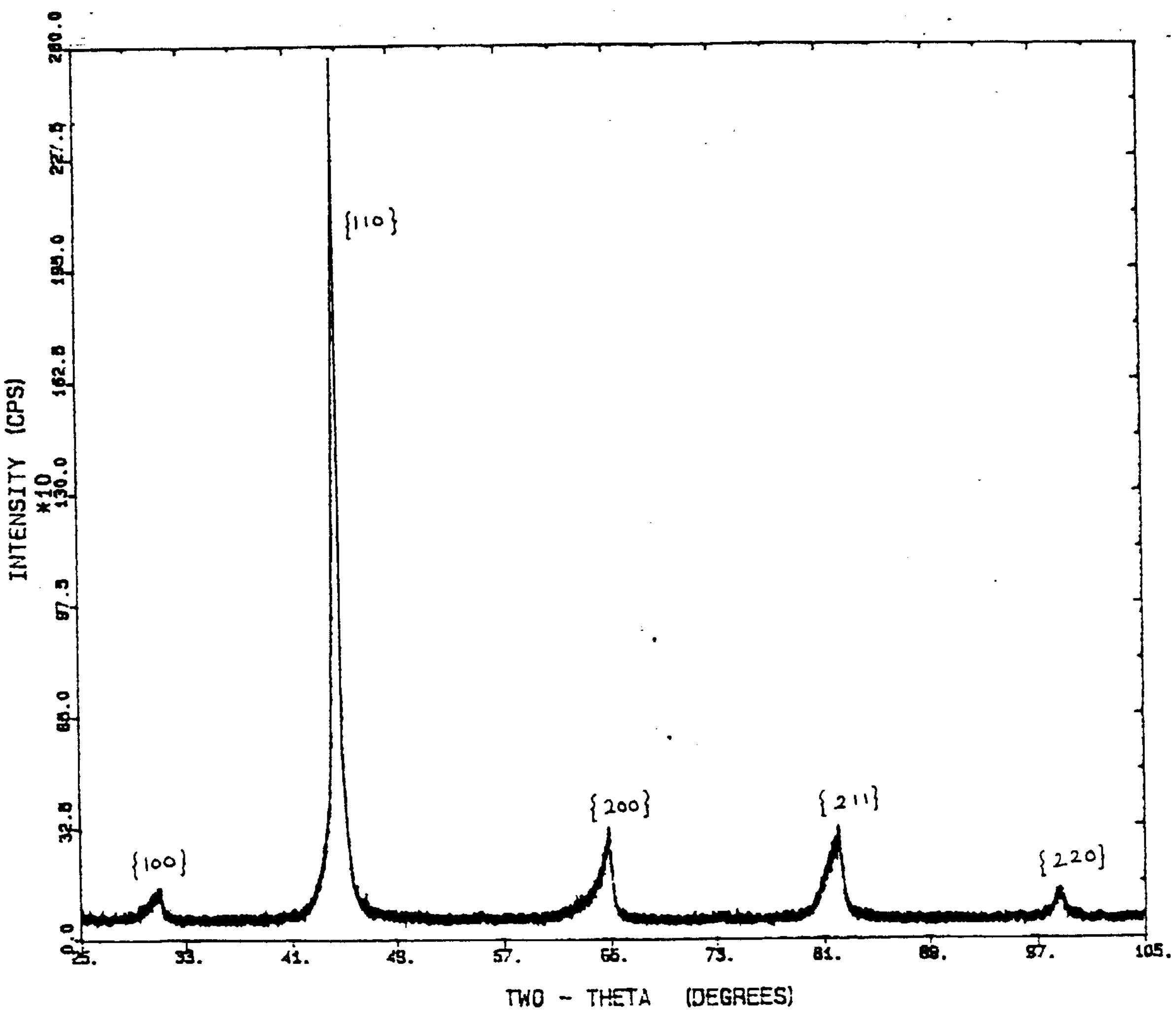

Figure 4.2.5b

Figure 4.2.5 continued.

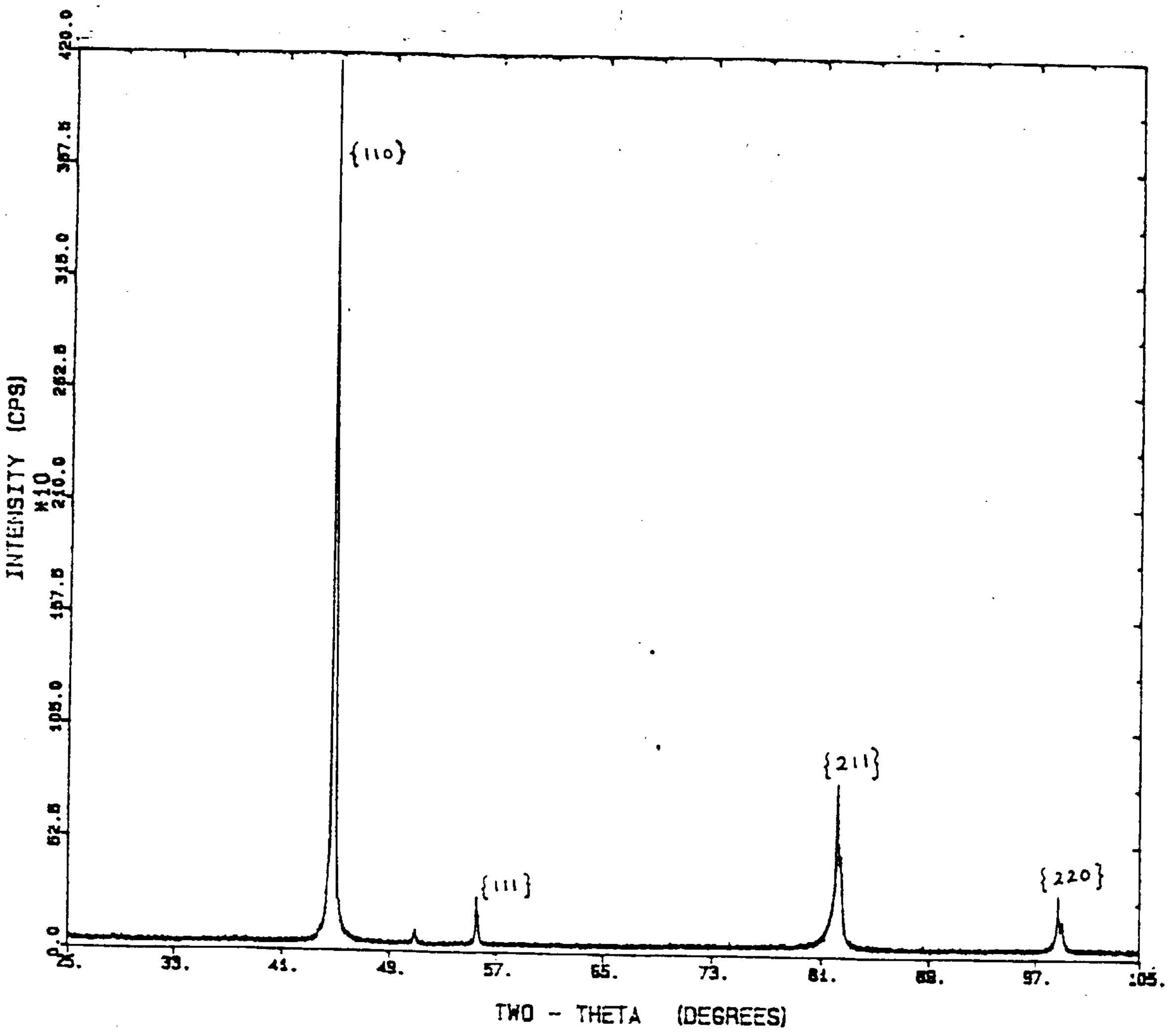

Figure 4.2.5 c

Figure 4.2.5 continued.

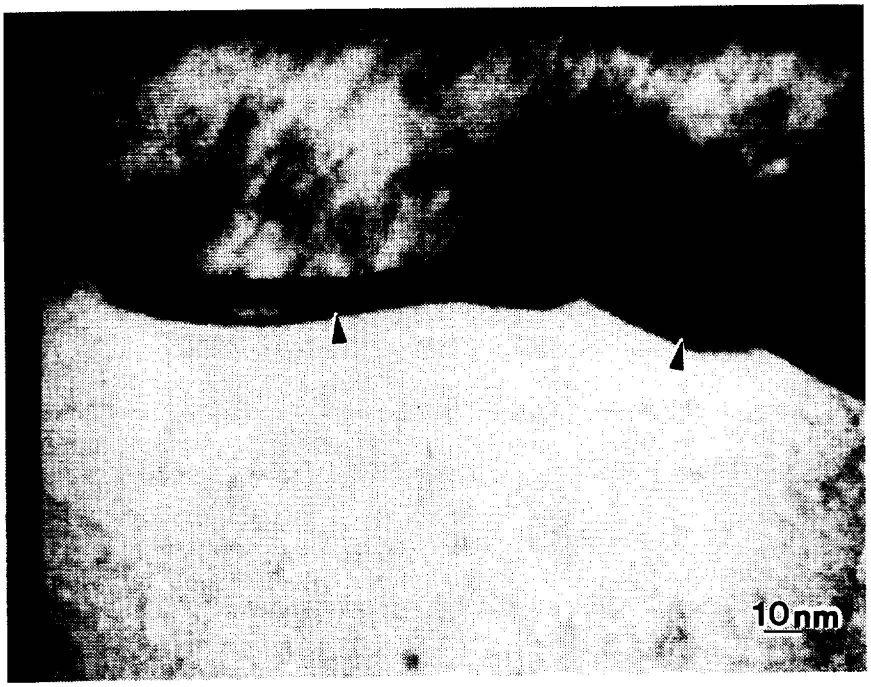

Figure 4.2.6 The microstructure of double-extruded β' Ni-30Al-20Fe under a Scanning Transmission Electron Microscope (STEM) showing a thin (~10nm), discontinuous grain boundary phase.

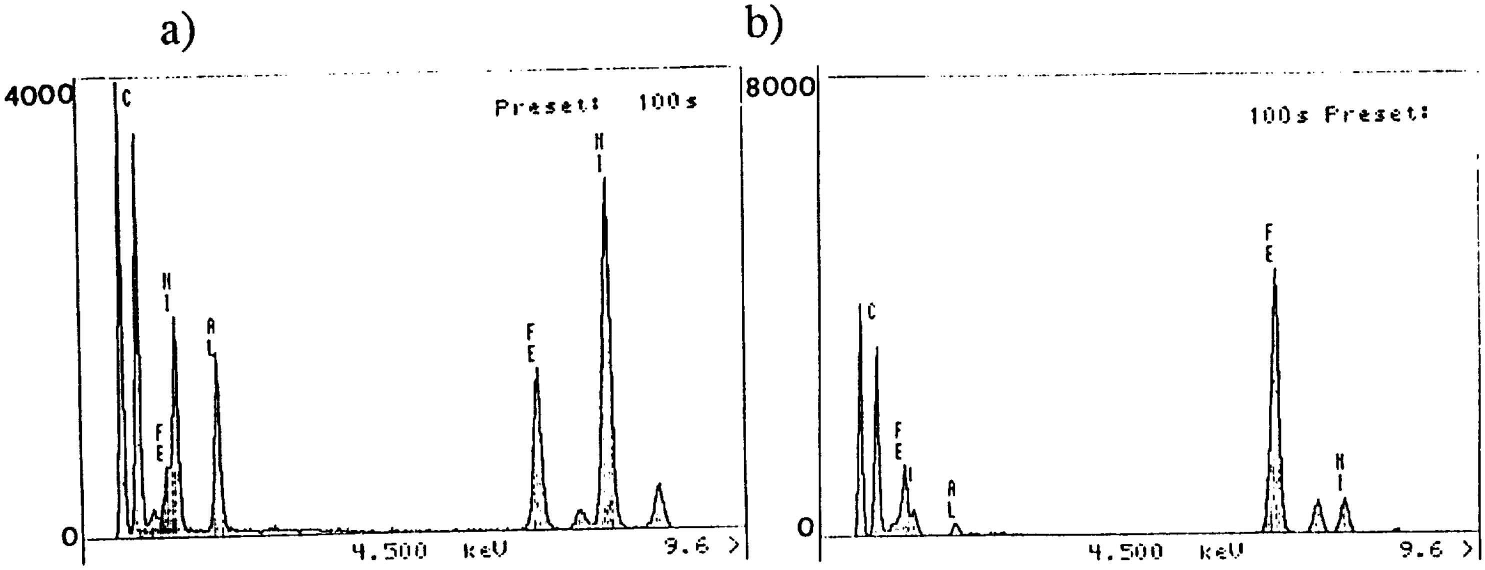

Figure 4.2.7 Compositional measurements using STEM from (a) matrix (b) grain boundary phase regions in Figure 6.2.6 indicate an iron-enrichment in the grain boundary phase [101].

ORIGINAL PAGE
BLACK AND WHITE PHOTOGRAPH

double-extruded alloy, with the intergranularly fractured regions exhibiting higher iron concentrations than the transgranular regions [102].

Boron-doped Multi-phase Alloy

The microstructure of the multi-phase alloy microalloyed with boron was generally similar to the undoped multi-phase alloy (figure 4.2.8), although the scale of the microstructure was coarser for the boron-doped alloy, presumably due to the high extrusion temperature necessitated by the high extrusion ratio (16:1). Thus, the pro-eutectic (presumably β'-structured) phase was ~50μm in diameter (fig. 4.2.8) rather than ~20μm for the undoped alloy (fig. 4.2.2b). Since the mechanical properties were observed to be somewhat similar to the undoped multi-phase alloy (see later), no detailed microstructural analysis was performed on the boron-doped multi-phase alloys.

4.2.2 Elevated Temperature

The elevated temperature (427°C, 627°C and 827°C) microstructures of the multi-phase alloy and alloys similar to its constituent phases were determined by examining specimens, sectioned from the unstrained ends of tensile tested specimens, annealed at each temperature for ~200 min. and water quenched.

Multi-phase ($\beta'+\gamma/\gamma'$) Ni-20Al-30Fe

The room temperature microstructure of the double-extruded multi-phase alloy was noted above to consist of a pro-eutectic β' phase, ~20μm in diameter, and elongated in the

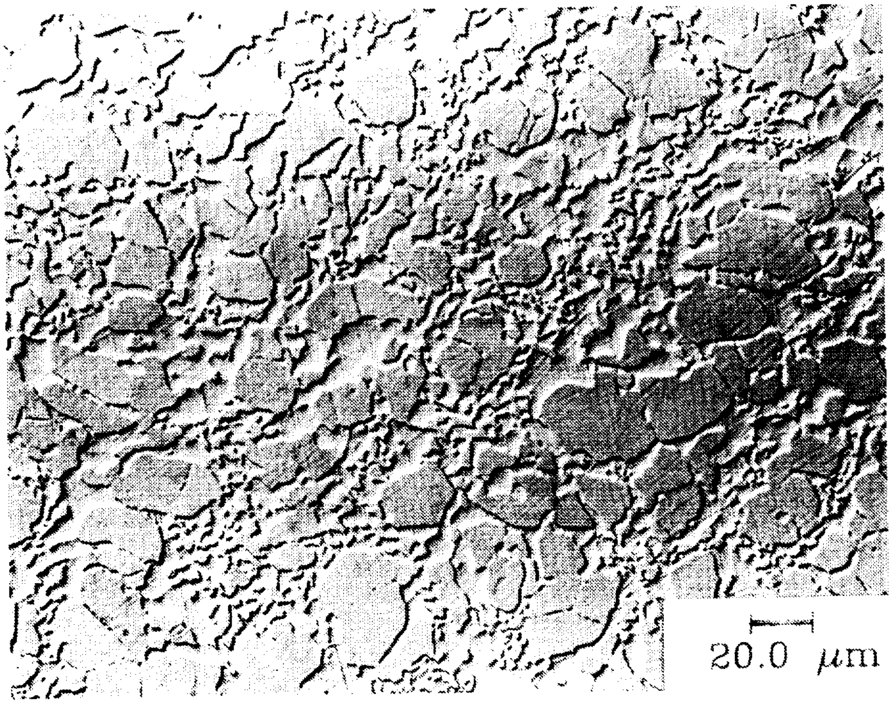

Figure 4.2.8 Optical micrograph (DIC contrast) of the boron-doped multi-phase alloy Ni-20Al-30Fe-0.17B showing a microstructure similar (although coarser) to the undoped multi-phase alloy.

direction of extrusion (also the stress-axis in multi-phase alloy specimens), dispersed between a fine eutectic β' + γ/γ' matrix (lamellae width ~0.5μm). The γ/γ' phase consisted of a fine (~10nm in diameter) dispersion of ordered (γ') precipitates in a disordered (γ) matrix. The compositions of the room temperature constituent phases are given in Table 4.2.1.

The microstructure of the multi-phase alloy at both 427°C and 627°C was similar to the room temperature microstructure. For example, figure 4.2.9 shows a TEM micrograph of the multi-phase alloy annealed at 627°C. The microstructure consisted of a pro-eutectic β' phase (marked 'A') in a eutectic structure. The eutectic phase marked 'B' was confirmed by selected area diffraction (SAD) to be β'; the composition was determined using energy dispersive spectroscopy (EDS) to be similar to that of the pro-eutectic phase (see Table 4.2.1). The β' phase exhibited a mottled 'tweed' contrast under two-beam imaging conditions [94] and streaking along <110> directions in SAD patterns. Such effects have been attributed either to a fine dispersion of ordered precipitates in a disordered matrix or pre-martensitic phenomena in similar materials [95,96]. The structure of the phase marked marked 'C' was determined to be $L1_2$ using selected area diffraction (SAD). The observation of superlattice reflections in SAD patterns (fig. 4.2.9b) from the phase 'C' and a fine dispersion of ordered (bright) particles in a disordered (dark) matrix in superlattice dark-field images (fig. 4.2.9c) of the same indicated a γ/γ' microstructure, similar to the room temperature microstructure reported earlier (see section 4.2.1). At neither temperature were any additional phases observed.

When annealed at 827°C the γ/γ'component became fully disordered as evidenced by the lack of superlattice reflections in SAD patterns (figure 4.2.9d). Both the pro-eutectic and eutectic β' phases remained ordered. Also, the compositions of the constituent phases were observed to change slightly from their room temperature compositions. Table 4.2.1 lists the compositions (an average of three measurements) of the pro-eutectic β' phase, and the eutectic β' and γ/γ' phases at 427°C, 627°C, and 827°C. At 827°C, the γ phase

TABLE 4.2.1. COMPOSITIONS OF PHASES OF MULTI-PHASE Ni-20Al-30Fe, β' Ni-30Al-20Fe, γ/γ Ni-12Al-40Fe AT ELEVATED TEMPERATURES (27°C DATA FROM PG.51)

TEST TEMPERATURE	MICROSTRUCTURE			COMMENTS
ALLOY:Ni-20Al-30Fe	PRO-EUTECTIC β'	EUTECTIC β'	EUTECTIC γ/γ	
27°C	Ni-30Al-20Fe	Ni-32Al-15Fe	Ni-12Al-40Fe	β'+ Ni-rich γ/γ
427°C	Ni-30Al-19Fe	Ni-31Al-18Fe	Ni-14Al-39Fe	β'+ Ni-rich γ/γ
627°C	Ni-29Al-19Fe	Ni-30Al-18Fe	Ni-13Al-39Fe	β'+ Ni-rich γ/γ
827°C	Ni-32Al-16Fe	Ni-32Al-16Fe	Ni-9Al-44Fe	β'+ Ni-rich γ
ALLOY : Ni-12Al-40Fe	γ/γ phase	β' phase		
427°C	Ni-16Al-37Fe	NONE		Fine dispersion of γ (size ~10nm) in γ
627°C	Ni-14Al-38Fe	NONE		" "
827°C	Ni-15Al-37Fe	Ni-33Al-16Fe		Coarsened γ/γ microstructure, γ size ~50nm
ALLOY : Ni-30Al-20Fe	β' phase	Precipitate		
27°C	Ni-27Al-18Fe	Iron-rich and Al-poor		Thin (~10nm) film at grain boundaries.
627°C	Ni-31Al-20Fe	Ni-12Al-47Fe		β'+ Fe-rich γ/γ phase at grain boundaries.
	Ni-31Al-20Fe	Ni-9Al-49Fe		β'+ Fe-rich γ phase at grain boundaries.
827°C	Ni-31Al-18Fe	Ni-7Al-58Fe		β'+ Fe-rich γ phase at grain boundaries.

Each quoted composition is the average of three measurements and rounded to nearest at.%; the standard deviation is ±1 at.%.

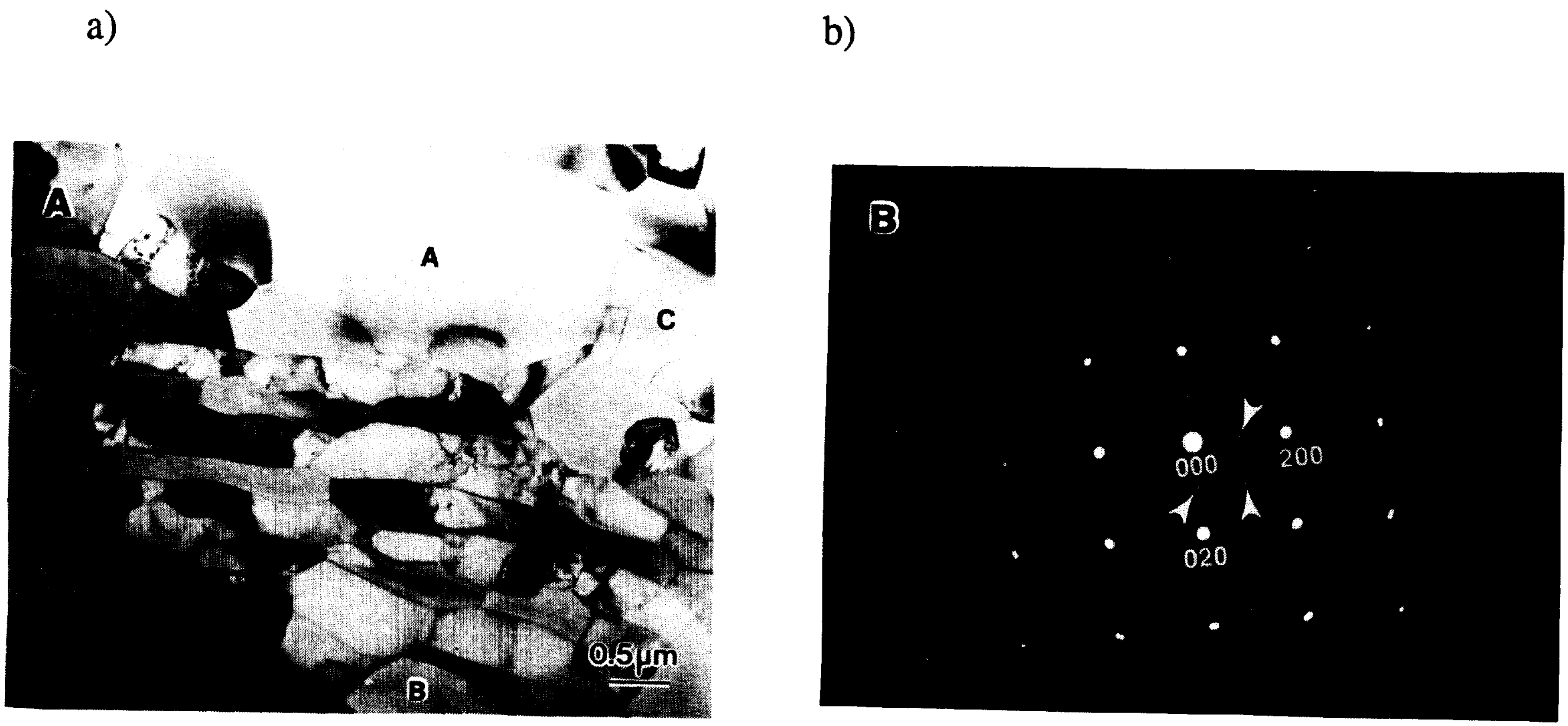

Figure 4.2.9 (a) Bright-field, TEM micrograph of double-extruded Ni-20Al-30Fe annealed at 627°C. A pro-eutectic phase (marked 'A') is present in a eutectic matrix of phases marked 'B' and 'C'. (b) SAD pattern (Beam direction = [001]) from the phase marked 'C'; the superlattice reflections (arrowed) indicate the presence of an $L1_2$ structure (c) superlattice dark-field image (using a 001 reflection) of the phase marked 'C' indicates a γ/γ' microstructure (d) SAD pattern (Beam direction = [001]) from the γ phase of double-extruded Ni-20Al-30Fe annealed at 827°C; the lack of superlattice reflections indicates a completely disordered microstructure.

ORIGINAL PAGE
BLACK AND WHITE PHOTOGRAPH

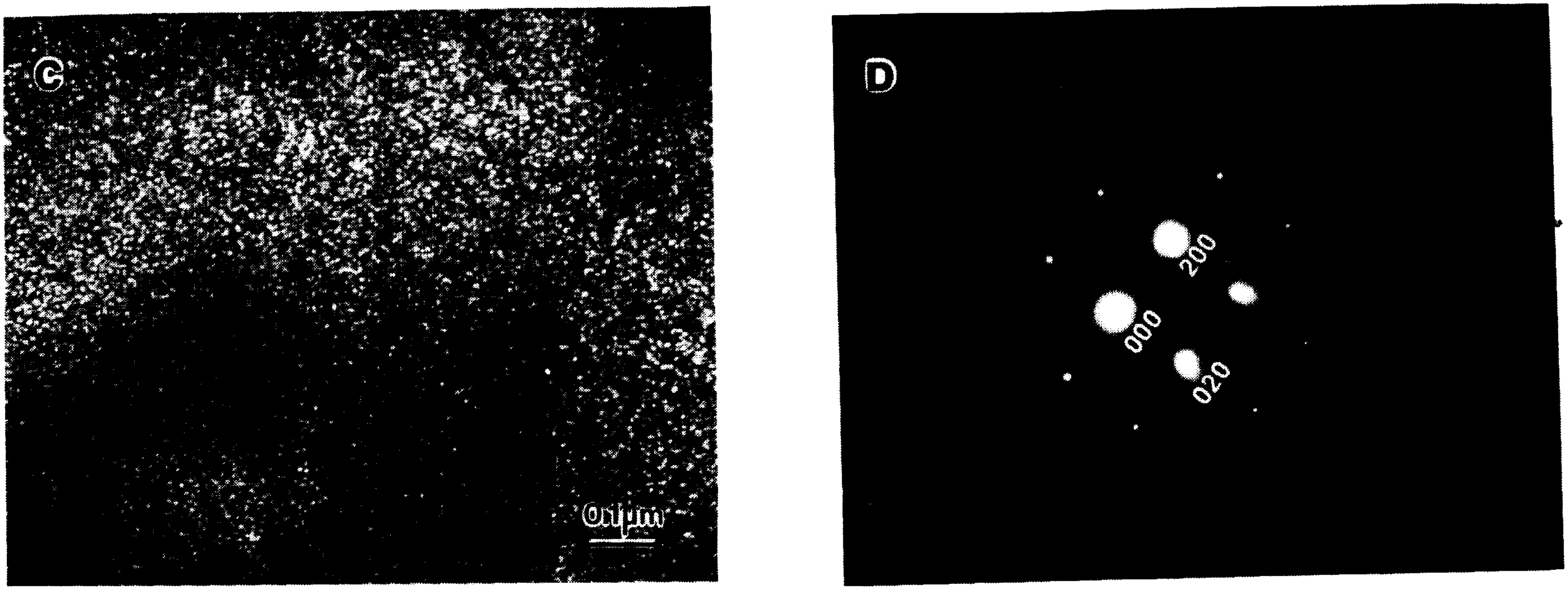
C
0.1µm
D
200
000
020

c)

d)

Figure 4.2.9 continued.

ORIGINAL PAGE
BLACK AND WHITE PHOTOGRAPH

appeared to become slightly depleted in aluminum and enriched in iron compared to the γ/γ' phase at both 427°C and 627°C.

γ/γ' Ni-12Al-40Fe

The room temperature microstructure of the single-extruded Ni-12Al-40Fe was noted above to consist of equiaxed grains (~50μm in diameter) containing a dispersion of fine ordered (γ') precipitates (~10nm in diameter) in a disordered (γ) matrix, that is, the same as the microstructure of γ/γ' component in the multi-phase alloy.

The microstructure of Ni-12Al-40Fe annealed at 427°C and 627°C were similar. Superlattice dark-field imaging of the alloy annealed at 627°C (fig. 4.2.10a) and 827°C (fig. 4.2.10b) revealed a dispersion of γ' particles in disordered (γ) matrix (γ/γ' microstructure) suggesting that the observed mottled appearance of the matrix under bright-field imaging conditions was related to the γ/γ' microstructure; coarsening of the γ' particles (from ~10 nm at 627°C to ~50 nm at 827°C) was evident at the highest temperature. Higher magnification images of the region marked 'D' in fig. 4.2.10a indicates it to be a sub-boundary, which is consistent with the earlier observations of incomplete recrystallization in the extruded state. At 827°C, an additional phase was observed at the grain boundaries (fig 4.2.10c) which was identified to be B2-structured using SAD (fig. 4.2.10d); EDS analysis indicated a composition of approximately Ni-32Al-16Fe. The small volume fraction (~1vol.%) of the precipitated β' phase has little effect on the aluminum content of the matrix.

Note that whilst the microstructures at 427°C and 627°C, consisting of γ' precipitates in a γ matrix, were similar to the γ/γ' component in the multi-phase alloy, the alloy still exhibited a γ/γ' microstructure at 827°C whereas the multi-phase alloy had only a γ phase. The difference could possibly be related to casting-segregation. The composition of the sample, as determined by EDS, indicated a composition slightly richer

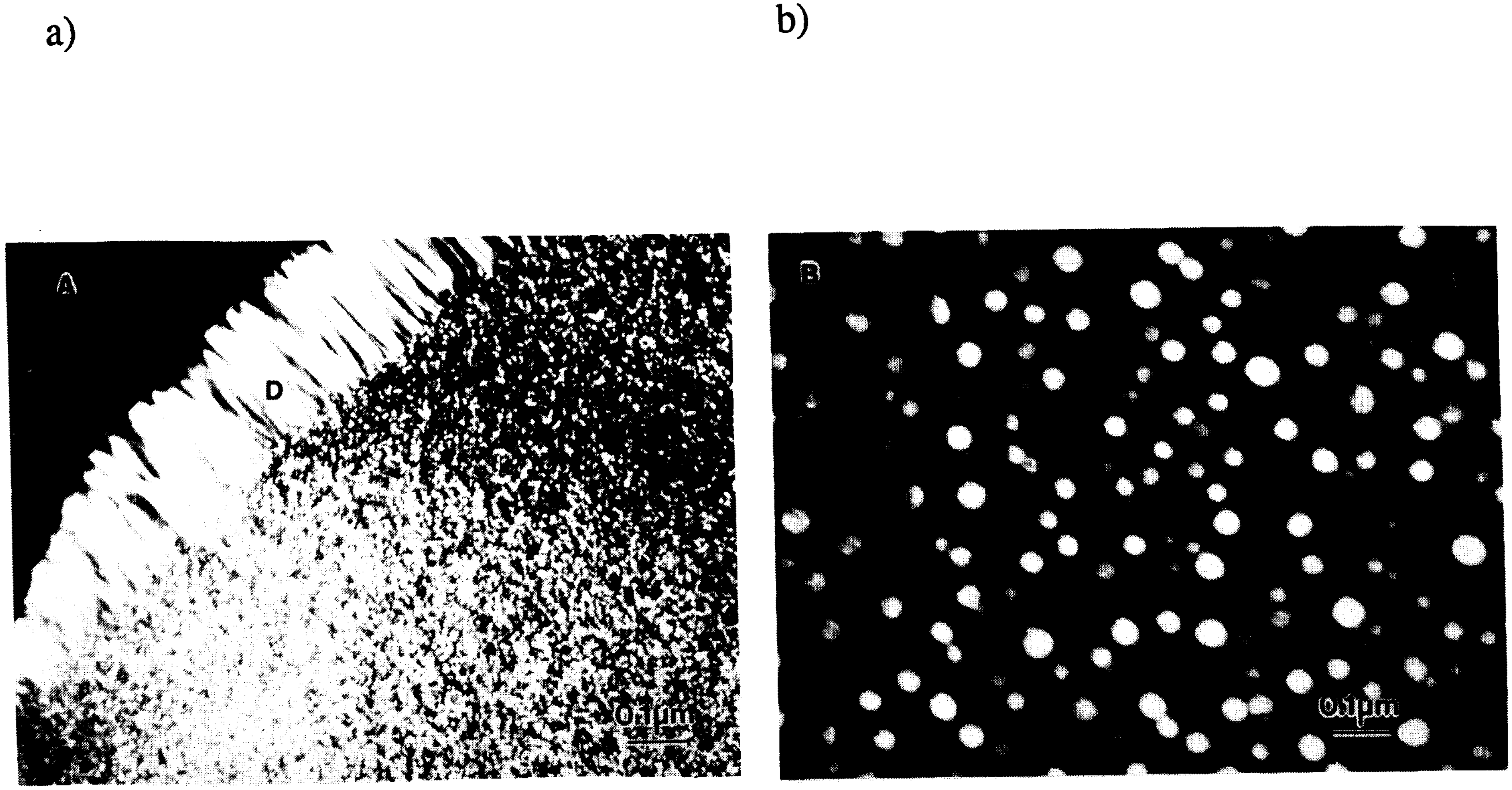

Figure 4.2.10. Superlattice dark-field images (using 001 reflections) of the alloy Ni-12Al-40Fe annealed at (a) 627°C (b) 827°C showing a γ/γ microstructure. Note the coarsening of γ with increasing annealing temperatures. (c) Bright-field image ($\vec{g} = 01\bar{1}$) of extruded Ni-12Al-40Fe, annealed at 827°C showing the presence of a grain boundary phase (arrowed). (d) SAD pattern from the grain boundary phase in (c) indicate a B2 structure (Beam direction ~ [011]). The extra reflections in the pattern arise from the γ matrix.

ORIGINAL PAGE
BLACK AND WHITE PHOTOGRAPH

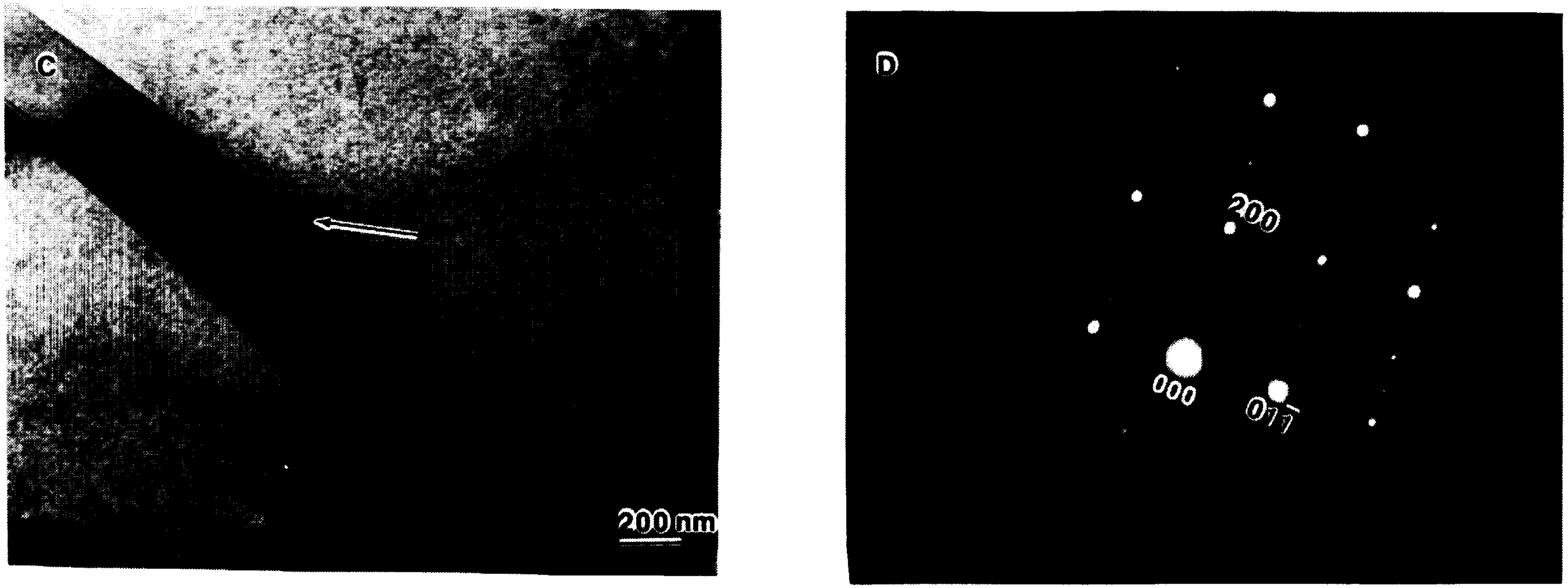
C
200 nm
D
200
000
$0\bar{1}\bar{1}$

c)

d)

Figure 4.2.10 continued.

ORIGINAL PAGE
BLACK AND WHITE PHOTOGRAPH

in aluminum ~15 %Al (see Table 4.2.1) than that from the Inductively Coupled Plasma (ICP) analysis of the alloy of ~12 at. %, which was close to the nominal composition. Comparison of the microstructure and composition of this alloy and the γ/γ' phase of the multi-phase alloy at 827°C suggests that a higher aluminum content leads to retention of the γ/γ' microstructure to higher temperatures.

β' Ni-30Al-20Fe

The room temperature microstructure of the β' alloy Ni-30Al-20Fe in both the single and double-extruded states was noted above. Briefly, the microstructure consisted of fully recrystallized equiaxed grains (~25μm diameter after both extrusions). A thin (~10 nm thick), iron-rich, discontinuous grain boundary film was also observed in the double-extruded alloy. After annealing at 627°C, additional phases were observed in the β' alloy microstructure. For example, regions such as that marked 'X' in fig. 4.2.11a were present at the β' grain boundaries. These regions exhibited a mottled appearance under bright-field imaging conditions similar to Ni-Fe-Al γ/γ' alloys. SAD patterns (figure 4.2.11b) from this phase indicated the presence of a $L1_2$ superlattice; the composition of these precipitates was measured by x-ray microanalysis to be Ni-12Al-47Fe, see Table 4.2.1. Based on the compositions of other γ/γ' alloys in Table 4.2.1, the precipitates in fig. 4.2.11a are probably γ/γ' rather than γ'. By contrast, the region marked 'Y' in fig. 4.2.11c while exhibiting a similar mottled appearance under bright-field imaging conditions, did not exhibit the $L1_2$ superlattice as evidenced by the lack of superlattice spots in positions marked with arrows in convergent-beam diffraction patterns (fig. 4.2.11d); the composition of this precipitate was measured to be Ni-9Al-49Fe. Again, the differences in composition of the precipitates are probably related to casting segregation. Also, a higher Al-level appears to favor a γ/γ' rather than γ microstructure which is consistent with the conclusions drawn in earlier sections. Similar regions were observed at the β' grain

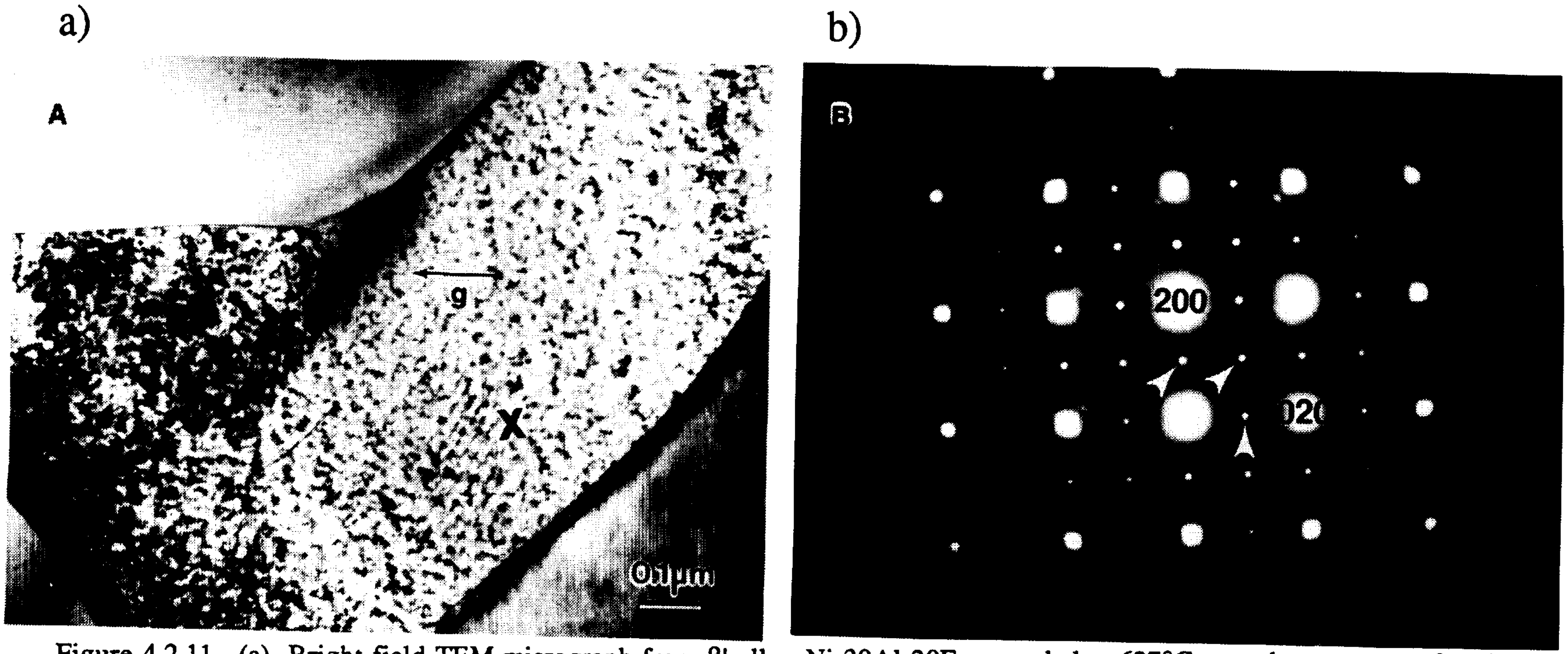

Figure 4.2.11. (a) Bright-field TEM micrograph from β' alloy Ni-30Al-20Fe annealed at 627°C note the presence of grain boundary phase, marked 'X', ($\vec{g}$ = 200, B ~ [001] referred to the grain boundary phase) (b) SAD pattern (Beam direction = [001]) from the grain boundary phase showing superlattice reflections, indicating the presence of a $L1_2$ structure (c) bright-field TEM micrograph from another region of the same foil showing a precipitate (marked 'Y') exhibiting similar mottled appearance (d) convergent-beam diffraction pattern (B = [011]) from precipitate indicates a f.c.c (γ) structure; note the absence of superlattice spots in arrowed positions (e) 827°C anneal: bright-field (polybeam) TEM micrograph. Note the presence of second phase (γ) at the grain boundaries of β' grains. (f) SAD pattern from the second phase indicate a f.c.c (γ) structure: note that no superlattice spots are present.

ORIGINAL
BLACK AND WHITE PHOTOGRAPH

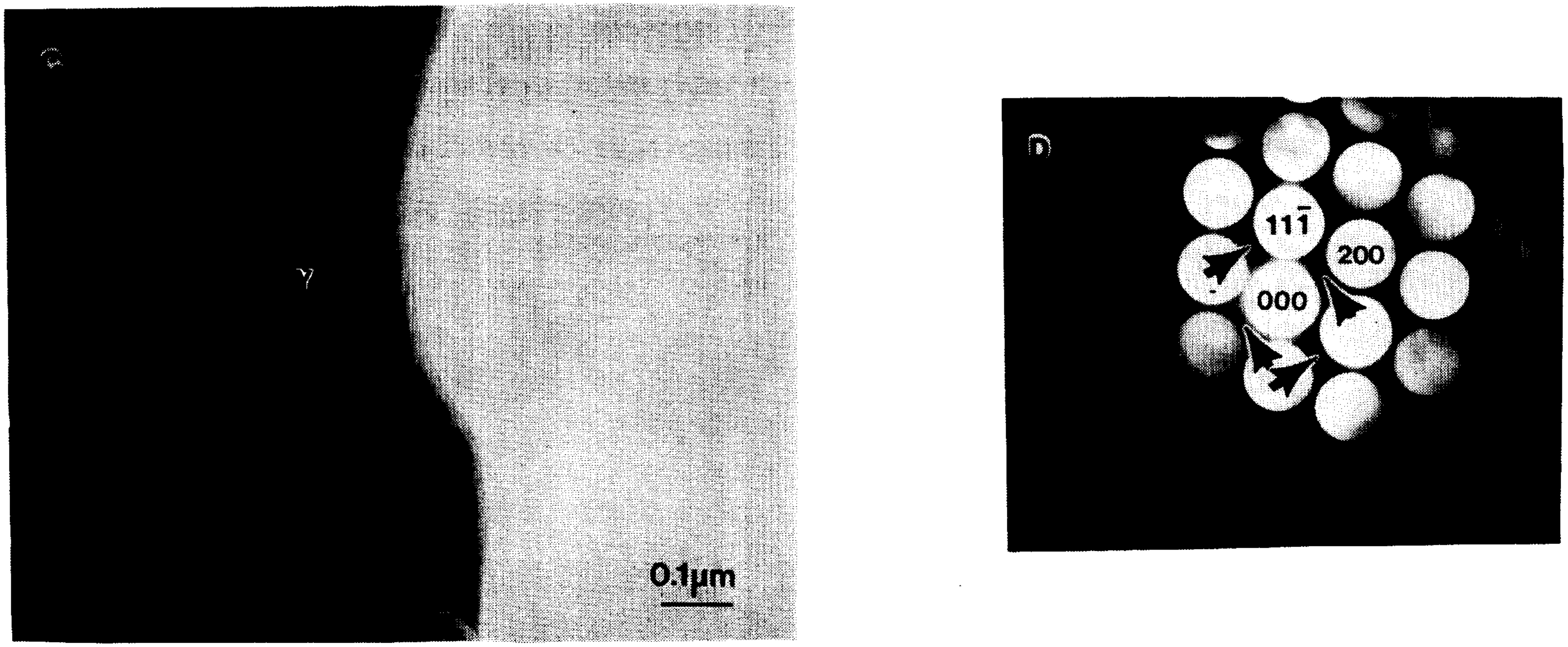
c) d)
γ
0.1µm
11$\bar{1}$
200
000

Figure 4.2.11 continued.

ORIGINAL PAGE
BLACK AND WHITE PHOTOGRAPH

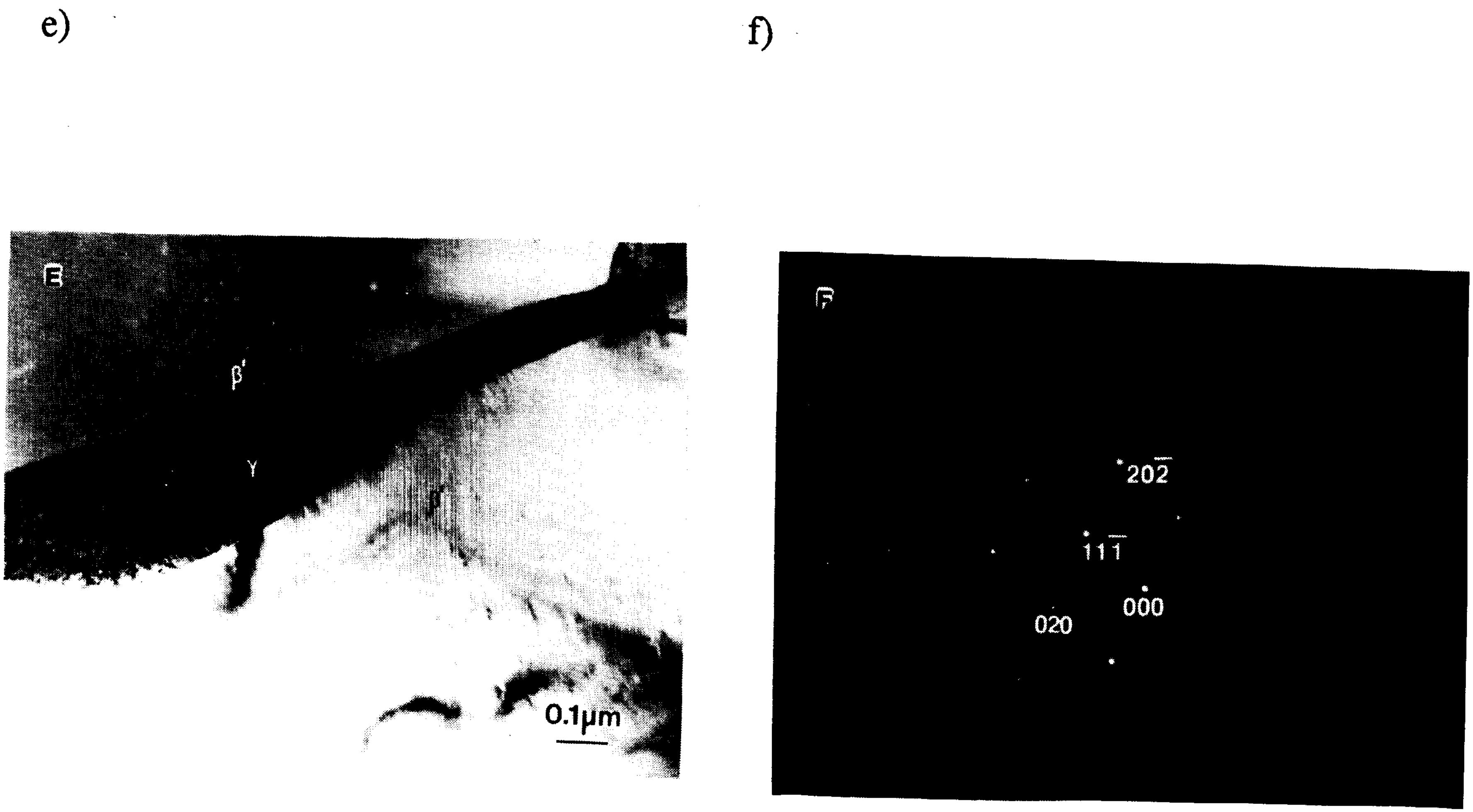
e)
f)
E
β'
γ
0.1μm
F
202̄
111̄
000
020

Figure 4.2.11 continued.

ORIGINAL PAGE
BLACK AND WHITE PHOTOGRAPH

boundaries after annealing at 827°C, see fig. 4.2.11e, but SAD patterns (figure 4.2.11f) did not contain superlattice spots, indicating that only a fcc (γ) phase was present. The volume fraction of the γ phase was small (~1%) and the phase was found again to be iron-rich using EDS, see Table 4.2.1.

Microstructural Stability

In order to assess whether the fine eutectic microstructure of the multi-phase alloy, with and without boron, would coarsen significantly during mechanical testing at elevated temperatures, specimens were annealed for 195 minutes at temperatures up to 1200°C and quenched into water. Figures 4.2.12 and 4.2.13 shows the results of such isochronal anneals in the temperature range 900°C-1200°C. It is clear that significant coarsening begins only above 1000°C for this annealing time which is higher than the highest temperature used for mechanical tests (827°C). Furthermore, microalloying with boron does not appear to alter the coarsening kinetics (fig.4.2.13). The stability of the fine microstructure at elevated temperatures indicates that the mechanical tests results can be assumed to be independent of any coarsening effects of the microstructure.

Comparison with Existing Ni-Fe-Al Phase Diagrams

The multi-phase alloy, and alloys similar to its constituent β' and γ/γ' phases have been marked in the isothermal sections of the ternary Ni-Fe-Al phase diagram at 400°C (fig.2.3j), 750°C (fig. 2.3i) and 850°C (fig. 2.3h), which are within or close to the range of tensile test temperatures, see section 2.3.

According to these figures, at 400°C and 750°C the multi-phase alloy is within the three-phase region ($\beta' + \gamma' + \gamma_{Ni}$), while the alloy Ni-12Al-40Fe which is γ/γ' at room temperature lies on the phase boundary between the two-phase ($\gamma_{Ni} + \gamma'$) and three-phase

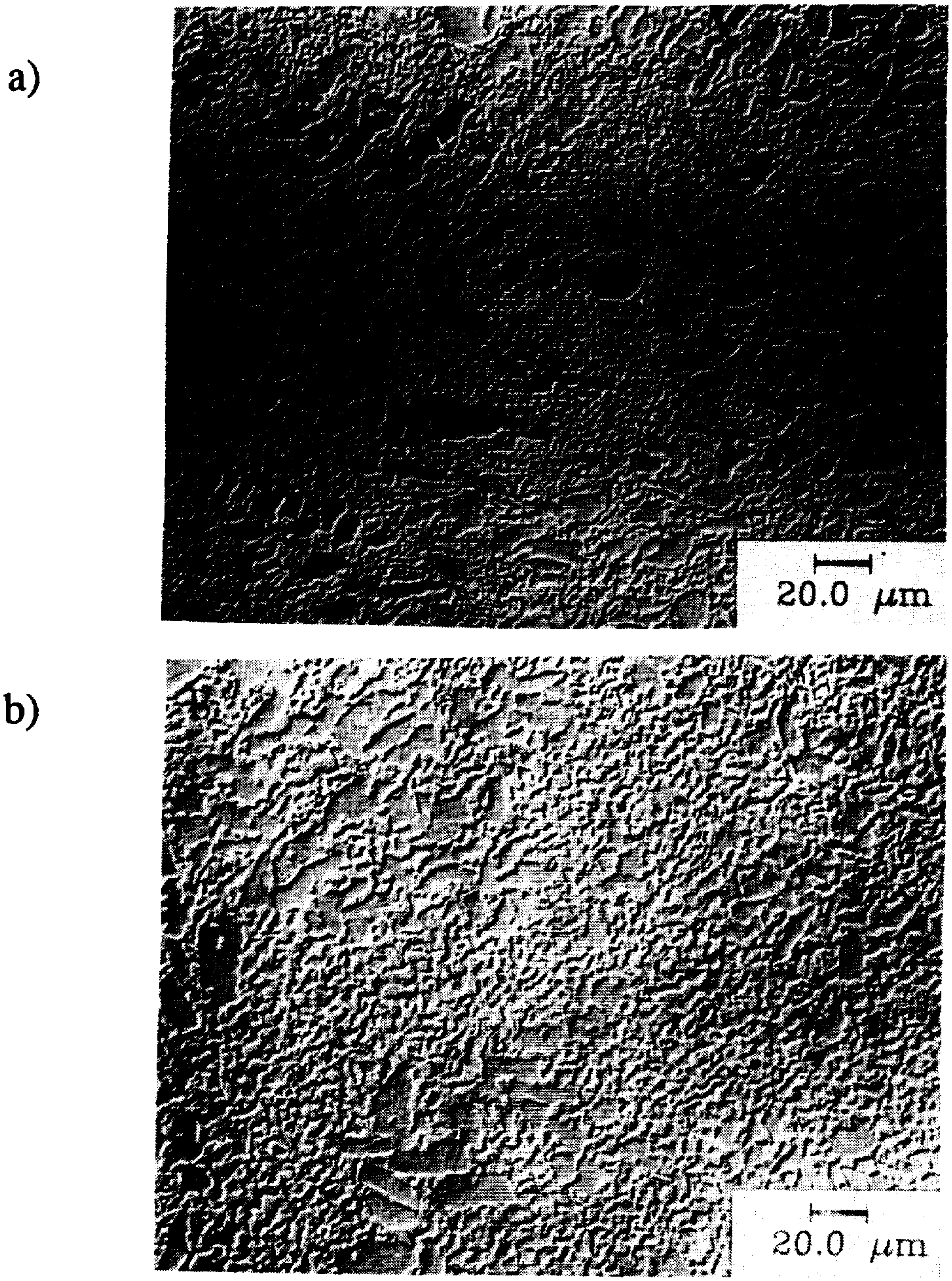

Figure 4.2.12. Optical micrographs using differential interference contrast of Ni-20Al-30Fe following isochronal annealing 195 minutes at (a) 900°C (b) 1000°C (c) 1100°C (d) 1200°C and water quenching. Note that significant coarsening begins only after 1000°C for this time.

ORIGINAL PAGE
BLACK AND WHITE PHOTOGRAPH

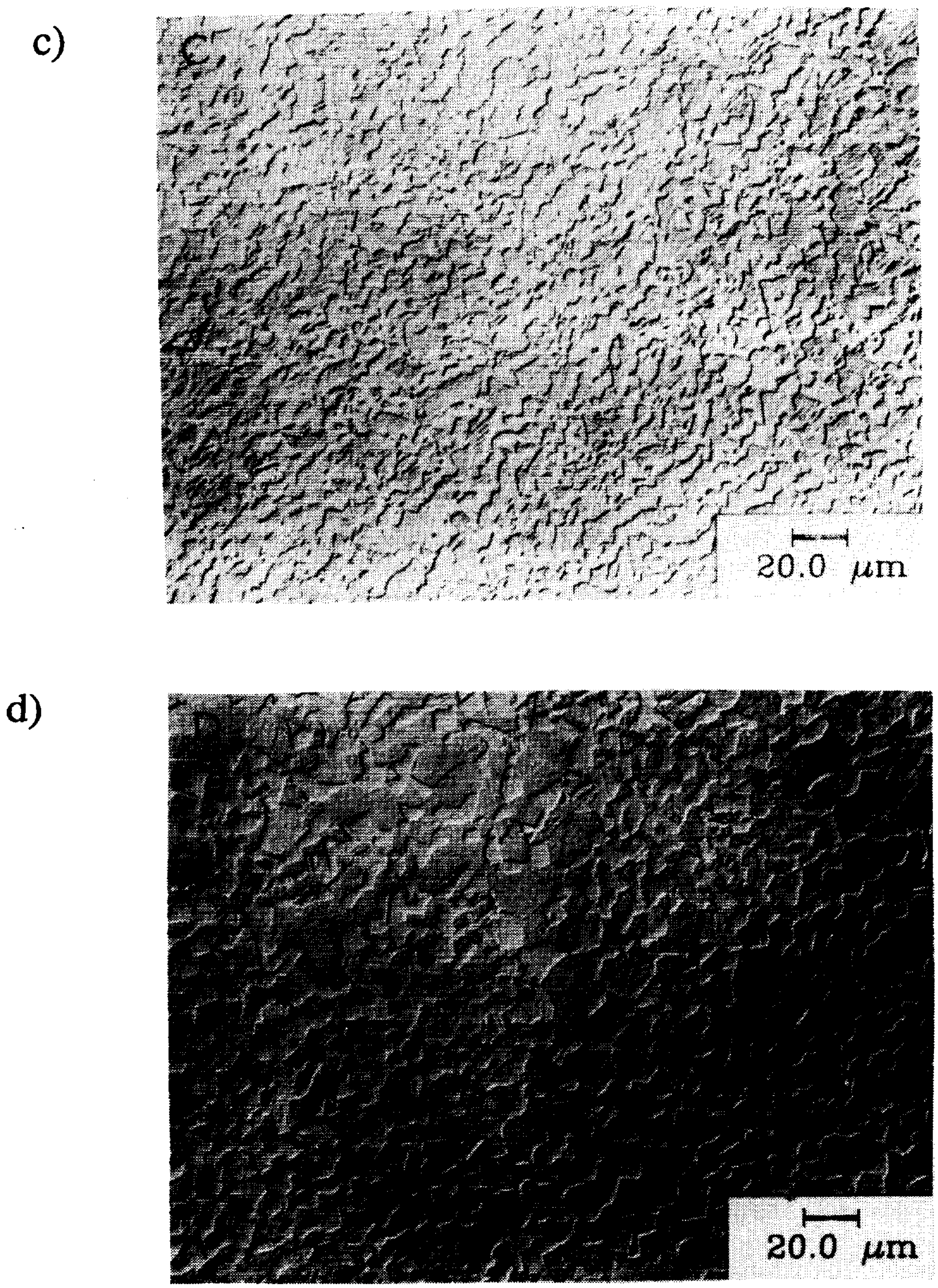
c)
20.0 µm
d)
20.0 µm

Figure 4.2.12 continued.

ORIGINAL PAGE
BLACK AND WHITE PHOTOGRAPH

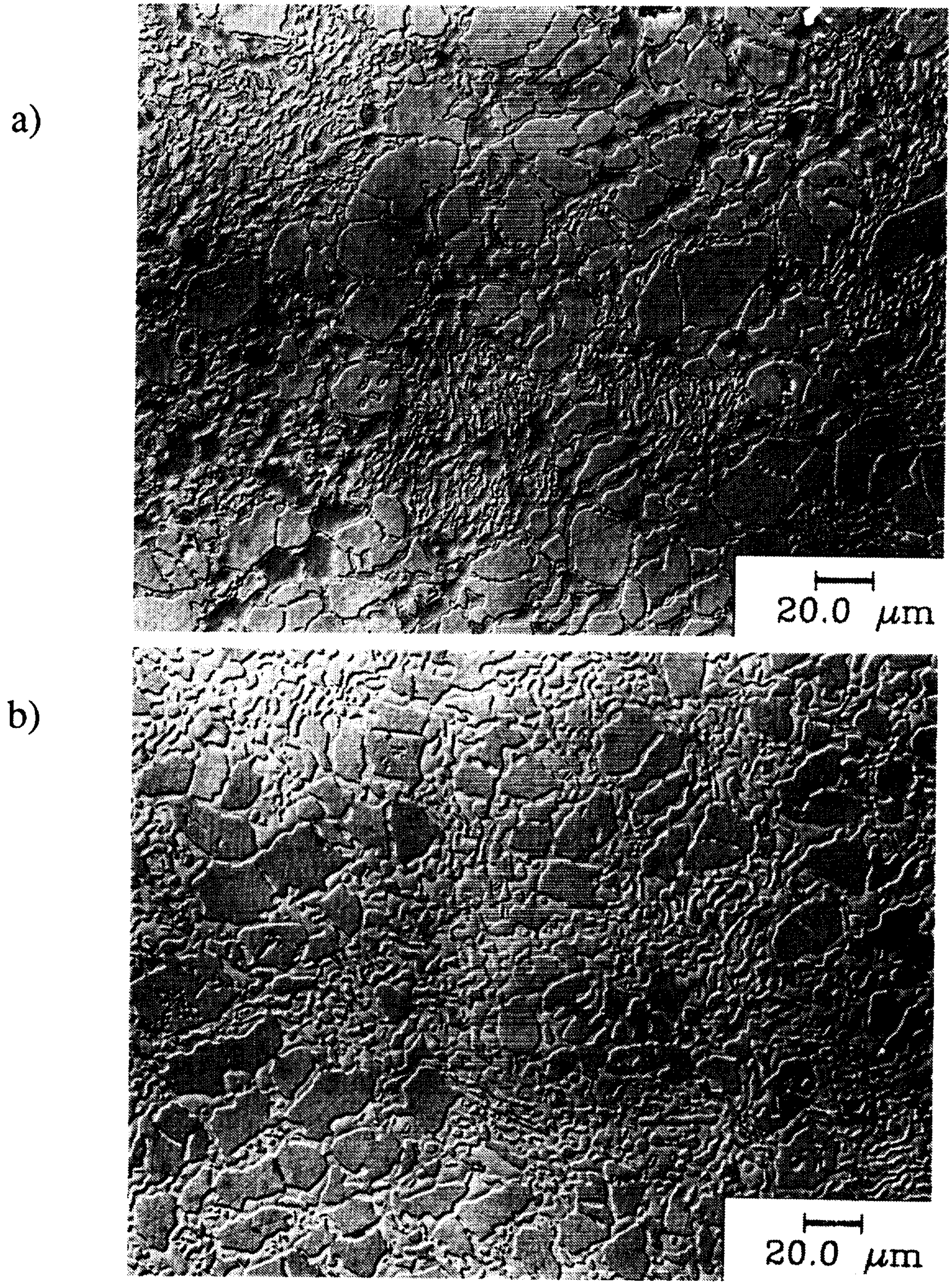

Figure 4.2.13. Optical micrographs using differential interference contrast of Ni-20Al-30Fe-0.17B following isochronal annealing 195 minutes at (a) 800°C (b) 900°C (c) 1000°C (d) 1100°C and water quenching. The coarsening characteristics are essentially similar to the undoped multi-phase alloy.

ORIGINAL PAGE
BLACK AND WHITE PHOTOGRAPH

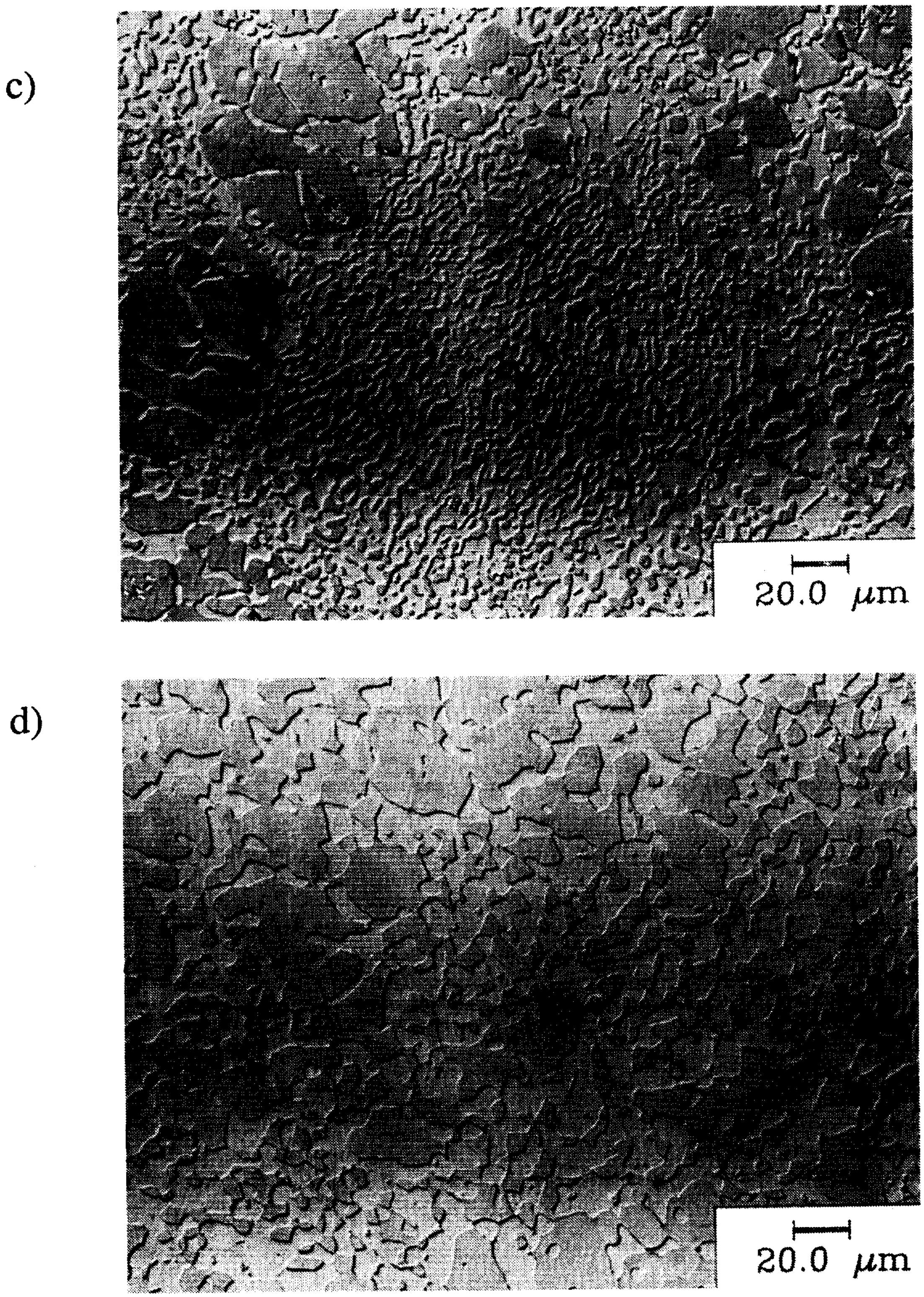
c)
20.0 μm
d)
20.0 μm

Figure 4.2.13.continued

ORIGINAL PAGE
BLACK AND WHITE PHOTOGRAPH

region ($\beta' + \gamma_{Ni} + \gamma'$). By contrast, the alloy Ni-30Al-20Fe which is simply β' at room temperature when cooled at 10°C hr^{-1} from 900°C [78] lies in a two-phase region ($\beta' + \gamma_{Fe}$) at both 400°C and 750°C. γ_{Ni} and γ_{Fe} represents Ni-rich and Fe-rich f.c.c solid solutions, respectively. At 850°C all the alloys lie in the two-phase ($\beta' + \gamma_{Ni}$) region, i.e. the γ' precipitates disorder/dissolve between 750°C and 850°C.

The experimentally observed microstructures for the multi-phase, β' and γ/γ' alloys at 427, 627 and 827°C were generally consistent with the available phase diagram information. A few exceptions were, however, observed. For example, for the β' alloy, Ni-30Al-20Fe, a $\beta' + \gamma_{Fe}$ microstructure would be expected in the temperature range 400°C-750°C from the two isotherms in figure (2.3i-j). Experimentally, along with the β' phase, an iron-rich γ/γ' phase was also observed instead of only the disordered γ phase (see superlattice reflections in fig. 4.2.11b). Also, at 827°C the second phase is iron-rich rather than nickel-rich as expected from the 850°C isotherm (fig. 2.3h). The microstructures and chemistry of the phases are tabulated in Table 4.2.1.

4.3 Mechanical Properties

4.3.1 Room Temperature

The comparative tensile test data of the multi-phase alloy and alloys similar to its constituent phases are summarized in Table 4.3.1 and described below.

The single-extruded multi-phase alloy, Ni-20Al-30Fe, exhibited ~7% elongation and a yield strength of 850 MPa; by contrast, the double-extruded alloy exhibited ~20% elongation and a yield strength of 760 MPa, see fig. 4.3.1. The observed fracture surfaces were similar in both the single and double-extruded multi-phase alloys, that is,

TABLE 4.3.1. SUMMARY OF ROOM TEMPERATURE TENSILE BEHAVIOR FOR AS-EXTRUDED Ni-20Al-30Fe, Ni-12Al-40Fe and Ni-30Al-20Fe

CONDITION	No.	YIELD STRESS (MPa)	FRACTURE STRESS (MPa)	ELONGATION (%)
Ni-20Al-30Fe ($\beta' + \gamma/\gamma'$)				
Single Extruded(SE)		850	1300	8
Double-extruded(DE)	(B#1)	765	1355	20
	(B#2)	760	1370	23
Ni-12Al-40Fe (γ/γ')				
Single Extruded(SE)	(D)	505	810	28
	(N)	505	820	38
Ni-30Al-20Fe (β')				
Single Extruded(SE)		-	780	0
		-	760	0
Double Extruded, DE	(#1)	800	930	2
	(#2)	825	1070	6
Ni-20Al-30Fe-0.17B ($\beta'+\gamma/\gamma'$)				
Single Extruded(SE)		700	1160	13

C-2

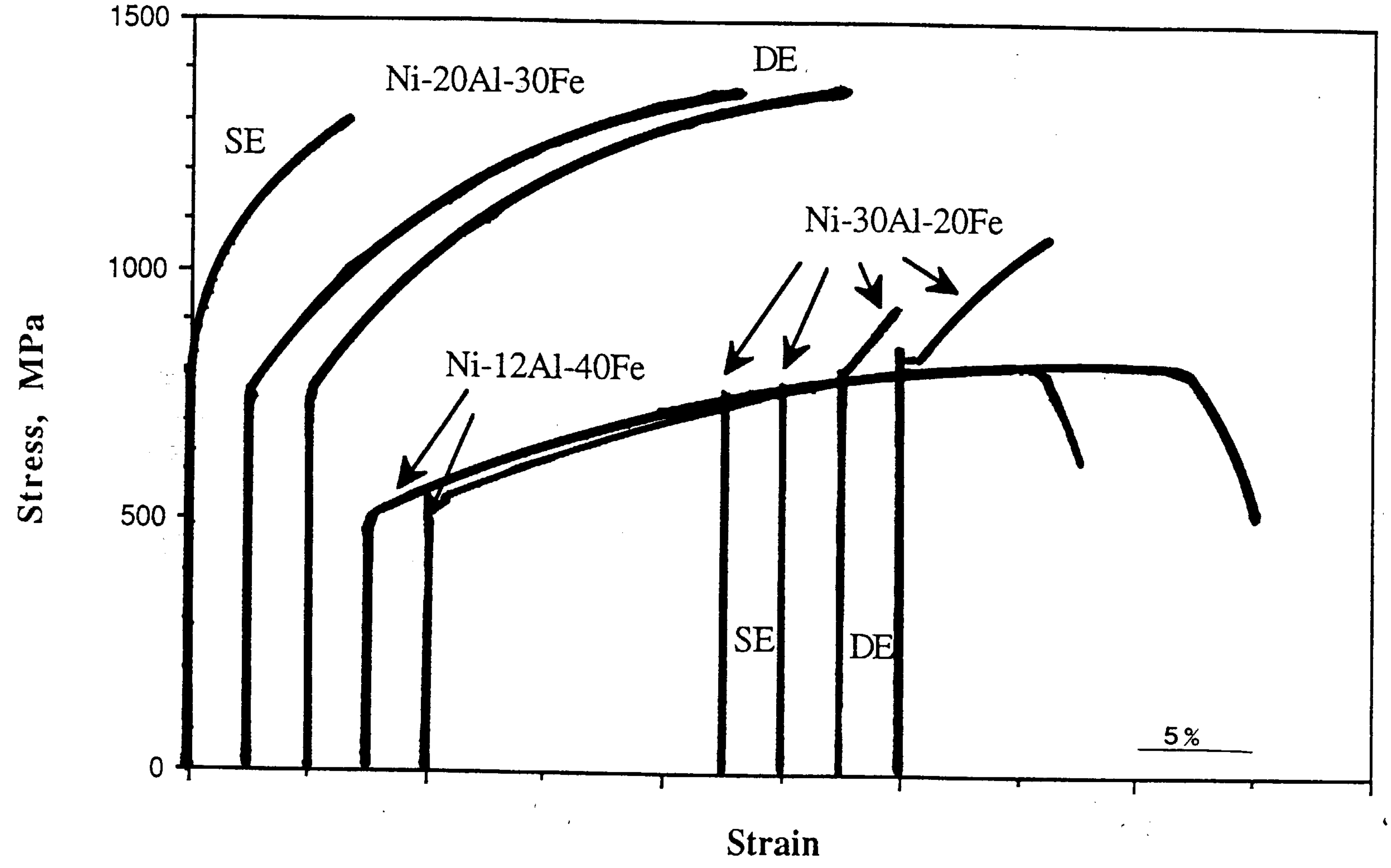

Figure 4.3.1 Stress-strain curves of single and double-extruded Ni-20Al-30Fe, Ni-30Al-20Fe and Ni-12Al-40Fe.

transgranular cleavage in the pro-eutectic β' phase and dimple fracture in the eutectic matrix (fig. 4.3.2a).

The single-extruded γ/γ alloy, Ni-12Al-40Fe, exhibited a lower yield stress of 507 MPa but a higher average tensile elongation of ~33% (two individual tests exhibiting 28 and 38% elongation) than the multi-phase or β' alloys. The fracture surfaces showed evidence of extensive plastic deformation prior to fracture, the fracture being of dimple transgranular type (see fig. 4.3.2b).

The β' alloy, Ni-30Al-20Fe, which is close to the composition of the pro-eutectic β' phase in the multi-phase alloy, fractured before 0.2% strain at 770 MPa in the single-extruded state and at ~2% tensile elongation with a 800 MPa yield stress in the double-extruded (at 6:1 area reduction ratio) state. A second test (double-extruded at 5:1 area reduction ratio) indicated ~6% tensile elongation and a similar (824 MPa) yield stress. The fracture surfaces, which were similar in both single and double-extruded states, showed transgranular cleavage, although a few intergranular surfaces were also observed (fig. 4.3.2c-d).

The differences between the mechanical behavior of the as-extruded single and double-extruded multi-phase Ni-20Al-30Fe and β' Ni-30Al-20Fe are partly related to the difference in cooling rates following extrusions (sand cooling for single-extruded alloys as opposed to air cooling for double-extruded alloys); the effect of different annealing treatments and cooling rates on mechanical properties were investigated, the results are reported in the following section on annealing effects.

The single-extruded boron-doped multi-phase alloy, Ni-20Al-30Fe-0.17B, exhibited a lower yield stress (700 MPa) and elongation (12%) than the undoped multi-phase alloy, presumably due to the coarser scale of the microstructure. The fracture surface of the boron-doped alloy was similar to those of undoped multi-phase alloy.

In order to further elucidate the failure behavior of the multi-phase alloy, tensile samples of the double-extruded alloy, annealed at 1300°C for 3.5 hours and air-cooled to

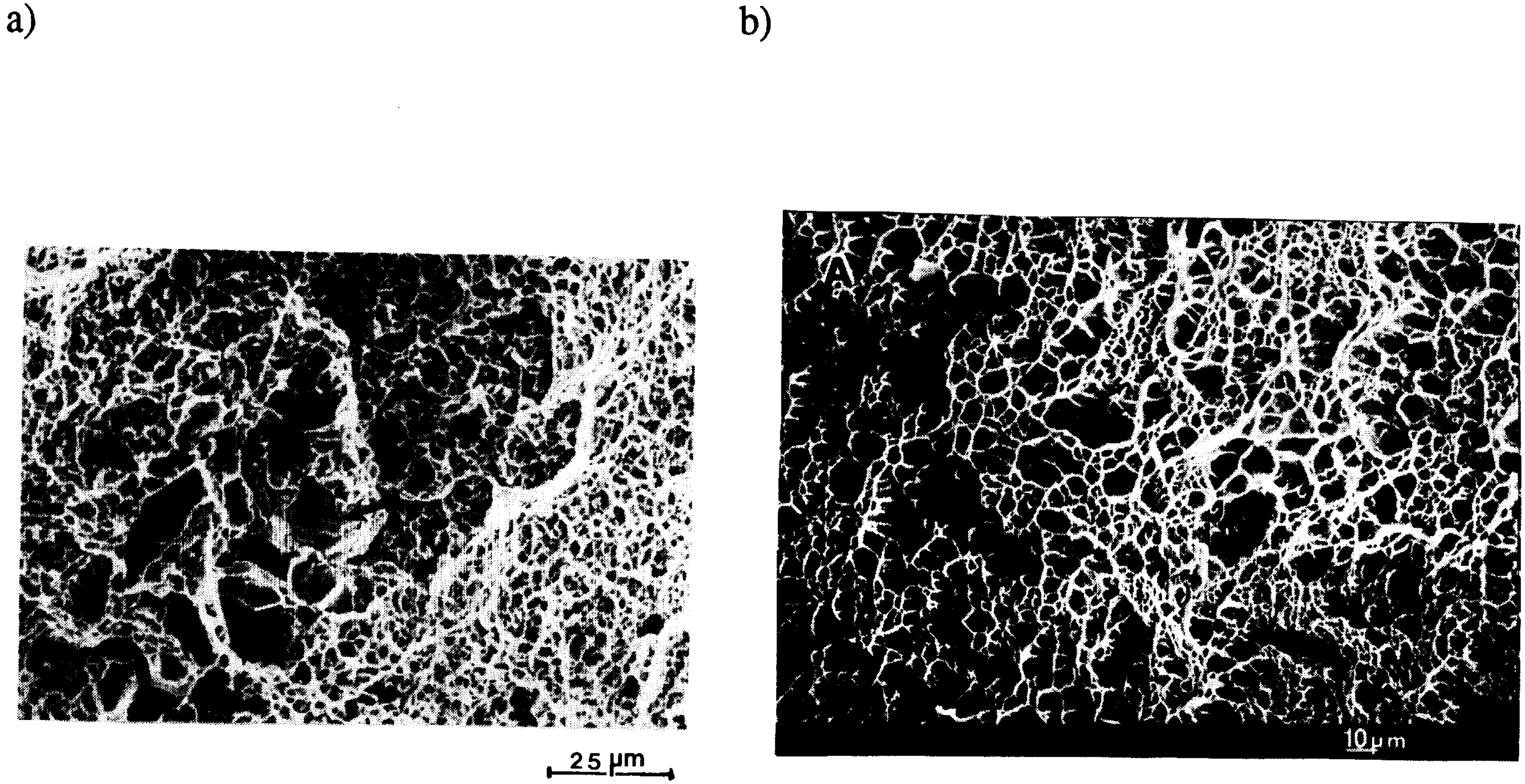

Figure 4.3.2 Fractographs of tensile tested specimens of: (a) double-extruded Ni-20Al-30Fe showing transgranular cleavage in the pro-eutectic β' phase (arrowed) and dimple fracture in the eutectic (b) single-extruded γ/γ' alloy Ni-12Al-40Fe showing a dimpled fracture surface (c) single-extruded β' Ni-30Al-20Fe showing predominantly transgranular cleavage type fracture, although some intergranular surfaces may be observed too (d) double-extruded β' Ni-30Al-20Fe after 6% elongation showing essentially similar fracture mode as in (c).

ORIGINAL PAGE
BLACK AND WHITE PHOTOGRAPH

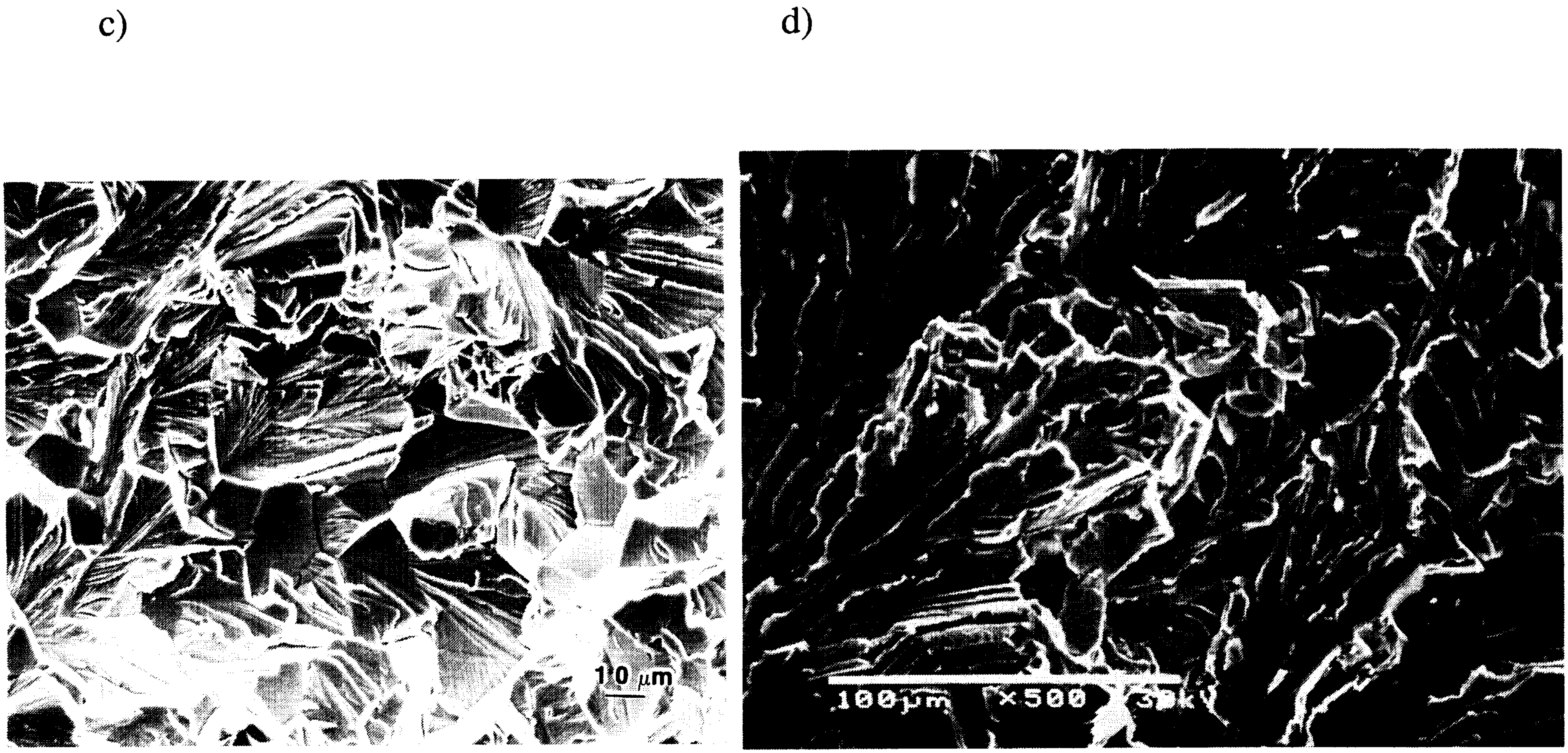
c)
d)
10 μm
100μm ×500

Figure 4.3.2 continued.

ORIGINAL PAGE
BLACK AND WHITE PHOTOGRAPH

produce a coarsened microstructure for easier optical observation, were strained to failure. Longitudinal sections of the tensile-tested specimen were examined by optical microscopy (fig. 4.3.3). Cracks which had developed in the pro-eutectic β' phase were clearly observed to stop at the interface of pro-eutectic β' phase and the γ/γ' phase (darker phase). No separation at the interface between the β' and the γ/γ' phases was observed. A few cracks were also observed in the β' phase of the coarsened eutectic. These were again arrested by the ductile γ/γ' phase, indicating that one way the γ/γ' phase improves ductility of the multi-phase alloy is by a crack-stopping mechanism. Similar examination of longitudinal sections from deformed as-extruded tensile specimens revealed a few cracks in the pro-eutectic phase, however, no cracks were observed in the eutectic. Clearly, the pro-eutectic β' phase exhibits a high propensity for cracking early during deformation, indicating the basically brittle nature of the alloy. Thus, failure in the extruded multi-phase alloy appears to be related to the catastrophic propagation of supercritical cracks nucleated in the coarse pro-eutectic phase.

4.3.2 Elevated Temperature

Hot Hardness Tests

As noted above, the fine scale (0.5μm lamellae width) of the double-extruded microstructure of the multi-phase alloy was found (see section 4.2.2) to be resistant to coarsening up to 1000°C for an annealing time of 195 minutes, which is longer than the duration of a typical tensile test or hot hardness test.

The hot hardness measurements of the multi-phase alloy, Ni-20Al-30Fe, and the β' alloy, Ni-30Al-20Fe (fig. 4.3.4a-b), indicate a behavior commonly noted for NiAl [9,51], and for B2 alloys in general [103], where a signficant loss of strength with increasing

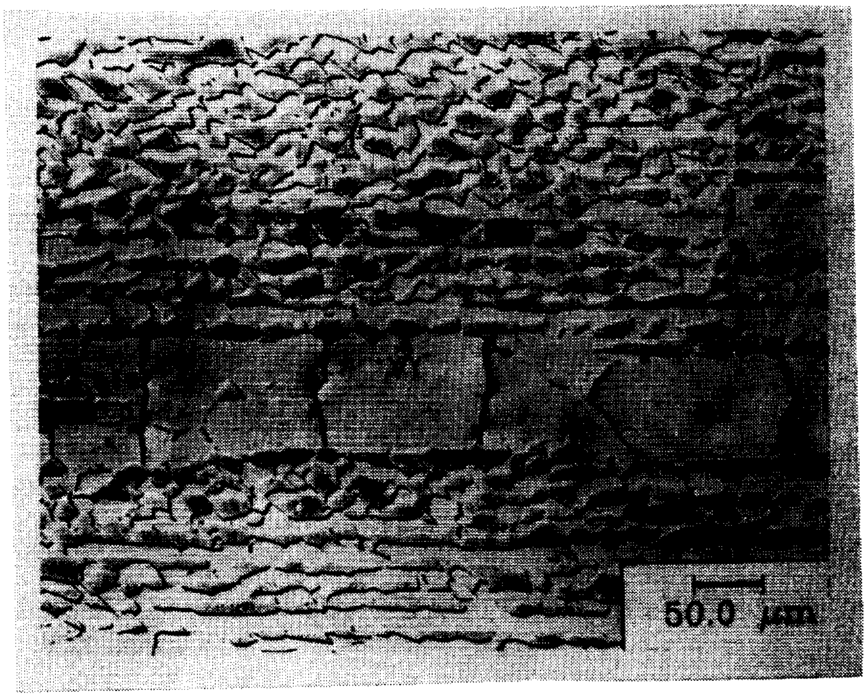

Figure 4.3.3 Polished longitudinal section of double-extruded, multi-phase Ni-20Al-30Fe, annealed at 1300°C and tested in tension, showing cracks in the pro-eutectic β' phase being arrested at the β'-γ/γ' interface.

ORIGINAL PAGE
BLACK AND WHITE PHOTOGRAPH

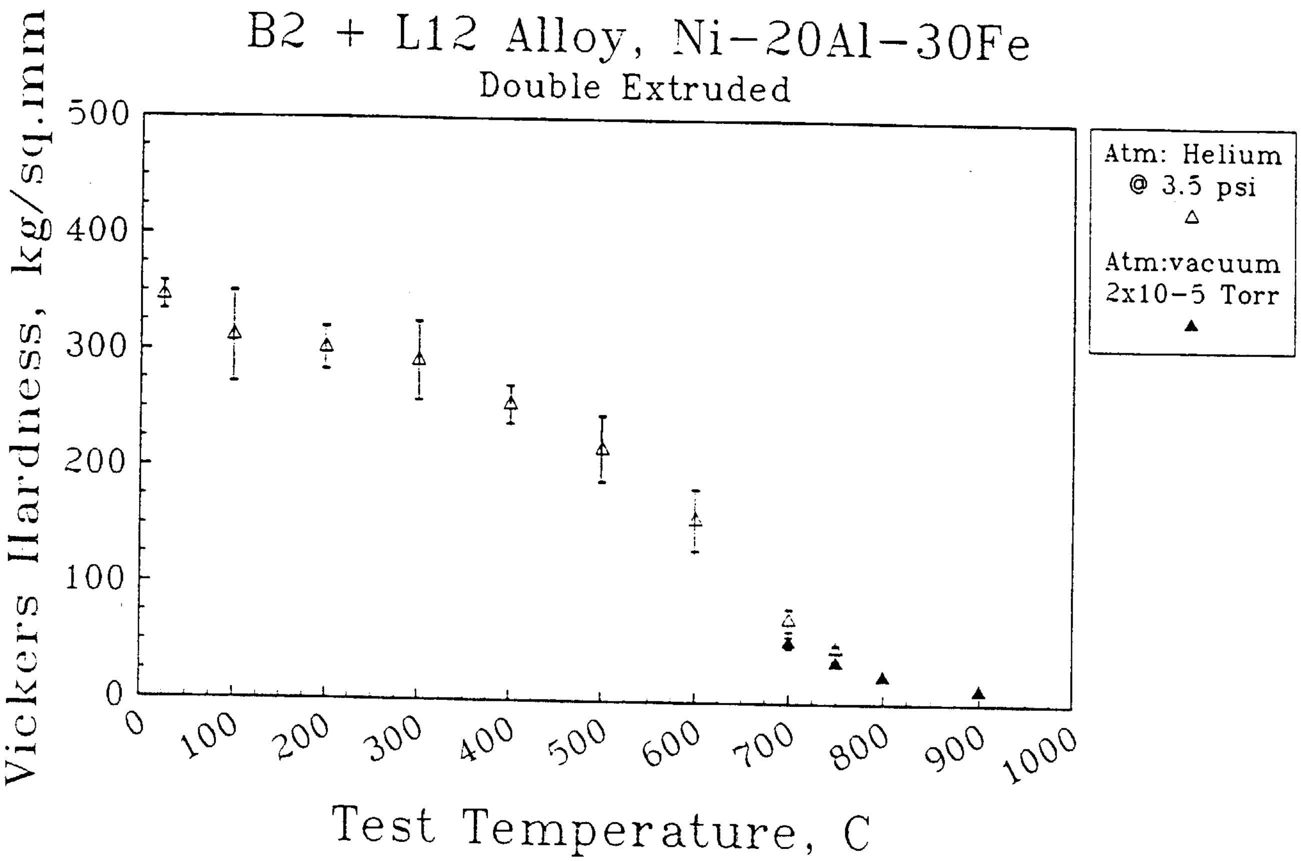

Figure 4.3.9a

Figure 4.3.4 The variation of strength with increasing temperature as determined by Vickers hot hardness tests for: (a) multi-phase Ni-20Al-30Fe (b) β' Ni-30Al-20Fe (c) γ/γ' Ni-12Al-40Fe (d) boron-doped multi-phase alloy Ni-20Al-30Fe-0.17B (e) boron-doped multi-phase alloy coarsened by annealing at 1100°C for 15 hrs and furnace cooled at 2°C/min. The γ/γ' alloy shows better strength retention than the multi-phase (undoped or boron-doped) and β' alloy. Error bars indicate 95% confidence intervals.

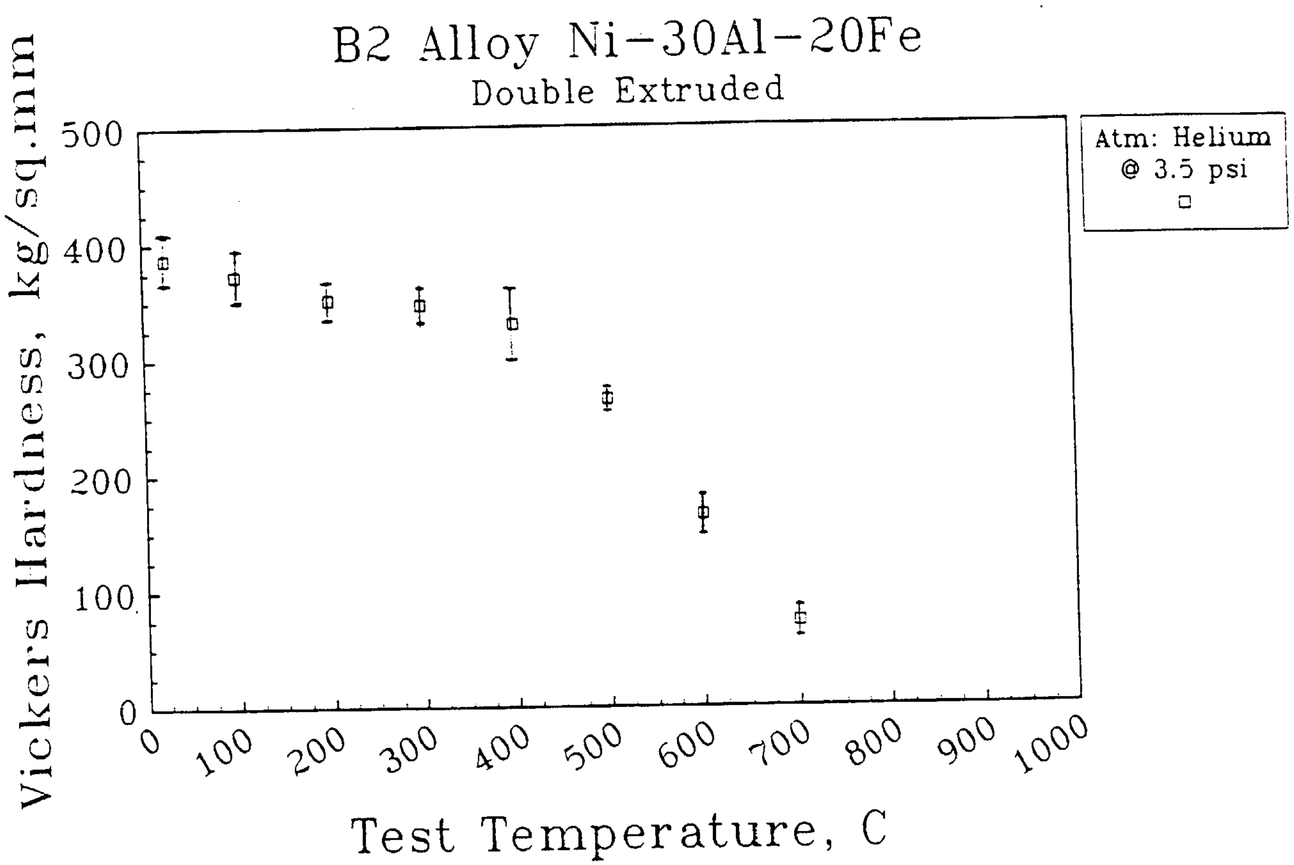

Figure 4.3.4b

Figure 4.3.4 continued.

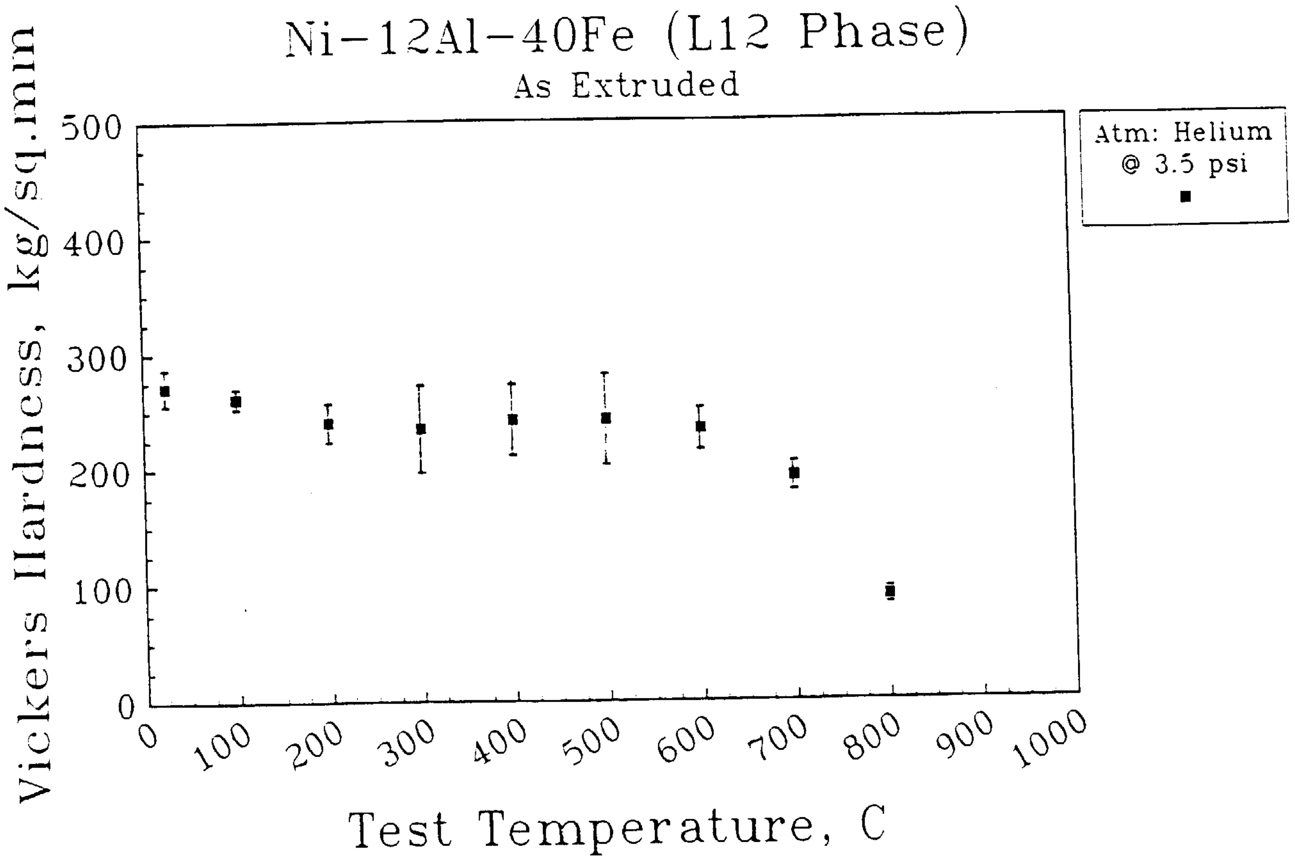

Figure 4.3.4c

Figure 4.3.4 continued.

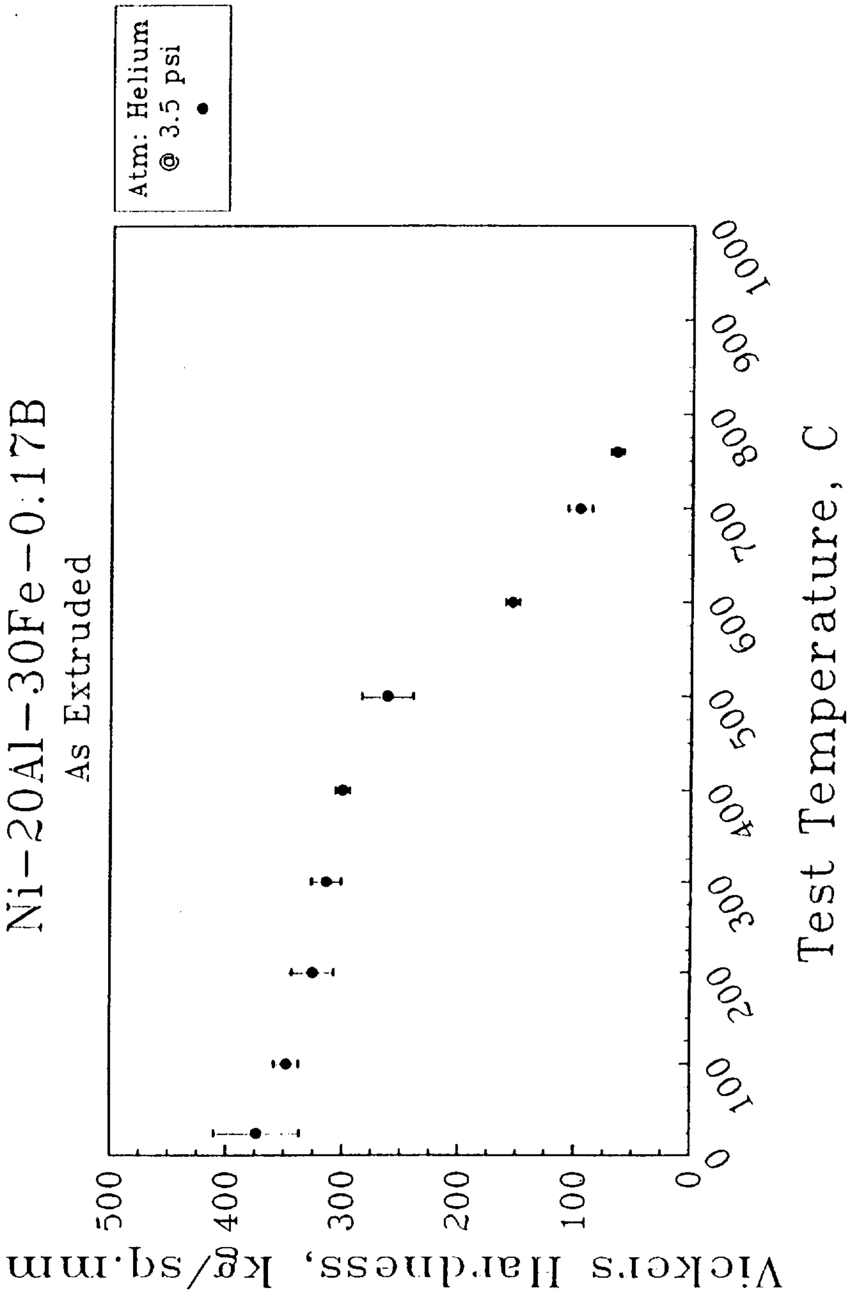

Figure 4.3.4d

Figure 4.3.4 continued.

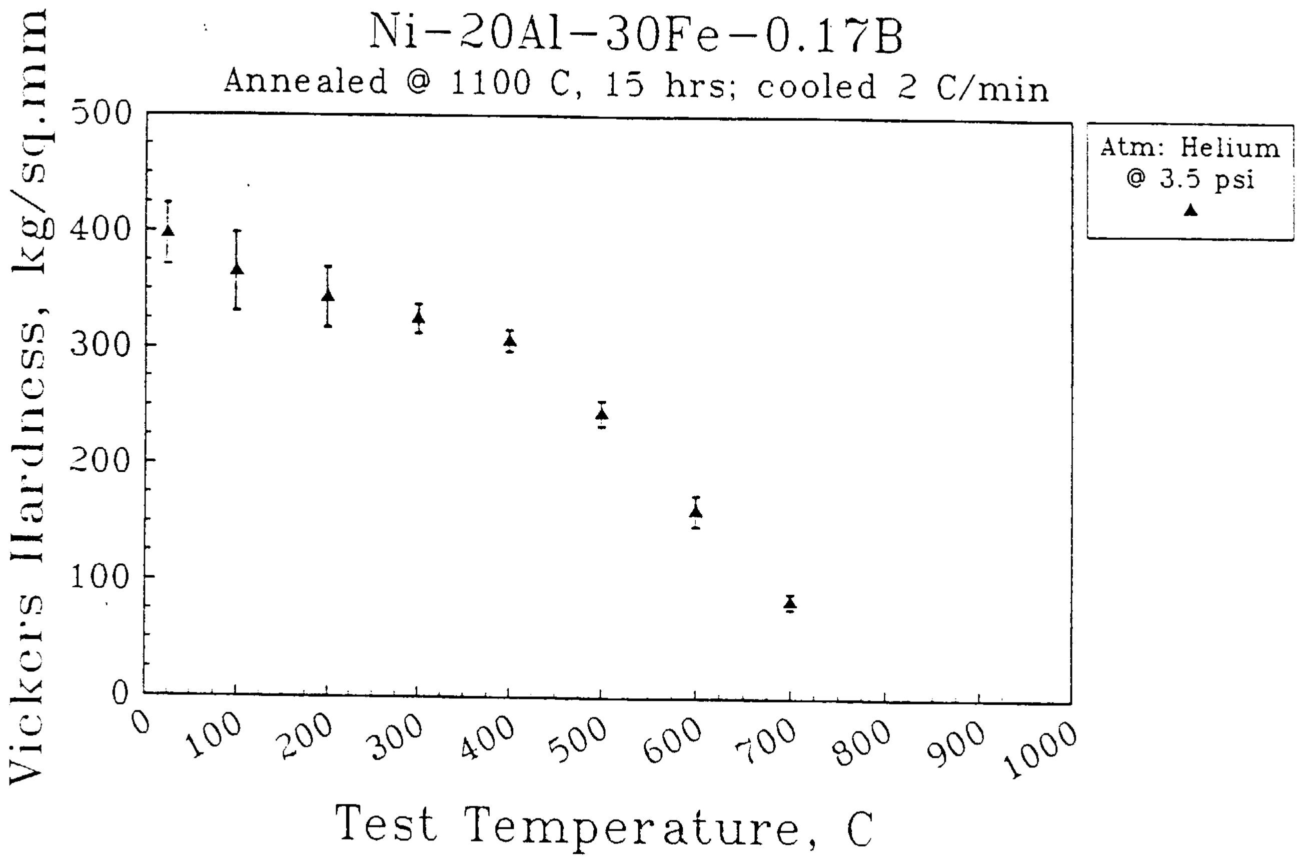

Figure 4.3.4e

Figure 4.3.4 continued.

ORIGINAL PAGE IS
OF POOR QUALITY

ORIGINAL PAGE IS
OF POOR QUALITY

temperatures occurs beyond a plateau or slow decrease in the temperature range ~ 27°C-400°C. The transition temperature T_t beyond which the stren[illegible]ecreases sharply scales with the solidus temperature indicating that diffusion-assisted mechanisms are responsible for such a decrease in strength. Thus, β' Ni-30Al-20Fe, which has a lower solidus temperature than stoichiometric NiAl (1400°C versus 1640°C), exhibits a lower T_t (~500°C) than stoichiometric NiAl (~627°C) [9].

The γ/γ' alloy, Ni-12Al-40Fe (fig. 4.3.4c), while exhibiting a lower hardness than the β' phase at lower temperatures (<400°C), retained its strength up to 700°C, beyond which a sharp decrease in strength occurred, presumably due to the observed coarsening of the γ' precipitates (see section 4.2.2) and eventually disordering/dissolution of γ' into γ. It should be noted that, although a positive temperature dependence of strength is often observed for γ'-based alloys, no such anomalous strengthening was observed for this particular γ/γ' alloy, presumably due to the constituent γ phase which itself does not exhibit any anomalous strengthening behavior. That the rate of loss of strength with temperatures greater than 400°C was lower for the multi-phase alloy than the single phase β' alloy is presumably due to the high temperature strength characteristics of the γ/γ' phase.

The hot hardness characteristics of the boron-doped multi-phase alloy (fig.4.3.4d) were similar to those without boron; a sharp decrease in strength was observed above 500°C. The higher hardness at all test temperatures is probably due to the solid solution strengthening effect of boron. The lack of any anomalous strengthening (or at least a plateau in strength) effect arising from the constituent γ/γ' is evident. Weihs et al.[61] noted the influence of scale of microstructure on anomalous strengthening behavior of Ni_3Al where, in contrast to coarse grained alloys, fine grained alloys were observed not to exhibit anomalous strengthening. Thus, to test if a coarse grained microstructure would exhibit better high temperature strength retention, the high temperature strength characteristics of a boron-doped multi-phase alloy specimen, annealed for 15 hrs at 1100°C and furnace cooled at 2°C/min, were determined. The results (fig.4.3.4e) are essentially similar to the as-extruded alloy indicating that limited coarsening of the microstructure does not influence the high temperature strength of multi-phase alloys significantly.

Elevated Temperature Tensile Tests

Stress-strain graphs of the elevated temperature tensile tests are shown in figs. 4.3.5 through 4.3.8 and the results are summarized in Table 4.3.2 and fig. 4.3.9.

Figure 4.3.5 shows the stress-strain curves of the multi-phase alloy for different test temperatures (the data for room temperature test also being included for comparison). At room temperature, the alloy exhibited a yield strength of 760 MPa and plastic strain to fracture, ε_f, of ~20%. At 427°C, the yield strength decreased to 610 MPa and the ε_f increased to ~34%. Note that the rate of work-hardening at 427°C is also lower than that at room temperature. At 627°C, the yield strength decreased to ~310 MPa and ε_f increased to ~41%; no work-hardening was observed at this temperature. At room temperature failure preceded necking, whilst at 427°C and 627°C slight necking was observed before final failure. Finally, at 827°C where the microstructure is known to be $\beta' + \gamma$ only, no work-hardening was observed after yielding at ~50 MPa and an elongation of 70% without any necking was observed before the test was stopped. The large elongation without any necking is indicative of the occurrence of either recovery or dynamic recrystallization. A second sample was strained in vacuum at 827°C, where an ε_f of almost 100% was observed before failure.

Figure 4.3.6 shows the stress-strain curves for the γ/γ' alloy, Ni-12Al-40Fe, at different test temperatures. At 27°C, the alloy exhibited a yield strength of 507 MPa and a fracture strain of 28%. At 427°C, the yield strength decreased to ~420 MPa and ε_f also decreased to 15%. At both 27°C and 427°C, necking preceded final failure and the work-

TABLE 4.3.2. SUMMARY OF ELEVATED TEMPERATURE TENSILE BEHAVIOR

TEST TEMPERATURE	YIELD STRESS (MPa)	FRACTURE STRESS (MPa)	PLASTIC STRAIN (%)
Ni-20Al-30Fe (β' + γ/γ')			
27°C	760	1350	20
427°C	610	930	34
627°C	310	345	41
827°C	50	-	>70*
Ni-12Al-40Fe (γ/γ')			
27°C	505	810	28
427°C	415	615	15
627°C	-	345	0
827°C	120	100	1
Ni-30Al-20Fe (β')			
27°C	800	930	2
627°C	200	125	27
827°C	55	-	97
Ni-20Al-30Fe-0.17B			
27°C	700	1160	13
427°C	570	755	6
627°C	320	360	10
827°C	85	25	33

---

* Test stopped after 70% elongation.

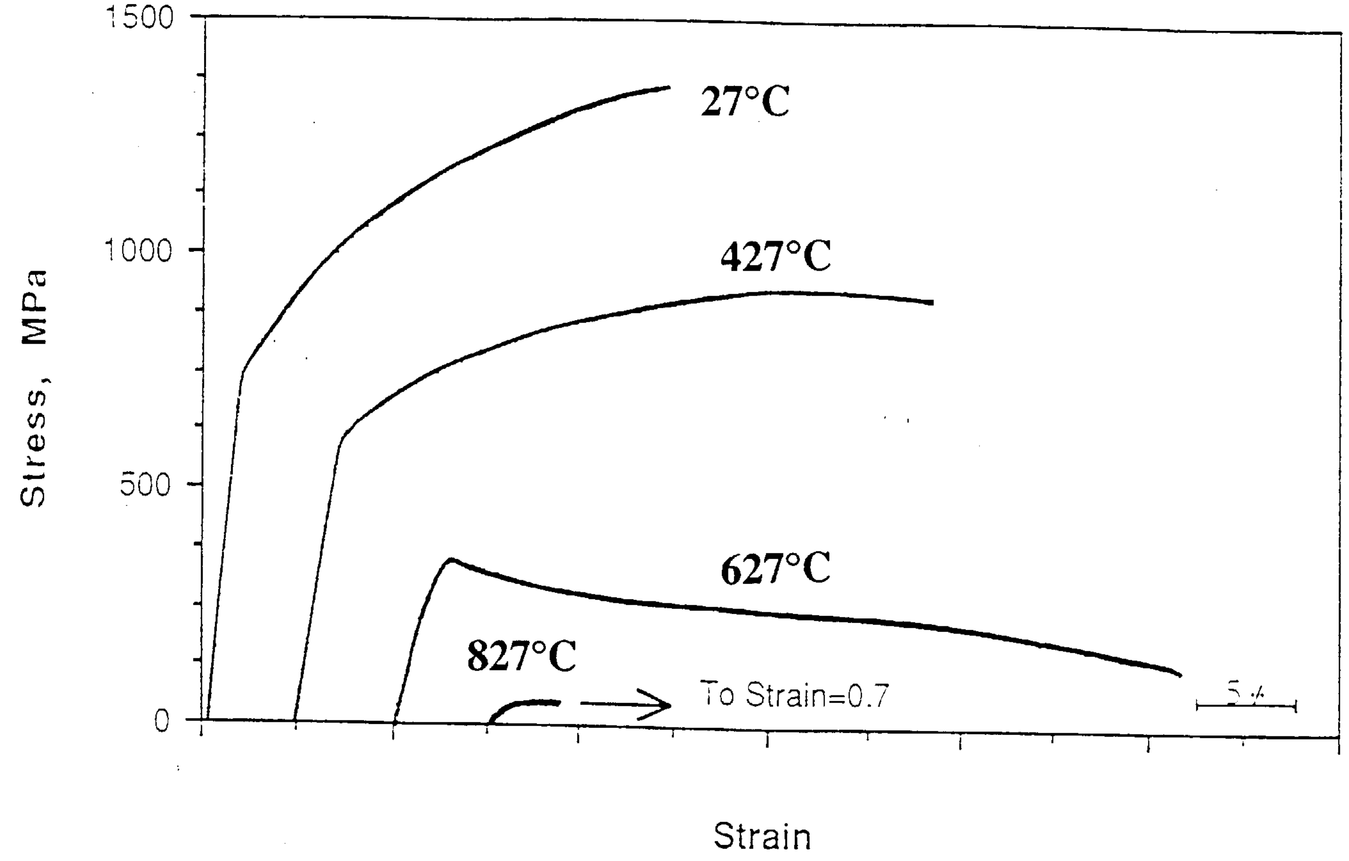

Figure 4.3.5 Stress-strain of multi-phase ($\beta'+\gamma/\gamma'$) alloy Ni-20Al-30Fe tested at 27°C, 427°C, 627°C and 827°C.

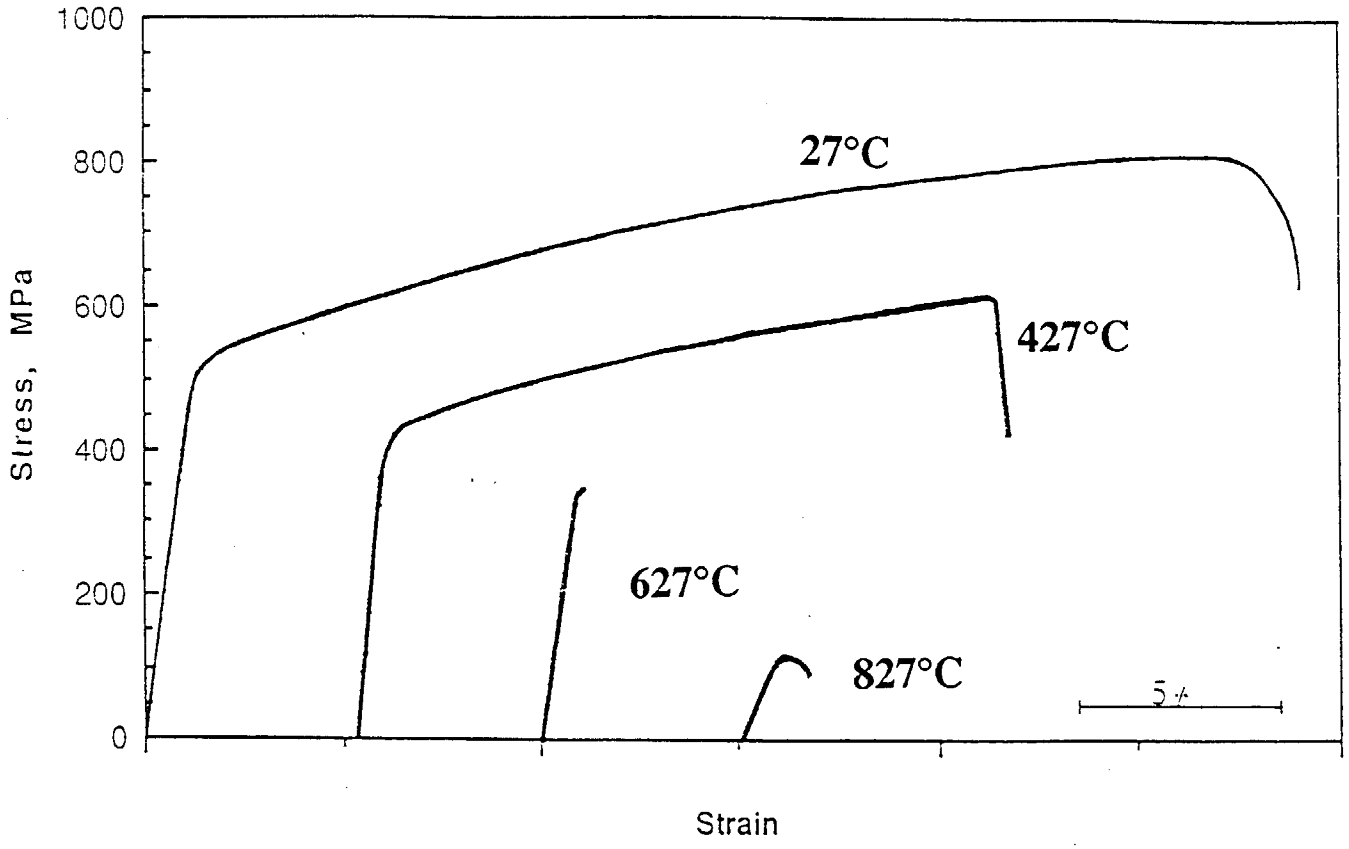

Figure 4.3.6 Stress-strain of the γ/γ alloy Ni-12Al-40Fe tested at 27°C, 427°C, 627°C and 827°C.

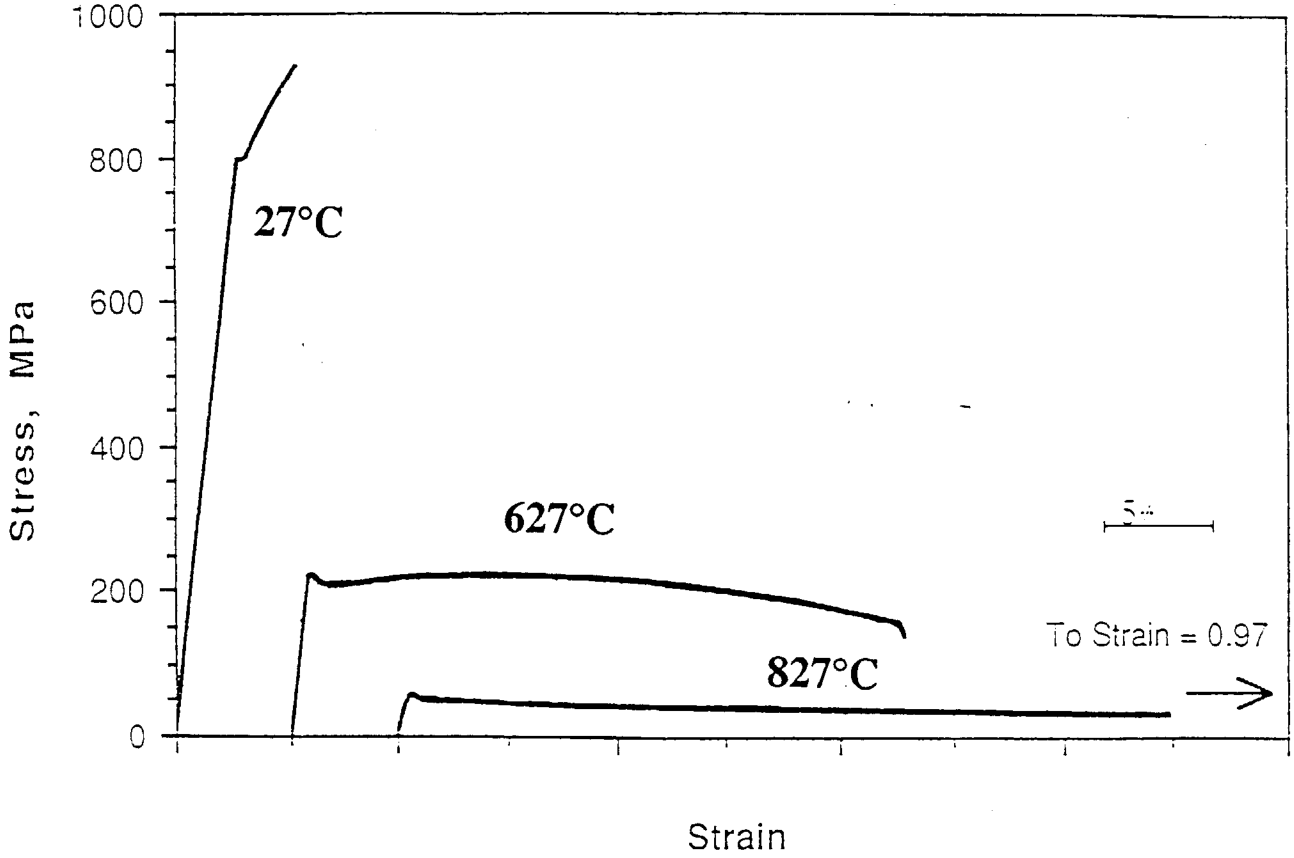

Figure 4.3.7 Stress-strain of the β' alloy Ni-30Al-20Fe tested at 27°C, 627°C and 827°C.

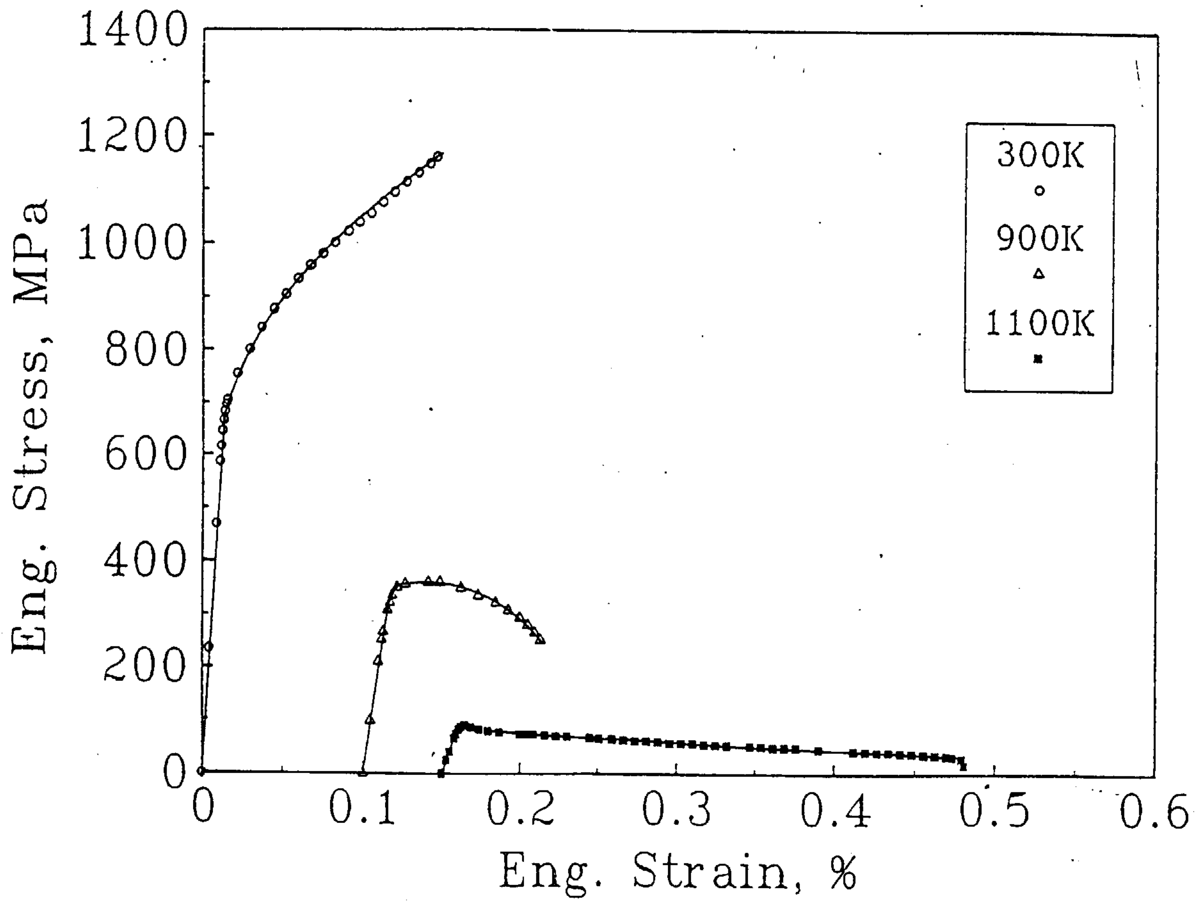

Figure 4.3.8 Stress-strain of the boron-doped multi-phase (β'+γ/γ') alloy Ni-20Al-30Fe-0.17B tested at 27°C, 627°C and 827°C.

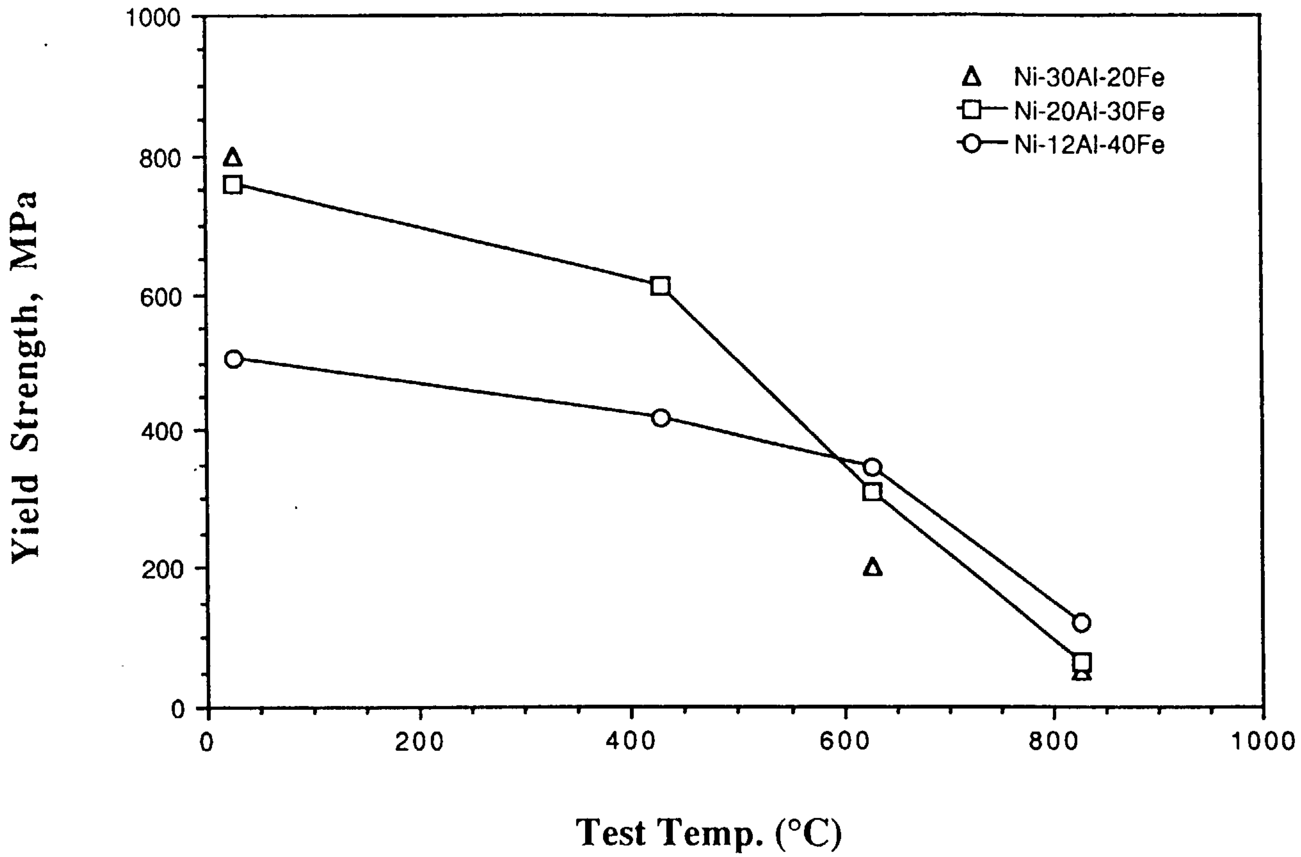

Figure 4.3.9a

Figure 4.3.9 Graph of temperature dependence of (a) yield strength and (b) elongation of the multi-phase alloy Ni-20Al-30Fe, the γ/γ' phase Ni-12Al-40Fe and the β' phase Ni-30Al-20Fe. The data points for yield strength or elongation the β' phase are not connected since the strength at 427°C is expected to be higher and the elongation lower than a linear interpolation between the values at 27°C and 627°C would indicate (β' alloys typically exhibit a strength plateau upto ~500°C).

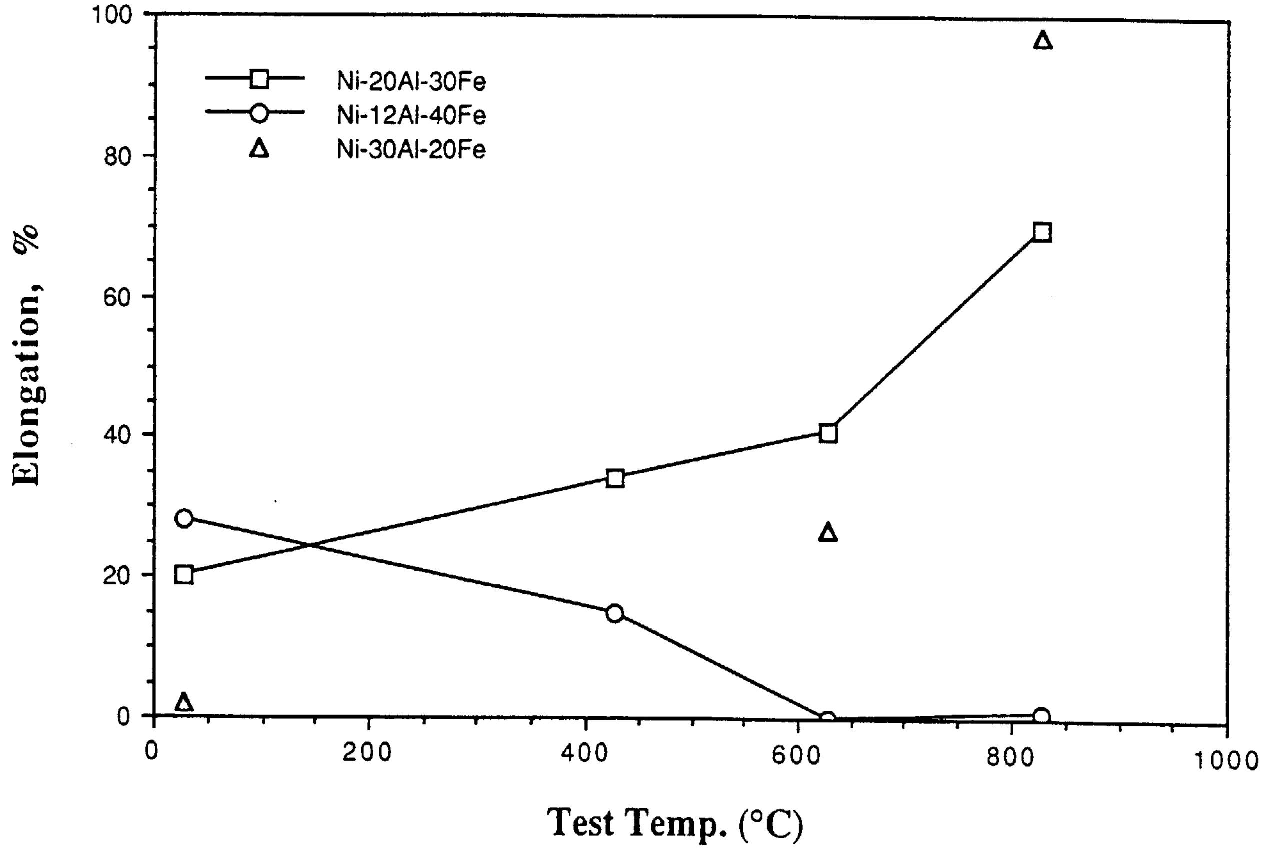

Figure 4.3.9b

Figure 4.3.9 continued.

hardening rate was insensitive to the temperature change. At 627°C, the alloy failed in a brittle manner at a stress of ~345 MPa immediately before 0.2% strain yield. At 827°C, where the alloy is known to exhibit a coarsened γ/γ' microstructure, a low yield strength of 119 MPa and ~1% fracture strain was observed. No work-hardening was observed at this temperature.

The stress-strain curves for the β' alloy, Ni-30Al-20Fe, are shown in fig. 4.3.7. At room temperature, only ~2% ε_f was observed following yielding at a stress of 800 MPa. A second test, however, exhibited 6% elongation and ~825 MPa yield strength. At 627°C, the yield strength decreased to 199 MPa and the ε_f increased to ~27%. At 827°C, the yield strength decreased further to only ~53 MPa and the ε_f increased dramatically to 97%. No strain-hardening was observed in either elevated temperature test. The high ε_f at 827°C is indicative of the occurrence of either recovery or dynamic recrystallization in the deformed microstructure of the multi-phase alloy.

Figure 4.3.8 shows the stress strain curves for the boron-doped multi-phase alloy tested over the temperature range 27-827°C (the data for 27°C test are included for comparison). It is clear that the nature of stress-strain response is similar to the undoped multi-phase alloy (fig.4.3.5) although the elongations are reduced. While the general trend of increasing ductility with increasing temperature is evident for test temperatures in excess of 427°C, the ductility at 427°C itself is lower than that observed at room temperature. The reasons behind the reduced elongation from 27°C test to 427°C test are not clear and additional tests are necessary to remove any uncertainity in test results. One possibility, however, is that the decreased ductility could be related to precipitation of α-Fe within the β' phase (see Chapter 5) in the temperature range 400-500°C which may decrease ductility; such decreased ductility is probably not observed in the undoped multi-phase alloy due to its fine scale of the microstructure which may overcome any embrittlement due to precipitation strengthening by α-Fe. Interestingly, while the yield strengths at 27°C and 427°C were slightly lower than the undoped multi-phase alloy, at higher temperatures

(627°C and 827°C), the boron-doped multi-phase alloy was slightly stronger which is again indicative of a solid solution strengthening effect of boron at high temperatures. Although boron doping is expected to increase the strength even at room temperature, the differences in the scale of the microstructure between the undoped and boron-doped alloys preclude any rigorous comparison of yield strengths.

Figure 4.3.9a summarizes the variation of the yield strength of the alloys with temperature, the data for the boron-doped multi-phase alloy being excluded in view of the uncertainity of its elongation. The data point for the γ/γ' alloy Ni-12Al-40Fe at 627°C represents the fracture stress at just below 0.2% plastic strain . The variation of yield strength with temperature was similar to the trends observed in hot hardness measurements for all the alloys. Figure 4.3.9b summarizes the tensile elongation for the alloys as a function of temperature. While the elongation of the multi-phase alloy increased continuously with increasing temperature, the elongation of the γ/γ' alloy shows a minimum at 627°C where the alloy failed around yield. By contrast, the elongation of the β' alloy increased continuously with increasing test temperatures. The high ductility of the multi-phase alloy at 627°C and 827°C thus appears to arise from the increased ductility of the β' phase, as shown in fig. 4.3.9b.

Fractography

The fracture surfaces of the tensile-tested specimens were examined using a scanning electron microscope (figs. 4.3.10-4.3.12). For the multi-phase alloy, fracture at 427°C was similar to that previously observed at 27°C (fig. 4.3.2a) consisting of transgranular cleavage failure in the pro-eutectic β' phase and dimple fracture in the eutectic (fig. 4.3.10a). At higher temperatures (fig. 4.3.10b-c), the pro-eutectic β' phase underwent a change from transgranular fracture to dimple fracture, indicating increased

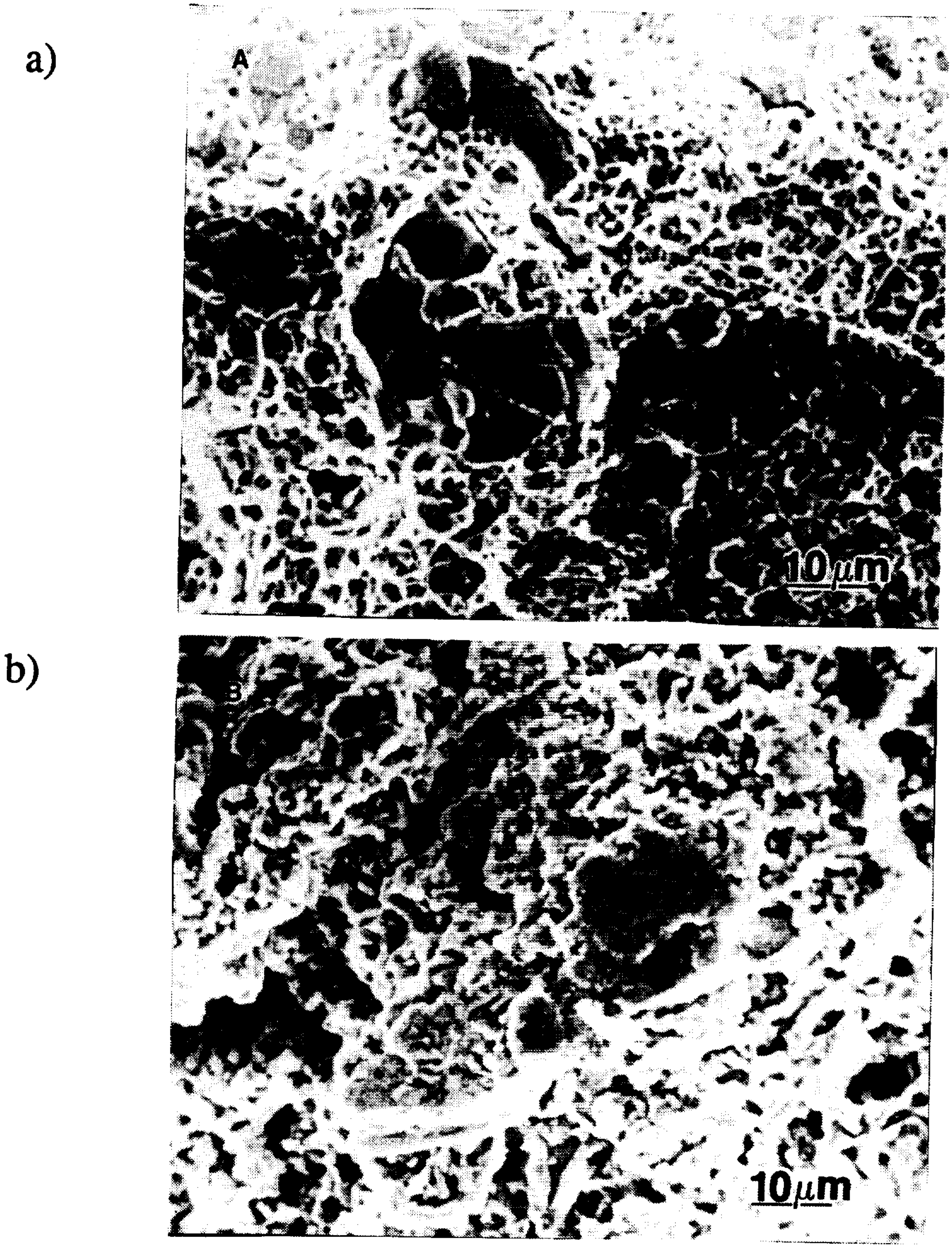

Figure 4.3.10 Fractographs of multi-phase alloy Ni-20Al-30Fe tested in tension at (a) 427°C (b) 627°C and (c) 827°C. The eutectic exhibits dimple fracture at all temperatures. The pro-eutectic β' phase, by contrast, undergoes a change in fracture mode from transgranular cleavage at 427°C to dimple fracture at 627°C.

ORIGINAL PAGE
BLACK AND WHITE PHOTOGRAPH

c)

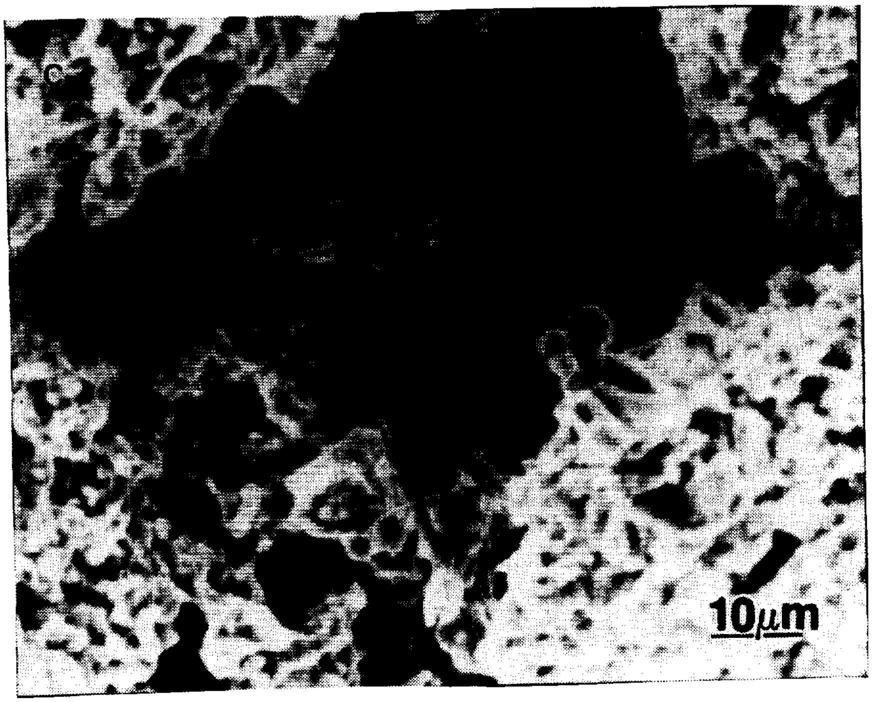

Figure 4.3.10 continued

ORIGINAL PAGE
BLACK AND WHITE PHOTOGRAPH

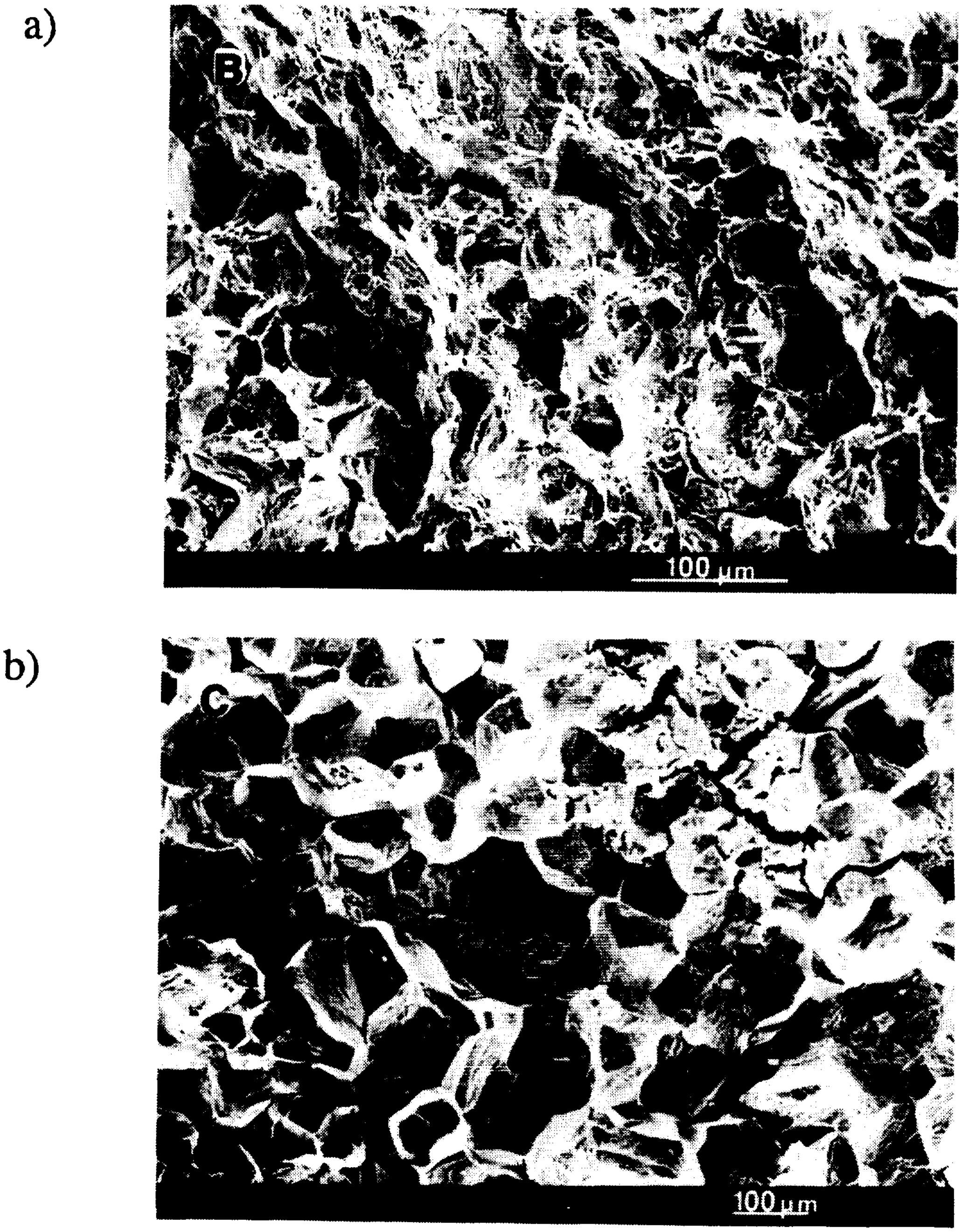

Figure 4.3.11 Fractographs of γ/γ' alloy Ni-12Al-40Fe tested in tension at (a) 427°C (b) 627°C. Fracture surface is dimpled at 27°C, mixed mode (dimple+intergranular) at 427°C and completely intergranular at 627°C and 827°C.

ORIGINAL PAGE
BLACK AND WHITE PHOTOGRAPH

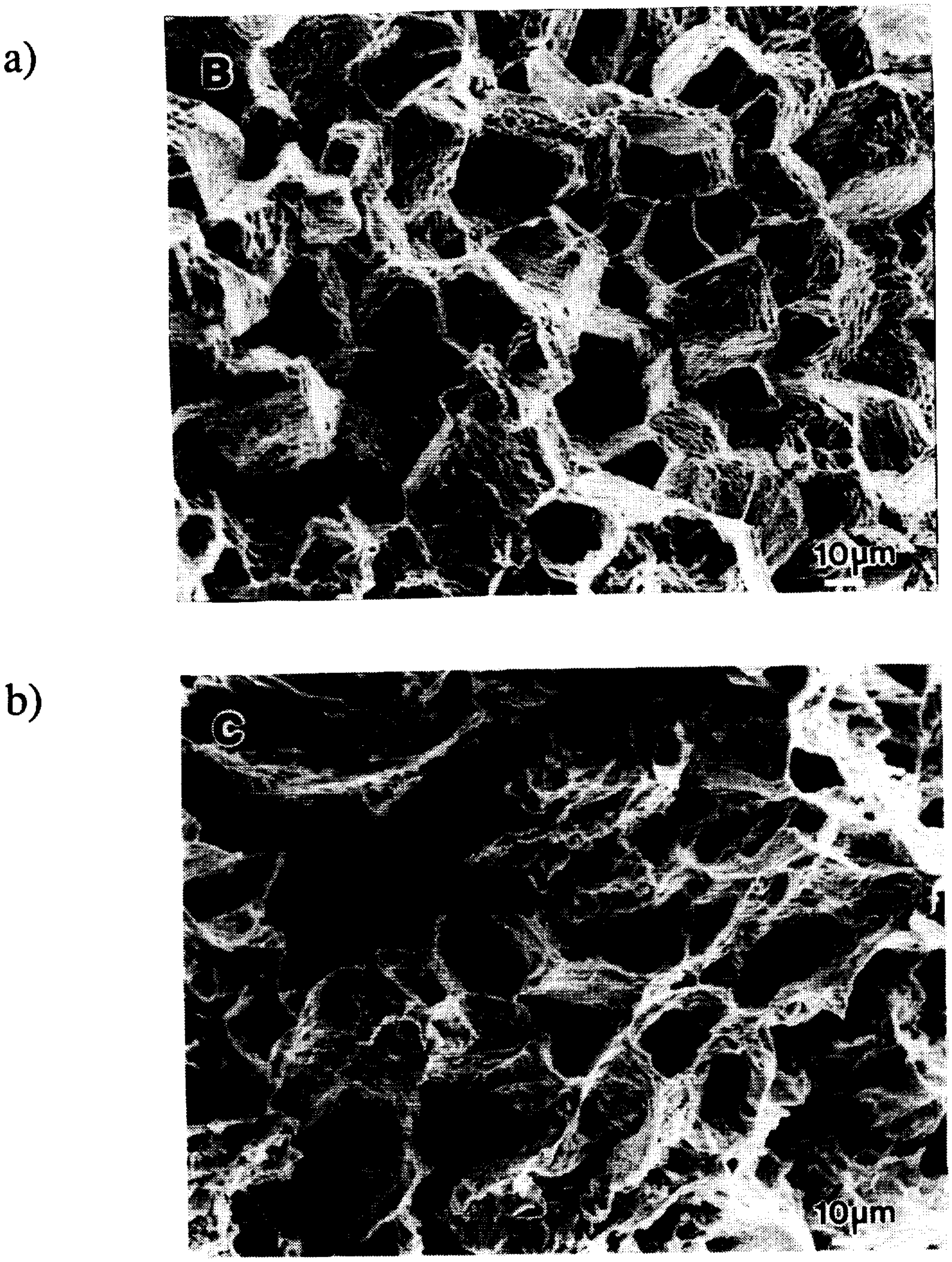

Figure 4.3.12 Fractographs of β' alloy Ni-30Al-20Fe tested in tension at (a) 627°C and (c) 827°C. The fracture is transgranular cleavage at 27°C, intergranular at 627°C and dimple fracture at 827°C.

ORIGINAL PAGE
BLACK AND WHITE PHOTOGRAPH

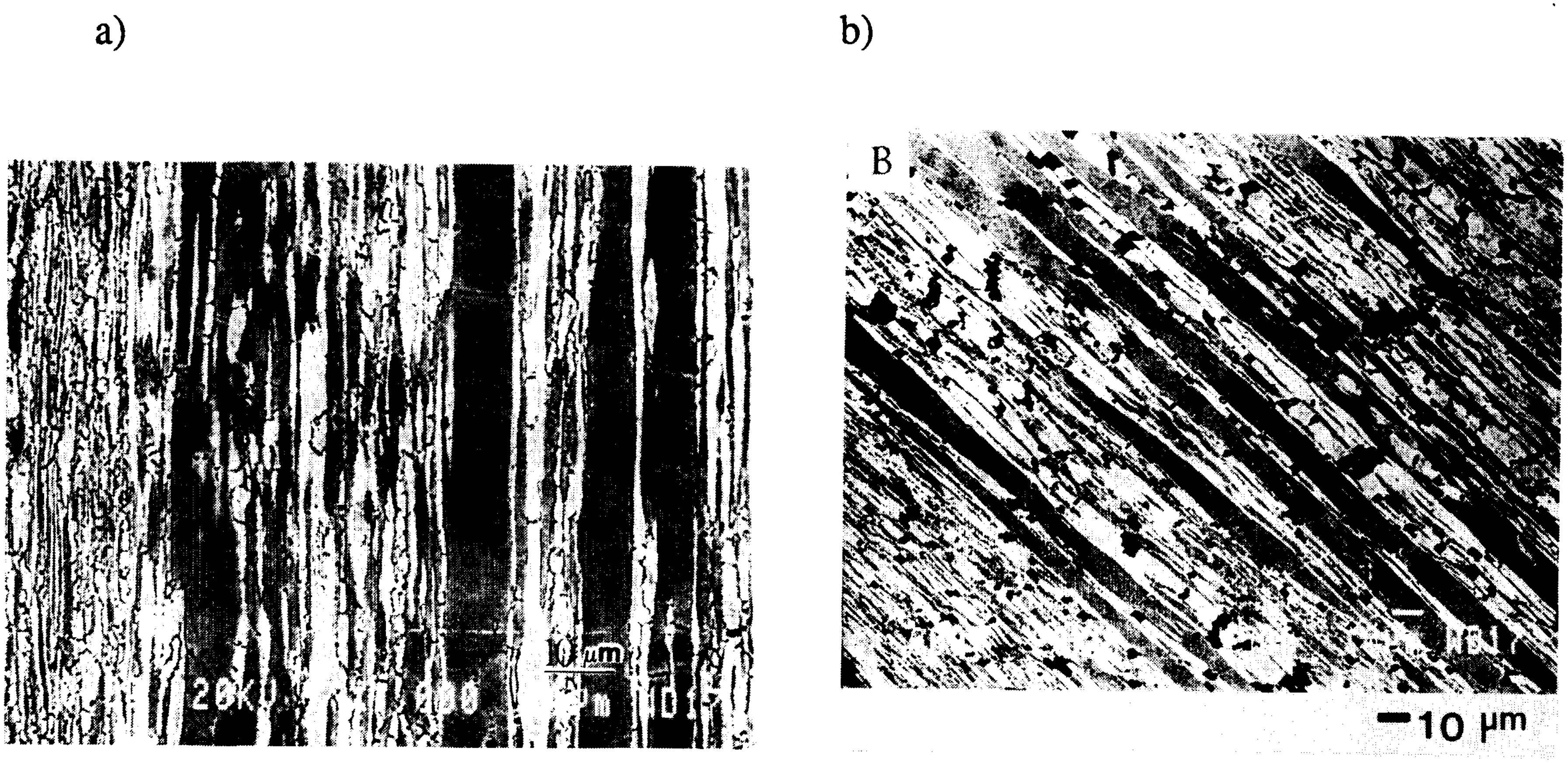

Figure 4.3.13. Backscattered electron images of polished longitudinal sections of Ni-20Al-30Fe tensile specimens tested in tension at (a) 427°C, (b) 627°C and (c) 827°C. Voids were observed at 427, 627 and 827°C, their size increasing with increasing temperatures. At 427°C, the fine voids were limited to the grain boundaries and interphase interfaces. At 627°C, the voids were concentrated in the brighter (γ/γ') phase, while at 827°C, the voids were observed in the darker (β') phase. (d) Optical micrograph of polished longitudinal section of tensile specimen tested at 827°C showing the coarse pro-eutectic phase breaking down into finer units.

ORIGINAL PAGE
BLACK AND WHITE PHOTOGRAPH

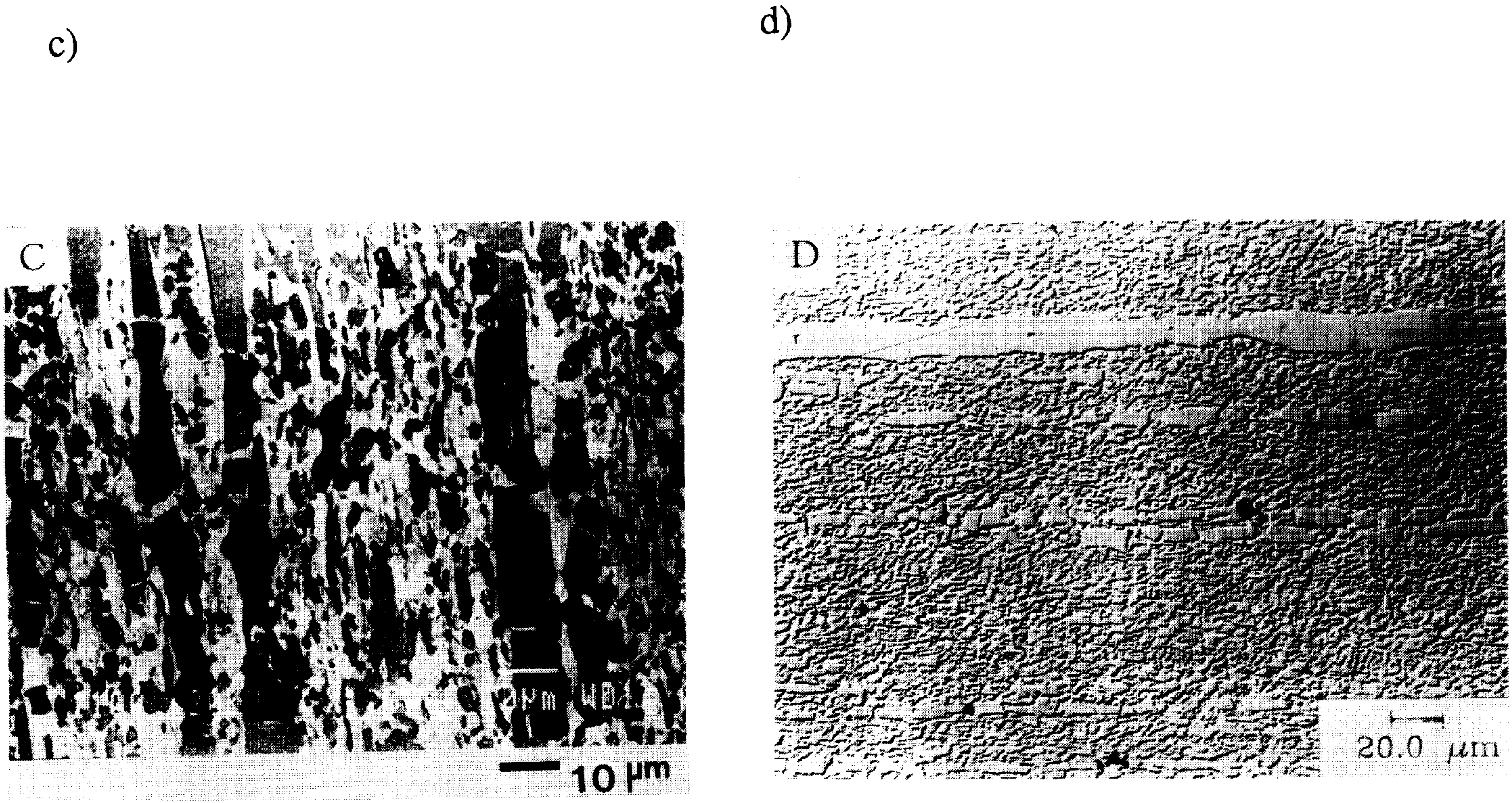
c)
C
10 µm
d)
D
20.0 µm

Figure 4.3.13 continued.

ORIGINAL PAGE
BLACK AND WHITE PHOTOGRAPH

ductility for the β' phase in the temperature range 427°C-627°C. This coincides with the loss of hardness of the β' alloy above around 500°C and the tensile test results where 27% elongation was observed at 627°C. The fracture surface at 827°C was essentially similar to 627°C, although some large voids were observed on the fracture surface at 827°C. Dimple fracture was observed in the eutectic at all test temperatures.

The fracture mode of the γ/γ' alloy also changed with increasing temperature. Dimple fracture was previously noted at room temperature, fig. 4.3.2b. This was replaced by a mixture of intergranular and dimple fracture at 427°C, fig. 4.3.11a, whereas at 627°C and 827°C, completely intergranular fracture occurred, fig. 4.3.11b. The decreased ductility and intergranular fracture of Ni_3Al and $(Ni,Fe)_3(Fe,Al)$ alloys has been noted before in the temperature range 600°C-800°C and ascribed to the dynamic embrittlement of grain boundaries by ambient oxygen [108].

The fracture surfaces of tensile-tested specimens of the β' alloy, Ni-30Al-20Fe also changed with temperature. Previously transgranular cleavage was reported at room temperature (fig.4.3.2b). The fracture mode was intergranular fracture at 627°C and dimple fracture at 827°C, fig. 4.3.12. Although the fracture is intergranular at 627°C, the individual grains shows evidence of plasticity (note the dimpled surface of individual grains in fig. 4.3.12a). At 827°C, extensive voiding was evident on the fracture surface (Fig. 4.3.12b). The results are similar to the observed fracture behavior of the pro-eutectic β' phase in the multi-phase alloy.

Fracture surfaces of boron-doped multi-phase alloy specimens indicate essentially similar characteristics as shown in figure 4.3.10 and, hence, are not included here.

Back-scattered electron images of the polished longitudinal sections of the multi-phase alloy specimens tested at 427°C, 627°C and 827°C revealed cavities, the size of the cavities increasing with increasing test temperatures, see fig. 4.3.13. Note that the γ/γ' phase, which is richer in higher atomic number elements, is the brighter phase. Figure 4.3.13a shows that at 427°C, most of the cavitation is limited to the grain boundaries and interfaces. By contrast, the voids were almost exclusively in the γ/γ' phase at 627°C, see fig. 4.3.13b, and in the β' phase at 827°C, see fig. 4.3.13c. At 827°C (fig. 4.3.13d), the elongated structure of the pro-eutectic phase was replaced by a more homogeneous and equiaxed microstructure. Combined with the large elongation observed for the multi-phase alloy at 827°C, this is indicative of a dynamically recrystallized microstructure.

Polished longitudinal sections of the γ/γ' alloy, Ni-12Al-40Fe, indicated the presence of grain boundary cracks at 627°C and 827°C, which are consistent with the observed intergranular fracture mode observed for this alloy at these temperatures, see fig. 4.3.14. Similarly, polished longitudinal sections of the β' alloy, Ni-30Al-20Fe, tested at 627°C (fig. 4.3.15a), indicated mainly the presence of grain boundary cracks, which is consistent with the observed fracture mode at this temperature, although a few longitudinal cracks along the stress axis were also observed. These longitudinal cracks were also observed at room temperature and are believed to be the result of processing (casting + extrusion). At 827°C (fig. 4.3.15b), however, extensive voiding was observed and the grain boundaries were no longer straight. The large voids observed in the micrograph are mostly situated at the grain boundaries and probably resulted from the coalescence of smaller voids nucleated by creep cavitation. The curved grain boundaries (arrowed in fig. 4.3.15b) indicate grain boundary migration which is indicative of the occurrence of dynamic recrystallization at this temperature.

Examination of polished longitudinal sections of Ni-20Al-30Fe-0.17B tensile specimens tested at 627°C and 827°C indicate some differences in size and distribution of voids in the microstructure, see fig. 4.3.16; while at 627°C (fig.4.3.16a), ~20μm sized voids were distributed uniformly over the microstructure, specimens tested at 827°C (fig.4.3.16b) exhibited large (100-200μm) cavities concentrated essentially near the fracture surface. The size of cavities away from the fracture surfaces were considerably smaller which is indicative of final failure occurring by void coalescence. Figure 4.3.16c is a high magnification optical micrograph of the region away from fracture surface showing

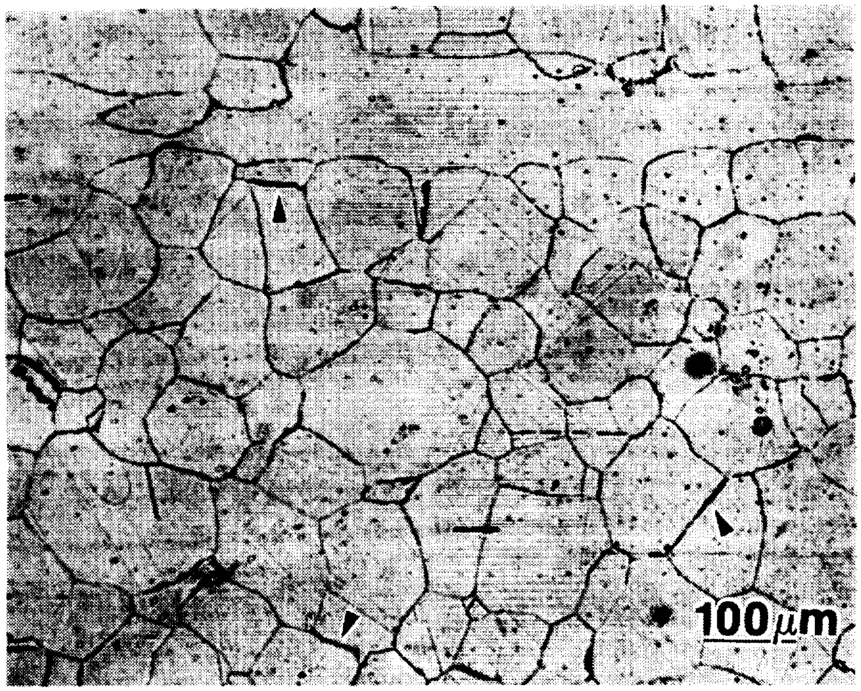

Figure 4.3.14. Optical micrograph of polished longitudinal section of γ/γ alloy Ni-12Al-40Fe, tested in tension at 627°C. Grain boundary cracks are observed (arrowed).

ORIGINAL PAGE
BLACK AND WHITE PHOTOGRAPH

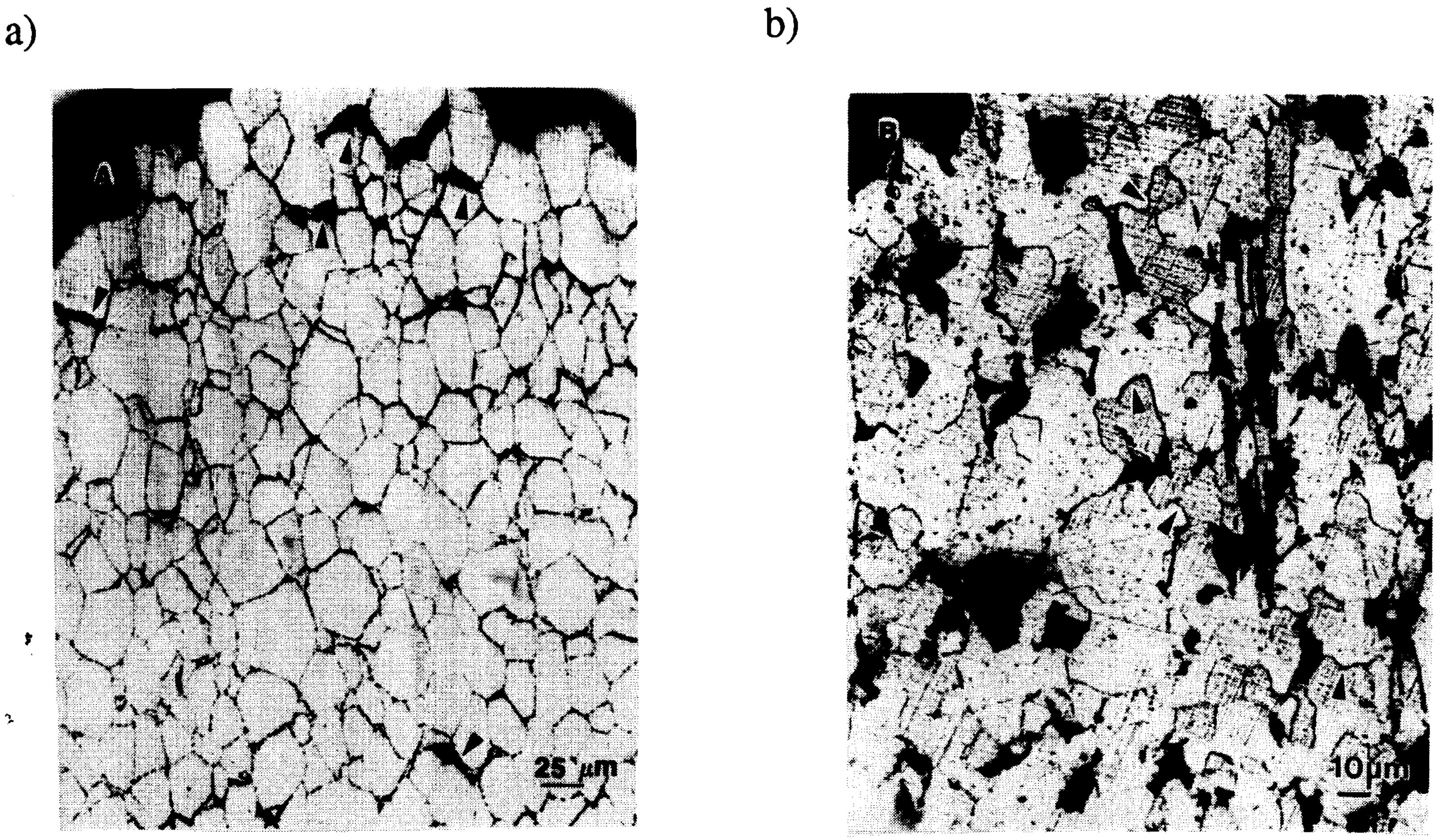

Figure 4.3.15. Optical micrographs of polished longitudinal sections of β' alloy Ni-30Al-20Fe, tensile-tested at (a) 627°C and (b) 827°C. Grain boundary cracks are observed at 627°C (arrowed), while at 827°C extensive voiding and grain boundary migration (arrowed) were observed.

ORIGINAL PAGE
BLACK AND WHITE PHOTOGRAPH

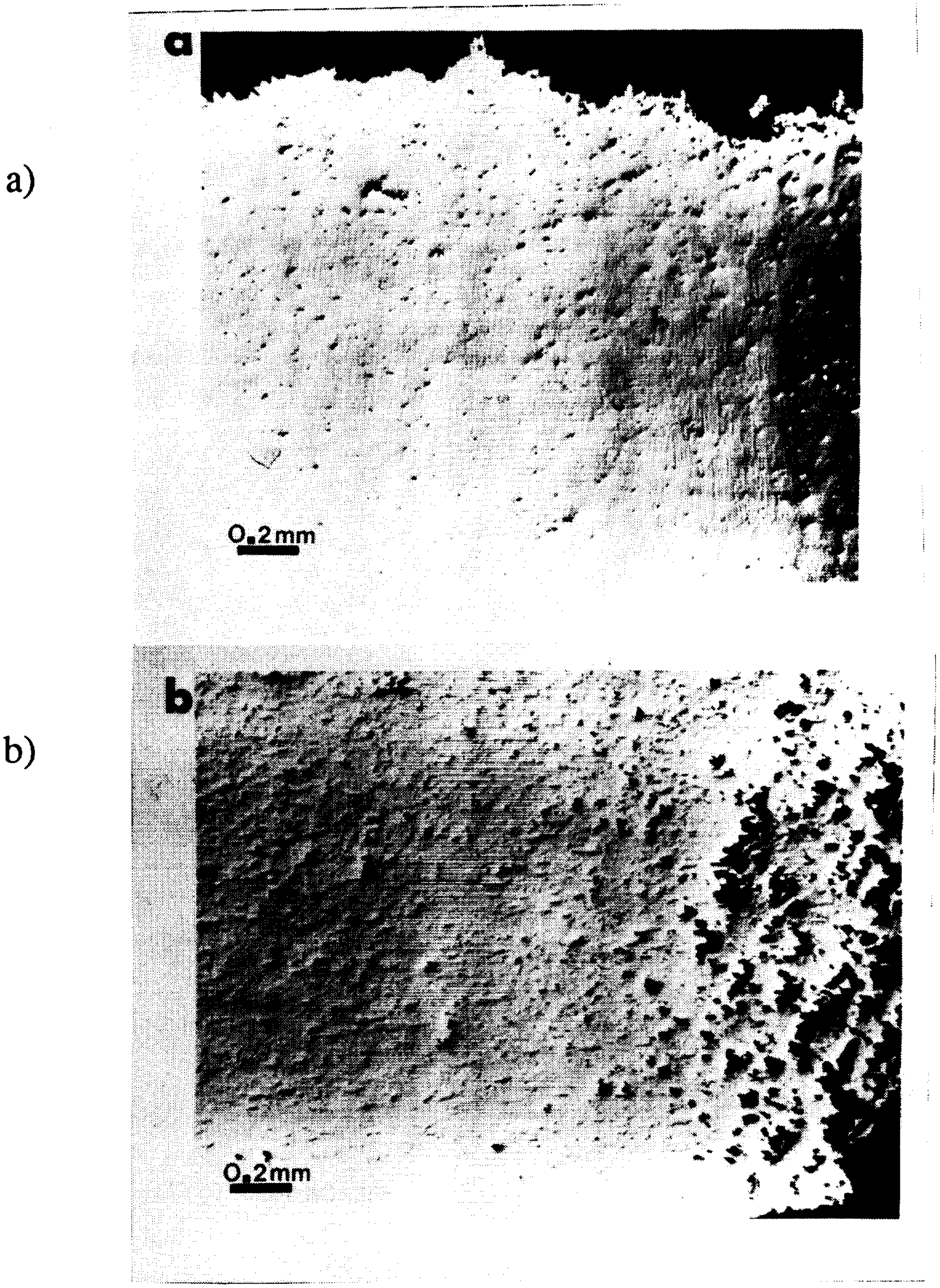

Figure 4.3.16 Optical micrographs (DIC contrast) of boron-doped multi-phase alloy Ni-20Al-30Fe-0.17B tested in tension at (a) 627°C (b) 827°C showing the size and distribution of voids nucleated. (c) higher magnification image of region away from fracture surface in (b) showing the nucleation of voids at the interphase interface (arrowed) presumably by interfacial sliding (see later).

ORIGINAL PAGE
BLACK AND WHITE PHOTOGRAPH

c)

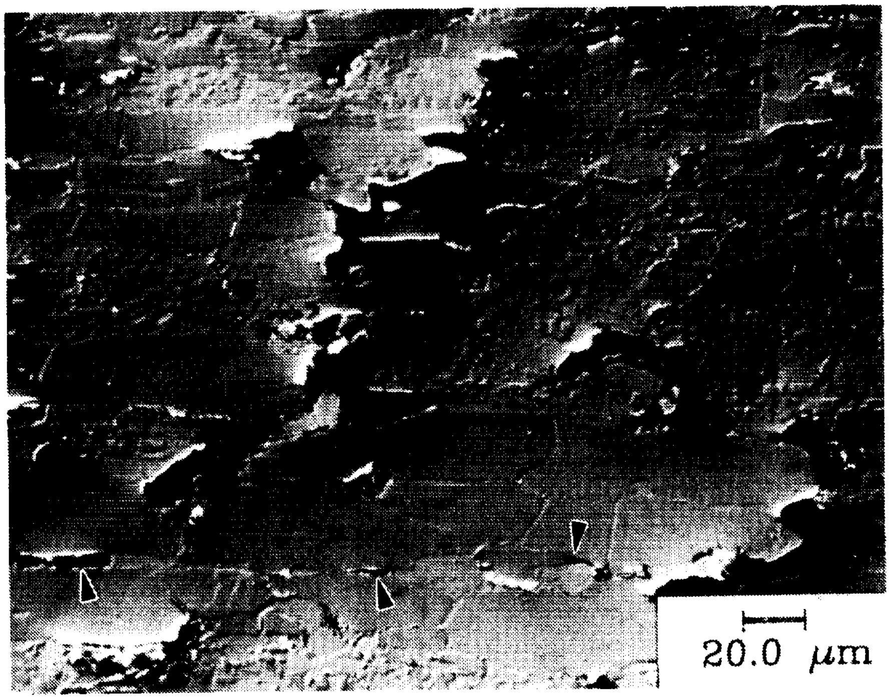

Figure 4.3.16 continued

ORIGINAL PAGE
BLACK AND WHITE PHOTOGRAPH

voids nucleating at the interphase interface (arrowed) which is indicative of grain boundary sliding. Like the boron-doped multi-phase alloy, large voids were also observed on the fracture surfaces of the boron-free multi-phase alloy indicating that void coalescence is responsible for final failure.

4.4 Deformation Mechanisms

4.4.1 Room Temperature

Figure 4.4.1a-d shows the dislocation sub-structure in the pro-eutectic β' phase of the multi-phase alloy, Ni-20Al-30Fe, strained ~2% in compression at room temperature. The dislocations labelled 'A', 'B', and 'C' are in contrast when imaged with $\vec{g} = [10\bar{1}]$ and $[1\bar{1}0]$, and out of contrast with $\vec{g} = [01\bar{1}]$ and [020], indicating a [100] Burgers' vector. No evidence of dislocation pile-ups was found. The residual contrast of some dislocations when the invisibility criteria for screw $\vec{g} \cdot \vec{b} = 0$ or edge dislocations ($\vec{g} \cdot \vec{b} = 0$ and $\vec{g} \cdot \vec{b} \times \vec{u} = 0$) are satisfied was probably due to the high elastic anisotropy of the β' alloy.

The Burgers' vector of dislocations in the γ/γ' phase in multi-phase alloy Ni-20Al-30Fe was also analysed after ~2% strain in compression. The contrast of dislocations when imaged with a variety of diffracting vectors are shown in figure 4.4.2a-d. The dislocations are in contrast when imaged with $\vec{g} = (\bar{2}20)$ and $(\bar{2}00)$ and out of contrast with $\vec{g} = (020)$ and $(\bar{1}11)$. Clearly, the Burgers' vector of these dislocations is 1/2[101]. The dislocations are paired and clearly exhibit planar slip; the slip plane was determined by trace analysis to be $(\bar{1}11)$ for the particular dislocations in figure 4.4.2. The pairs were determined to be superpartials and not dislocation dipoles, since, on imaging them with $+\mathbf{g}$ and $-\mathbf{g}$, no change in separation was observed [104]. The dislocations appear to pile up at the grain boundary. The separation

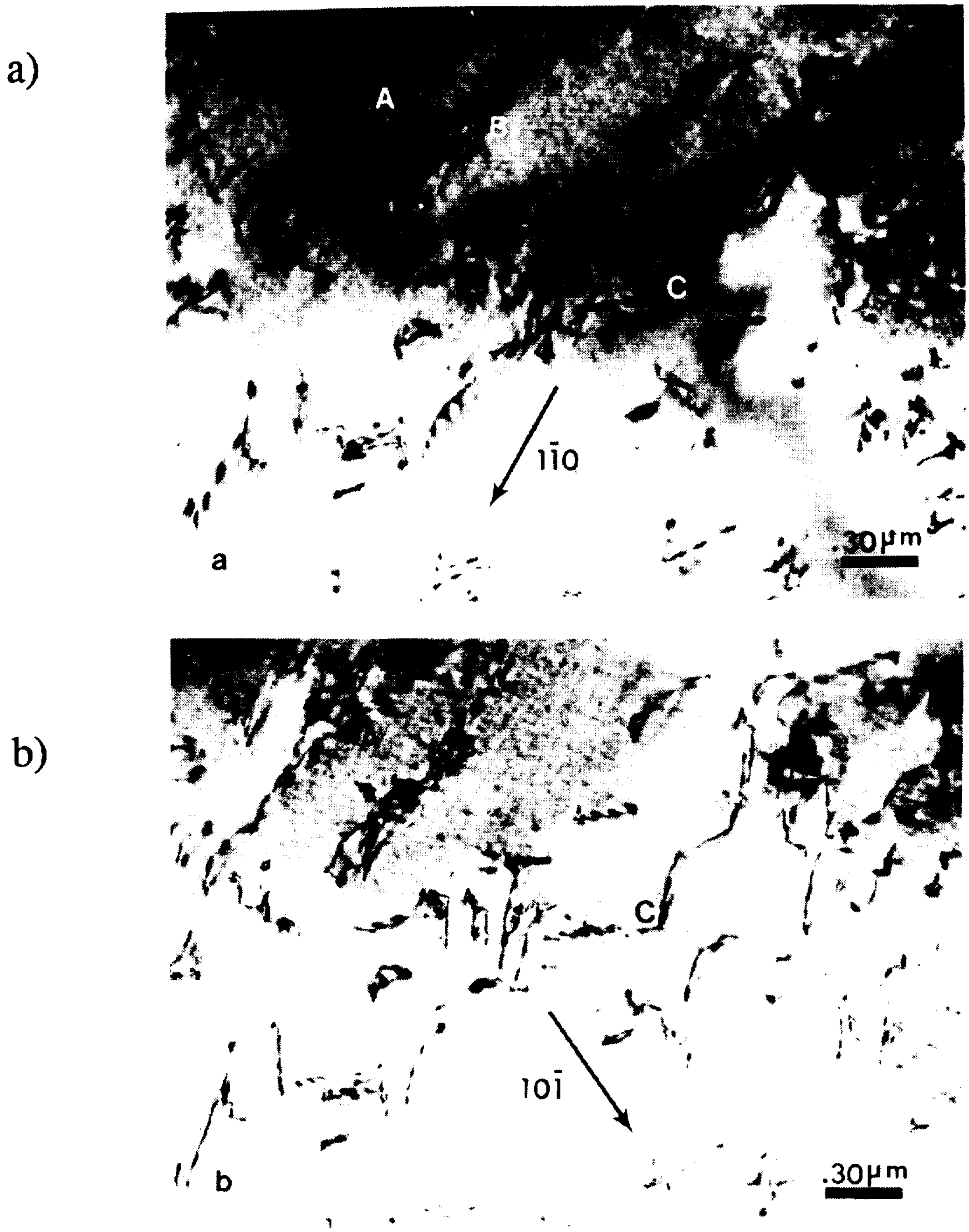
a)
A
B
C
$1\bar{1}0$
a
.30μm
b)
C
$10\bar{1}$
b
.30μm

Figure 4.4.1 Dislocations in the pro-eutectic β' phase in extruded, multi-phase Ni-20Al-30Fe, strained ~2% at room temperature. Imaging conditions: (a) $\vec{g}$ = [$10\bar{1}$] (b) $\vec{g}$ = [$1\bar{1}$)0] (c) $\vec{g}$ = [$01\bar{1}$] (d) $\vec{g}$ = [020]. Beam directions near [111] for (a), (b) and (c) and [101] for (d).

ORIGINAL PAGE
BLACK AND WHITE PHOTOGRAPH

c)

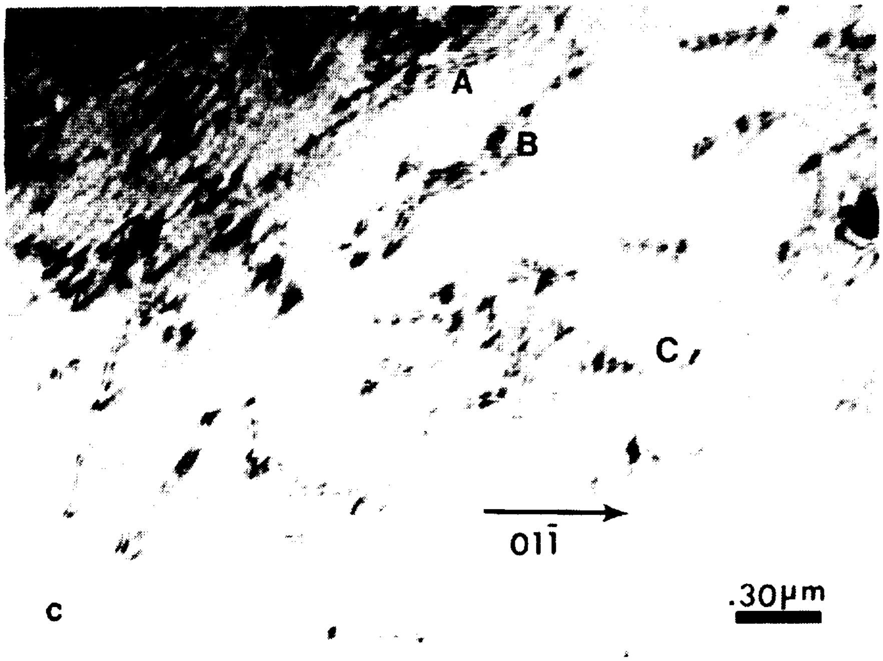
A
B
C
011̄
c
.30μm

d)

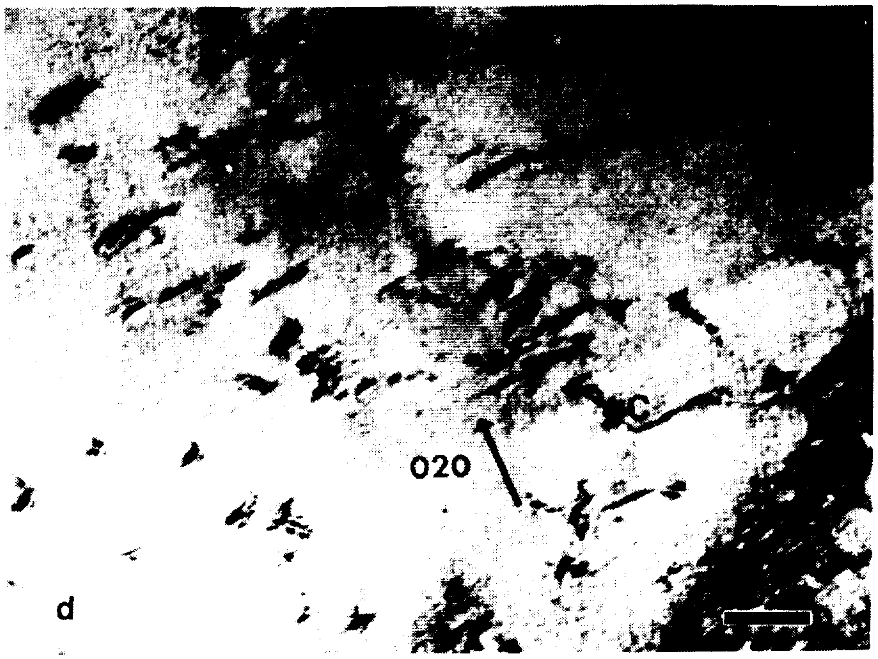

Figure 4.4.1 continued

ORIGINAL PAGE
BLACK AND WHITE PHOTOGRAPH

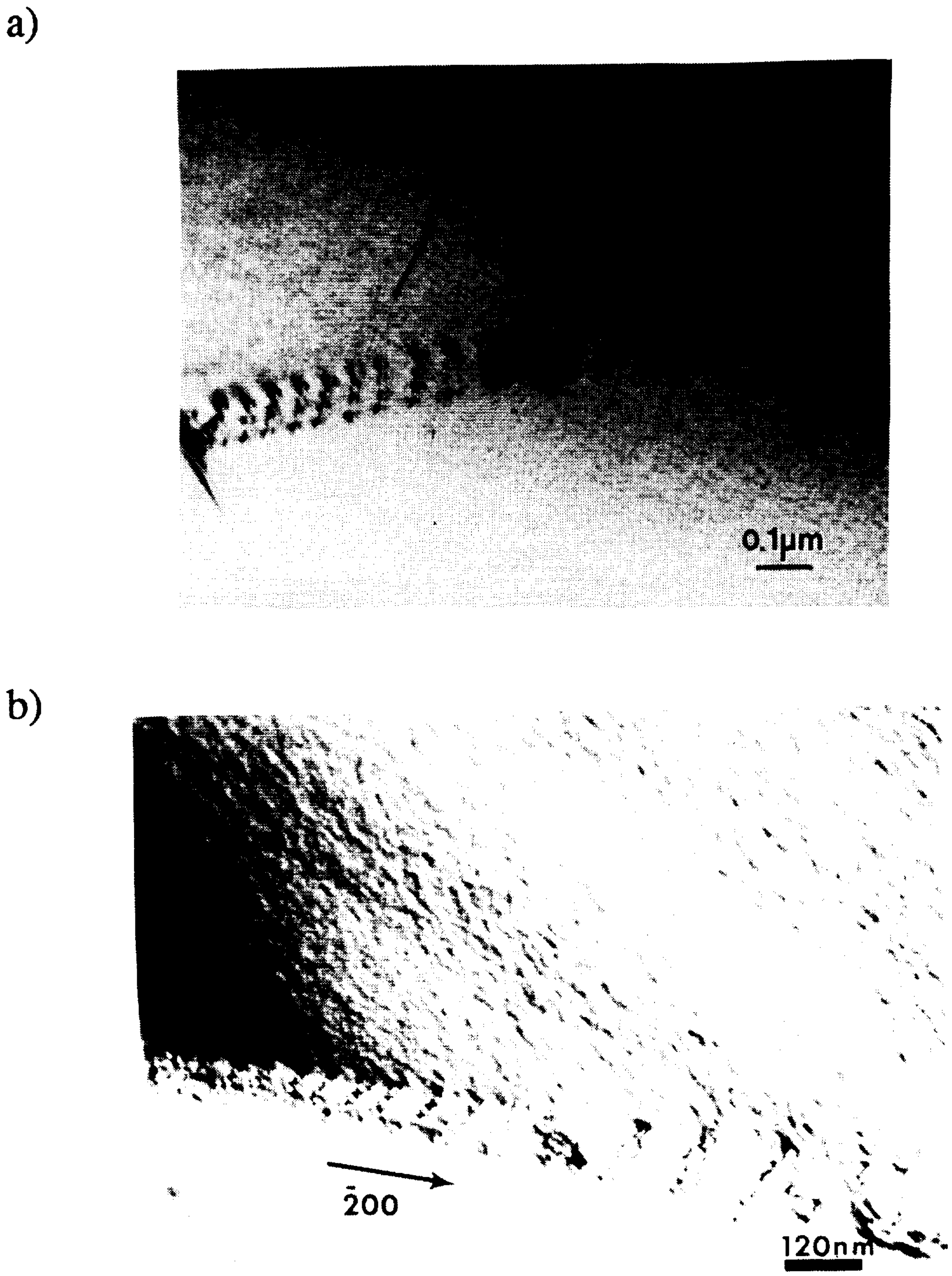

Figure 4.4.2 Dislocations in the eutectic γ/γ' phase in extruded, multi-phase Ni-20Al-30Fe, strained ~2% at room temperature. Imaging conditions: (a) $\vec{g} = [\bar{2}20]$ (b) $\vec{g} = (\bar{2}$)00) (c) $\vec{g} = (020)$ (d) $\vec{g} = (\bar{1}11)$. Beam directions near [001] for (a), (b) and (c) and [101] for (d).

ORIGINAL PAGE
BLACK AND WHITE PHOTOGRAPH

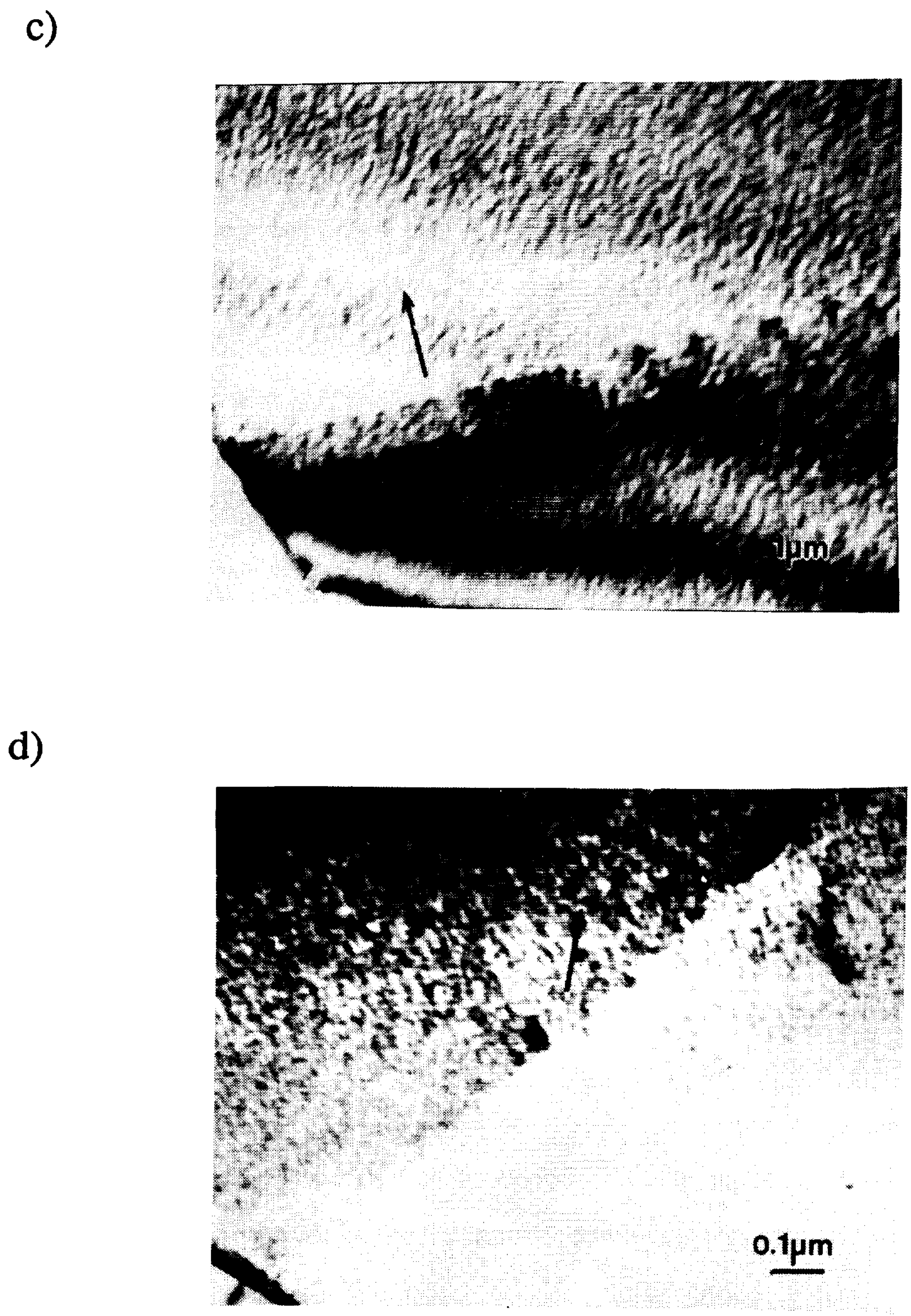

Figure 4.4.2 continued

between the superpartials is about 15nm at the head of the pile-up, and increases with distance away from the boundary, suggesting that the APB energy decreases with passage of dislocations on the slip plane. This supports the idea of slip plane disordering [105], where the disorder is deduced to arise from the shearing of the γ' precipitates by the passage of dislocations resulting in a decrease in the net area of ordered precipitates along the slip plane thereby reducing the degree of order. Also, the 'scalloped' appearance of dislocations in the γ/γ' phase is similar to the observations by Horton et al.[106] and Baker et al.[107] during in-situ straining of single-phase Ni_3Al which has been suggested to arise from the pinning of slip dislocations by faulted dislocation loops (with a Burgers' vector not in the original slip plane). These are produced by the passage of many slip dislocations of the same Burgers' vector in a thin slip band. Alternatively, the 'scalloped' appearance of dislocations in the γ/γ' phase could simply be related to the bowing of discontinuous dislocations around γ' precipitates.

Figure 4.4.3a-d shows the dislocations in a sample of the β' alloy, Ni-30Al-20Fe, strained to fracture and imaged with different diffracting vectors. The dislocation structure is similar to that in the pro-eutectic phase of the multi-phase alloy at similar strain levels (fig. 4.4.1). The dislocations labelled 'A' and 'B' are in contrast when imaged with $\vec{g}$= (200) and $(\bar{1}01)$ and exhibit invisibility when imaged with $\vec{g}$= (020) and $(0\bar{1}1)$. The Burgers' vector of dislocations was, thus, found to be <100>. (Again, note the residual contrast when the screw or edge dislocation invisibility criterion is satisfied). The observation of dislocations of <100> Burgers' vectors in double-extruded β' Ni-30Al-20Fe is consistent with earlier analyses of Burgers' vector in the pro-eutectic β' phase of the multi-phase alloy Ni-20Al-30Fe.

Figure 4.4.4 shows the distribution of dislocations in the two eutectic phases of the multi-phase alloy after ~2% strain. The dislocation density is much higher in the β' phase than the γ/γ' phase, a feature probably related to the higher work-hardening rate of the β' phase (Ni-30Al-20Fe) than the γ/γ' phase (Ni-12Al-40Fe) (see fig. 4.3.1). Note also

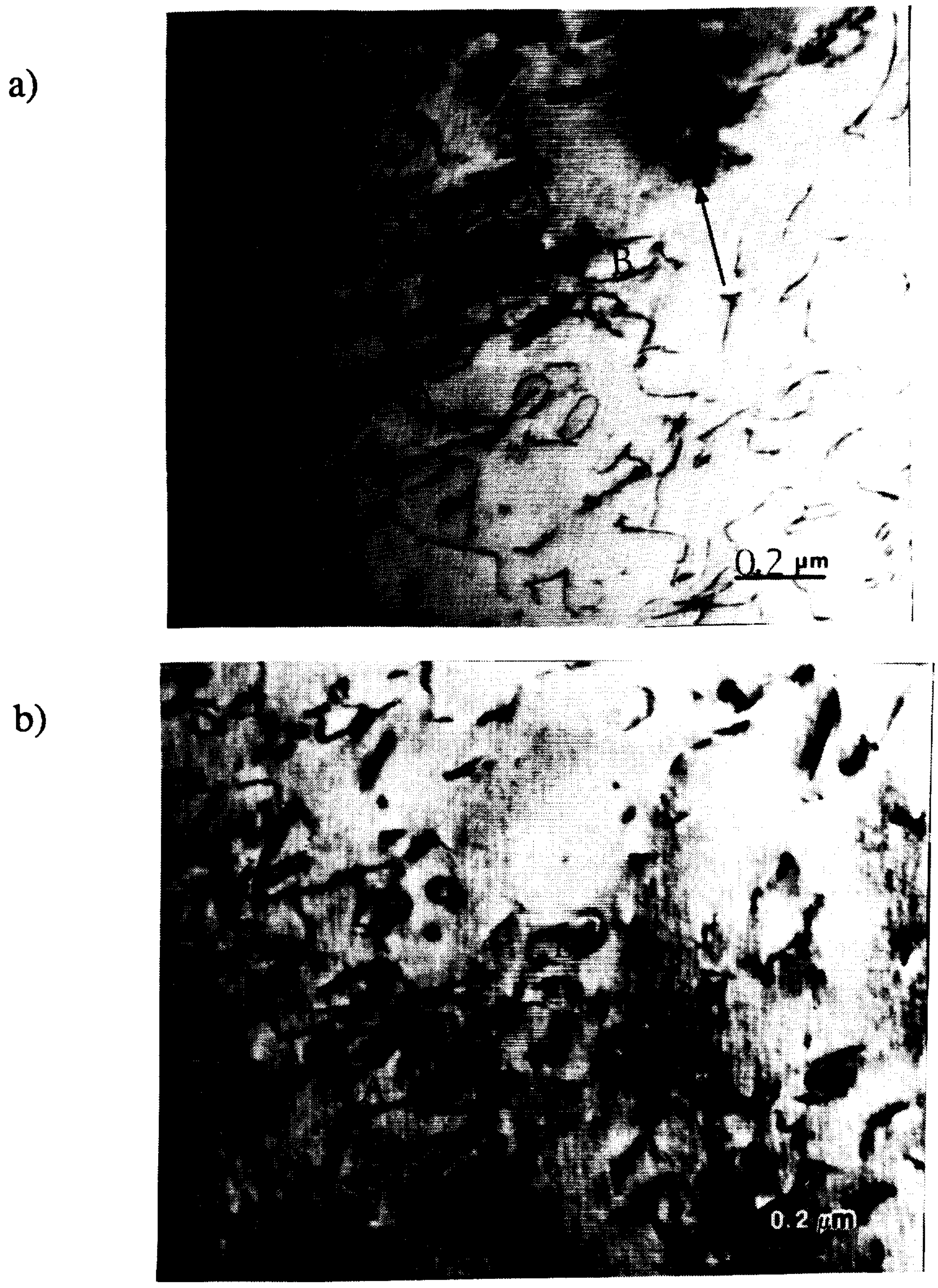

Figure 4.4.3 Dislocations in the β' phase in extruded Ni-30Al-20Fe, strained to failure (~2%) at room temperature. Imaging conditions: (a) $\vec{g}=[200]$ (b) $\vec{g}=[\bar{1}01]$ (c) $\vec{g}=[020]$ (d) $\vec{g}=[0\bar{1}1]$. Beam directions near [011], [111], [101] and [111] for (a), (b), (c) and (d) respectively.

ORIGINAL PAGE
BLACK AND WHITE PHOTOGRAPH

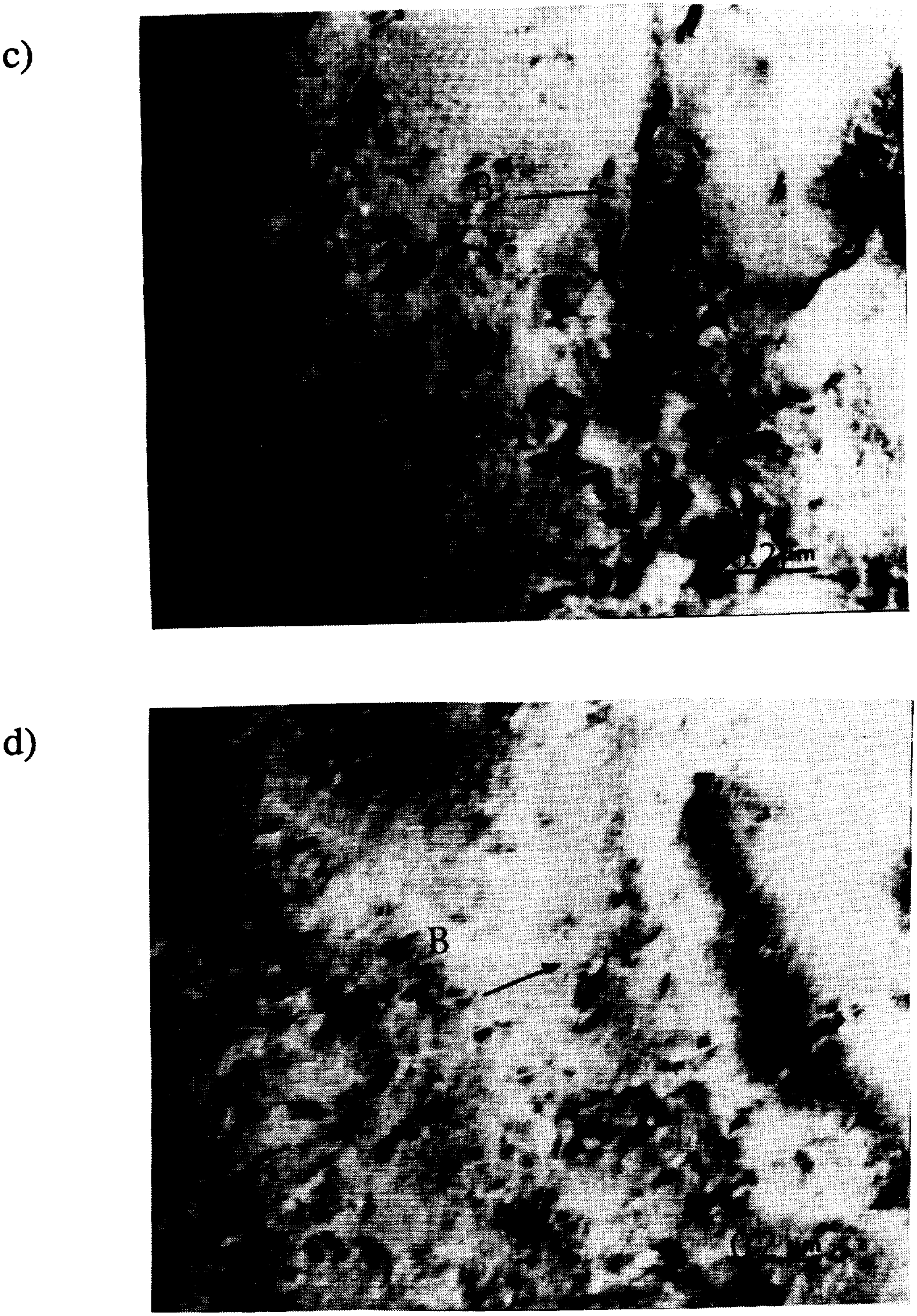

Figure 4.4.3 continued

ORIGINAL PAGE
BLACK AND WHITE PHOTOGRAPH

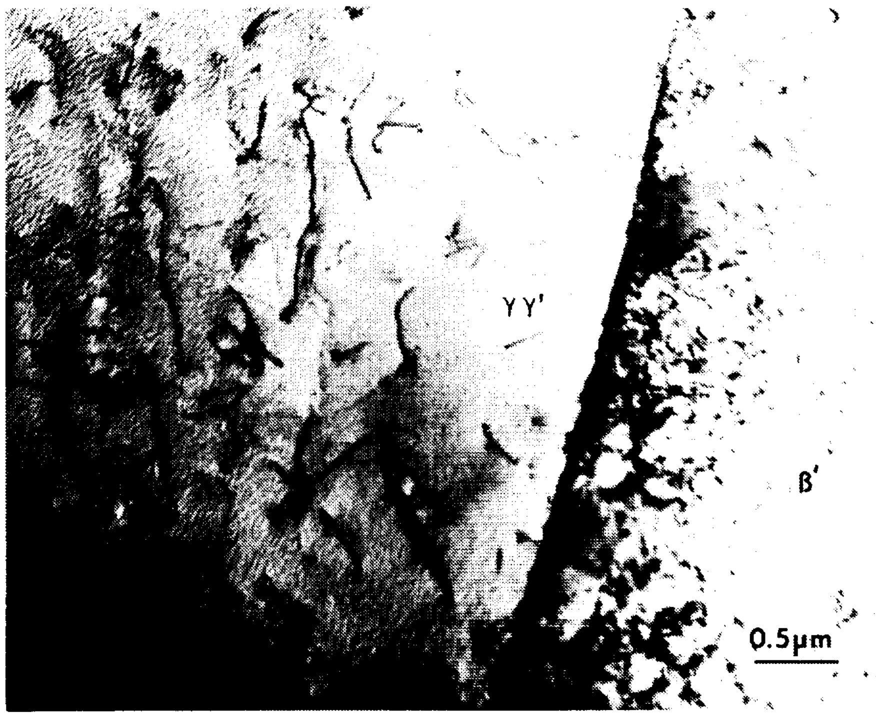

Figure 4.4.4 TEM micrograph of extruded, multi-phase Ni-20Al-30Fe, strained ~2% in compression. Note that the dislocation density is higher in the β' phase than in the γ/γ' phase. Also, note the absence of any ledges arising from the deformation process at the β'-γ/γ' interface.

ORIGINAL PAGE
BLACK AND WHITE PHOTOGRAPH

that, while Field et al.[97] reported the observation of ledges at the interphase interfaces arising from the deformation process, no grain boundary ledges or evidence of dislocation transmittal across the interface were observed in thin foils made from bulk-deformed material.

4.4.2 Room Temperature TEM In-Situ Straining Experiments

The deformation mechanisms in bulk samples strained ~2% at room temperature have been determined above; the Burgers' vectors of dislocations in β' and γ/γ' phases of the extruded multi-phase alloy were determined to be, respectively, <001> and <110>. While the slip in the γ/γ' phase was planar, no dislocation pile-ups were observed in the β' phase. The latter observation was in contrast to those by Field et al.[97], who reported slip bands in both β' and γ/γ' grains of rapidly solidified ribbons of Ni-20Al-30Fe. Interestingly, while Field et al.[97] also reported the observation of both <001> and <111> dislocations in the β' phase of the rapidly solidified multi-phase alloy ribbon and deformation-induced ledges at the interphase interface, no <111> dislocations or deformation-induced grain boundary ledges were observed in the extruded alloys. A mechanism of deformation transfer across the β'-γ/γ' interfaces of rapidly solidified Ni-20Al-30Fe, as proposed by Huang et al.[108], could not be reconciled with the deformation mechanisms as observed in the extruded multi-phase alloys. To resolve the differences between these two investigations, it was decided to study the deformation behavior of the extruded multi-phase alloy by in-situ straining in a TEM.

Specimens for in-situ straining were prepared from transverse sections of the extruded alloy. Figure 4.4.5 shows the geometry of the specimens and its relation to the extrusion axis. The specimens were mechanically ground to 0.25mm thickness and jet-polished to perforation, as for the 3mm disks described earlier. The specimens were strained in a single tilt straining stage.

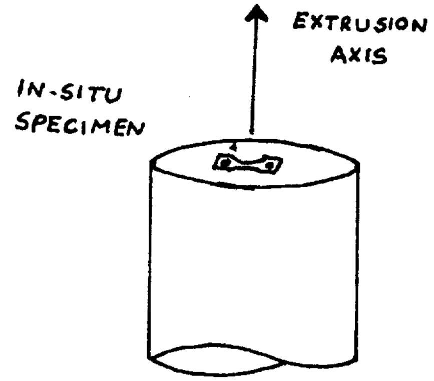

Fig. 4.4.5 Geometry of in-situ specimens and their relation to the extrusion axis.

It is important to note that the stress axis for the in-situ specimen was normal to the extrusion axis (unlike the thin foils examined from bulk deformed material where the stress axis coincided with the extrusion axis). Also, the Kurdjumov-Sachs relationship is observed between the eutectic phases when viewed along the extrusion axis (normal to the in-situ specimen surface). The geometry of the specimen (stress axis and arrangement of grains satisfying the orientation relationship) is similar to that in the rapidly solidified ribbon examined by Field et al.[97]. This similarity allows a comparison between the rapidly solidified and extruded Ni-20Al-30Fe.

Preliminary experiments on the as-extruded alloy specimens proved difficult due to the magnetic nature of the specimen and the small scale of the microstructure (0.5μm lamellae width) which made tilting experiments difficult. Subsequently, the specimens were annealed at 1275°C for 3 hrs. followed by furnace cooling to room temperature at a controlled rate (5°C/min) to coarsen the microstructure. This made observation of dislocation substructures in individual phases easier.

Figure 4.4.6 is a low magnification TEM micrograph of the region under study showing the β' phases (labelled 'B') and γ/γ' phases (labelled 'G'). Figure 4.4.7 is a sketch of the region; note that the β' grain marked '2' is not visible in fig. 4.4.6 and is situated below the γ/γ' grain. A twin (identifying feature) is observed in the γ/γ' grain. Upon straining, the first crack appeared in the β' grain marked '1' (see fig. 4.4.6). The crack in the β' phase is indicative of its relatively brittle nature; simultaneously, a thin slip band (arrowed in fig.4.4.6) in the γ/γ' phase, running from the β' grain '1' to the β' grain '3', was observed. No slip bands were, however, observed in the β' grain. With further strain increments, the crack in the β' phase was observed to grow and stop at the γ/γ' boundary, fig.4.4.8. Interestingly, unlike observations in bulk specimens where no cracks were observed in the γ/γ' phase of Ni-20Al-30Fe samples strained to failure, cracks were observed to form in the γ/γ' phase of in-situ straining specimens by thinning of a prior slip band, see fig.4.4.9. It is worth noting that the cracks in the β' and γ/γ' phases did not join with further strain increments, rather, the crack in the β' grain was blunted, see fig.4.4.10. This observation is consistent with observations in the bulk-deformed specimens where cracks nucleated in the β' phase were observed to be arrested at the γ/γ' phase. Interestingly, the crack in the γ/γ' grain was transmitted to the adjacent β' grain (fig.4.4.10), a phenomenon not observed in the bulk-deformed specimens where post-failure analysis of specimens indicated cracks only in the β' phase (see Fig. 4.3.3). With additional strain, a new crack was initiated in the β' grain '2' while slip bands in the adjacent γ/γ' grain were observed to be reflected at the β' grain '1', see fig. 4.4.11. Although no dislocation activity was observed in the β' phase at the head of the slip band (in the γ/γ' phase at the point of intersection with the grain boundary), it is possible that the dislocations are out of contrast. Intense dislocation activity was, however, observed at the head of the crack tip in the β' phase, fig. 4.4.12. Further straining led to the reorientation of the crack in the β' phase (turning sharply, almost at right angles, fig. 4.4.13) along the grain boundary in the β'-γ/γ' interface (fig. 4.4.14), joining one of the reflected slip bands in the γ/γ' phase (fig.4.4.15), and then proceeding along the slip band in the γ/γ' phase (fig.4.4.16) by thinning of material as shown earlier. It should be noted that no significant planar slip activity was observed in the β' phase examined above.

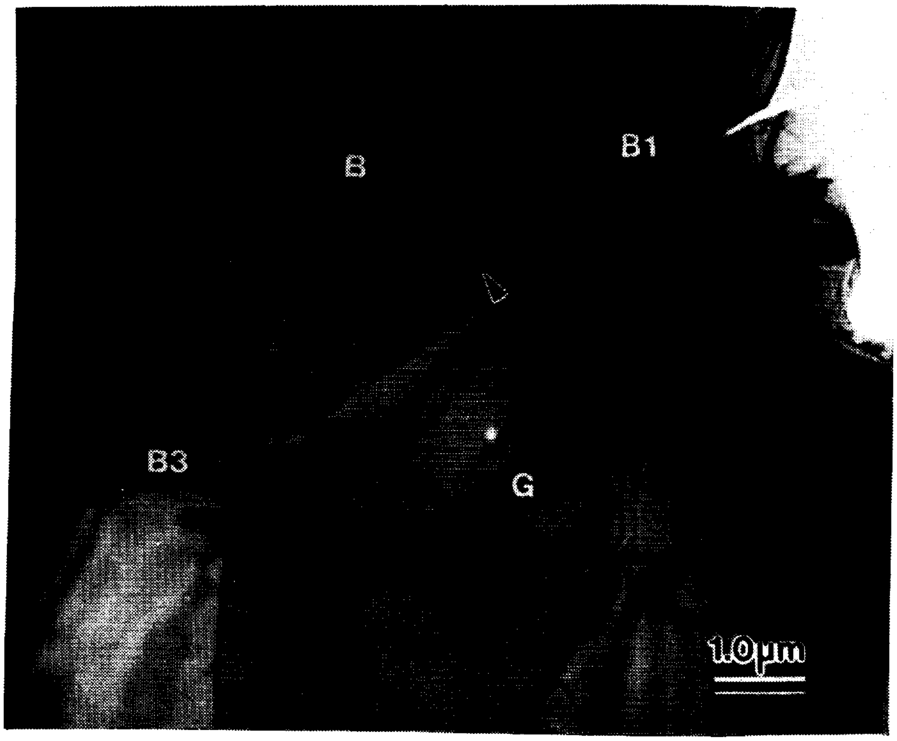

Figure 4.4.6 Low magnification TEM micrograph of the portion of the multi-phase alloy thin foil examined in detail during in-situ straining.

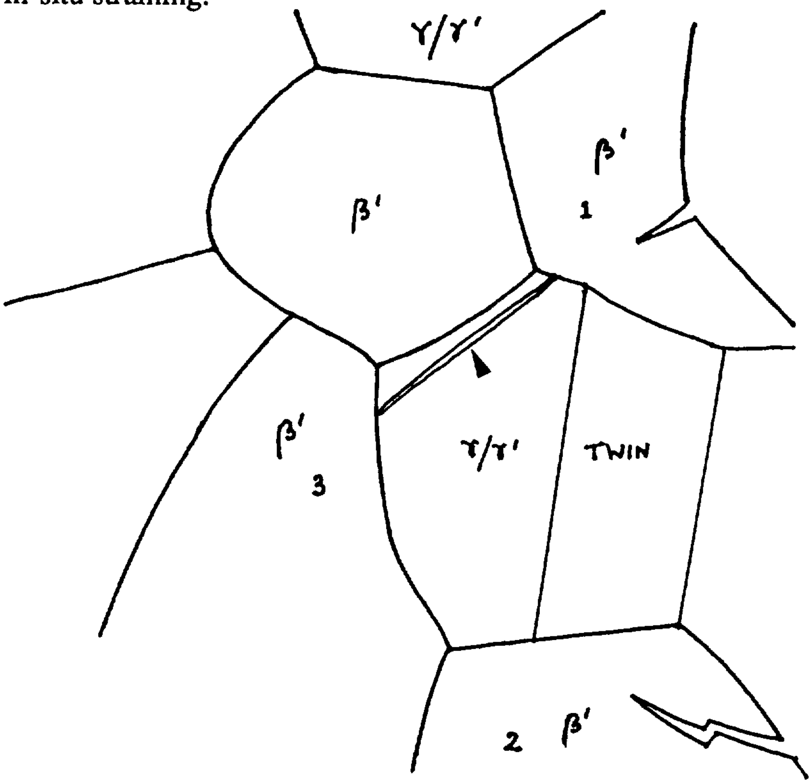

Figure 4.4.7 A schematic of the region of thin foil under investigation. Note that part of this schematic is shown in the above figure.

ORIGINAL PAGE
BLACK AND WHITE PHOTOGRAPH

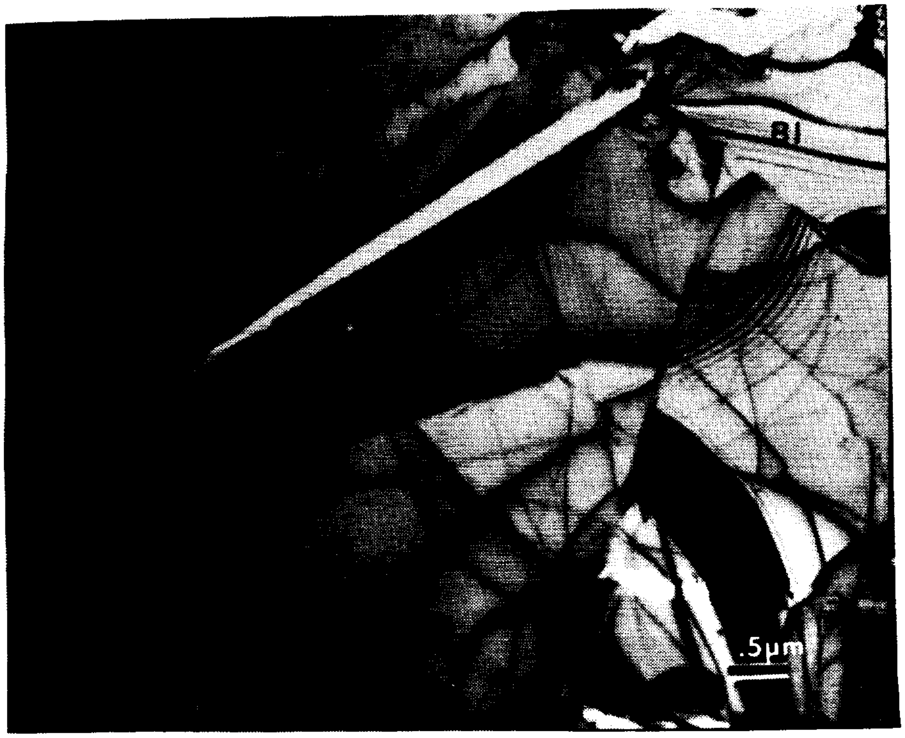

Figure 4.4.8 The crack in the β' phase in fig. 4.4.6 grows with additional strain and is arrested at the γ/γ' interface.

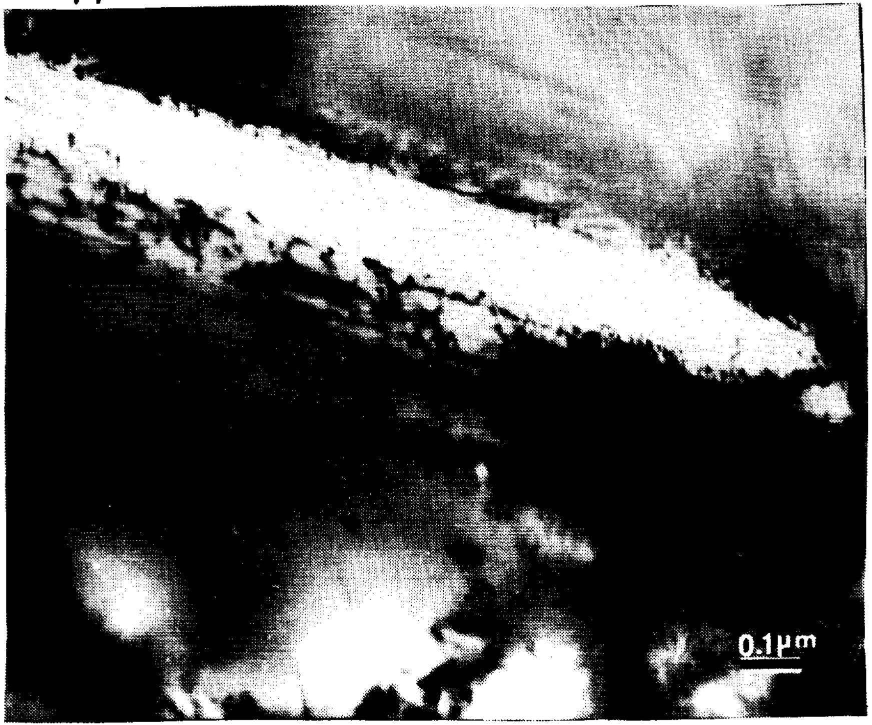

Figure 4.4.9 Unlike the bulk-deformed samples, thin foils of the γ/γ' grain were observed to crack due thinning of material (intense dislocation activity) within the slip band.

ORIGINAL PAGE
BLACK AND WHITE PHOTOGRAPH

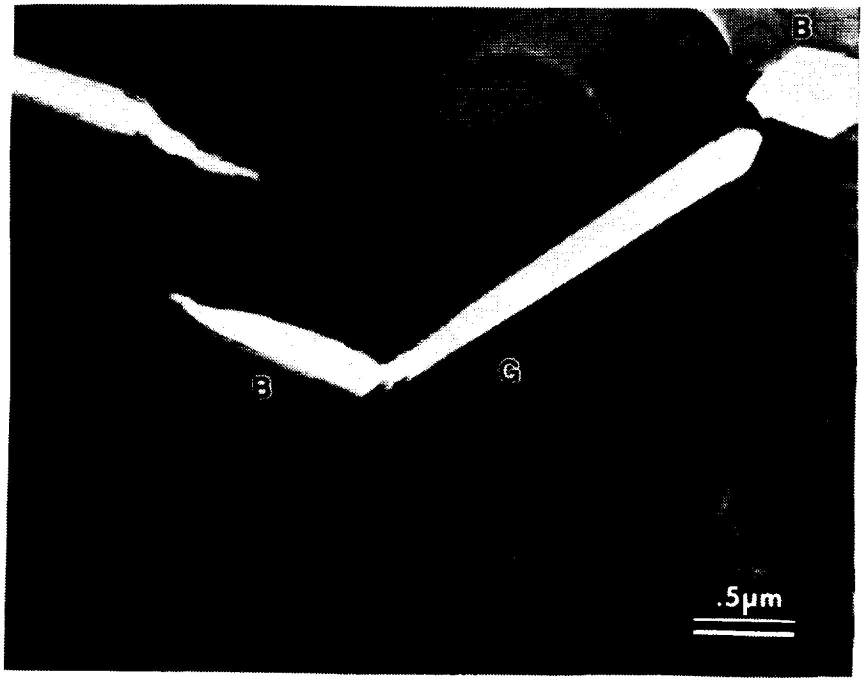

Figure 4.4.10 Cracks in the β' phase were observed to be blunted at the β'-γ/γ' interface during in-situ straining. Also, the cracks in the γ/γ' phase were transmitted to the more brittle β' phase.

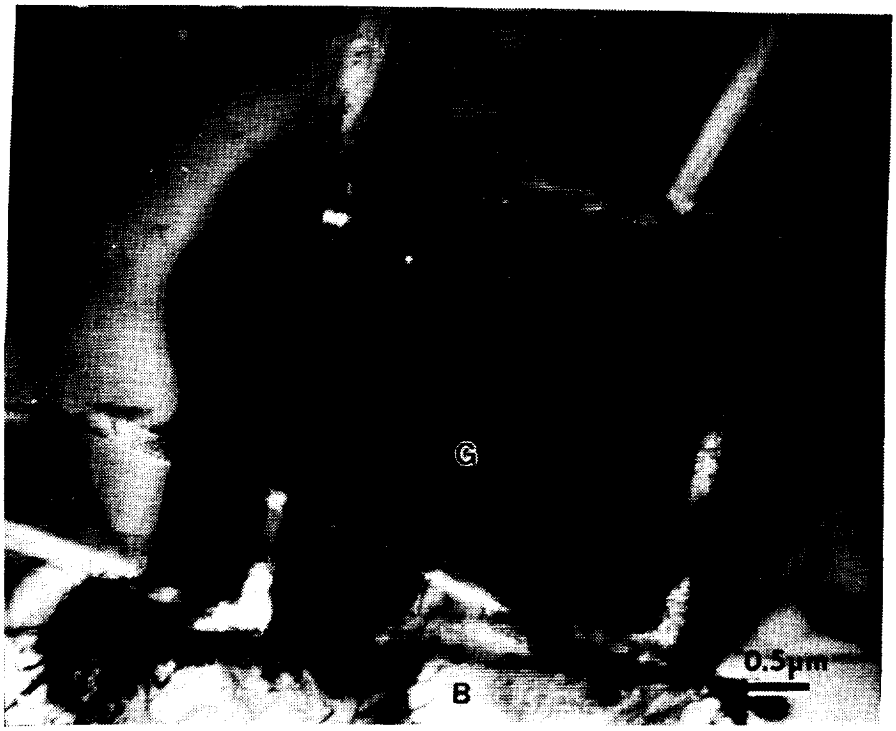

Figure 4.4.11 Slip bands in the γ/γ' phase were observed to be reflected at the β'-γ/γ' interface.

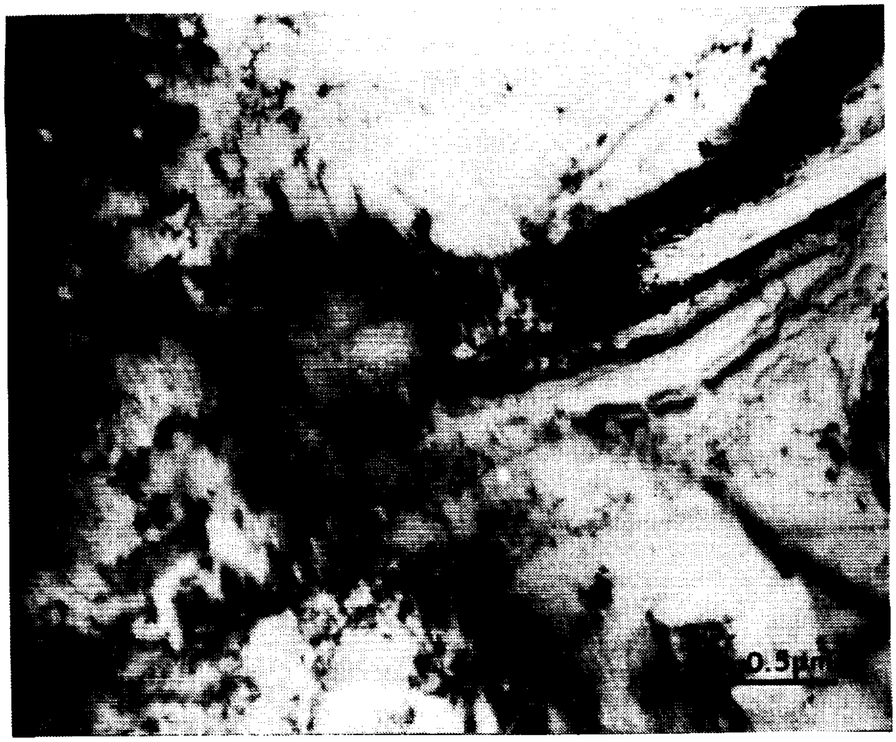

Figure 4.4.12 Intense dislocation activity was observed at the head of the crack tip; note that the deformation in the β' phase for this orientation is homogeneous (i.e. non-planar).

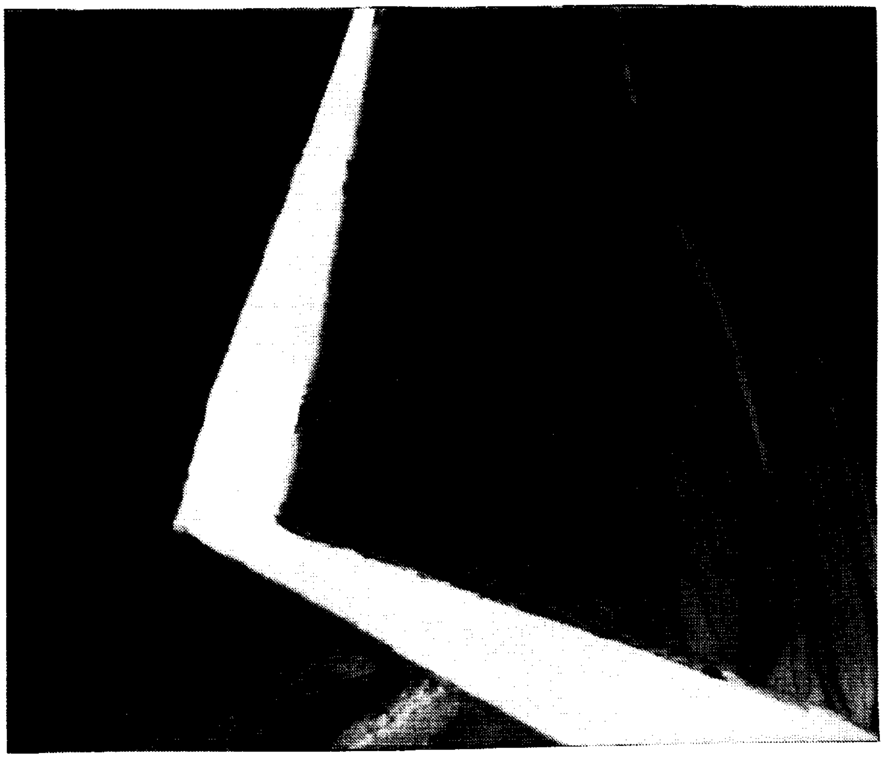

Figure 4.4.13 With additional strain, the crack in fig.4.4.12 advances to the interphase interface.

ORIGINAL PAGE
BLACK AND WHITE PHOTOGRAPH

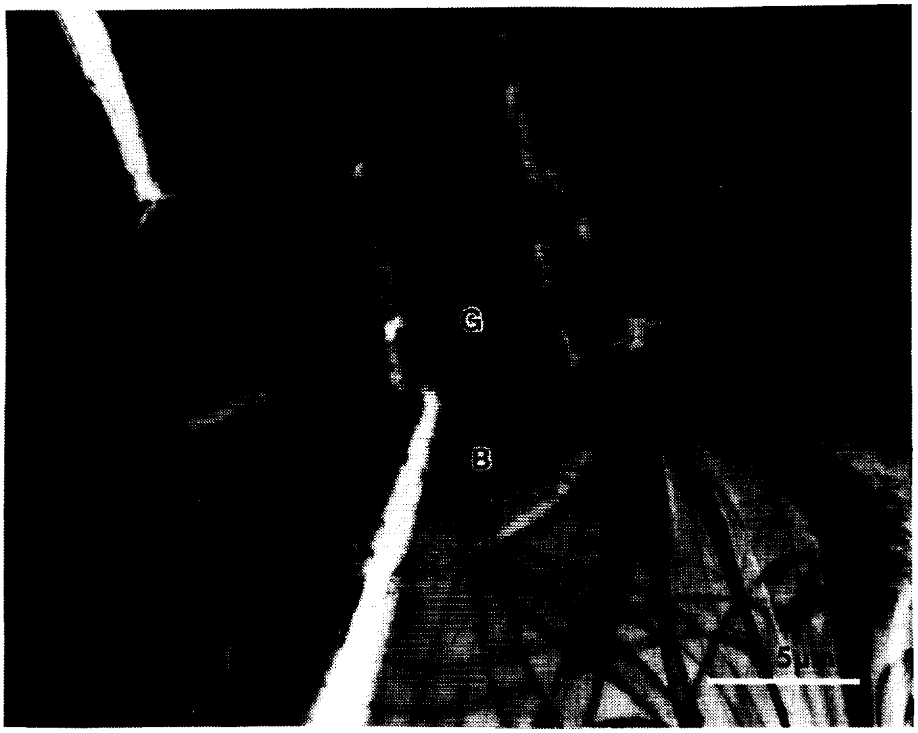

Figure 4.4.14 The crack in the β' phase after encountering the γ/γ' phase re-orients itself along the β'-γ/γ' interface.

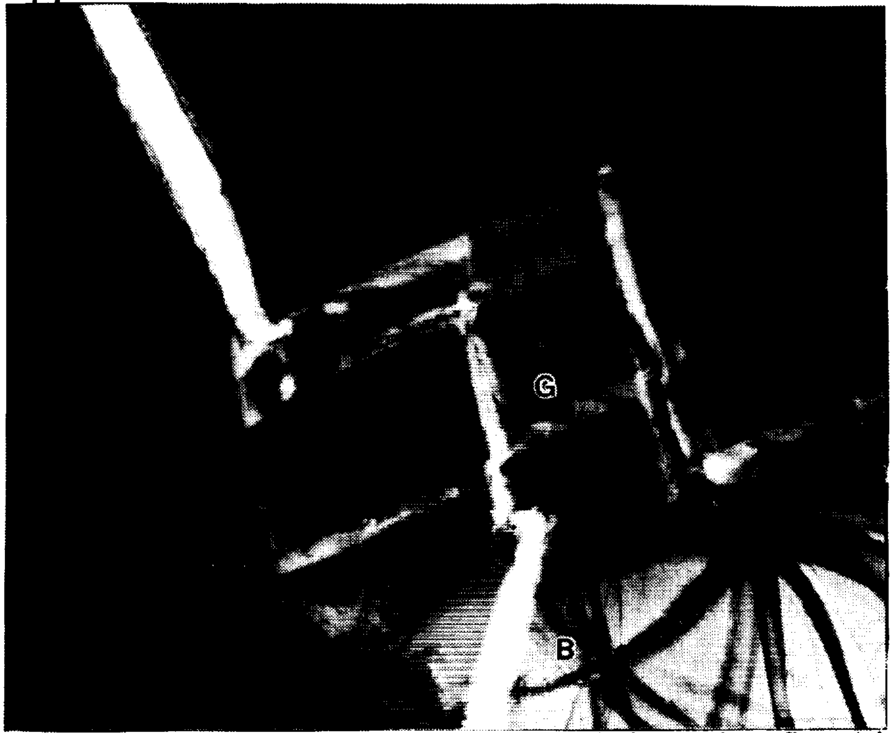

Figure 4.4.15 With additional strain, the re-oriented crack (in previous figure) joins one of the existing slip bands in the γ/γ' phase.

ORIGINAL PAGE
BLACK AND WHITE PHOTOGRAPH

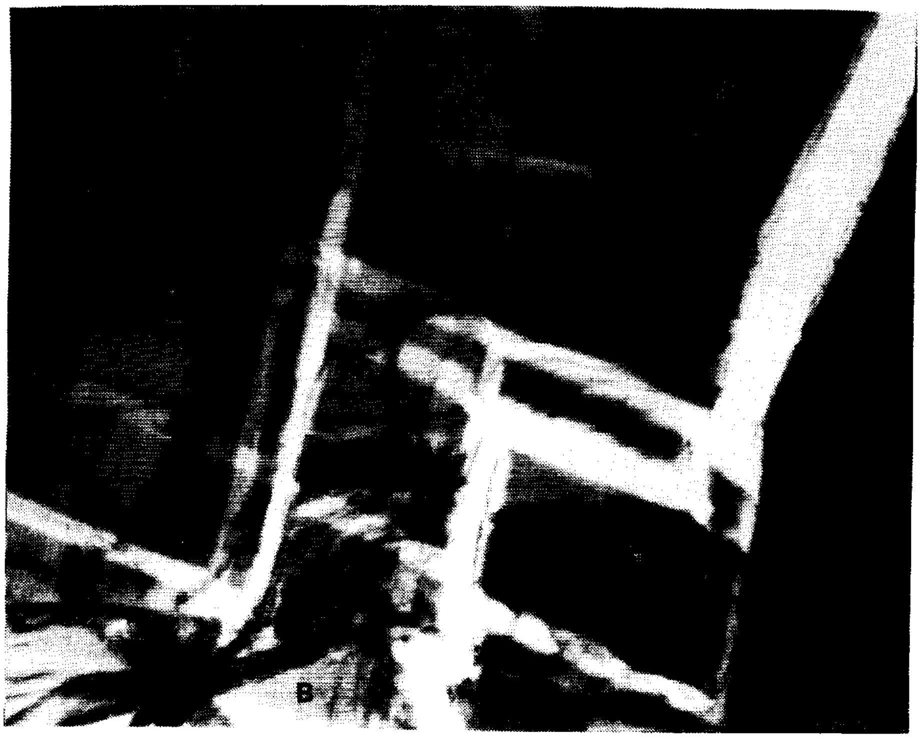

Figure 4.4.16 With further strain increments, the crack in previous figure, after joining with the slip band in the γ/γ' phase, advances along the slip band by thinning of material as shown earlier in figure 4.4.9.

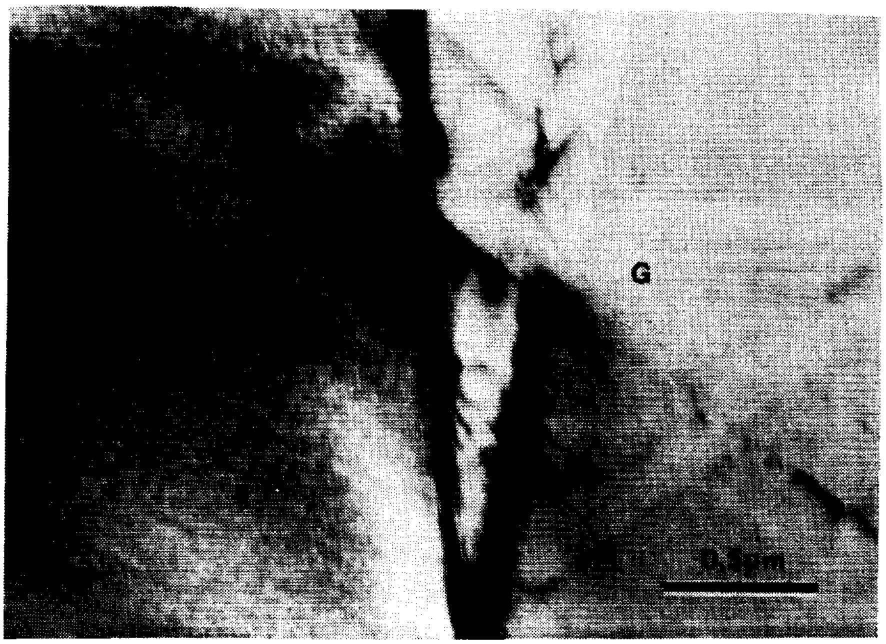

Figure 4.4.17 TEM micrographs from regions separate from those shown in fig. 4.4.6 showing planar slip activity in both the β' and γ/γ' phases. The β' grain is to the left of the interface.

ORIGINAL PAGE
BLACK AND WHITE PHOTOGRAPH

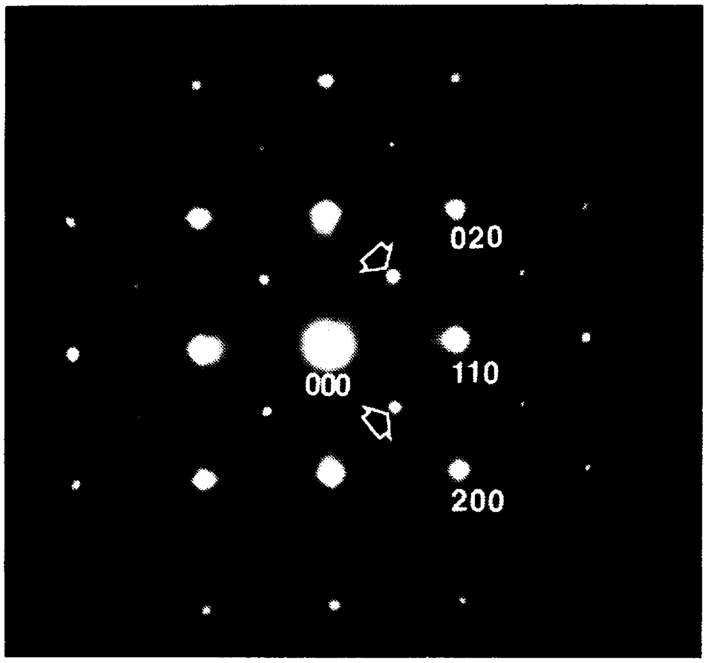

Figure 4.4.18 SAD pattern from the β' phase in previous figure. Beam direction near [001]. Comparing figs. 4.4.17-18, the slip plane of dislocations in the β' phase appears to be {100}.

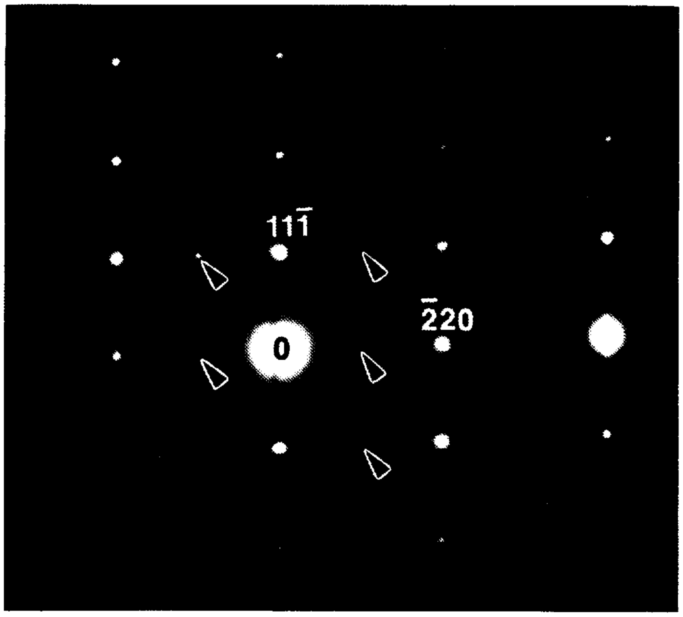

Figure 4.4.19 SAD pattern from the γ/γ' phase in figure 4.4.17. Beam direction near [112]. Comparing figs. 4.4.17&19, the slip plane of dislocations in the γ/γ' phase appears to be {111}.

ORIGINAL PAGE
BLACK AND WHITE PHOTOGRAPH

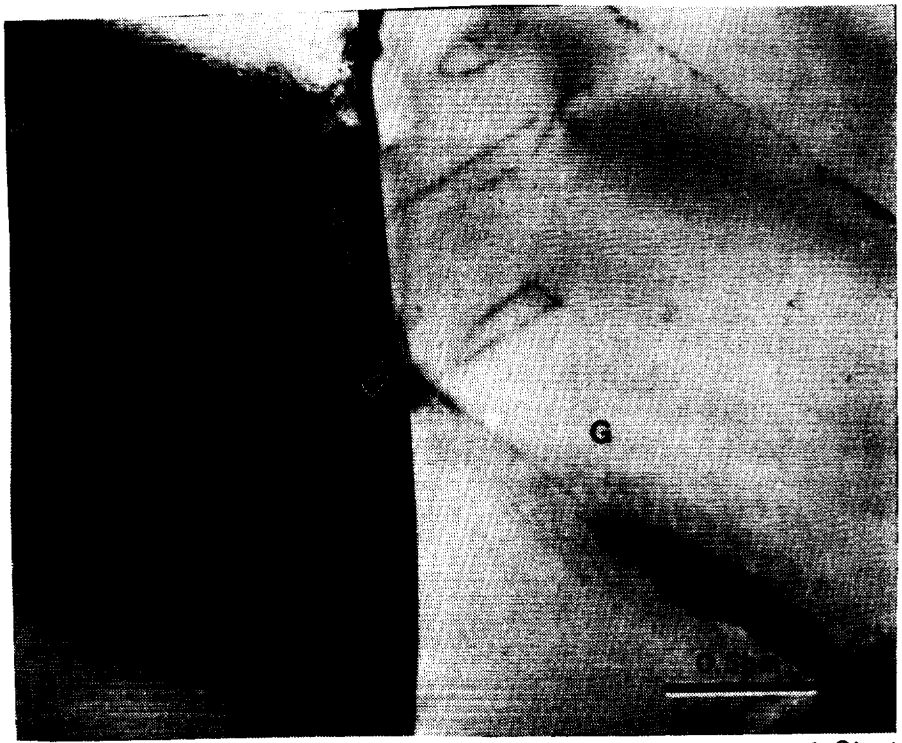

Figure 4.4.20 In-situ straining TEM micrograph showing a jogged β'-γ/γ' interface (ledge).

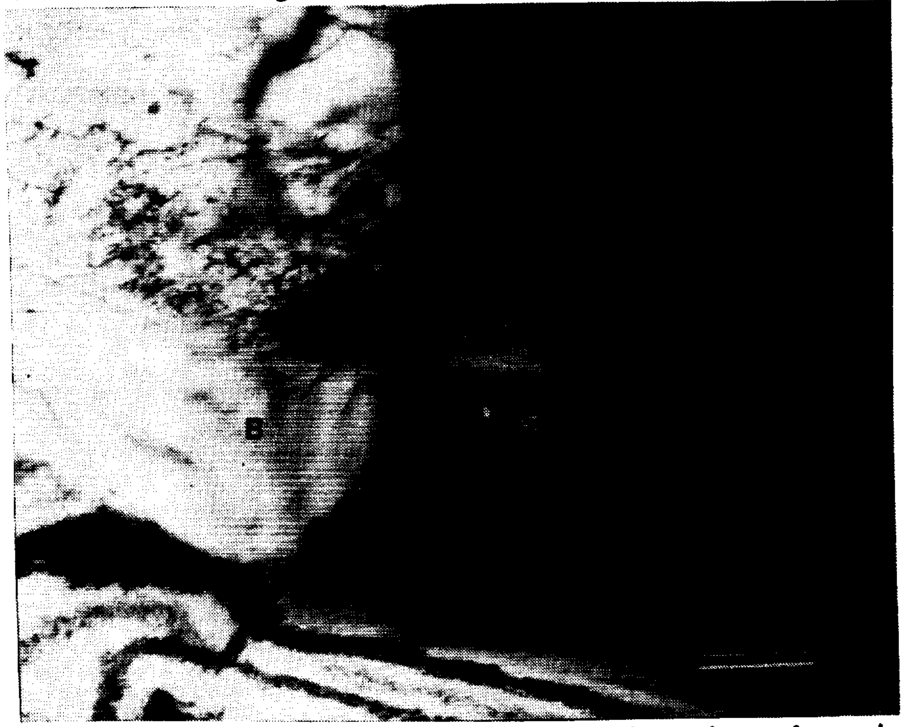

Figure 4.4.21 TEM micrographs from regions distinct from those shown in either fig. 4.4.6 or in fig. 4.4.17. The micrograph again shows a slip band in the γ/γ' phase intersecting the β'-γ/γ' interface with the β' grain to the left of the micrograph. Intense dislocation activity is observed in the β' phase at the head of the pile-up.

ORIGINAL PAGE
BLACK AND WHITE PHOTOGRAPH

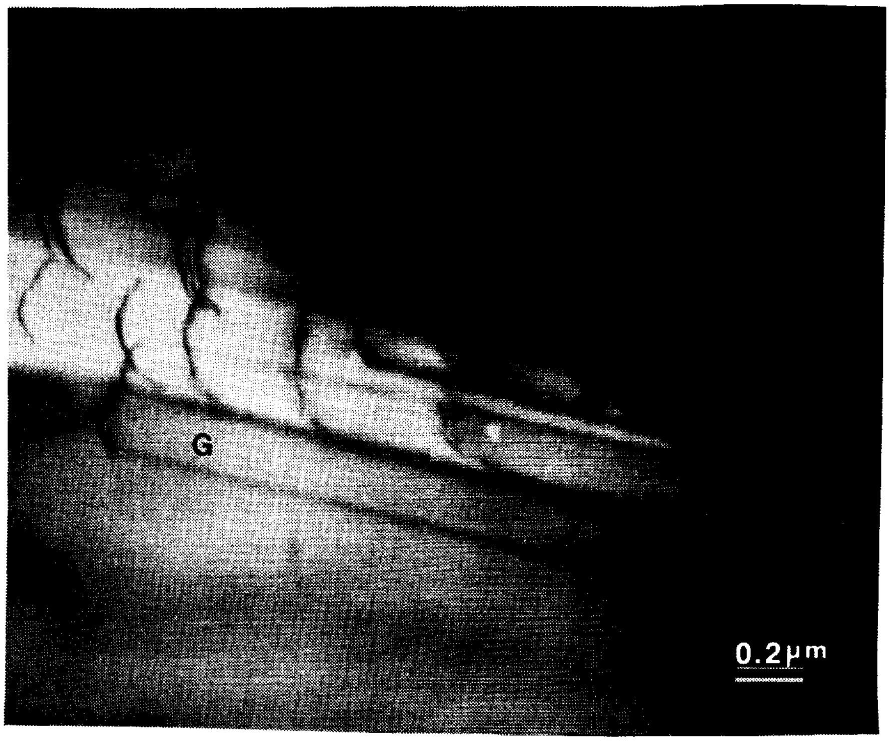

Figure 4.4.22 Higher magnification image of dislocations in the slip band in the γ/γ phase in the previous figure showing the dislocations to be bowed in the direction towards the β'-γ/γ interface. Thus, figures 4.4.21-22 indicate transfer of deformation from the γ/γ phase to the β' phase.

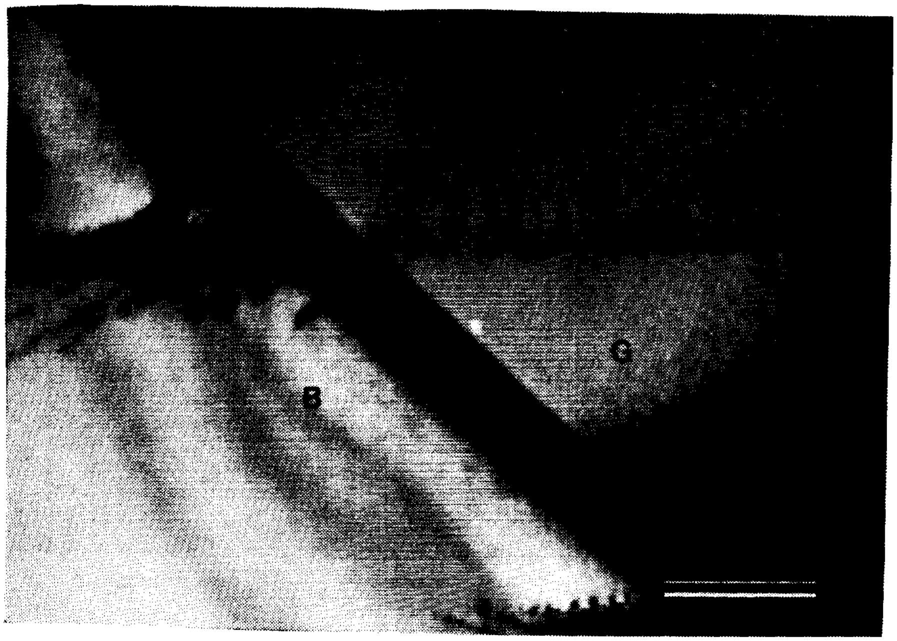

Figure 4.4.23 TEM micrograph indicates that the reverse deformation transfer process, that is from the β' phase to the γ/γ phase (note the direction of dislocation bowing), was also operative.

ORIGINAL PAGE
BLACK AND WHITE PHOTOGRAPH

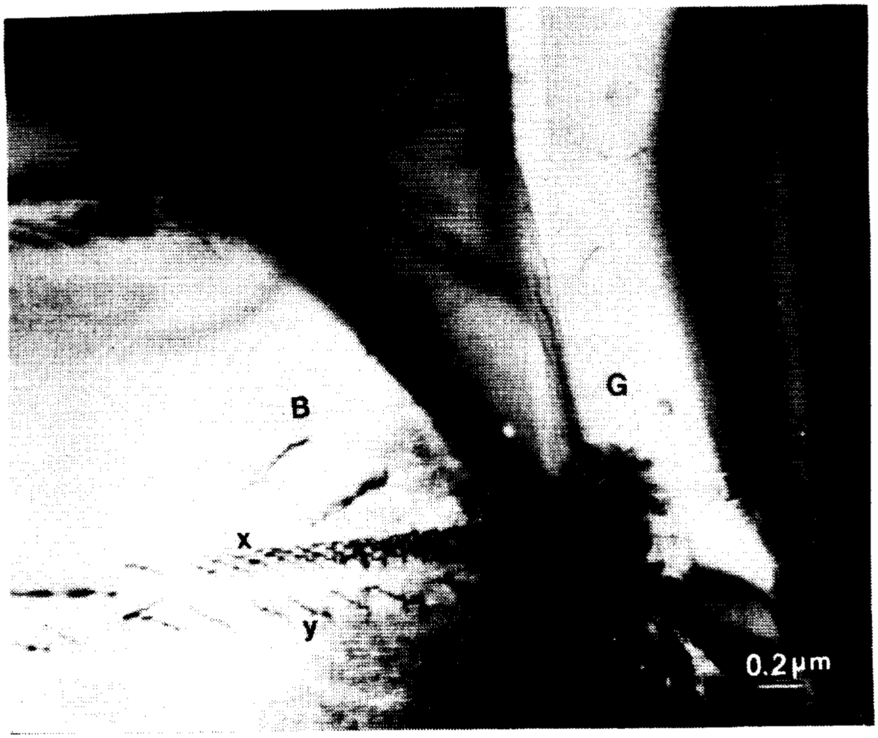

Figure 4.4.24 In-situ straining TEM micrograph showing the transfer of deformation from β' phase to the γ/γ' phase and vice-versa.

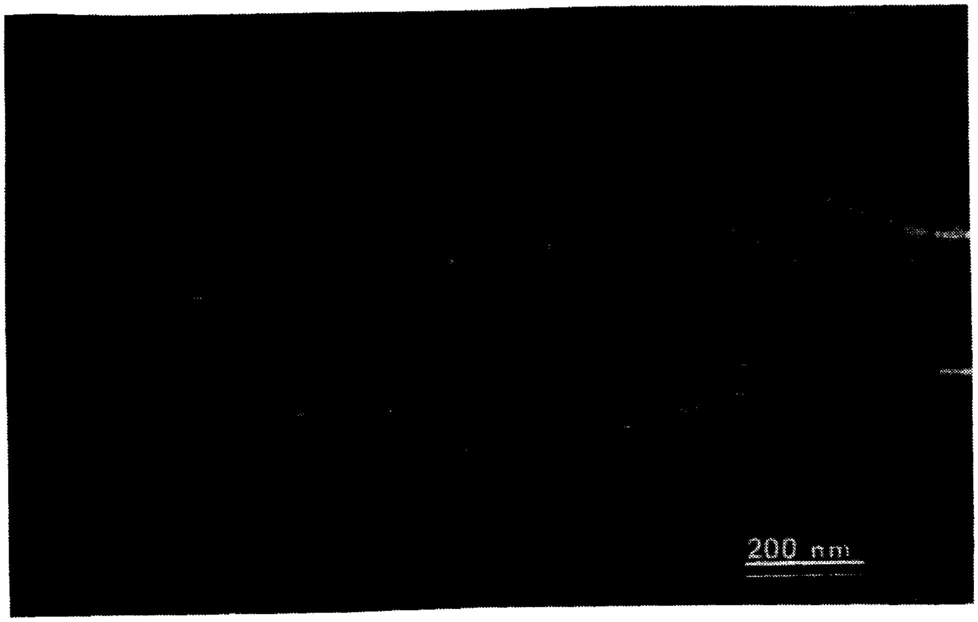

Figure 4.4.25 A $\vec{g}/3\vec{g}$ weak-beam image of the dislocation pile-up in the β' phase (fig. 4.4.24) showing single rather than paired dislocations which is consistent with the expectation for <100> Burgers' vector.

ORIGINAL PAGE
BLACK AND WHITE PHOTOGRAPH

Figure 4.4.17, by contrast, is a micrograph from a different region of the foil showing planar slip in both β' and γ/γ' phases and deformation transmittal across the interphase interface; note that the β' grain is to the left of the interface and that the direction of deformation transmittal, that is, from β' to γ/γ' or vice-versa, is not clear. The thin slip bands in both phases are indicative of the viewing direction being almost end-on to the slip plane. Since the diffracting vector $\vec{g}_{hkl}$ is normal to a plane of indices (hkl) in the reciprocal lattice space, and because the planes are viewed almost end-on, selected area diffraction patterns from both phases (figures 4.4.18-19) indicate a (100) and (111) slip plane for the β' and γ/γ' phases respectively. The beam directions are also close to [001] and [112] for the β' and γ/γ' phases respectively, indicating that the two grains do not satisfy Kurdjumov-Sachs relationship. Figure 4.4.20 is a micrograph showing the same interface as in figure 4.4.17 but a different pair of aligned slip bands. Note that the interface is jogged (arrowed) which is indicative of slip transfer across the interface for these two specific grains.

Jogged interfaces or aligned slip bands in β' and γ/γ' phases are not the sole mode of deformation transfer across the interface. For example, fig.4.4.21 is another micrograph of the interphase interface, the β' and γ/γ' grains are labelled 'B' and 'G' respectively. Note that the interaction between the slip band in the γ/γ' phase and the interface causes generation of dislocations in the β' phase without any obvious slip band or relationship. Figure 4.4.22 is higher magnification image of dislocations in the slip band in γ/γ' phase (fig.4.4.21); note that the curvature of dislocations in the slip band is indicative of dislocations piling up at the interphase interface thereby generating a stress which is relieved by the generation of dislocations in the β' phase. The reverse process, that is, deformation transmittal from β' to γ/γ' grains is also visible (fig. 4.4.23, note the direction of bowing of dislocations in the γ/γ' phase). In contrast to the observations by Field et al.[97] who reported only the passage of dislocations across the interface along properly aligned slip bands as the mechanism of deformation transfer, the deformation transfer by stress-assisted nucleation of slip under the stress field of a pile-up was also observed frequently.

Interestingly, fig.4.4.24 is a micrograph where both the above-mentioned deformation modes are observed simultaneously. Again, the β' grain is to the left of the interface. For the slip band marked 'X' in the β' grain, the curvature of dislocations and increasing spacing between dislocations with increasing distance from the interface are indicative of dislocations piling up at the grain boundary. Similarly, judging from the direction of bowing, dislocations in the slip band in the γ/γ' phase are also observed to pile up at the boundary, meeting the boundary almost at the intersection point of the β' slip band with the grain boundary. The resulting stress generated at the boundary is relieved by generation of dislocations on both sides of the interface including a slip band (marked 'Y') in the β' phase (note the direction of bowing of arrowed dislocations). A weak beam image (fig. 4.4.25) of dislocations in the slip band in the β' phase indicate single (unpaired) dislocations which is consistent with expectation for dislocations with <100> Burgers' vector. The above experiments confirm that one of the factors responsible for good ductility in the multi-phase alloy is arrest of cracks generated in the β' phase by the γ/γ' phase. The observation of cracks in the γ/γ' phase generated by thinning of material in the slip band due to intense dislocation activity is unique to the thin-foil specimen, presumably due to differences in geometry (limited thickness) and stress-state. Similarly, the observation of planar slip in the β' phase is also not consistent with observations in the bulk deformed specimens. The lower ductility reported by Field et al.[97] in rapidly solidified ribbons compared to those observed in extruded bulk specimens is possibly related to the generation of cracks in the γ/γ' phase by thinning of material along the slip band and transmittal of such cracks to the β' phase. In-situ experiments, however, do confirm the deformation transmittal across the interphase interface to be an additional factor contributing to the ductility of the multi-phase alloys.

4.4.3 Elevated Temperature

The room temperature deformation behavior of the cast and extruded multi-phase alloy and alloys similar to its constituent phases have been noted above. Briefly, the observed operative slip vector in the β' alloy Ni-30Al-20Fe and the pro-eutectic β' phase of the multi-phase alloy was <100>. The Burgers' vector of dislocations in the γ/γ' phase of the multi-phase alloy was observed to be <110>, with the 1/2<110> dislocation partials easily resolvable.

Thin foils from gauge sections of the multi-phase alloy samples strained to failure at 427°C and 627°C, and up to 70% at 827°C were examined in the TEM. Thin foils from samples tested at 427°C exhibited a high dislocation density in both the β' and γ/γ' phases. The dislocation densities in both the β' and γ/γ' phases were, however, observed to decrease with increasing test temperatures. At 827°C, the deformed microstructure was almost dislocation-free. Low angle boundaries were observed within the deformed grains of both β' and γ/γ' phases at 627°C and 827°C, indicating that recovery processes contribute to the elevated temperature deformation of the multi-phase alloy. The occurrence of dynamic recrystallization in the β' phase at 827°C could not be proved unambiguously due to the difficulty in differentiating between dynamically recrystallized new, dislocation-free grains from prior existing small (~0.5μm width) β' grains from a dynamically recovered deformation substructure. However, as noted earlier, optical micrographic observations (fig. 4.3.13d) indicated the occurrence of dynamic recrystallization in the pro-eutectic β' phase at 827°C. Furthermore, the wavy nature of the grain boundaries (which is usually indicative of dynamic recrystallization processes) observed in the β' alloy, Ni-30Al-20Fe strained to failure at 827°C (fig. 4.3.15b) also support such a conclusion. Thus, while recovery processes are active in both the β' and γ/γ' phases during the elevated temperature (627°C - 827°C) deformation of the multi-phase alloy, it is possible that dynamic recrystallization also occurs during deformation of the β' phase.

For the β' alloy, Ni-30Al-20Fe, thin foils from tensile specimens strained to failure (~27% strain) at 627°C (fig. 4.4.26b) exhibited a lower dislocation density than that observed for ~2% strain at room temperature (fig. 4.4.26a); sub-grain formation was also observed. Thin foils from gauge sections of samples strained 97% at 827°C (fig. 4.4.26c) exhibited even an lower dislocation density; again, sub-grain formation was observed. The low dislocation densities and low angle boundaries are indicative of recovery processes being operative in the β' alloy Ni-30Al-20Fe at both 627°C and 827°C and are consistent with the observations for the β' phase of the multi-phase alloy reported above.

For the purpose of analysis of elevated temperature deformation mechanisms, a multi-phase alloy specimen was strained only 5% and thin sections prepared from its gauge sections and analyzed in the TEM. The microstructure consisted mostly of grains free of dislocations, although a few grains with low dislocation densities were also observed. Figure 4.4.27 shows a dislocation network in the β' phase along with two individual dislocations imaged with different diffracting vectors. The individual dislocations marked"a" and "b" and the segments of the dislocation network marked "c", "g" and "i" are in contrast with imaged with $\vec{g}$ = $10\bar{1}$ and $0\bar{1}1$ and out of contrast with $\vec{g}$ = 200 and $1\bar{1}0$, indicating a [001] Burgers' vector. By contrast, the segment marked "e" was in contrast with $\vec{g}$ = $10\bar{1}$ and $1\bar{1}0$ and out of contrast with $\vec{g}$ = $0\bar{1}1$ and 200, indicating a [011] Burgers' vector, see fig. 4.4.27a-c. Similarly, the segments "i", "h" and "j" exhibit contrast consistent with [001], $[\bar{1}00]$ and $[\bar{1}01]$. The $[\bar{1}01]$ appear to have formed by the dislocation reaction [001] + $[\bar{1}00]$ -> $[\bar{1}01]$. The residual contrast of dislocations when the invisibility criteria for screw $\vec{g} \cdot \vec{b} = 0$ or for edge dislocations ($\vec{g} \cdot \vec{b} = 0$ and $\vec{g} \cdot \vec{b} \times \vec{u} = 0$) were satisfied was probably due to the high elastic anisotropy of the β' alloy.

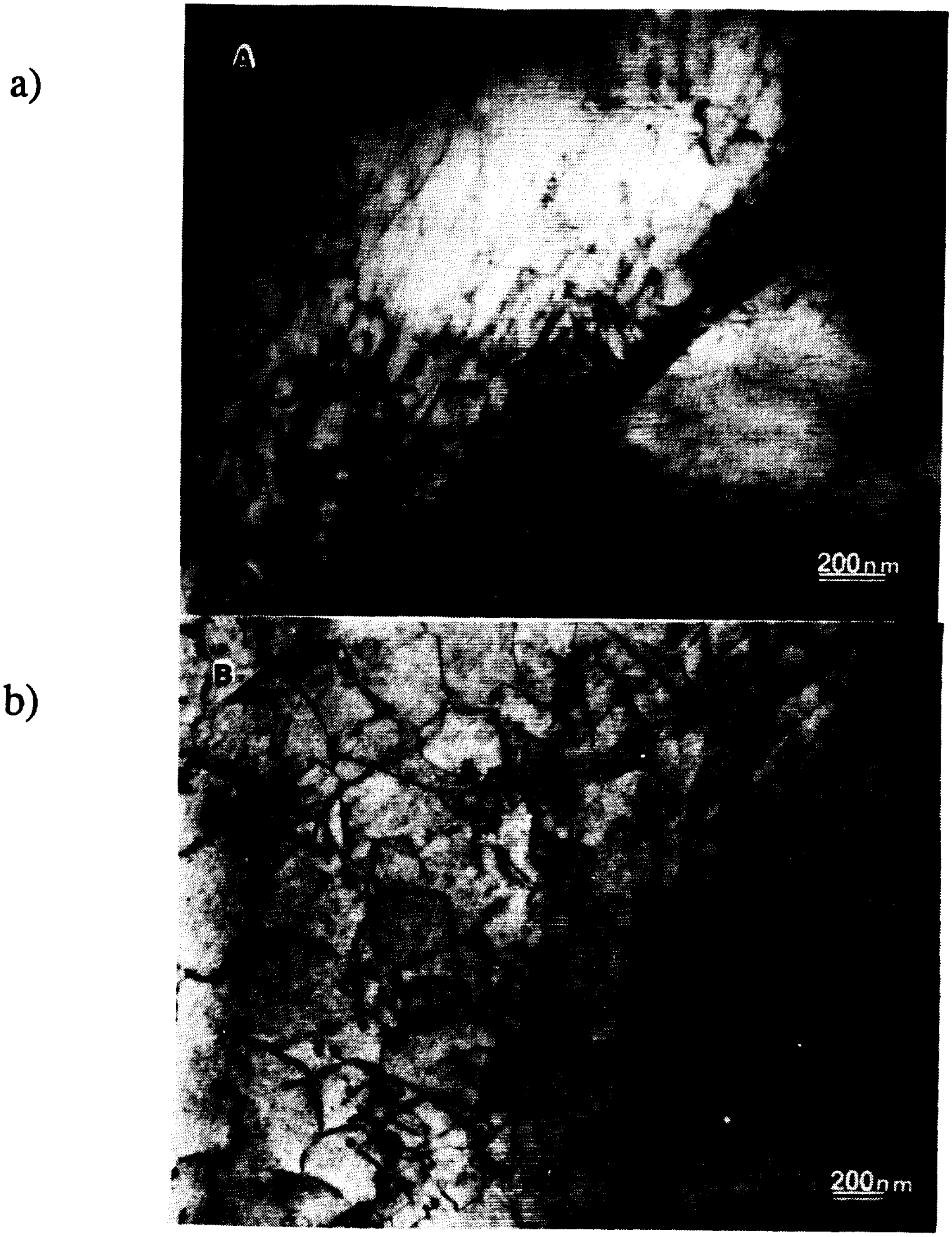

Figure 4.4.26 Bright-field TEM micrographs of β' alloy Ni-30Al-20Fe deformed (a) 2% at room temperature (b) ~27% at 627°C (c) ~97% at 827°C. Note the decrease in dislocation density with increasing deformation temperature.

ORIGINAL PAGE
BLACK AND WHITE PHOTOGRAPH

c)

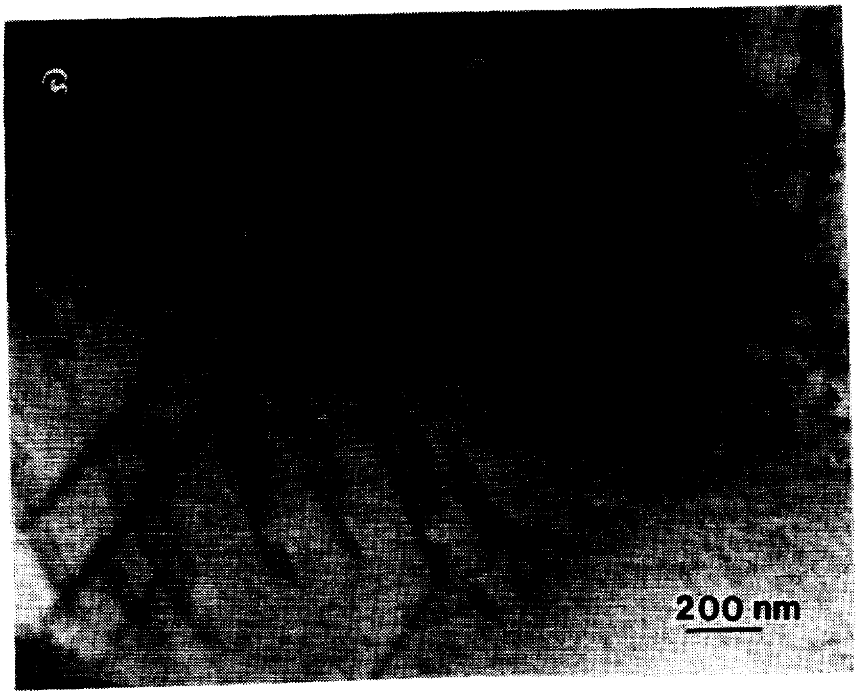

Figure 4.4.26 continued

ORIGINAL PAGE
BLACK AND WHITE PHOTOGRAPH

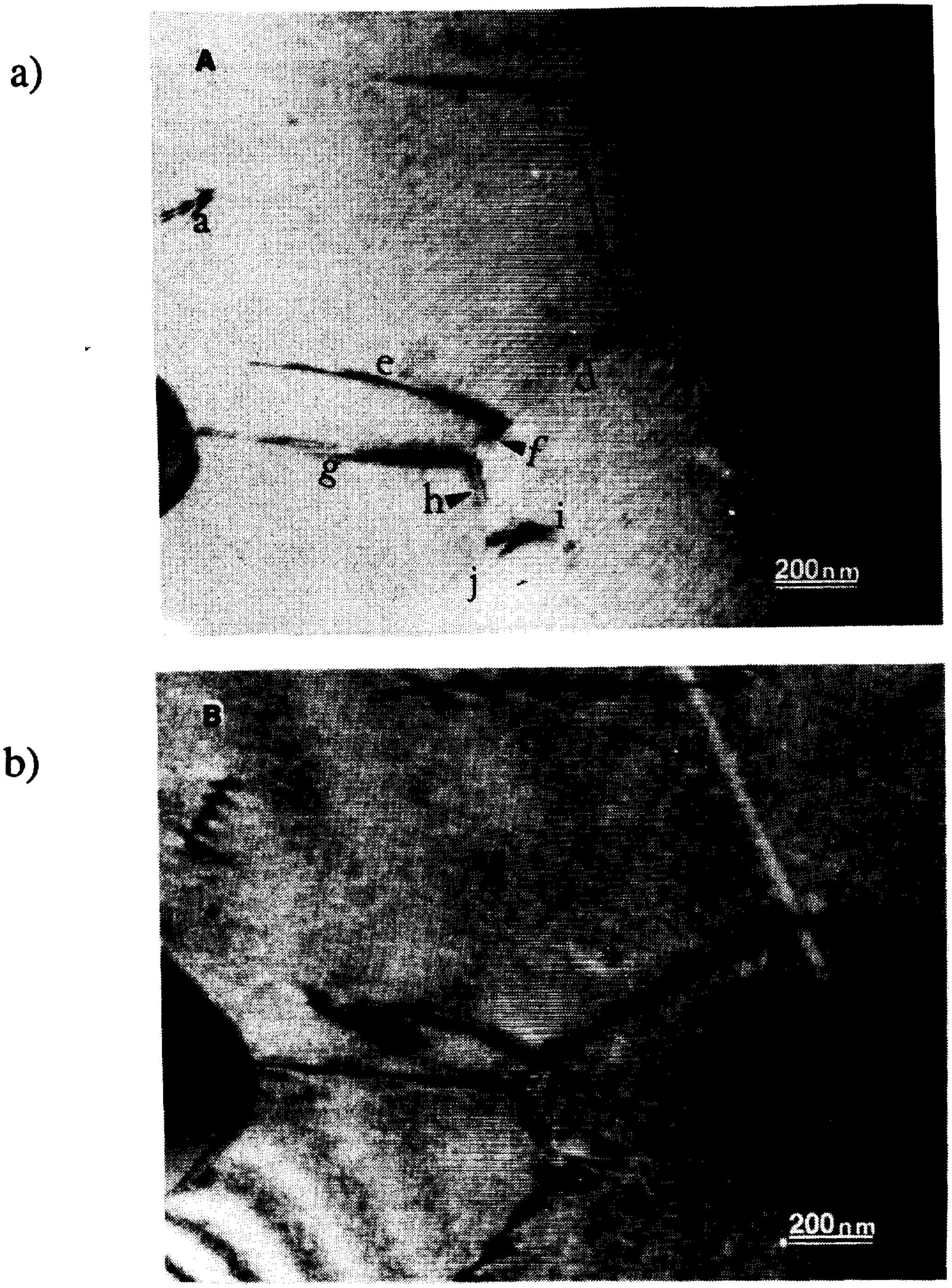

Figure 4.4.27 Dislocations in the β' phase in extruded multi-phase Ni-20Al-30Fe, strained ~5% at 827°C and air-cooled to room temperature. Imaging conditions: (a) $\vec{g}$ = (020) (b) $\vec{g}$ = (0$\bar{1}$1) (c) $\vec{g}$ = (200). Beam direction near [101] for (a), near [111] for (b) and near [001] for (c). (d) A schematic sketch of the network indicating their Burgers' vectors.

ORIGINAL PAGE
BLACK AND WHITE PHOTOGRAPH

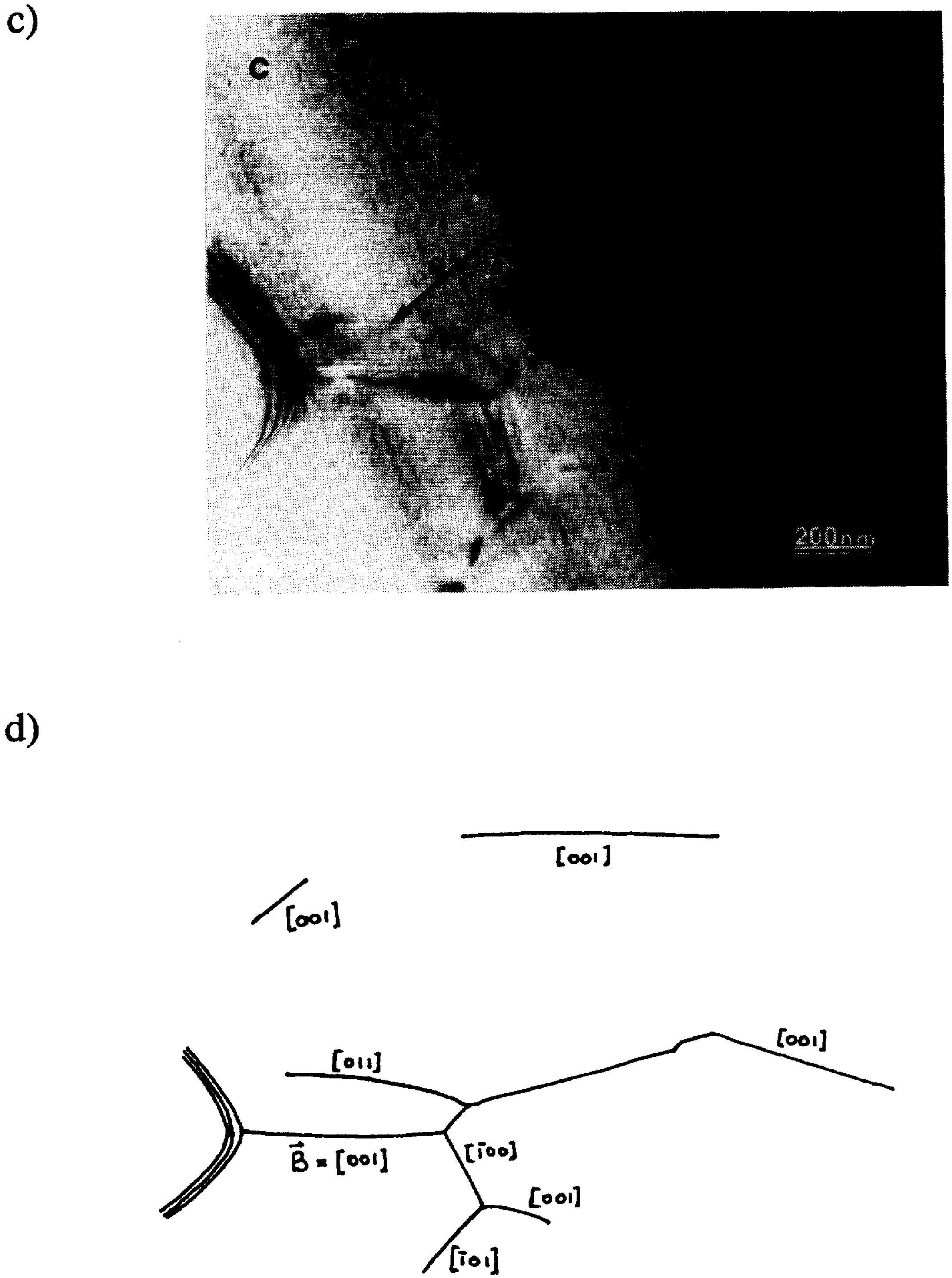
c)
c
200nm
d)
[001]
[001]
[011]
[001]
$\vec{B} = [001]$
$[\bar{1}00]$
[001]
$[\bar{1}01]$

Figure 4.4.27 continued.

ORIGINAL PAGE
BLACK AND WHITE PHOTOGRAPH

Figure 4.4.28 shows a dislocation network in the γ/γ' phase of the multi-phase alloy. The dislocations in the network were in contrast when imaged with g= (020) and (220) and out of contrast when imaged with g = $(2\bar{2}0)$, which is consistent with a <110> Burgers' vector which, again, is similar to the room temperature observations. It should be noted, however, that at 827°C the dislocations are unit dislocations ($\vec{b}$ = 1/2<110>) rather than paired. This is consistent with the microstructure of the fcc-based phase being disordered γ only rather than γ/γ' (see section 4.2.2).

Since the Burgers' vectors of dislocations strained at 27°C and 827°C are similar in both the β' and γ/γ' phases, it would be reasonable to presume similar deformation mechanisms being operative at intermediate temperatures 427°C and 627°C.

4.5 Creep Behavior

The creep behavior of the multi-phase alloy, Ni-20Al-30Fe, and the alloys similar to its constituent phases were examined in compression at 827°C at a constant load corresponding to an initial stress of 60 MPa. Although the alloys Ni-30Al-20Fe and Ni-12Al-40Fe were chosen based on the room temperature microstructure of the multi-phase alloy to represent the constituent β' and γ/γ' phases, the nature of the Ni-Fe-Al ternary phase diagram at higher temperatures resulted in these alloys being multi-phase themselves at 827°C. Since the volume fractions of precipitate phases were observed to be small, these alloys are still referred to as only β' and γ/γ' respectively. The degree to which the small volume fraction of discontinuous grain boundary precipitates influences the creep behavior of the β' or γ/γ' alloys is not clear.

Figure 4.5.1 shows a comparison of the creep rates at 827°C of the as-extruded multi-phase alloy and alloys similar to its consituent phases. While the γ/γ' phase is very creep resistant for the stress applied, both the β' alloy and the multi-phase alloy creep

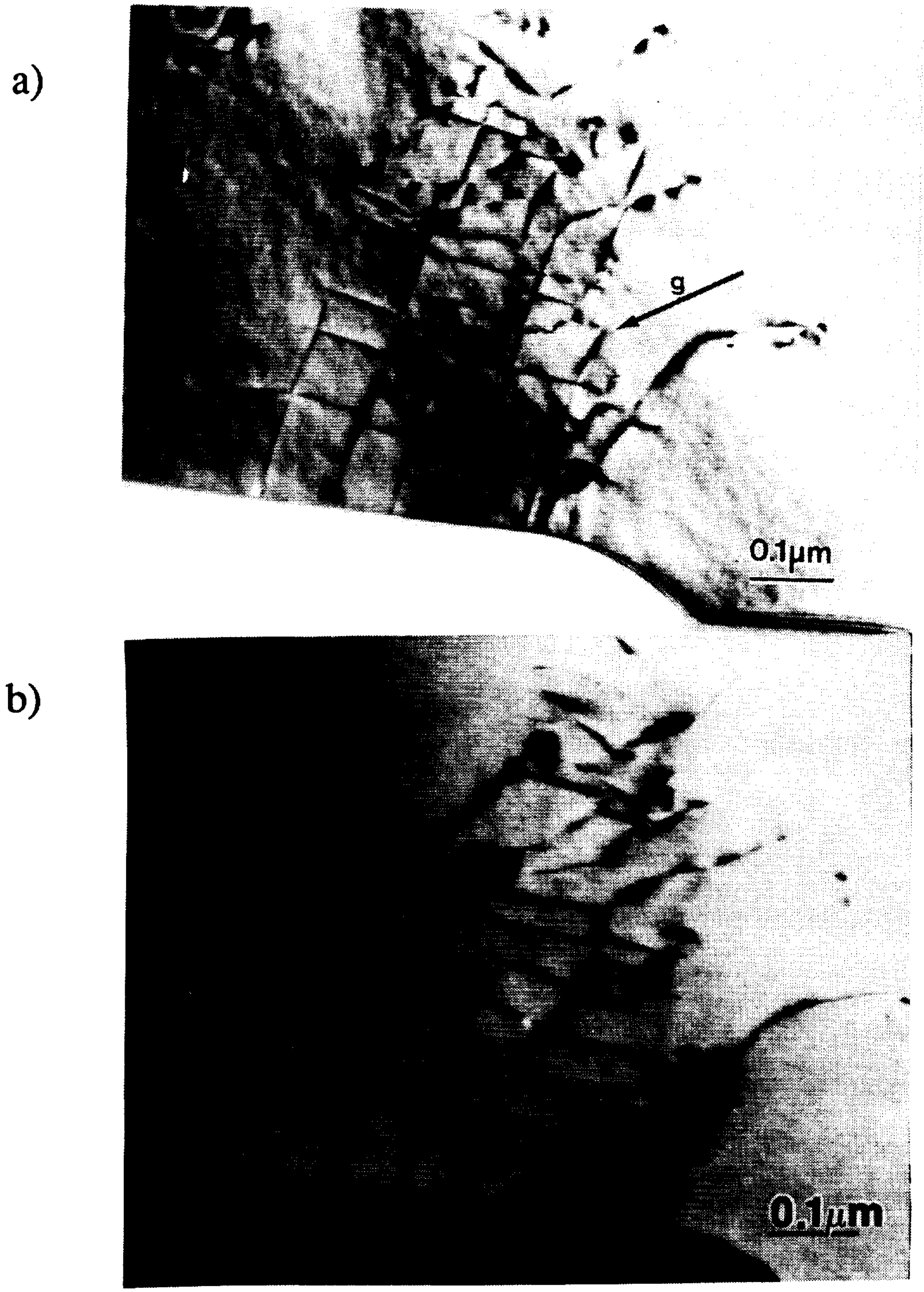

Figure 4.4.28 Dislocations in the γ phase in extruded multi-phase Ni-20Al-30Fe, strained ~5% at 827°C and air-cooled to room temperature. Imaging conditions: (a) $\vec{g}$ = (020) (b) $\vec{g}$ = (220) (c) $\vec{g}$ = $(2\bar{2}0)$. Beam direction near [001] for (a), (b) and (c).

ORIGINAL PAGE
BLACK AND WHITE PHOTOGRAPH

c)

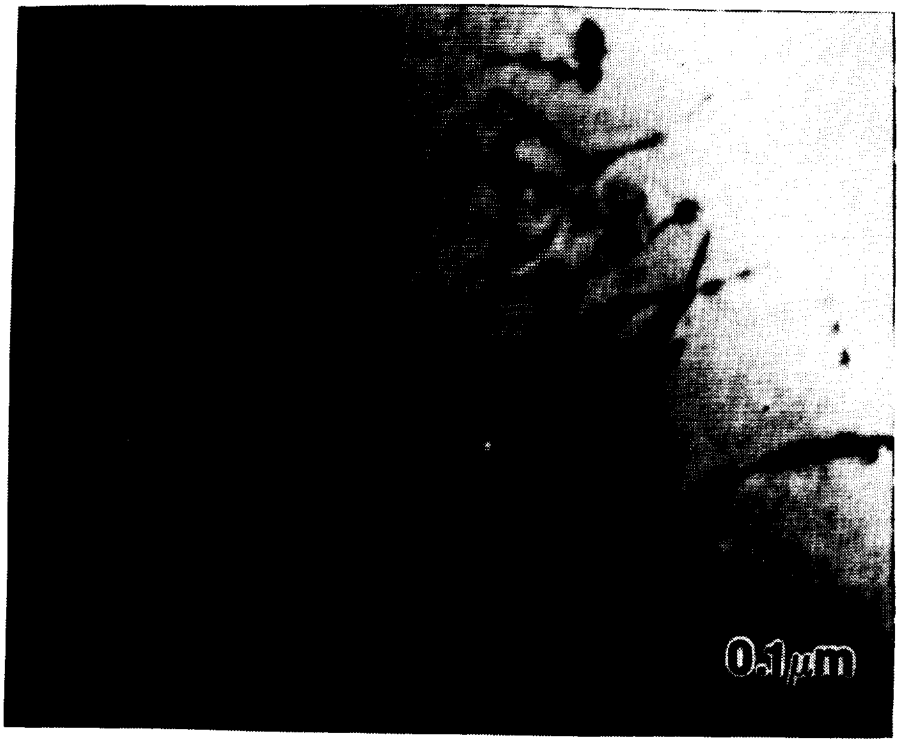

Figure 4.4.28 continued.

ORIGINAL PAGE
BLACK AND WHITE PHOTOGRAPH

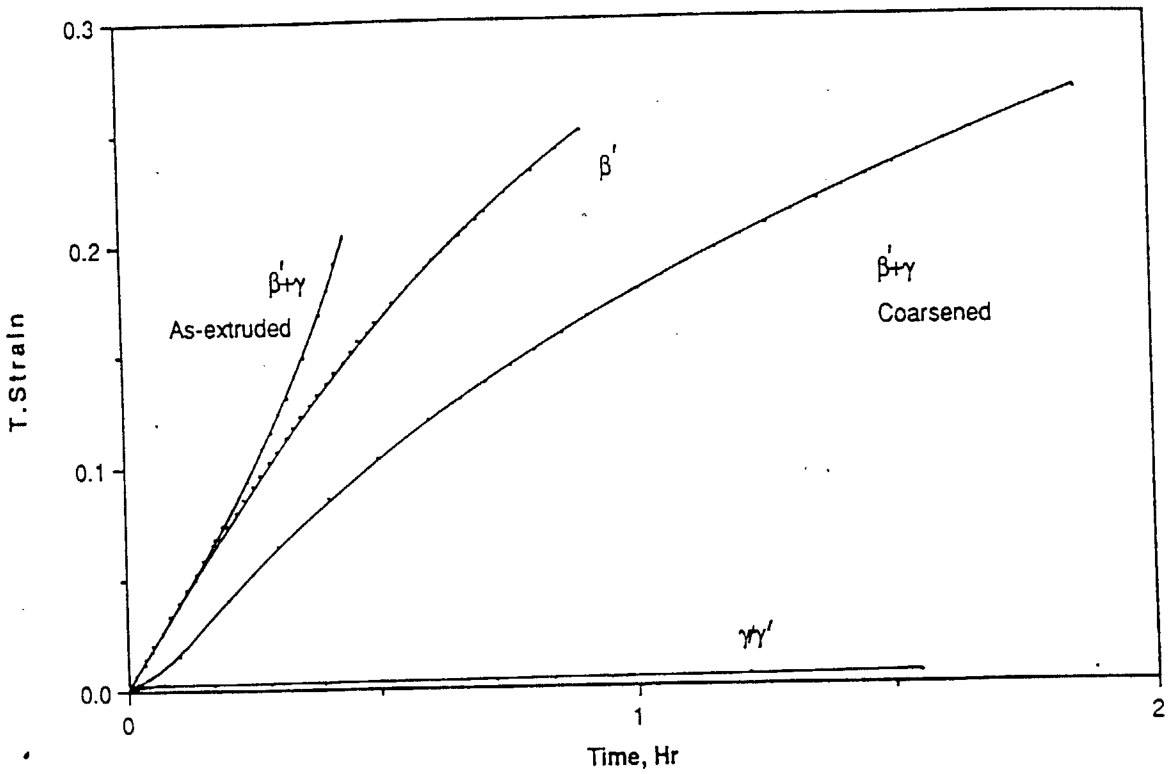

Figure 4.5.1. Compressive creep rates of the multi-phase alloy Ni-20Al-30Fe and alloys similar to its constituent β' and γ/γ' phases, Ni-30Al-20Fe and Ni-12Al-40Fe, respectively. Note that the creep rate of the multi-phase alloy is considerably lower when the microstructure is coarsened. Test temperature 827°C; initial applied stress 60 MPa.

rapidly. To a first approximation, the creep properties of the multi-phase alloy would be expected to be intermediate between those of the β' alloy and those of the γ/γ' alloy. That the as-extruded multi-phase alloy and the β' alloy exhibit similar creep rates indicates that either the β' phase governs the creep behavior of the multi-phase $\beta'+\gamma$ aggregate or the creep properties are strongly affected by the scale of the microstructure.

Nathal et al. [109] have shown that for the γ/γ' superalloy NASAIR100, alloys similar to its constituent γ' phase were more creep resistant than the γ phase. Furthermore, the two-phase γ/γ' alloy was more creep resistant than either single phase γ and γ' alloys, indicating the importance of γ/γ' interfaces in improving creep properties. Thus, for the Ni-Fe-Al alloys, it is possible that, while a fine dispersion of ordered γ' precipitates in a disordered (γ) matrix may result in improved creep properties, the inherent creep properties of the disordered γ phase itself may be poor, thereby leading to the observed poor creep properties of the multi-phase $\beta'+\gamma$ alloy.

An alternative explanation for the poor creep properties of the multi-phase alloy is the fine scale of the microstructure, since fine-grained alloys are generally known to exhibit worse creep properties than coarse-grained alloys. Interestingly, Klöwer [110] has studied the effect of lamellar spacing on the creep behavior of directionally solidified (lamellar eutectic) Ni-18Al-40Fe at 800°C. At 800°C, Ni-18Al-40Fe was reported to be two-phase $\beta'+\gamma$, similar to the phases present in Ni-20Al-30Fe at 827°C studied here. With decreasing spacing, the creep resistance of Ni-18Al-40Fe became increasingly higher than that of the coarse alloy [110]. It was suggested that the narrowly-spaced interfaces gave rise to additional strengthening, the threshold creep stress being inversely proportional to the interlamellar spacing, a behavior commonly observed in dispersion-strengthened alloys [110]. Interestingly, for temperatures between 800 and 1000°C, Vandervoort et al. [111] and Yang and Dodd [112] reported a decrease in creep rate of NiAl with decreasing grain sizes and increasing deviation from stoichiometry. In contrast, Whittenberger [16], while confirming the above-mentioned trend of increased creep resistance with decreased grain sizes (≤15μm) and increasing deviation from stoichiometry, also demonstrated that low strain rates and higher deformation temperatures (927-1127°C) minimized such disparaties in observed creep rates.

To test the influence of the scale of microstructure on the creep properties, the compressive creep properties of the coarsened multi-phase alloy (produced by annealing at 1275°C for 3 hrs and furnace cooling at 5°C/min) were measured at 827°C at an initial stress of 60 MPa. Figure 4.5.2a-b of polished longitudinal sections of crept samples shows the differences in the microstructure of the as-extruded and coarsened alloy. Note that the microstructure showed only minor changes during testing, the changes being limited to mainly the pro-eutectic phase which was observed to be transformed by deformation from its coarse, elongated morphology into many fine and equiaxed units. The results (fig.4.5.1) indicate that coarsening the microstructure results in improved creep properties, the creep rate being intermediate between those of the β' and γ/γ' phases. Since the only difference between the two microstructures is the reduced number of grain boundaries and interphase-interfaces for the coarsened alloy, grain boundary sliding and interfacial sliding were concluded to be an important factor contributing to the creep of the multi-phase alloys. This result is at odds with the work of Klöwer[110] which suggests that an increased interfacial area to be beneficial to creep properties. The difference, however, lies in the processing routes of the alloys, which lead to differences in the nature of the interfaces. While the interfaces in the cast and extruded alloy are likely to be incoherent due to the recrystallization following the hot-extrusion process, those of Klöwer[110] are likely to be semi-coherent (due to directional solidification) since such semi-coherent interfaces have already been observed for directionally solidified Ni-20Al-30Fe by Larsen [113].

The stress exponents of the multi-phase, β' and γ/γ' alloy were not calculated due to scatter in the data.

Thin foils of as-crept microstructures of the multi-phase alloy, Ni-20Al-30Fe, and the β' alloy, Ni-30Al-20Fe, were examined using the TEM. Both the β' alloy and the β'

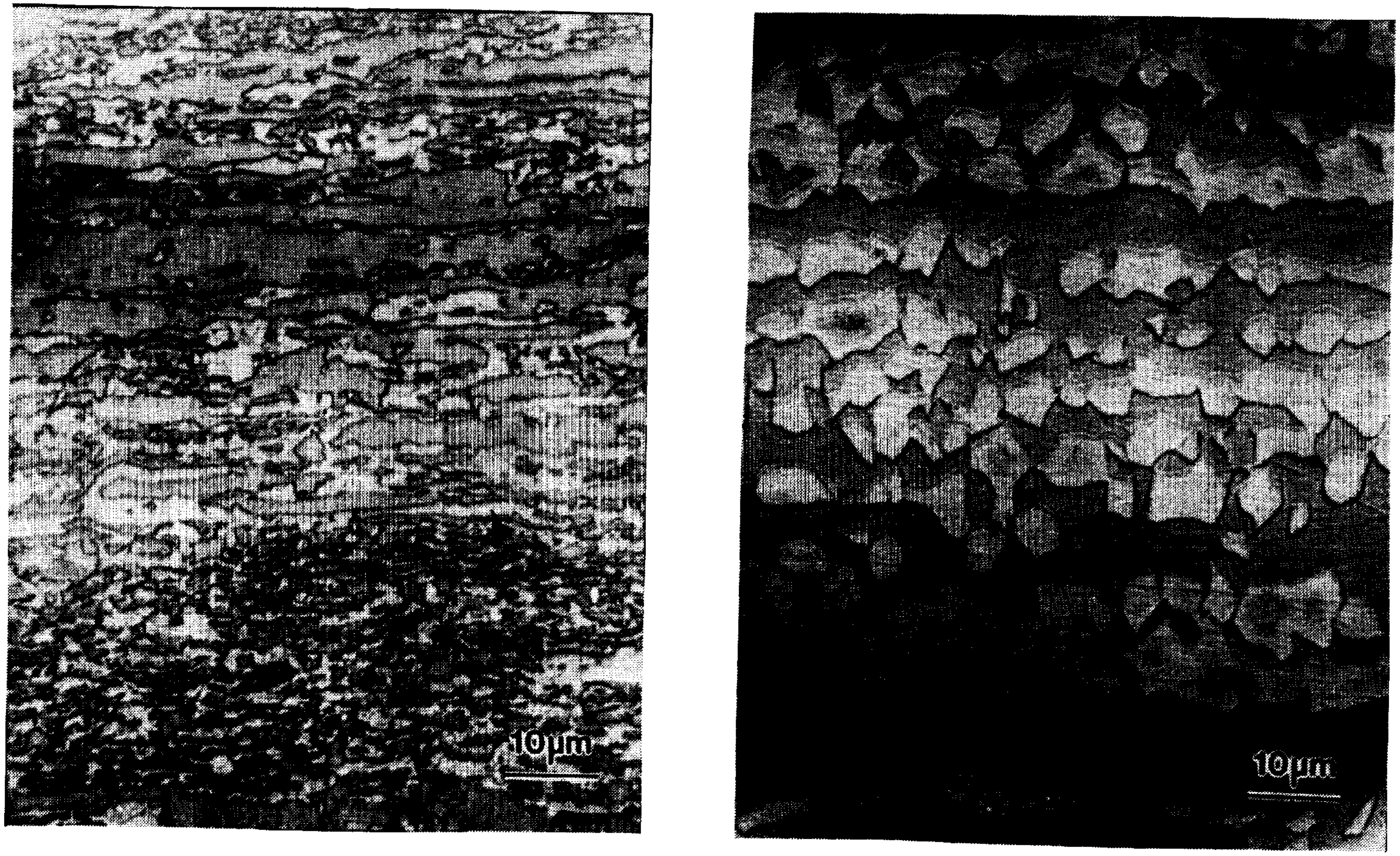

Figure 4.5.2. Polished longitudinal sections of as-crept samples of the (a) as-extruded, (b) coarsened $\beta'+\gamma$ multi-phase alloy. The lighter constituent is the γ phase (arrowed). Note the difference in scale of microstructure.

ORIGINAL PAGE
BLACK AND WHITE PHOTOGRAPH

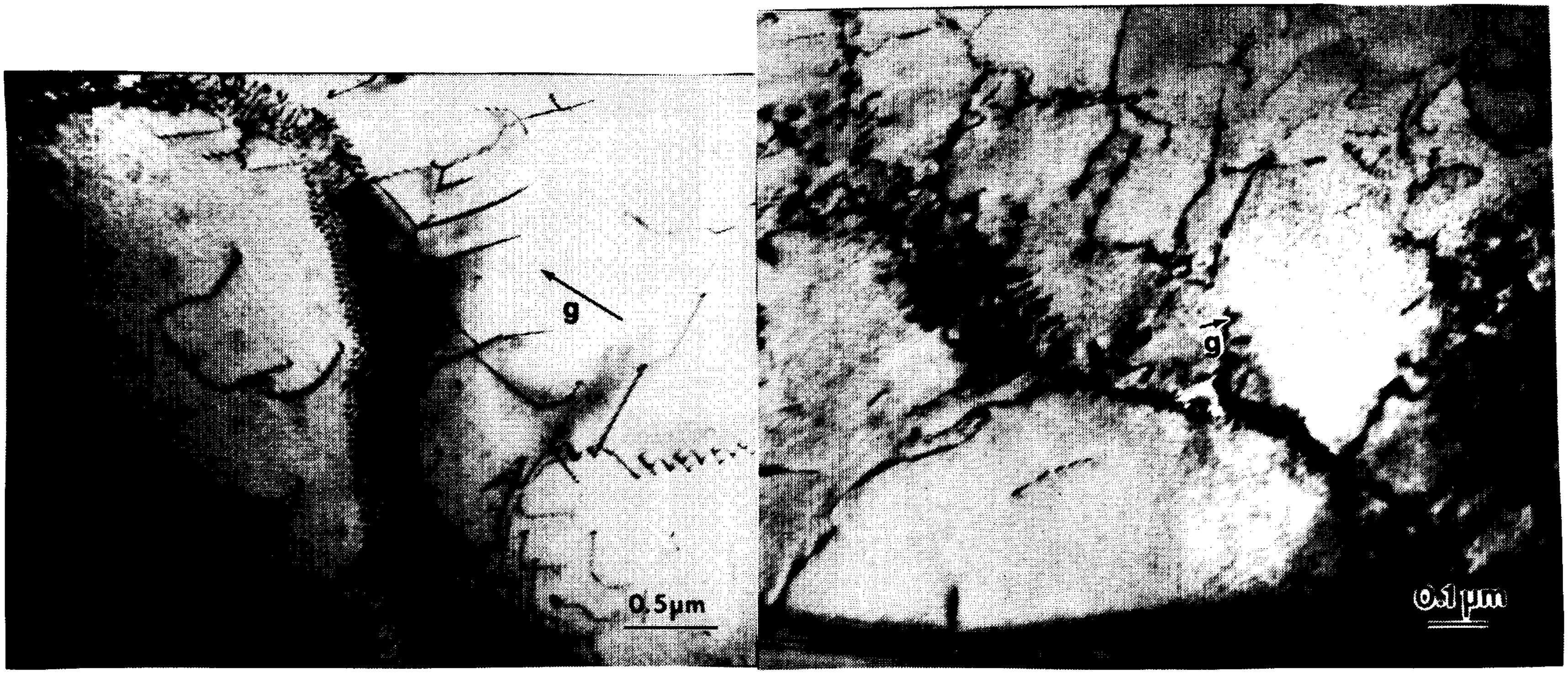

Figure 4.5.3. Deformation substructures in (a) the β' phase ($\vec{g} = (1\bar{1}0)$, B~[111]) and (b) the γ phase ($\vec{g} = (\bar{1}11)$, B~[211]) of as-extruded multi-phase alloy samples tested under constant load compressive creep at 827°C. Note that sub-grain formation occurs in both phases. The Burgers' vector of the dislocations was **a**<001> in the β' phase and **a**/2<110> in the γ phase.

ORIGINAL PAGE
BLACK AND WHITE PHOTOGRAPH

phase of the multi-phase alloy exhibited sub-grain structures. For example, figure 4.5.3a shows the subgrain structure observed in the β' phase of the multi-phase alloy which crept in compression at 827°C. The Burgers' vector of the dislocations in the sub-boundary were determined by the standard **g.b** analysis to be <001> type. Jung et al. [114] have studied the creep behavior of both nickel-rich and iron-rich β' (Ni,Fe)(Fe,Al) alloys. For nickel-rich β' alloys, both a well-defined subgrain structure formation and <100> dislocations were observed, consistent with the observed creep behavior of the β' alloy Ni-30Al-20Fe in this study. A well-defined subgrain structure is characteristic of climb-controlled creep, often referred to as pure metal type creep [89]. For iron-rich Ni-Fe-Al β' alloys[114], the deformation substructure is characteristic of glide-controlled alloy-type [89] creep, which is indicative of the increased resistance to dislocation mobility by increasing iron additions. Thus the creep behavior (climb or glide controlled) of Ni-Fe-Al β' alloys is strongly dependent upon solute (Ni/Fe ratio) effects on dislocation mobility.

Figure 4.5.3b shows the dislocation substructure in the γ phase of the multi-phase alloy after creep deformation at 827°C, in which the dislocations were observed to be arranged to form subgrains, similar to the β' phase. The Burgers' vectors of the dislocations were determined, by imaging them with different diffracting vectors, to be <110>. Unlike room temperature deformation where the dislocations were observed to be paired, these dislocations are unit 1/2<110> dislocations and are consistent with the expectation of unpaired dislocations in a disordered microstructure.

Examination of the deformed substructure indicated that both β' and γ phases contribute to the creep behavior of the multi-phase alloy. For the as-extruded alloy (fig. 4.5.2a), the deformed microstructure was similar to that observed in tension at 827°C (see fig. 4.3.13d), although, unlike deformation in tension, no voids were observed during compressive creep deformation. The deformation mechanisms observed during constant-load creep deformation are similar to those observed during constant cross-head speed tensile tests at 827°C reported earlier.

4.6 Summary

The microstructure of the multi-phase alloy, Ni-20Al-30Fe, processed through a casting and hot-extrusion route, consisted of a pro-eutectic β' phase in a fine (0.5μm lamellae width) eutectic. The eutectic consisted of $\beta'+\gamma$(fcc) phases; the γ phase itself contained γ' (ordered fcc or $L1_2$-structured) precipitates. The microstructures were also examined after water quenching following annealing at 427°C, 627°C and 827°C. The microstructure of the multi-phase alloy at 427°c and 627°C was similar to the room temperature microstructure but at 827°C, the γ' dissolved. The alloy Ni-12Al-40Fe, which was of similar composition to the eutectic γ/γ' phase, while exhibiting a γ/γ' microstructure from room temperature to 627°C, also exhibited a $\beta'+\gamma/\gamma'$ microstructure at 827°C instead of the $\beta'+\gamma$ microstructure expected from the phase diagram. The γ' precipitates were observed to coarsen with increasing temperatures. The β' alloy, Ni-30Al-20Fe, which was of similar composition to the pro-eutectic and eutectic β' phases, exhibited an equiaxed microstructure at room temperature with a thin (~10nm), discontinuous iron-rich grain boundary film. At 627°C, both γ/γ' and γ precipitates were observed instead of only γ as predicted by the phase diagram. At 827°C, however, the microstructure was again two-phase $\beta'+\gamma$, which was consistent with the phase diagram.

When tested in tension at room temperature, Ni-20Al-30Fe exhibited up to 20% elongation and a yield strength up to 850 MPa. Examination of polished longitudinal specimens and TEM in-situ straining experiments suggested both crack stopping action by the γ/γ' phase and deformation transfer across the β'-γ/γ' interfaces to be important factors contributing to the ductility of the alloy. In contrast, the alloy Ni-12Al-40Fe, exhibited 28% tensile elongation and a yield strength of 507 MPa; the alloy deformed by <110> slip. Finally, the β' alloy, Ni-30Al-20Fe, exhibited a yield stress of ~800 MPa but up to 6% tensile elongation.

At elevated test temperatures (427°C, 627°C and 827°C), the multi-phase alloy exhibited increased ductility, reaching an elongation in excess of 70% at 827°C without necking or fracture. The γ/γ' phase, however, showed greatly reduced ductility with increasing temperature and was brittle at 627°C and 827°C. In contrast, the β' phase demonstrated increased ductility with increasing test temperatures. Thus, whilst at room temperature the γ/γ' phase improved the ductility of the $\beta' + \gamma/\gamma'$ aggregate, at elevated temperatures the β' phase alleviated the brittleness of the γ/γ' phase, thereby preventing any embrittlement of the multi-phase alloy over the temperature range 27-827°C. Also, whilst the β' phase improved the room temperature strength of the multi-phase alloy, at elevated temperatures where the β' phase is known to be weak, the γ/γ' phase improved the strength of the multi-phase alloy up to 627°C, beyond which the strength deteriorated due to disordering and lack of anomalous strengthening in the γ/γ' component.

The differences in the scale of the microstructures between the boron-doped and undoped multiphase alloys prevented a rigorous comparison of the influence of boron on the mechanical properties. The limited microstructural analysis and mechanical testing of boron-doped alloys, however, suggested that microalloying did not significantly change the mechanical behavior of the multi-phase alloy.

CHAPTER 5

ANNEALING EFFECTS ON ROOM TEMPERATURE MICROSTRUCTURE AND MECHANICAL PROPERTIES

In this chapter, the effect of annealing in the temperature range 27°C to 1200°C on the room temperature mechanical properties are described. These experiments were undertaken in order to explain the differences in the mechanical properties of the multi-phase alloy Ni-20Al-30Fe and the β' alloy Ni-30Al-20Fe after different extrusions. Since the first extrusions were sand-cooled following extrusion while the second extrusions were air-cooled, the mechanical properties of the undoped and boron-doped multi-phase alloys and alloys similar to its constituent phases, were examined in an annealed state so as to detect any difference from the as-extruded state. Samples from the double-extruded multi-phase and β' alloys and the single-extruded boron-doped multi-phase alloy and γ/γ' alloy, were annealed at different temperatures for a constant time of ~200 min and water quenched. Room temperature hardness and tensile tests were performed on these annealed samples and their microstructures examined in a TEM.

5.1 Microstructures

Multi-phase β'±γ/γ' Ni-20Al-30Fe

The room temperature microstructure of the double-extruded multi-phase alloy was reported earlier and the compositions of the constituent phases given in Table 4.2.1. Examination of the microstructure in a TEM indicated that the β' pro-eutectric grains were oriented close to a <111> zone axis. A strong tweed contrast was also observed in the β' grains.

Figure 5.1a is a superlattice dark-field image of the pro-eutectic β' phase in the multi-phase alloy after annealing at 500°C. A strong tweed contrast is observed and the microstructure is two-phase, that is, a dispersion of fine (~2-3 nm), disordered (β phase which appears dark under superlattice dark-field imaging) precipitates in the ordered β' matrix. Superlattice dark-field images of the γ/γ' phase (figure 5.1b), by contrast, show ordered (bright) precipitates in a disordered (dark) matrix. The size of the precipitates (~10 nm) is similar to those observed in the double-extruded state. For multi-phase alloy samples annealed at 750°C for ~200 min., some differences were observed in the microstructure from that at 500°C. Superlattice dark-field imaging of the pro-eutectic β' (figure 5.2a) and eutectic γ/γ' (figure 5.2b) phases indicated a single phase microstructure for the β' phase and a two-phase (ordered precipitates in a disordered matrix) microstructure for the γ/γ' phase. Note that the size of the ordered precipitates (~20 nm) is almost twice that of those in the double-extruded alloy. Figure 5.3a is a bright field image showing the pro-eutectic β' plus eutectic lamellae; note the negative curvature of the β' grain and the precipitates (arrowed) at the β'-β' boundary. These precipitates are thought to have precipitated during the annealing treatment. Figure 5.3b is a higher magnification image of the same boundary showing that the precipitates are ~1μm in diameter. Figures 5.3c is a convergent beam diffraction pattern from the second largest grain boundary precipitate. Based on the Kikuchi pattern, the grain boundary precipitate was identified to be of f.c.c symmetry and no superlattice spots were observed which indicates that the precipitate was disordered.

γ/γ' Ni-12Al-40Fe

After annealing at 500°C for 200 mins., small precipitates, typically ~100 nm in diameter, were observed at the grain boundaries, although occasionally elongated precipitates were also observed, see figure 5.4a. EDS measurements from the precipitates from regions adjacent grains indicate that the precipitates were enriched in Al. Since the Al

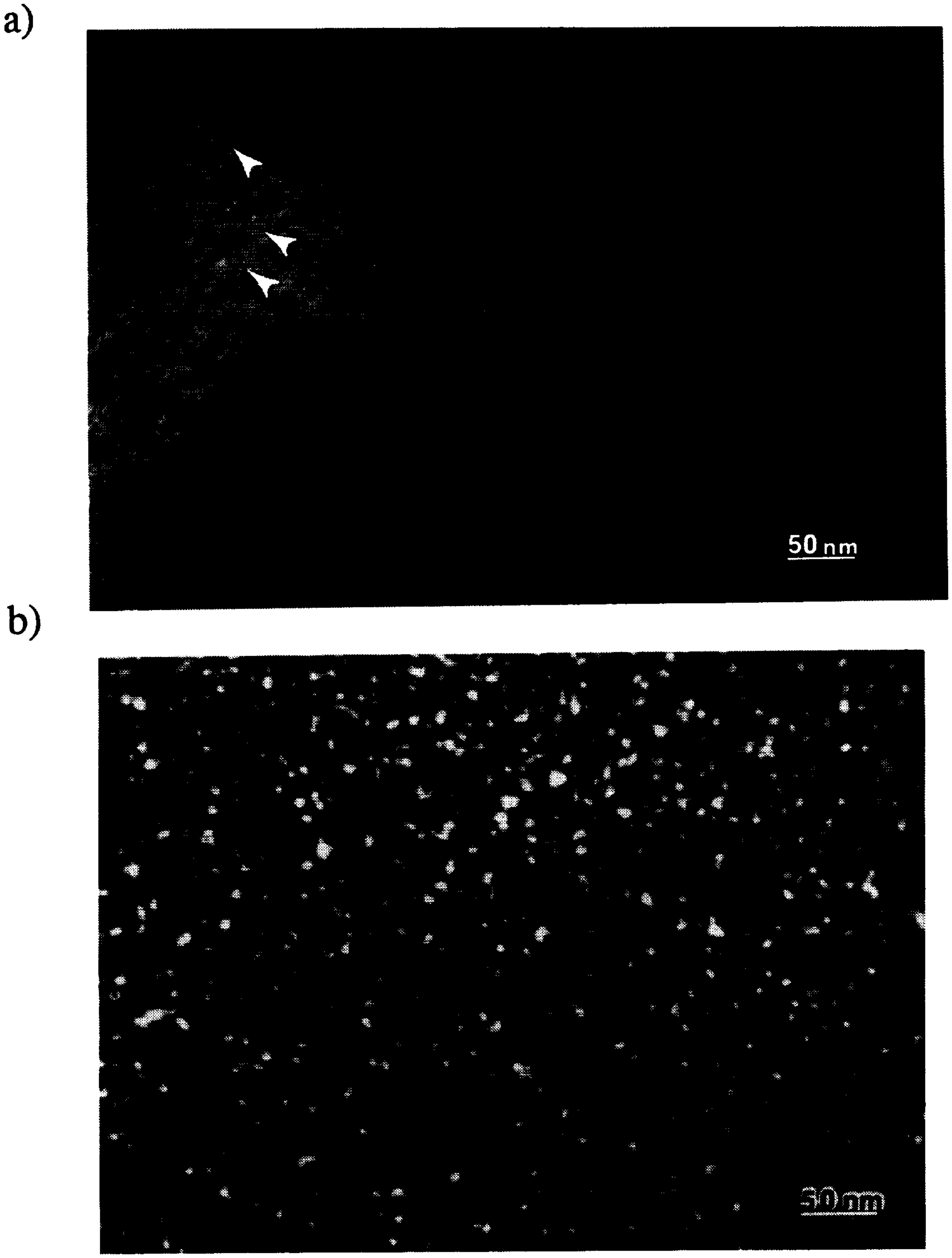

Figure 5.1 Superlattice dark-field images for (a) β' phase (b) γ/γ' phase in the multiphase alloy Ni-20Al-30Fe annealed at 500°C. The microstructure of the β' phase is two-phase (~2-3 nm disordered b.c.c precipitates in the ordered matrix) while the size of γ' precipitates is ~10nm.

ORIGINAL PAGE
BLACK AND WHITE PHOTOGRAPH

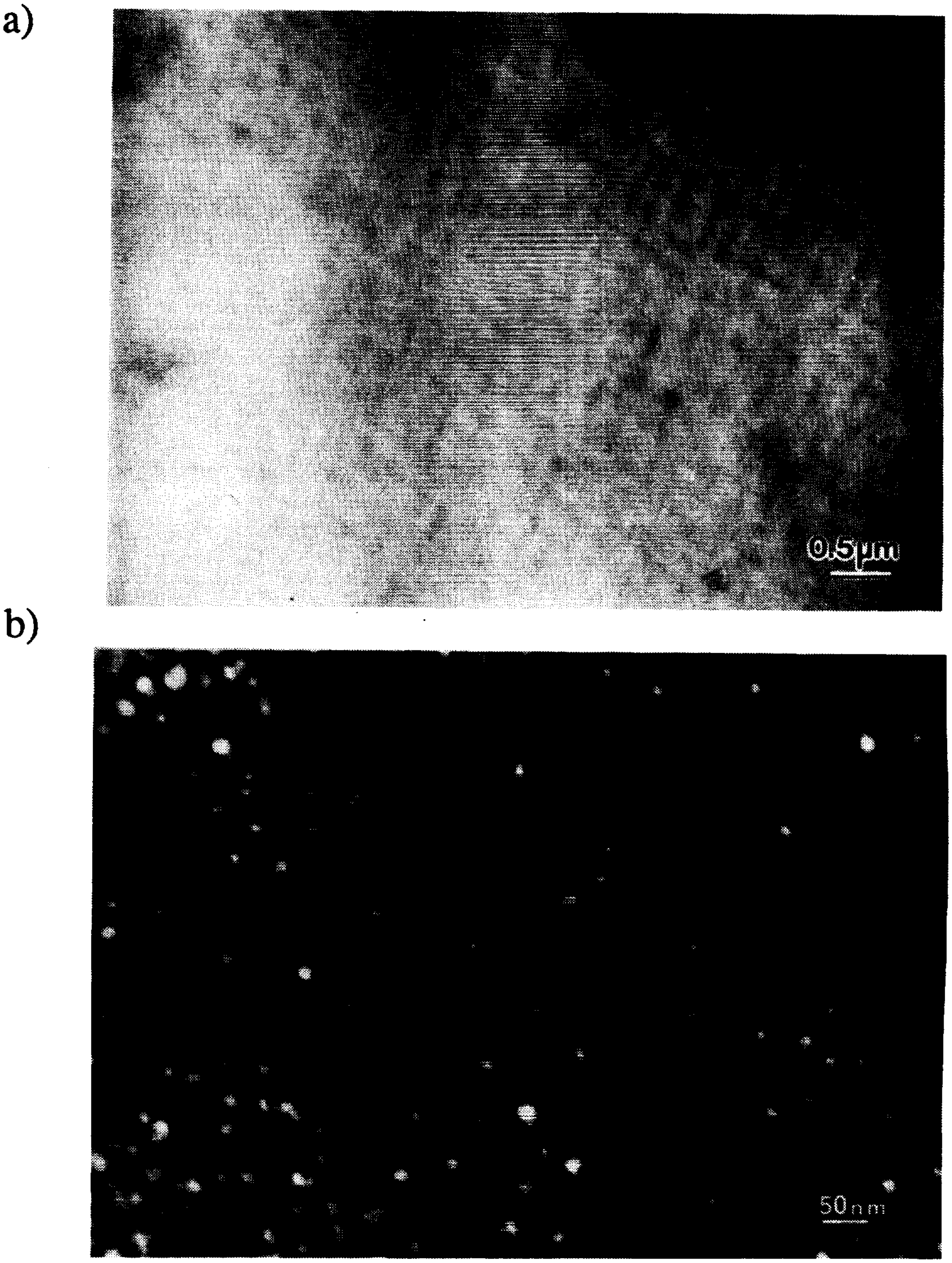

Figure 5.2 Superlattice dark-field images for (a) β' phase (b) γ/γ' phase in the multi-phase alloy Ni-20Al-30Fe annealed at 750°C. The β' phase is again single phase while the size of γ' precipitates is ~20nm.

ORIGINAL PAGE
BLACK AND WHITE PHOTOGRAPH

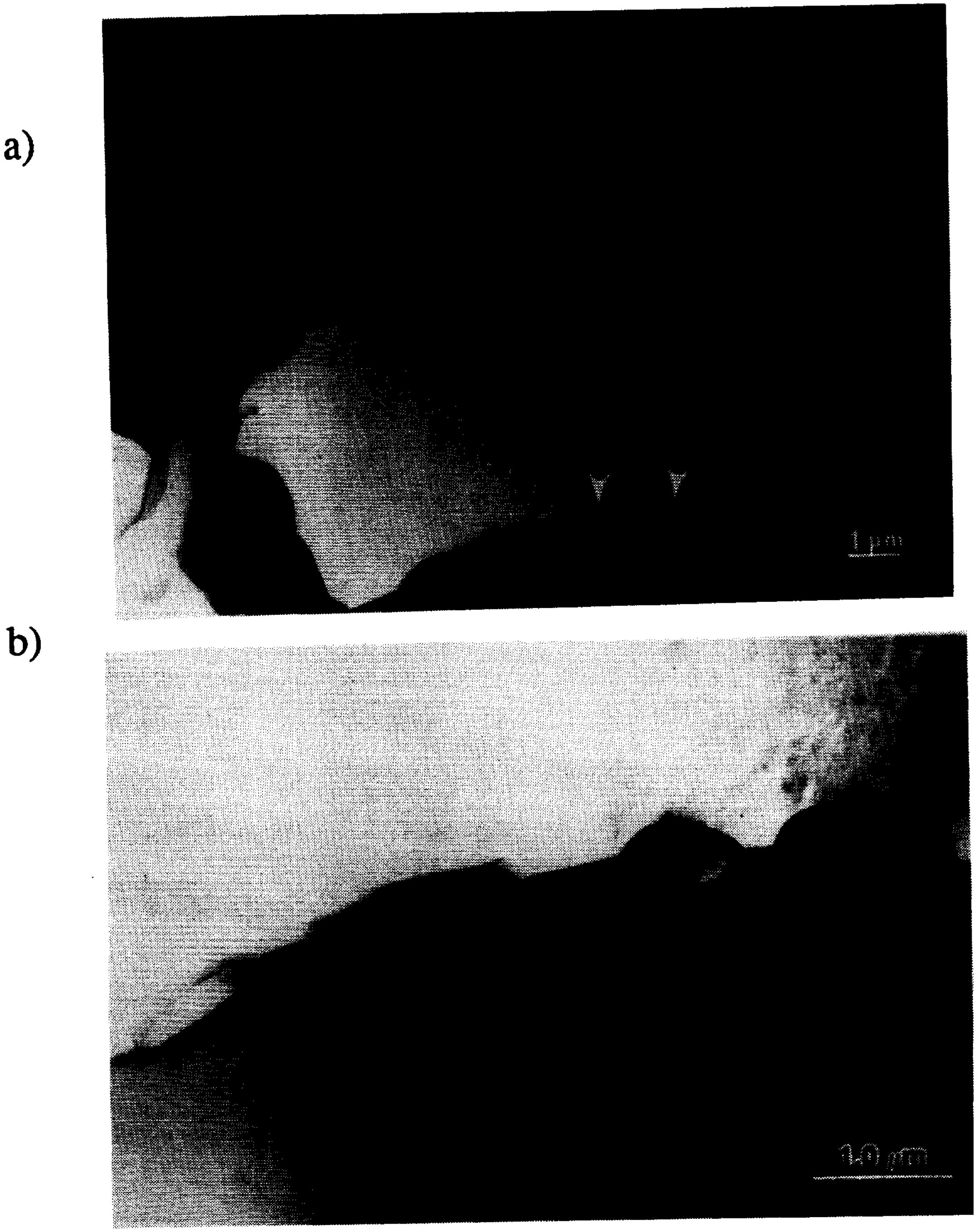

Figure 5.3 (a) Bright-field TEM micrograph of the multi-phase alloy annealed at 750°C showing β' grains with negative grain boundary curvature and precipitates (arrowed) at the β'-β' interface (b) higher magnification image of the precipitates at the β'-β' grain boundaries (c) convergent beam diffraction pattern (<112> pole) from the grain boundary precipitate showing a disordered f.c.c (γ) structure.

ORIGINAL PAGE
BLACK AND WHITE PHOTOGRAPH

c)

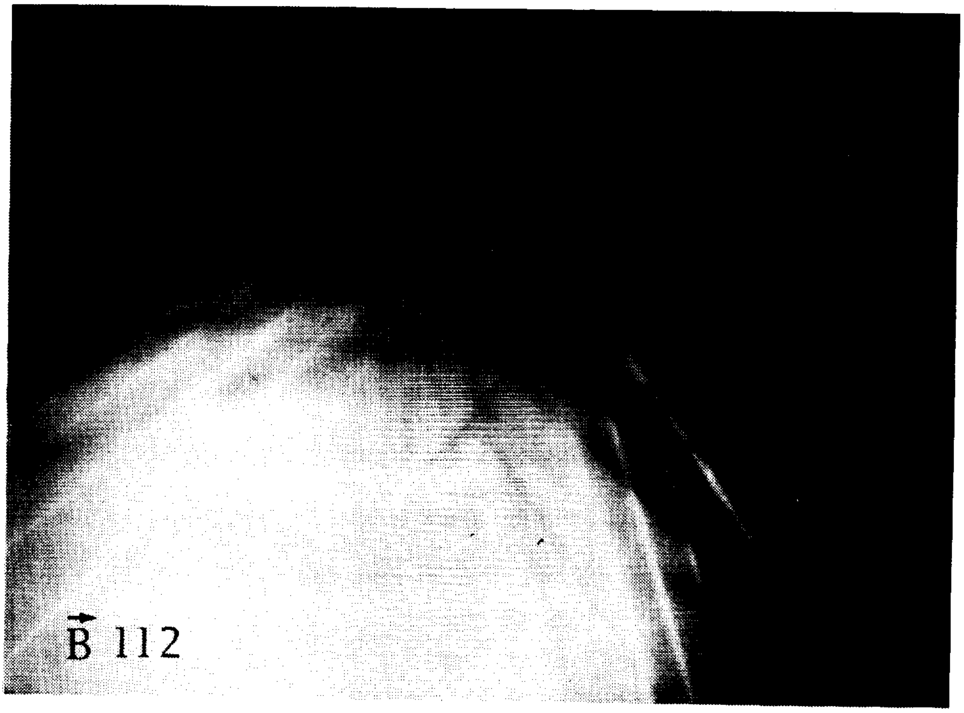

Figure 5.3 continued

ORIGINAL PAGE
BLACK AND WHITE PHOTOGRAPH

contents in the Ni-Fe-Al β' alloys are higher than the γ/γ' phases, the Al-enrichments indicative of the precipitates being β'. Convergent beam electron diffraction patterns from the grain boundary phase in figure 5.4a indicate an ordered b.c.c crystal structure, see fig. 5.4b. Superlattice dark-field imaging showed that the grains were still γ/γ', figure 5.4c, with the size of the ordered precipitates in the disordered matrix being similar (~10 nm) to those in the as-extruded state.

When annealed at 750°C for 200 min., the matrix microstructure was still γ/γ' but the size of the ordered precipitates increased to ~20 nm, see figure 5.5a. The grain boundary precipitates observed during the 500°C anneal were more frequent in the 750°C annealed state and their size had increased to ~250 nm. Occasionally, elongated grain boundary precipitates were also observed, see figure 5.5b. Convergent beam diffraction patterns and EDS measurements from the grain boundary precipitate in indicate an ordered b.c.c (B2) crystal structure (β' phase), and Al-enriched (with respect to the γ/γ' matrix) compositions.

Thus, the microstructure of Ni-12Al-40Fe following annealing at 500°C and 750°C is three phase β'+γ/γ'.

β' Ni-30Al-20Fe

As reported earlier, the microstructure of the double-extruded β' alloy consisted of a thin (~10 nm), discontinuous, disordered (f.c.c), iron-rich grain boundary phase lining the grains of the β' matrix. When annealed at 500°C for 200 mins., no grain boundary phases were observed. However, superlattice dark-field imaging showed the presence of disordered (dark) precipitates in an ordered (bright) β' matrix, similar to that shown in fig. 1a. The microstructure was similar (although somewhat coarser) after a long time (250 hours) anneal at 500°C. Figure 5.6a is a superlattice dark-field image of the alloy after the long time annealing treatment showing ~10 nm disordered (dark) precipitates in the ordered β' matrix. No extra reflections were observed in the SAD patterns, figure 5.6b, indicating

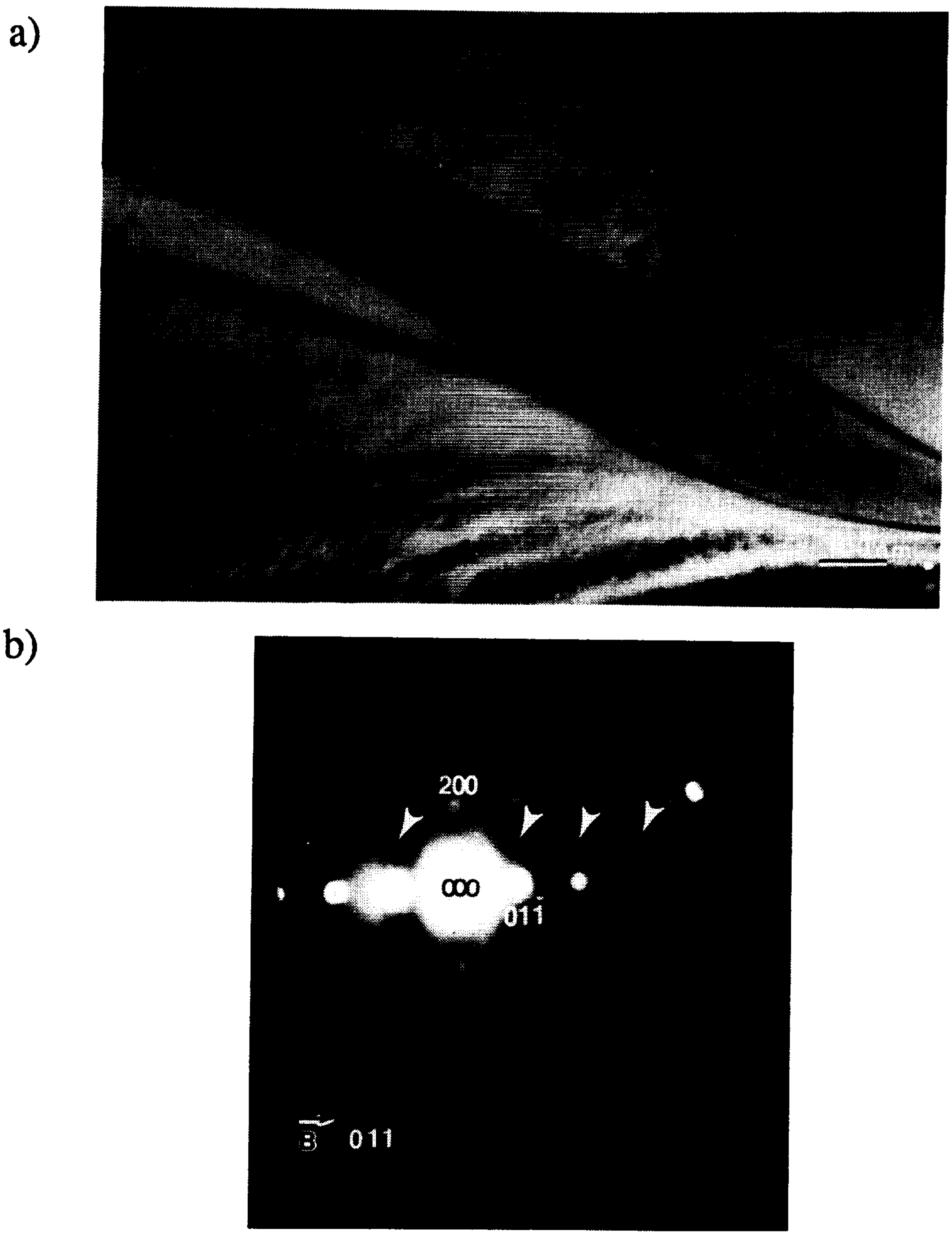

Figure 5.4 TEM micrographs for the γ/γ' alloy Ni-12Al-40Fe annealed at 500°C (a) bright field micrograph showing an elongated grain boundary phase (b) convergent beam diffraction pattern from the grain boundary phase indicates an ordered b.c.c (β') structure (c) superlattice dark field images show the matrix microstructure to be two-phase γ/γ' with the size of the γ' precipitates being ~10nm.

ORIGINAL PAGE
BLACK AND WHITE PHOTOGRAPH

c)

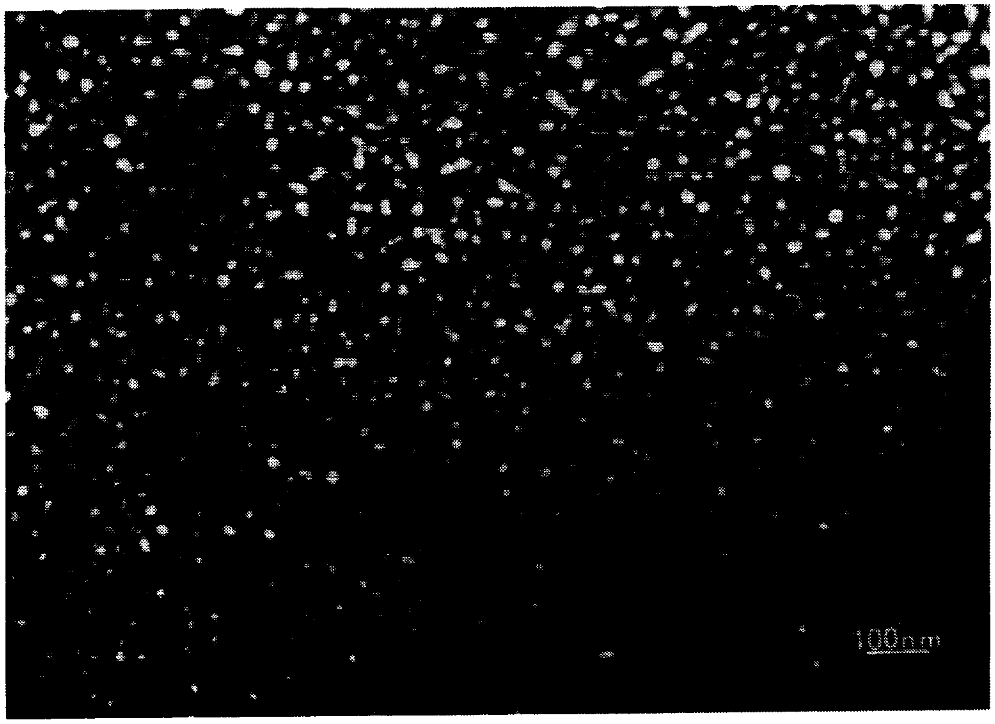

Figure 5.4 continued

ORIGINAL PAGE
BLACK AND WHITE PHOTOGRAPH

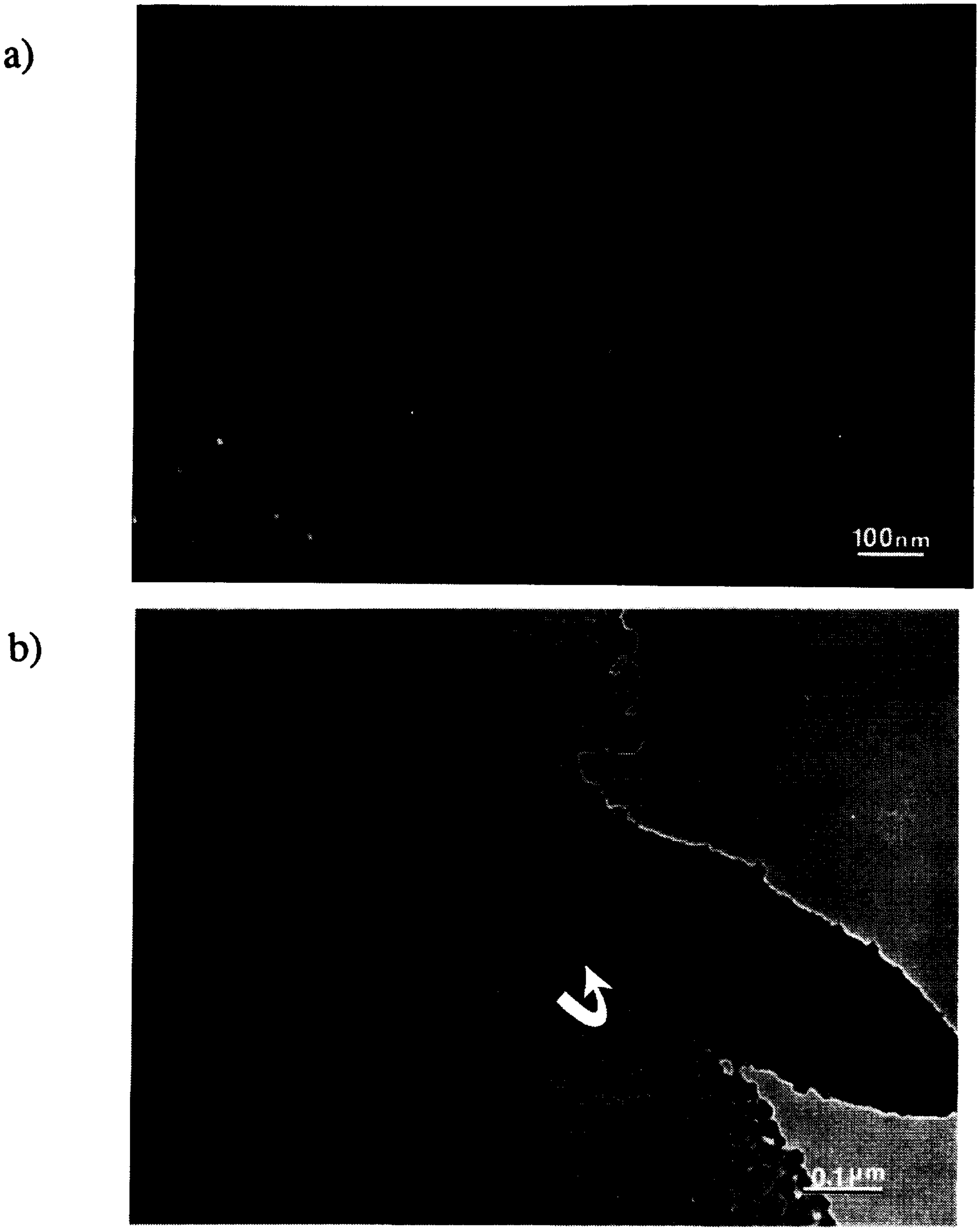

Figure 5.5 TEM micrographs for the γ/γ' alloy Ni-12Al-40Fe annealed at 750°C for 200 min. (a) superlattice dark field images show a two-phase γ/γ' microstructure for the matrix with the size of the ordered γ' precipitates being ~20nm (b) grain boundary phases were observed which were identified to be β', similar to the microstructure at 500°C.

ORIGINAL PAGE
BLACK AND WHITE PHOTOGRAPH

that the precipitates were b.c.c (α-Fe), rather than f.c.c (γ-Fe) structured. Despite the precipitation of α-Fe in β', the matrix composition as measured by EDS was similar to the nominal composition indicating that no gross redistribution of constituent elements occured during the precipitation. The low x-ray count rate with a small EDS probe, required for the precipitates, prevented measurement of the precipitate composition.

The degree of long range order was measured for as-rapidly solidified (powder made by inert gas atomization techniques was kindly supplied by Dr. M.V. Nathal at NASA Lewis) and annealed (500°C) powders using CuK_α and CuK_β radiation, a step size of 0.032° (2-theta) and a count time of 200sec. The intensities of (100) superlattice and (200) fundamental peaks were measured and the long range order parameter (LRO) was proportional to the ratio of superlattice intensity to the fundamental. Note that this ratio is independent of any effect of texture on diffracted intensities since the {100} and {200} planes are parallel. The results indicated that annealing at 500°C does not change the LRO significantly. The results and diffractometer scans are presented in APPENDIX II.

By contrast, when aged at 750°C for 200 min., superlattice dark-field imaging indicated the alloy to be single phase. However, a thin (~100 nm) grain boundary phase was observed, see figure 5.7a, which was found to be f.c.c (note the lack of superlattice reflections in expected (arrowed) positions in the convergent beam diffraction pattern, figure 5.7b). EDS measurements indicated that the phase was iron-rich with respect to the matrix, similar to that shown in figure 4.2.7. Thus, the microstructure following aging at 750°C was β'+γ-Fe, similar to the microstructure observed in air-cooled alloys, indicating that the air-cooling from 1000°C (second extrusion) mostly produces a room temperature microstructure similar to that produced by aging and quenching from 750°C. Thus, the microstructure of the double-extruded β' alloy Ni-30Al-20Fe was α-Fe+β' when quenched after annealing at 500°C and γ-Fe+β' when quenched after annealing at 750°C.

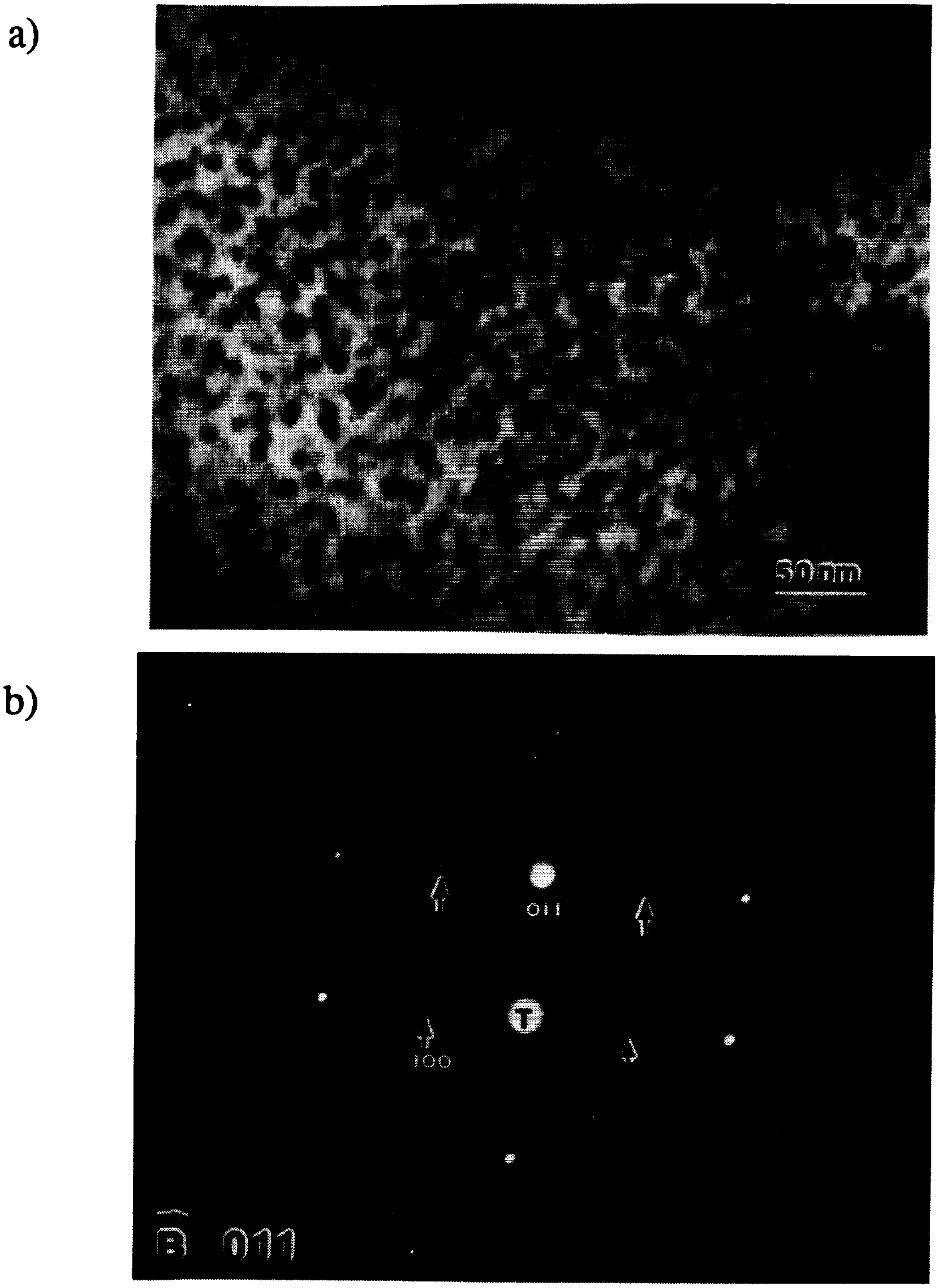

Figure 5.6 β' alloy Ni-30Al-20Fe after annealing at 500°C for 250 hours: (a) superlattice dark field images indicate a dispersion of ~10nm disordered (dark) precipitates in the ordered (bright) β' matrix (b) SAD patterns from the matrix indicate only a B2 structure indicating that the precipitates are probably b.c.c structured.

ORIGINAL PAGE
BLACK AND WHITE PHOTOGRAPH

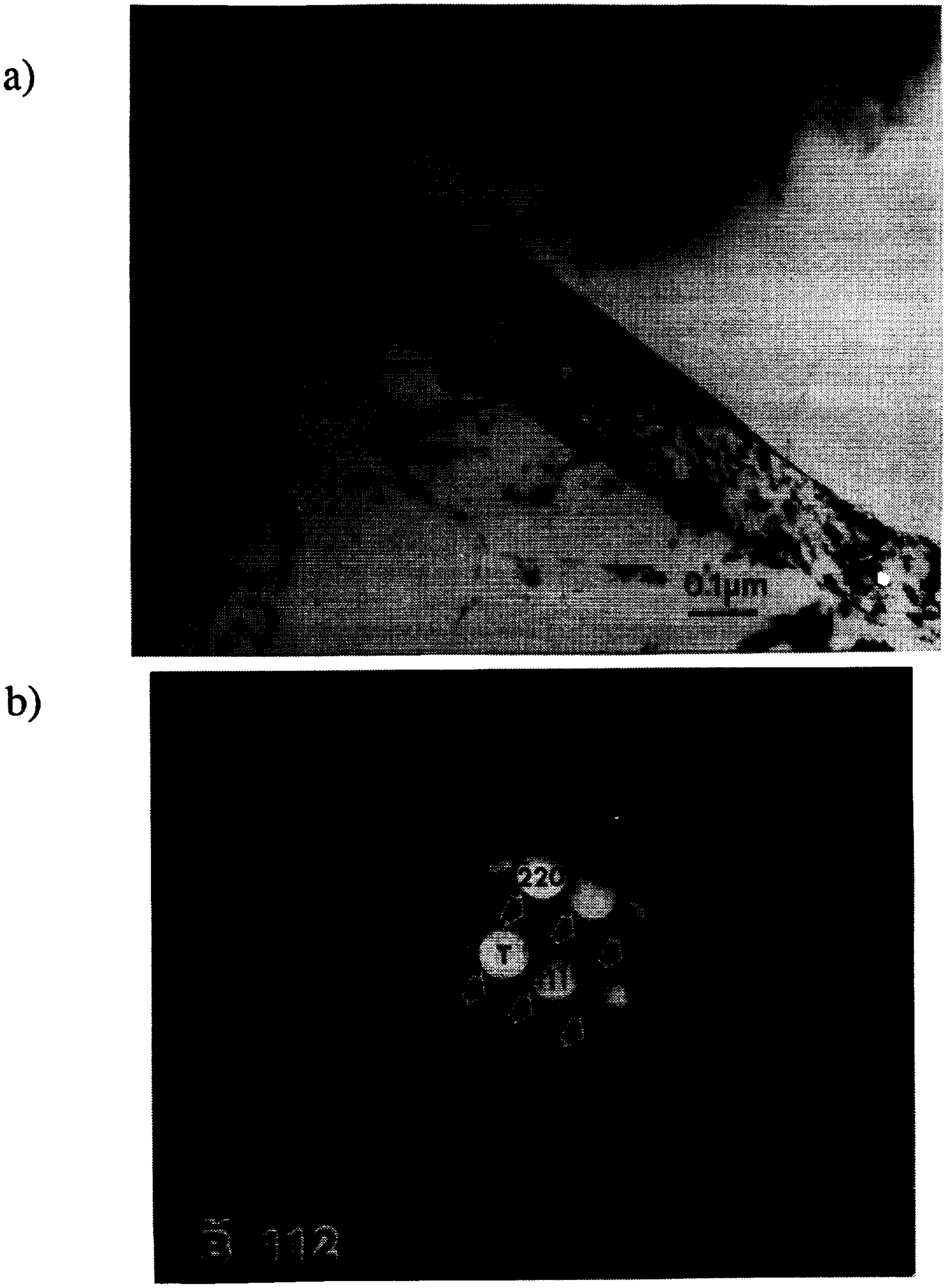

Figure 5.7 β' alloy Ni-30Al-20Fe after annealing at 750°C for ~200 min.: (a) superlattice dark field images indicate only a single phase β' matrix although a grain boundary phase (~100 nm thick) is observed (b) convergent beam diffraction pattern from the grain boundary phase indicates a γ (f.c.c) structure; note the absence of superlattice reflections.

ORIGINAL PAGE
BLACK AND WHITE PHOTOGRAPH

In summary, the microstructure of the double-extruded β' alloy was similar to that after aging at 750°C. Also, annealing at 500°C resulted in a α-Fe+β' microstructure for the β' alloy, similar to the β' constituent of the multi-phase alloy. Long term annealing results in a coarsening of the α-Fe+β' microstructure as shown in fig.5.1a and fig.5.6a, where the size of the α-Fe precipitates increased from ~2-3 nm for an annealing time of ~200 min to ~10nm for an annealing time of 250 hours. The annealing behavior of the γ/γ' alloy Ni-12Al-40Fe and the γ/γ' phase in the multi-phase alloy was, however, similar, with a slight microstructural coarsening (size of ordered precipitates increasing from ~10nm at 500°C to ~20 nm when annealed at 750°C) being observed in both cases. Precipitation of β' phase at the γ/γ' grain boundaries in the multi-phase would be unidentifiable due to the existing fine scale of the extruded microstructure.

5.2 Mechanical Behavior

Room Temperature Hardness Tests

Figures 5.8-10 show the effect of isochronal annealing (200 mins.) on the room temperature hardness of the alloys Ni-20Al-30Fe, Ni-30Al-20Fe and Ni-12Al-40Fe. Note that, while the hardness of the alloys Ni-30Al-20Fe and Ni-12Al-40Fe was examined only in a water quenched state, those of the alloy Ni-20Al-30Fe was examined in both water-quenched and furnace-cooled state (furnace cooling being investigated to compare the effect of scale of microstructure on mechanical properties in an ordered state). The hardness reported is an average of at least seven measurements and the error bars indicate a 95% confidence interval.

For the multi-phase alloy (figure 5.8), the hardness increased with increasing annealing temperatures up to 500°C, after which it declined. Interestingly, when annealed at 700°C, the hardness of the multi-phase alloy is similar in both the water-quenched and

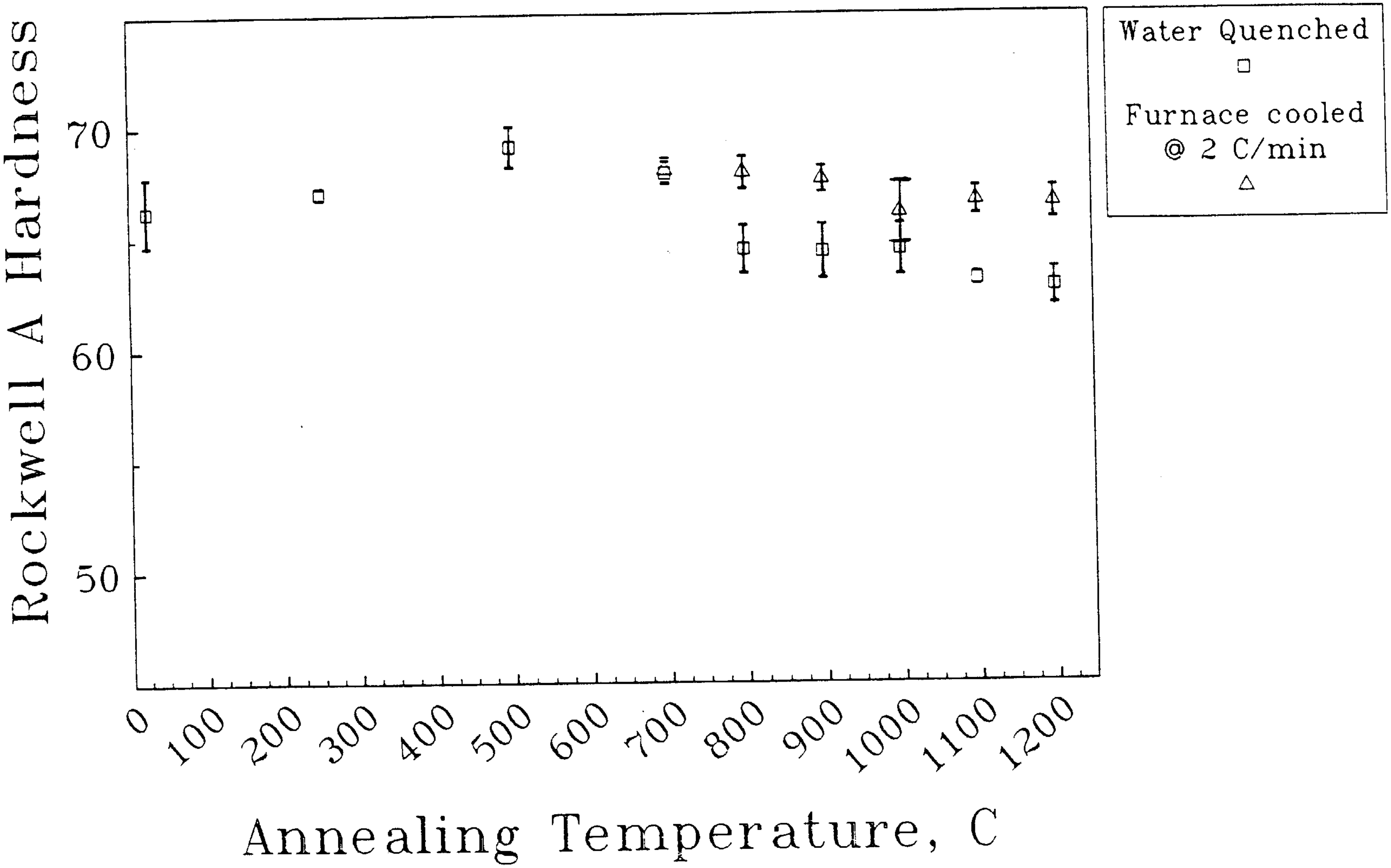

Figure 5.8 Effect of isochronal annealing on the room temperature hardness of double-extruded multi-phase alloy Ni-20Al-30Fe.

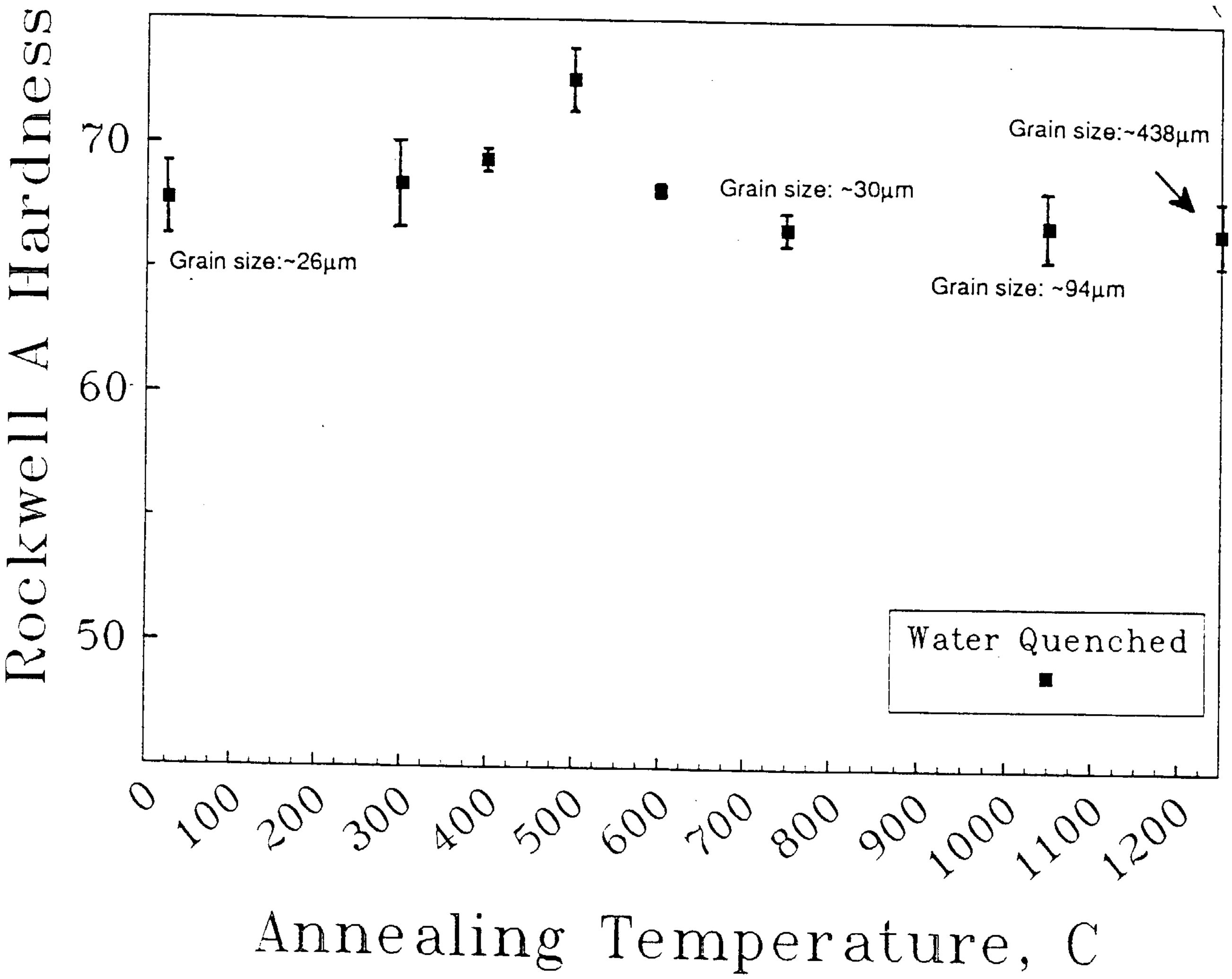

Figure 5.9 Effect of isochronal annealing on the room temperature hardness of double-extruded β' alloy Ni-30Al-20Fe.

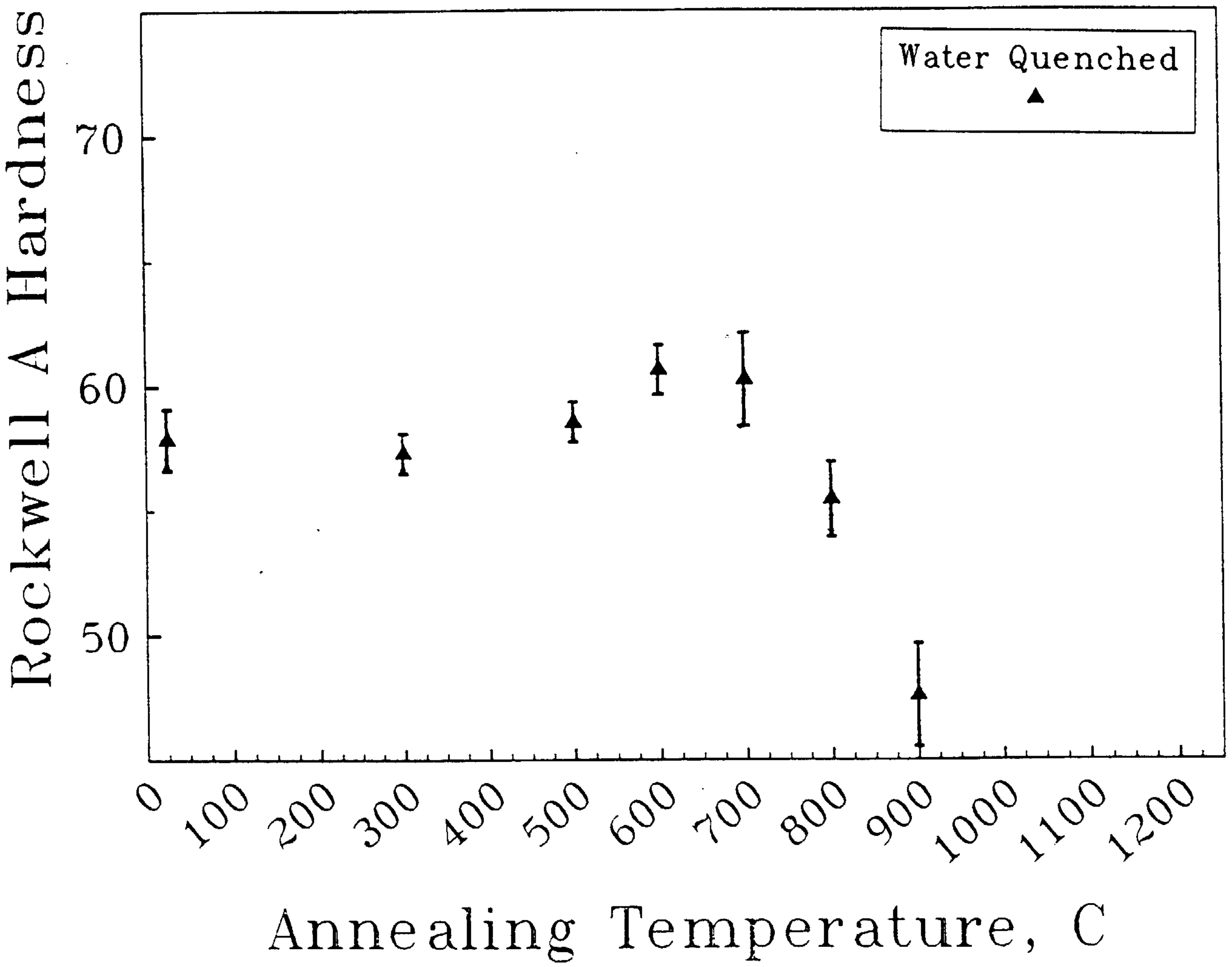

Figure 5.10 Effect of isochronal annealing on the room temperature hardness of single-extruded γ/γ alloy Ni-12Al-40Fe.

furnace-cooled states. However, for higher annealing temperatures, the hardness in the as-quenched state is lower than the furnace cooled state, which is indicative of disordered phases being retained in the microstructure at the higher cooling rates. Due to the scatter in the measured hardness values, it is not clear if the hardness of the multi-phase alloy annealed in the temperature range 800°C to 1000°C is lower than the as-extruded hardness. For annealing temperatures in the range 1100°C to 1200°C, however, the hardness is lower than that in the as-extruded state, a feature which is attributable to the coarsening of the microstructure, see figure 4.3.4.

Like the multi-phase alloy, the β' alloy (figure 5.9) also exhibits an increased room temperature hardness with increasing temperatures up to 500°C beyond which the hardness decreases to a level similar to the as-extruded (27°C) state. The increased hardness when annealed at 500°C is presumably due to the dispersion strengthening effects of α-Fe precipitates in the ordered β' matrix. The measured grain sizes for different annealing temperatures are also indicated in figure 5.9; the similar grain sizes (~ 25μm) in the as-extruded state and when annealed at 750°C indicate that the decrease in hardness in the annealing temperature range 500°C-750°C is not related to grain growth. Rather, the decrease is probably related to the precipitation of the weaker (hardness-wise), disordered γ (f.c.c) grain boundary phases [115] as observed at 627°C and 750°C (see fig. 4.3.3 and fig. 5.7) and as expected from the ternary isotherm at 750°C (fig. 2.3i).

Unlike the β' phase, the γ/γ' phase exhibits (figure 5.10) slightly increased room temperature hardnesses with increasing annealing temperatures up to 700°C, beyond which the hardness decreases sharply. The slight increase in hardness is probably due to the precipitation of the harder β' phase at the grain boundaries [115] while the sharp decrease in hardness for annealing temperatures greater than 700°C is probably related to the coarsening of the γ/γ' microstructure and the eventual dissolution of the γ' phase in the γ matrix.

From figures 5.8-10, it is clear that the annealing response of the multi-phase alloy is strongly influenced by its constituent phases. For example, the hardness peak after annealing at 500°C is probably related to the annealing characteristics of the constituent β' phase while the gentle decrease in hardness for temperatures higher than 700°C is probably related to the annealing characteristics of the constituent γ/γ' phase. Furthermore, since disordered alloys are usually weaker than ordered alloys (e.g. FeCo, Ni_3Fe etc. [116-117]), the difference in hardness of the multi-phase alloy in the water-quenched and the furnace cooled state (note that while water quenching is likely to retain a disordered microstructure, furnace cooling will likely result in re-ordering of the microstructure) is indicative of a disordered constituent in the microstructure. Since the microstructure at 827°C was shown (figure 4.2.9) to be $\beta'+\gamma$, while that at lower temperatures to be $\beta'+\gamma/\gamma'$, the disordered γ phase possibly results from the dissolution/disordering of the ordered γ' precipitates above 700°C. Furnace cooling possibly allows re-precipitation of the ordered precipitates resulting in improved strength.

The effects of the annealing time on hardness for constant annealing at both 500°C or 750°C were also studied on water quenched samples of β' and γ/γ' phases. Figure 5.11 shows the variation in hardness for the β' phase for both temperatures. For the four annealing times shown in the figure, it is clear that the as-extruded hardness increases significantly after annealing for 11 hours at 500°C, and then increases more gradually, reaching a peak after around 125 hours, beyond which a slight decrease (although within the error bar limits) is observed. Such a decrease is probably related to the coarsening of a dispersion strengthened microstructure (increased inter-particle spacing which will decrease the stress required for dislocations to bow between the dispersoids). By contrast, the as-extruded hardness is almost similar to the annealed hardness for extended periods (125, 250 hours) at 750°C which is consistent with the fact that the as-extruded and 750°C-annealed microstructures are similar (precipitation of γ-Fe phase at the β' grain boundaries). Figure 5.12 shows the influence of similar isothermal annealing on

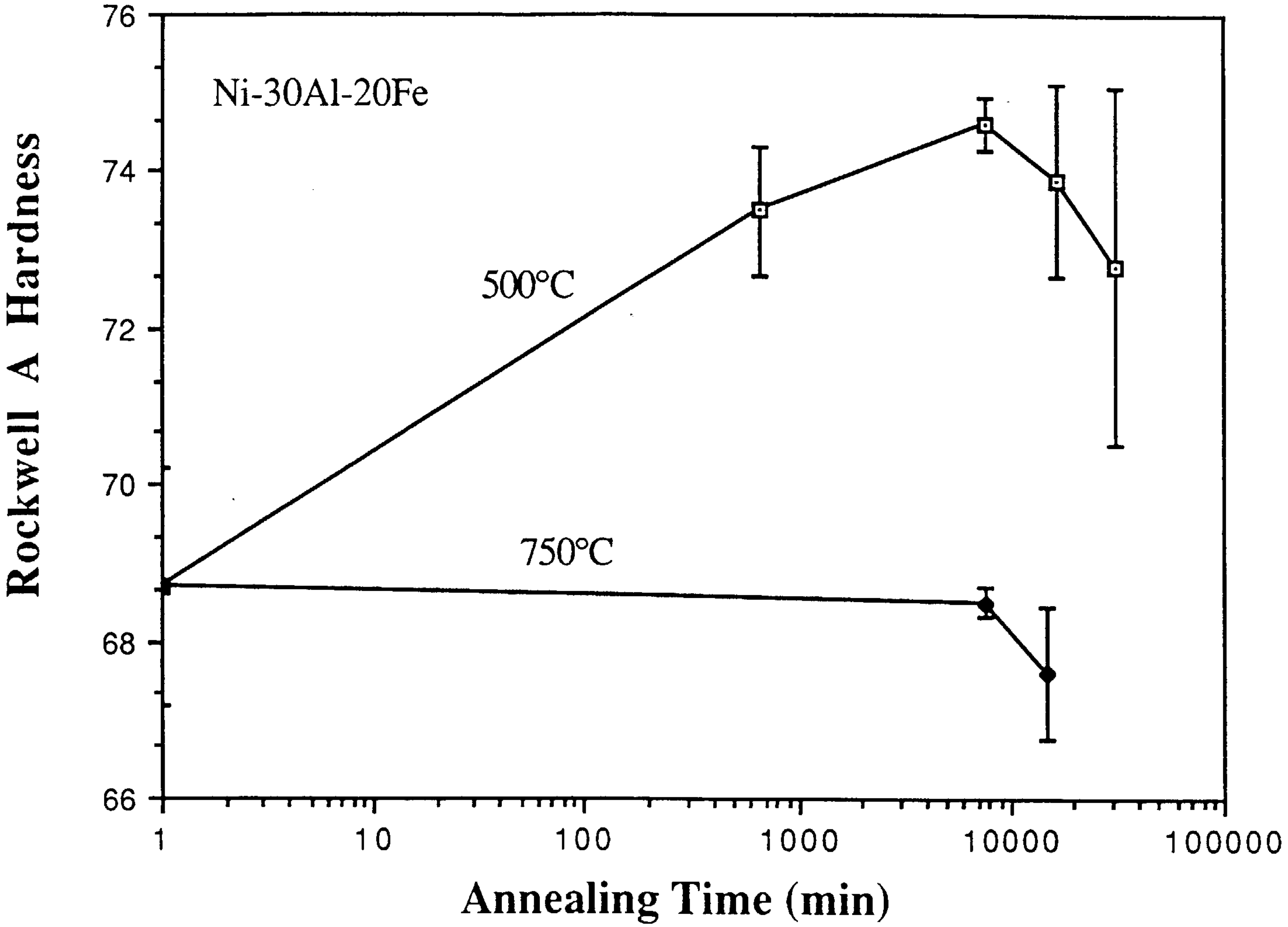

Figure 5.11 Effect of isothermal (500°C and 750°C) annealing on the room temperature hardness of the double-extruded β' alloy Ni-30Al-20Fe for long annealing times.

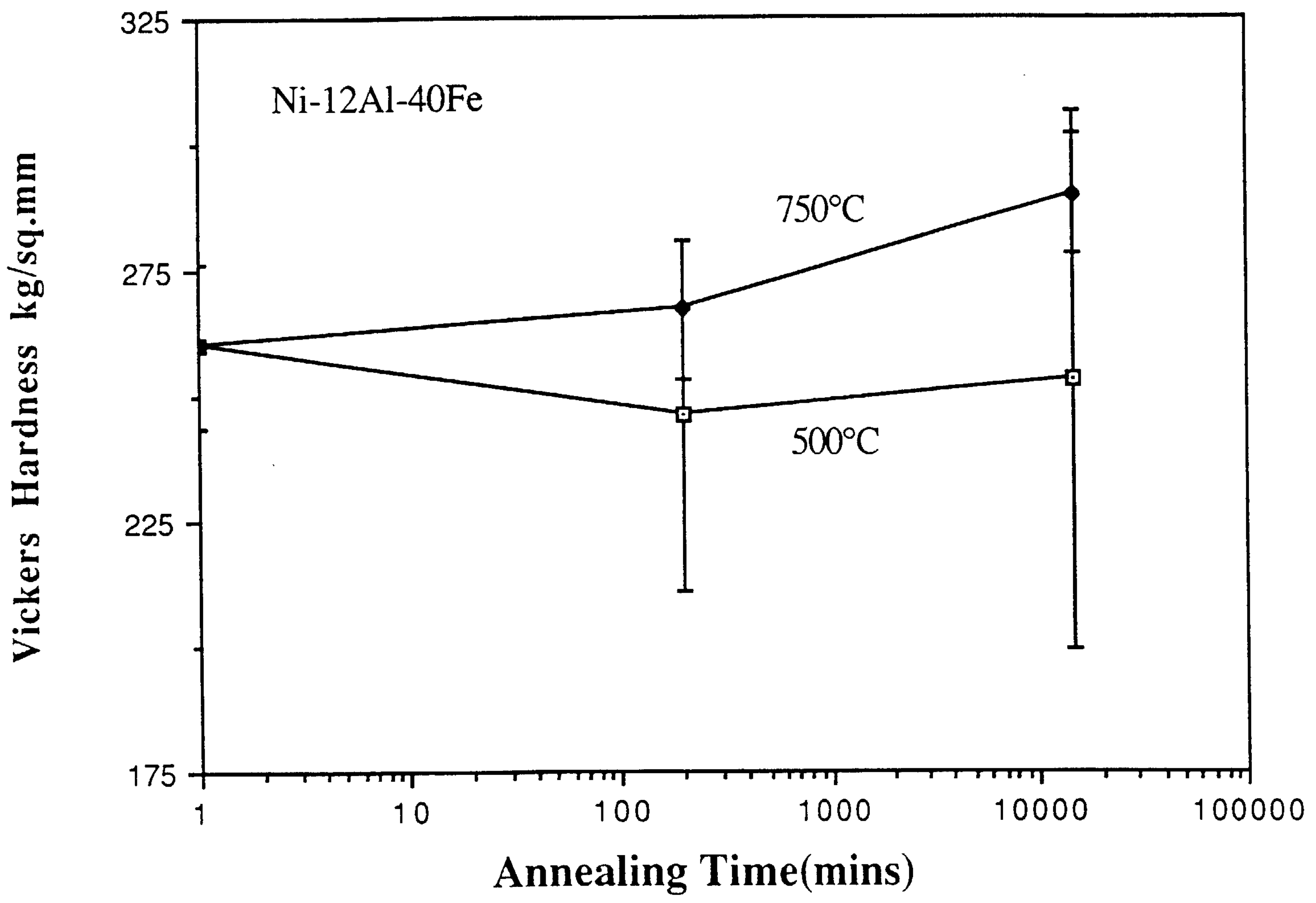

Figure 5.12 Effect of isothermal (500°C and 750°C) annealing on the room temperature hardness (Vickers) of the single-extruded γ/γ' alloy Ni-12Al-40Fe for long annealing times.

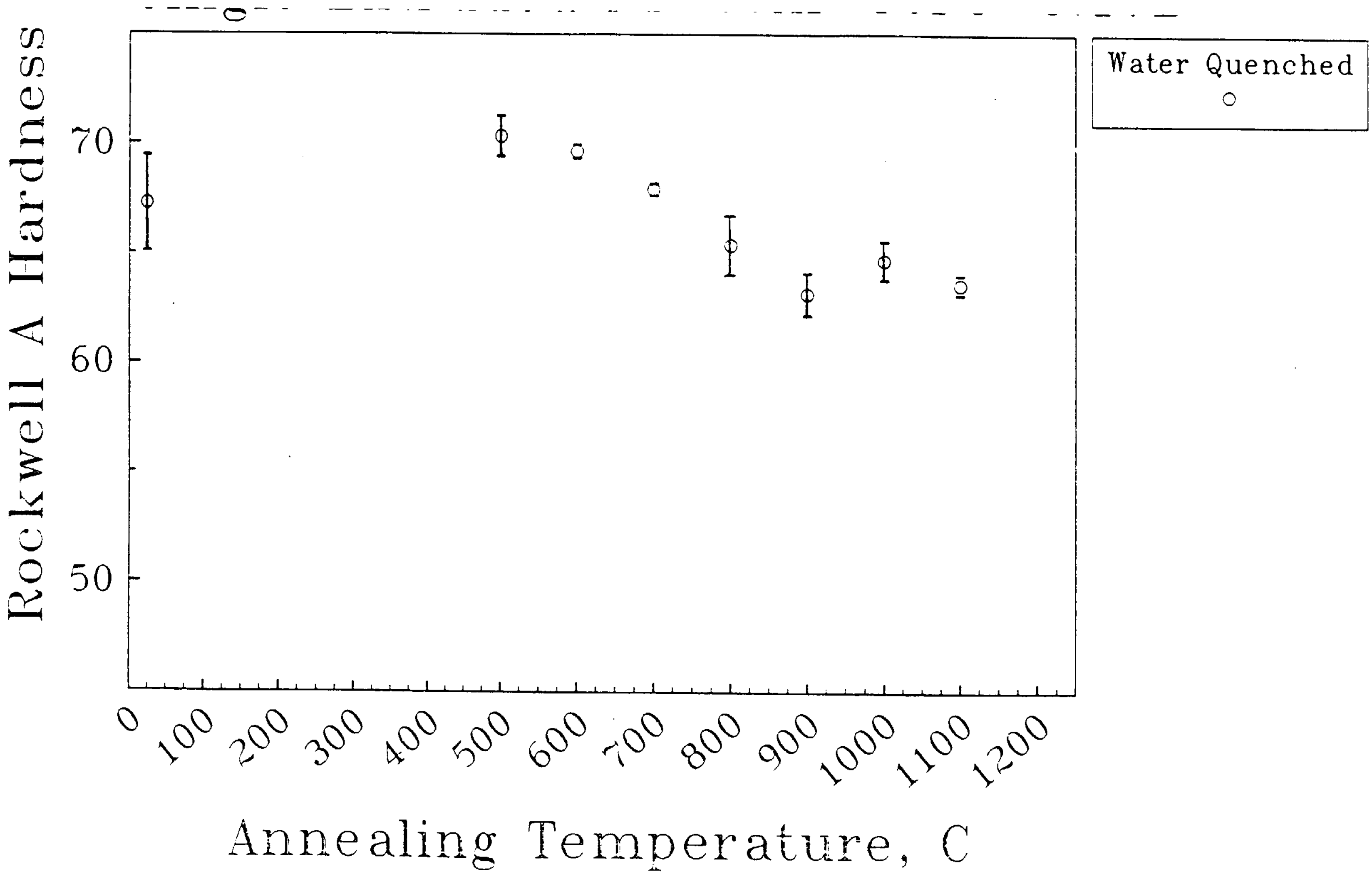

Figure 5.13 Effect of isochronal annealing on the room temperature hardness of single-extruded boron-doped multi-phase alloy Ni-20Al-30Fe-0.17B.

C-3

the γ/γ' phase, the hardness reported being the Vickers hardness (instead of Rockwell A) due to limited thickness of the specimen. When annealed at 500°C for 250 hours, the hardness is similar to the as-extruded hardness. By contrast, for the annealing temperature of 750°C, a slight increase in hardness is observed even after only 3.25 hours annealing, presumably due to the precipitation of the harder β' phase at γ/γ' grain boundaries. For an annealing time of 265 hours at 750°C, the mean microhardness of the annealed specimen is almost ~10% higher than the as-extruded material.

The boron-doped multi-phase alloy exhibits (fig. 5.13) an isochronal annealing response similar to the undoped multi-phase alloy indicating that boron does not alter the influence of annealing on mechanical strength at room temperature.

Tensile Tests

Stress-strain curves of room temperature tensile tests for each of the above alloys and for the boron-doped multi-phase alloy in the as-extruded state and after annealing at 500°C and 750°C, are shown in figures 5.14 through 5.17. The results are summarized in Table 5.1 and figure 5.18.

Figure 5.14 shows the stress-strain graphs of the multi-phase alloy in a double-extruded condition and also after annealing at 500°C, 750°C and 1300°C. The batch 1 and batch 2 stress-strain graphs being similar, only the batch 2 graphs are shown. In a single extruded condition, the multi-phase alloy exhibited a yield strength of 850 MPa, a fracture strength of 1300 MPa and ~8% elongation (see fig.4.3.1). In a double-extruded condition, however, the alloy exhibited an average yield strength of 760 MPa, an ultimate tensile strength of 1360 MPa and a plastic strain to failure of ~20%. When annealed at 500°C, the yield and tensile strength of the double-extruded alloy increased to ~850 MPa and 1400 MPa respectively while the elongation decreased to 12%. This is partly attributable to the dispersion strengthening of the β' constituent phase. When annealed at 750°C, however, the yield and fracture strength were both lower at 680 MPa and 1230 MPa respectively, while the alloy exhibited about 21% elongation. The annealing temperature of 1300°C produced a coarsened microstructure which had similar yield and fracture strengths (710 and 1200 MPa, respectively) to the 750°C annealed alloys but reduced (12%) elongation. In both the as-extruded as well as annealed condition, the alloy exhibited continuous yielding and a high work-hardening rate (higher than the γ/γ' alloys, see below). Also, while the work-hardening rates were similar in the double-extruded and 750°C annealed state, the alloy annealed at 500°C exhibited a higher work-hardening rate. Despite the high elongations, no necking was observed prior to failure.

The stress-strain curves for the double-extruded β' alloy, Ni-30Al-20Fe, are shown in figure 5.15. Samples labelled #1 were re-extruded (from the single-extruded condition) at a 6:1 area reduction ratio and tested at Dartmouth using a MTS loading frame while those labelled #2 were re-extruded at a 5:1 area reduction and tested at NASA Lewis Research center using an Instron. Although no microstructural differences were observed between the two conditions, the tensile properties are somewhat different and are attributed to better machine alignment at NASA Lewis (including better mating between grips and specimens). In the single-extruded condition, the alloy exhibited fracture prior to yield at an average stress of 770 MPa (two tests), see fig.4.3.1. In the double-extruded condition, the alloy exhibited up to 6% elongation, an average of 810 MPa yield strength and 1000 MPa fracture stress. An upper yield point followed by Lüders band formation was observed. After annealing at 500°C, however, the alloy was brittle (fracture stress of 430 MPa and 900 MPa for tests #1 and #2 respectively), the higher fracture stress again being ascribed to better test machine alignment. When annealed at 750°C, the double-extruded alloy exhibited a lower yield strength of 700 MPa, an ultimate tensile strength of 840 MPa and ~2% elongation (test lot #1). The work-hardening rate of the β' alloys was higher than the γ/γ' alloy (see below) and similar to the multi-phase alloy. Furthermore, the work-hardening rate was observed to be independent of annealing. Since the brittleness in tension precluded any measurement of yield strength of the β' alloy annealed at 500°C, the

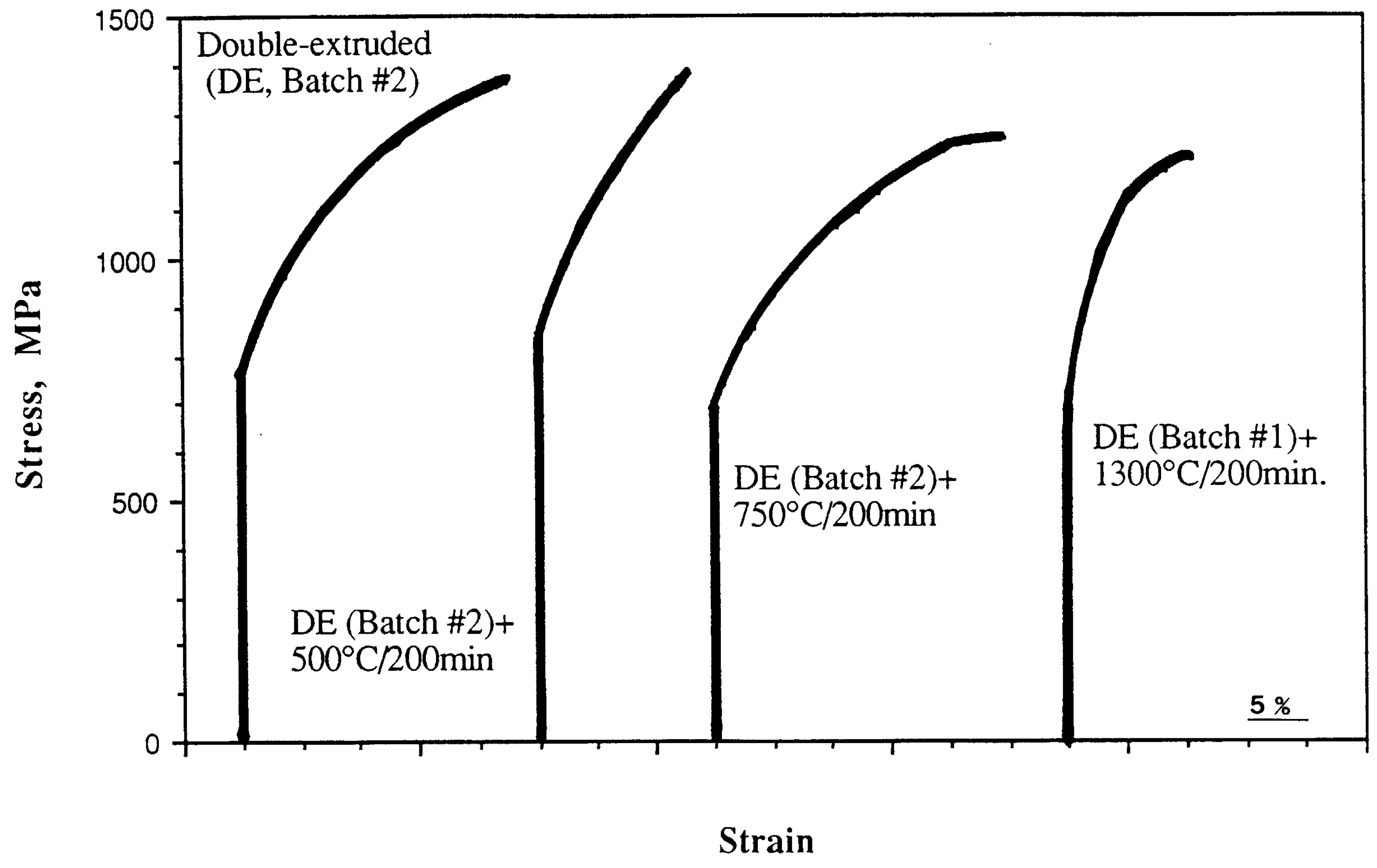

Figure 5.14 Stress-strain graphs of the double-extruded multi-phase alloys Ni-20Al-30Fe in the as-extruded state and after annealing at 500°C, 750°C and 1300°C.

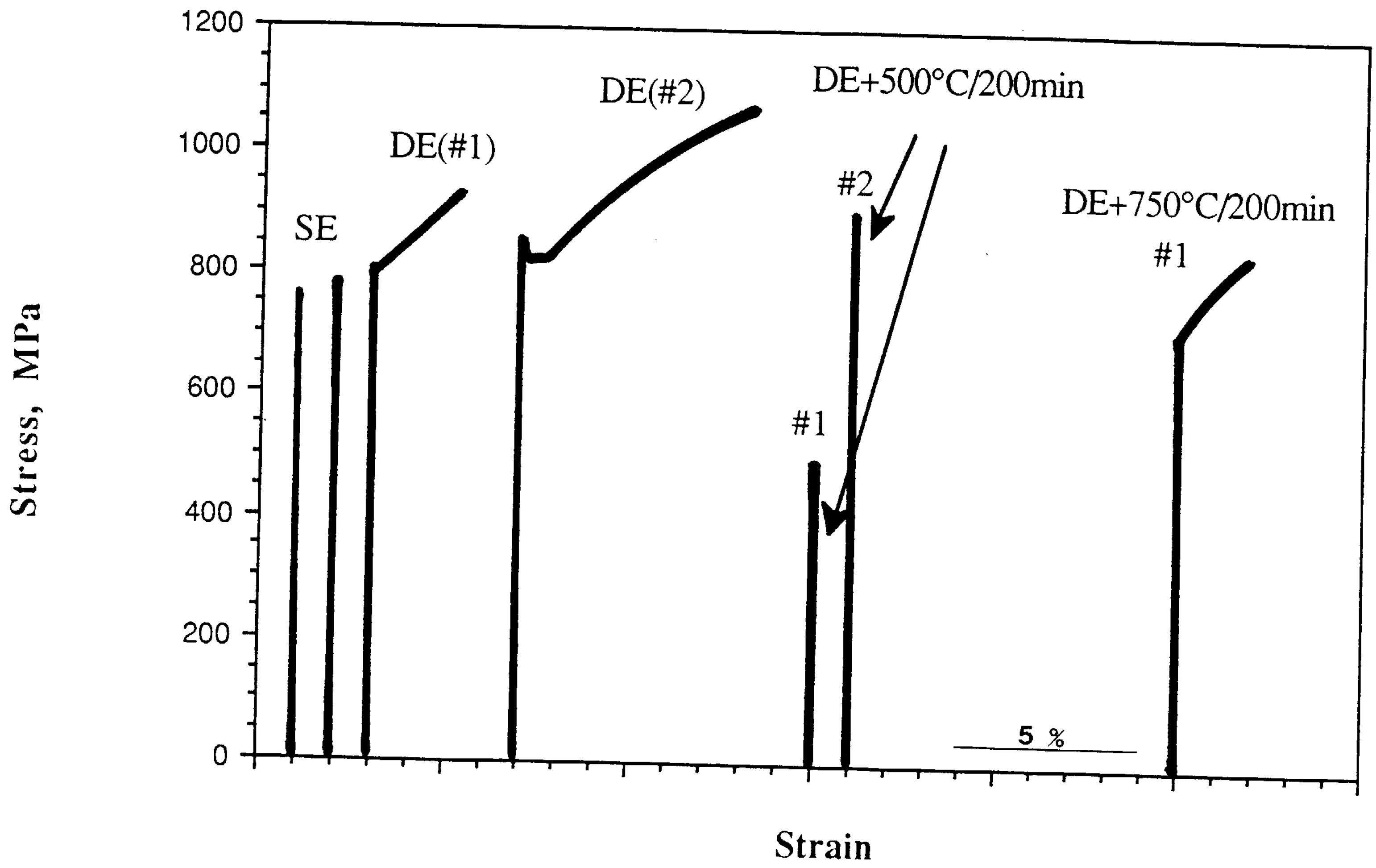

Figure 5.15 Stress-strain graphs of the double-extruded β' alloy Ni-30Al-20Fe in the as-extruded state and after annealing at 500°C and 750°C.

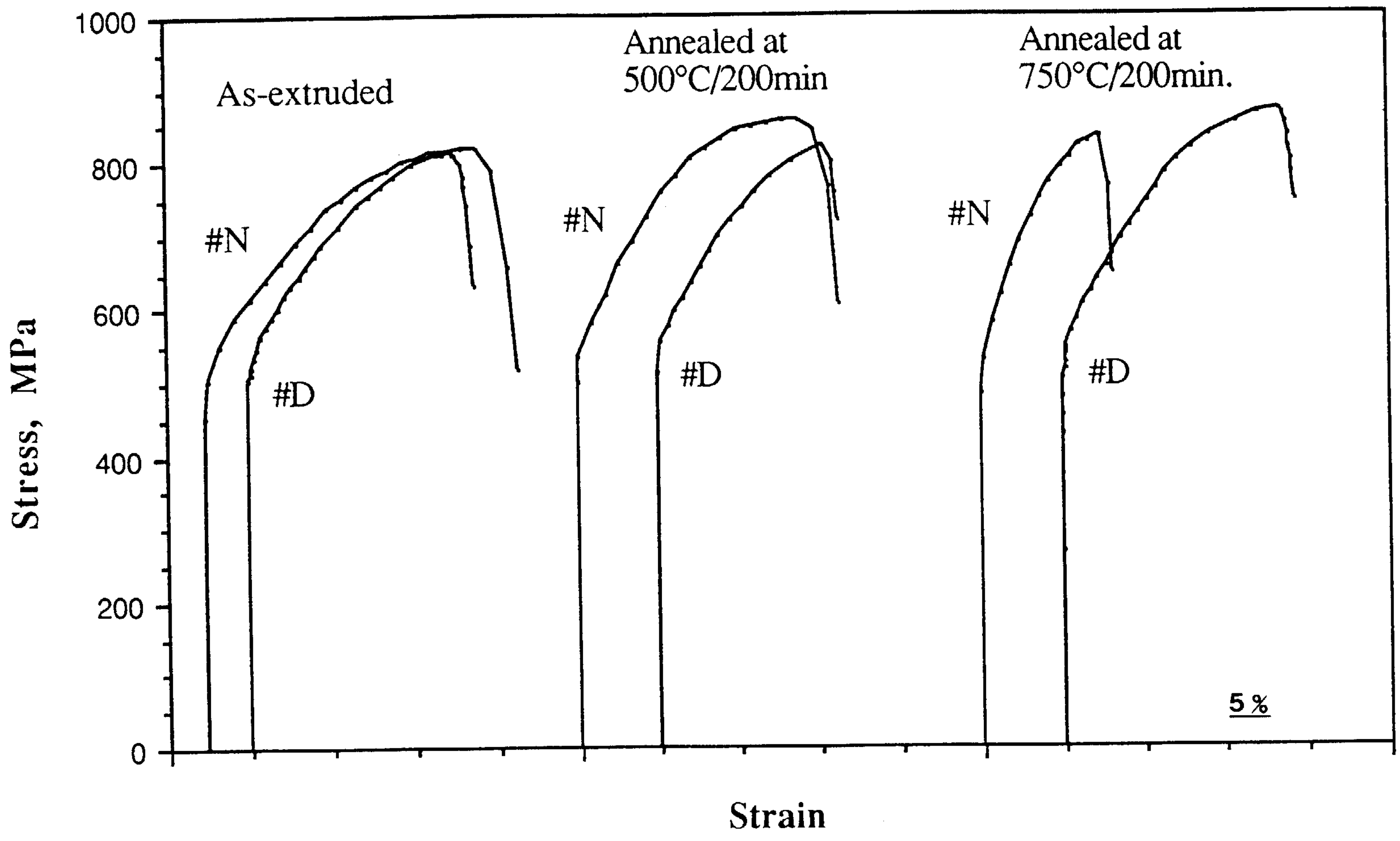

Figure 5.16 Stress-strain graphs of the single-extruded γ/γ' alloy Ni-12Al-40Fe in as-extruded, 500°C-annealed and 750°C-annealed state.

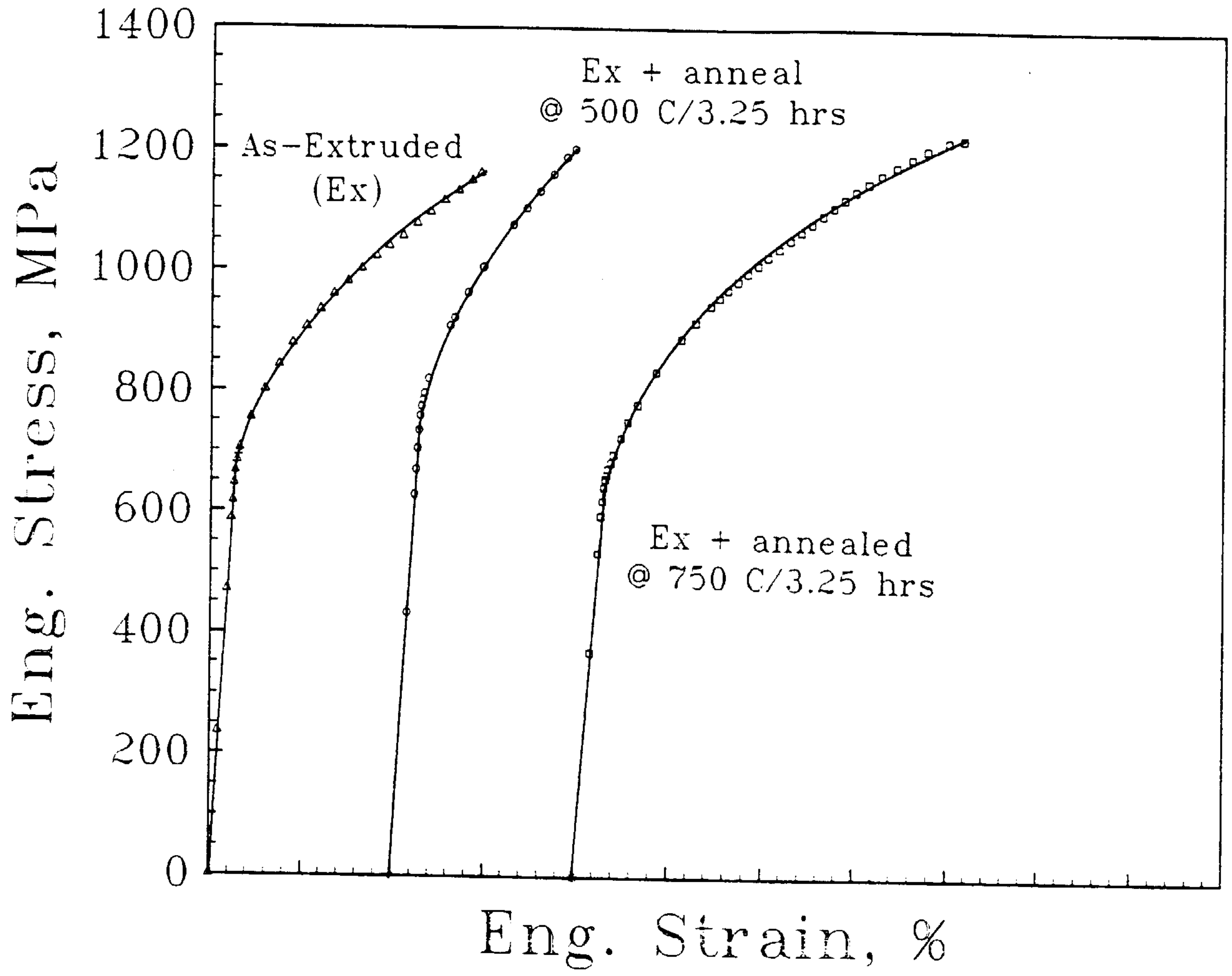

Figure 5.17 Stress-strain graphs of the single-extruded boron-doped multi-phase alloy Ni-20Al-30Fe in the as-extruded, 500°C-annealed and 750°C-annealed state.

TABLE 5.1. SUMMARY OF ANNEALING EFFECTS ON ROOM TEMPERATURE TENSILE BEHAVIOR

CONDITION	No.	YIELD STRESS (MPa)	FRACTURE STRESS (MPa)	ELONGATION (%)
Ni-20Al-30Fe ($\beta' + \gamma/\gamma'$)				
Single Extruded(SE)		850	1300	8
Double-extruded(DE)	(B#1)	760	1350	20
	(B#2)	760	1370	23
DE+500°C anneal	(B#1)	870	1400	12
	(B#2)	850	1390	13
DE+750°C anneal	(B#1)	670	1190	18
	(B#2)	695	1255	25
DE+1300°C anneal	(B#1)	710	1200	12
Ni-12Al-40Fe (γ/γ')				
Single Extruded(SE)	(D)	505	810	28
	(N)	505	820	38
SE+500°C anneal	(D)	520	820	23
	(N)	535	860	32
SE+750°C anneal	(D)	535	865	29
	(N)	530	835	25
Ni-30Al-20Fe (β')				
Single Extruded(SE)		-	780	0
		-	760	0
Double Extruded, DE	(#1)	800	930	2
	(#2)	825	1070	6
(compression x2)	(#2)	835, 840	-	-
DE+500°C anneal	(#1)	-	490	0
	(#2)	-	900	0
(compression x2)	(#2)	975, 1000	-	-
DE+750°C anneal	(#1)	700	840	2
(compression x2)	(#2)	718, 740	-	-
Ni-20Al-30Fe-0.17B ($\beta'+\gamma/\gamma'$)				
Single Extruded(SE)		700	1160	13
SE+500°C anneal		795	1200	8
SE+750°C anneal		670	1220	19

yield strength was determined in compression and found to be 1000 MPa. Also, the measurement of compressive yield stresses for double-extruded and 750°C annealed β' alloys indicated that the yield strength in compression was similar to that in tension implying the lack of any significant tension-compression asymmetry behavior. Interestingly, specimens annealed at 500°C and re-annealed at 750°C exhibit a decrease in yield strength (to ~700 MPa yield strength). Further annealing at 500°C restores the yield strength to ~1000 MPa level which is indicative of the yield strength being related to dissolution/precipitation reactions. The increased strength is thus attributable to dispersion strengthening effects of the α-Fe precipitates in the β' matrix while the decreased strength at 750°C is the result of dissolution of such α-Fe dispersoids and the precipitation of a γ grain boundary phase [115].

Figure 5.16 shows the stress-strain curves for the γ/γ' alloy, Ni-12Al-40Fe, in the as-extruded and annealed (500°C and 750°C) conditions. Unlike the β' alloy, the γ/γ' alloy exhibits continuous yielding, similar to the multi-phase alloys. Two tests were performed in each condition and the labels #D and #N refer to test specimens machined (at Dartmouth) and centerless ground (at NASA Lewis) respectively. Although test specimens from both sets were electropolished prior to testing and tested using an Instron at NASA Lewis, some differences in ductility were observed in each condition which is attributable to differences in surface conditions (high or low residual stresses) resulting from different methods of specimen preparation. The yield strengths, by contrast, were unaffected.

The as-extruded alloy exhibited an average (two tests) yield strength of 505 MPa and ultimate tensile strength of 815 MPa; elongations of 28% and 37.5% were observed for tests #D and #N respectively. When annealed at 500°C, the observed average yield strength and ultimate tensile strength were similar at 525 MPa and 840 MPa respectively; the elongations for tests #D and #N were also similar but slightly less at 23 and 32% respectively. Upon annealing at 750°C, the average yield and UTS for tests #D and #N were 530 MPa and 850 MPa respectively as were the elongations at 28% and 25%

respectively. The work-hardening rate of the γ/γ' alloy was lower than that of both the β' and multi-phase alloys. Furthermore, the work-hardening rate increased with increasing annealing temperatures. The room temperature hardness and tensile test data both suggest a slight hardening of the alloy with increasing annealing temperatures (for a fixed annealing time). The ductility data (both tests #D and #N) suggest slightly decreased elongations for samples annealed at 500°C compared to the as-extruded state. The trend, however, is less clear for samples annealed at 750°C since the #D test indicates a ductility level almost similar to the as-extruded state while the #N test indicates a ductility level even lower than the 500°C annealed specimens. The lack of any remaining extruded material prevented us from investigating this point further. The better specimen preparation and testing techniques for #N tests, the trend of gradual increase in hardness and strength with increasing annealing temperatures and the observed increasingly continuous grain boundary film of the more brittle (β') phase at 750°C, however, indicate that the test data set #N is probably more reliable. Interestingly, irrespective of heat treatment, some necking was observed prior to failure in all γ/γ' samples.

The effect of annealing on the room temperature tensile behavior of the boron-doped multi-phase alloy was also investigated and the results are shown in figure 5.17. The alloy exhibited both a lower yield strength and a lower ductility than the double-extruded undoped multi-phase alloy, presumably due to the coarser scale of the microstructure resulting from the higher extrusion temperature. The trends in the deformation behavior as a function of annealing temperature are similar to the undoped multi-phase alloys; the values for yield stress, fracture stress and elongation are listed in Table 5.1.

Figures 5.18a-c summarize the variation of yield strength, fracture strength (UTS in case of the γ/γ' alloys) and ductility of the alloys with annealing temperature. The variation of yield strength with annealing temperature is similar to the trends observed in the room temperature hardness data, fig. 18a. The variation in fracture stress (fig. 5.18b)

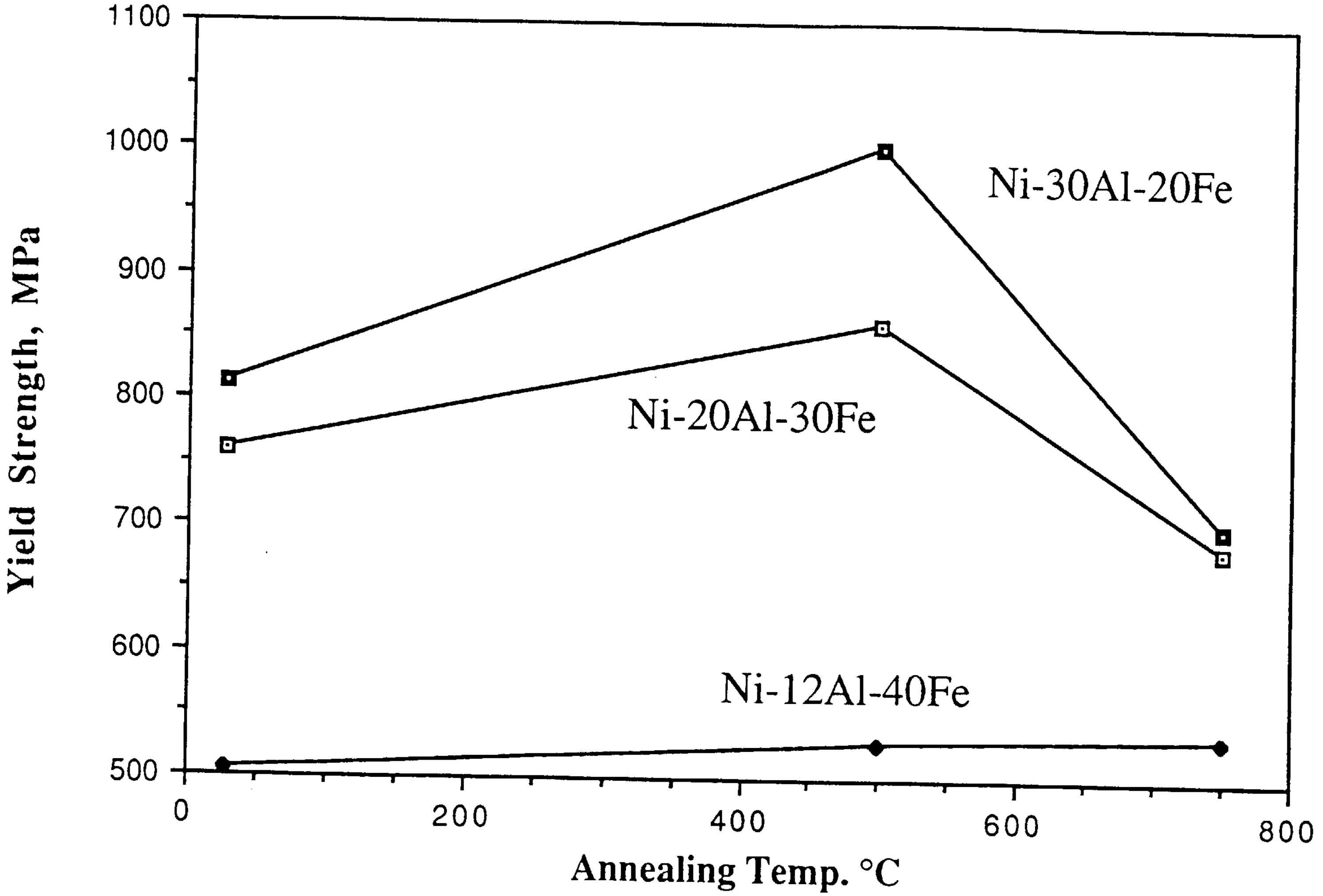

Figure 5.18a

Figure 5.18 The effect of isochronal annealing on the room temperature tensile properties of multi-phase Ni-20Al-30Fe and alloys similar to its constituent phases, β' Ni-30Al-20Fe and γ/γ' Ni-12Al-40Fe: (a) yield strength (b) fracture stress (c) elongation.

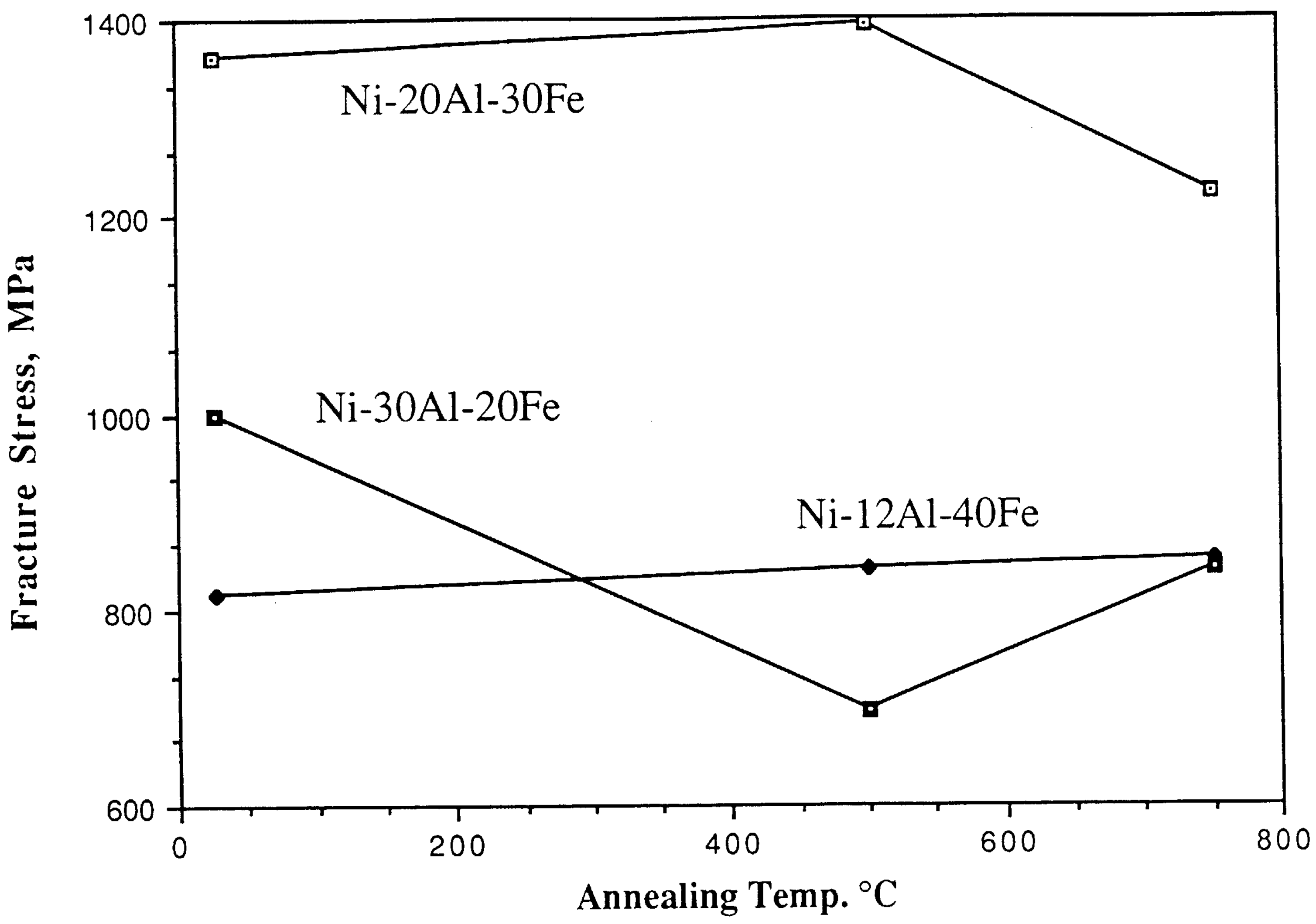

Figure 5.18b

Fig. 5.18 continued

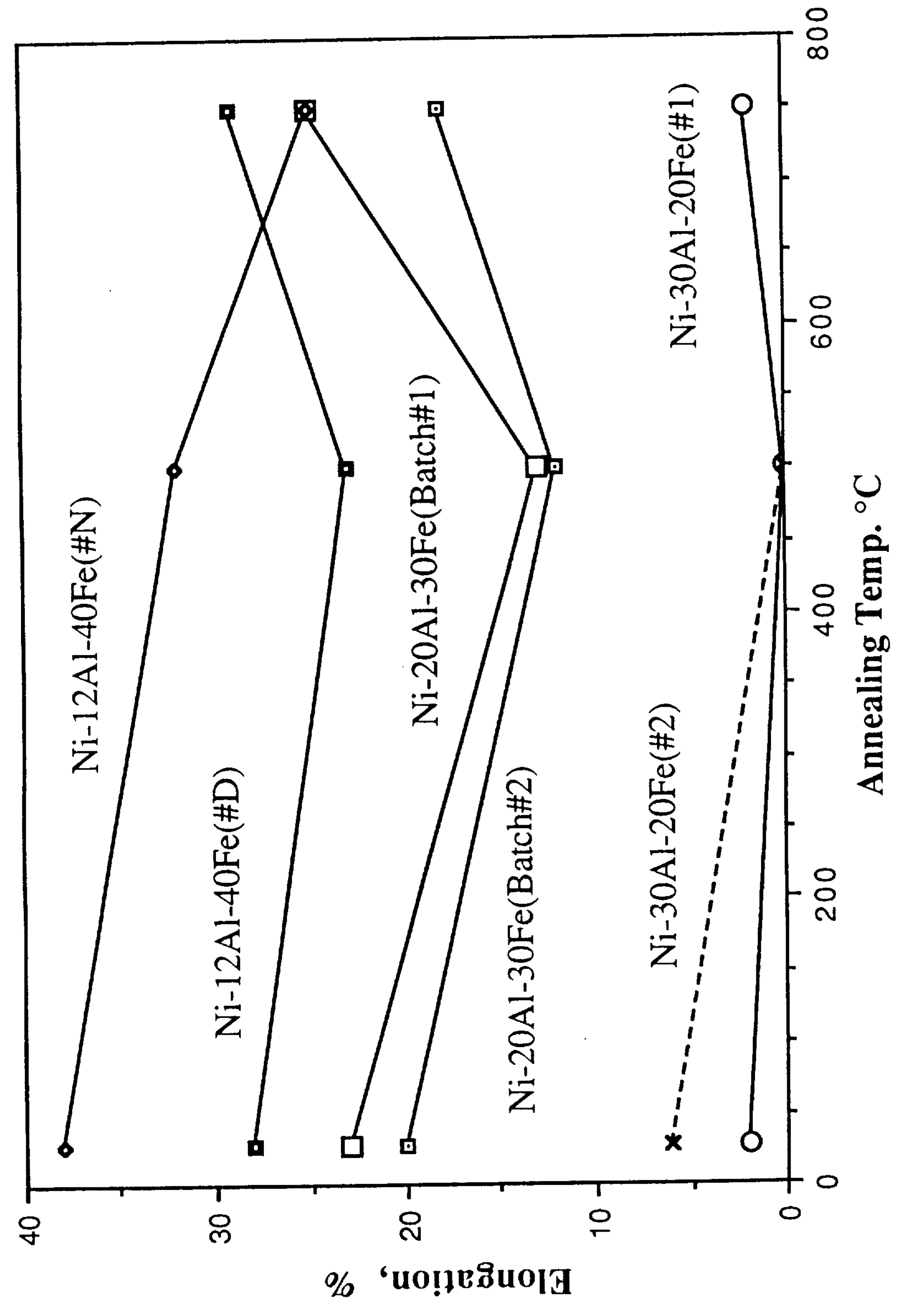

Figure 5.18c

Fig. 5.18 continued

is less clear, being influenced by the yield strength, the work-hardening rate and the ductility of the alloys. Figure 5.18c summarizes the tensile elongation for the alloys as a function of annealing temperature. A reduced ductility level (compared to the as-extruded state) is observed for all three alloys when annealed at 500°C. The reasons behind the restoration of ductility to levels similar to the as-extruded state in multi-phase alloy samples annealed at 750°C is less clear in view of the uncertainity associated with the ductility of the γ/γ' alloy. The #D test results would indicate that restoration is primarily the result of increased ductility of the γ/γ' phase when annealed at 750°C. However, assuming that the ductility of the β' alloy is similar in the as-extruded and 750°C annealed state (i.e. ~6%), it is possible that the reduced ductility in the γ/γ' alloy (test #N) is compensated for by the increased ductility (expected due to precipitation of disordered grain boundary phases) of the β' phase when annealed at 750°C. Additional tests of the γ/γ' alloy samples annealed at 750°C are required to resolve this point. Thus, the mechanical behavior of the multi-phase alloy appears to be influenced strongly by those of its constituent phases.

Fractography

The fracture surfaces of the tensile-tested specimens were examined using a scanning electron microscope (figures 5.19-22). For the multi-phase alloys (fig. 5.19), fracture surfaces of all samples except those annealed at 1300°C were similar and consisted of brittle cleavage failure in the pro-eutectic β' phase and dimple fracture in the $\beta'+\gamma/\gamma'$ eutectic. The sample annealed at 1300°C exhibited (fig.5.19d) predominantly clevage fracture due to the higher volume fraction of the β' phase. Similarly, irrespective of heat treatment, the fracture mode of the β' alloy Ni-30Al-20Fe was predominantly transgranular cleavage although some intergranular facets were also observed, see fig. 5.20. By contrast, the γ/γ' alloy, Ni-12Al-40Fe, exhibited dimple fracture and the fracture mode was insensitive to heat treatment, see fig. 5.21.

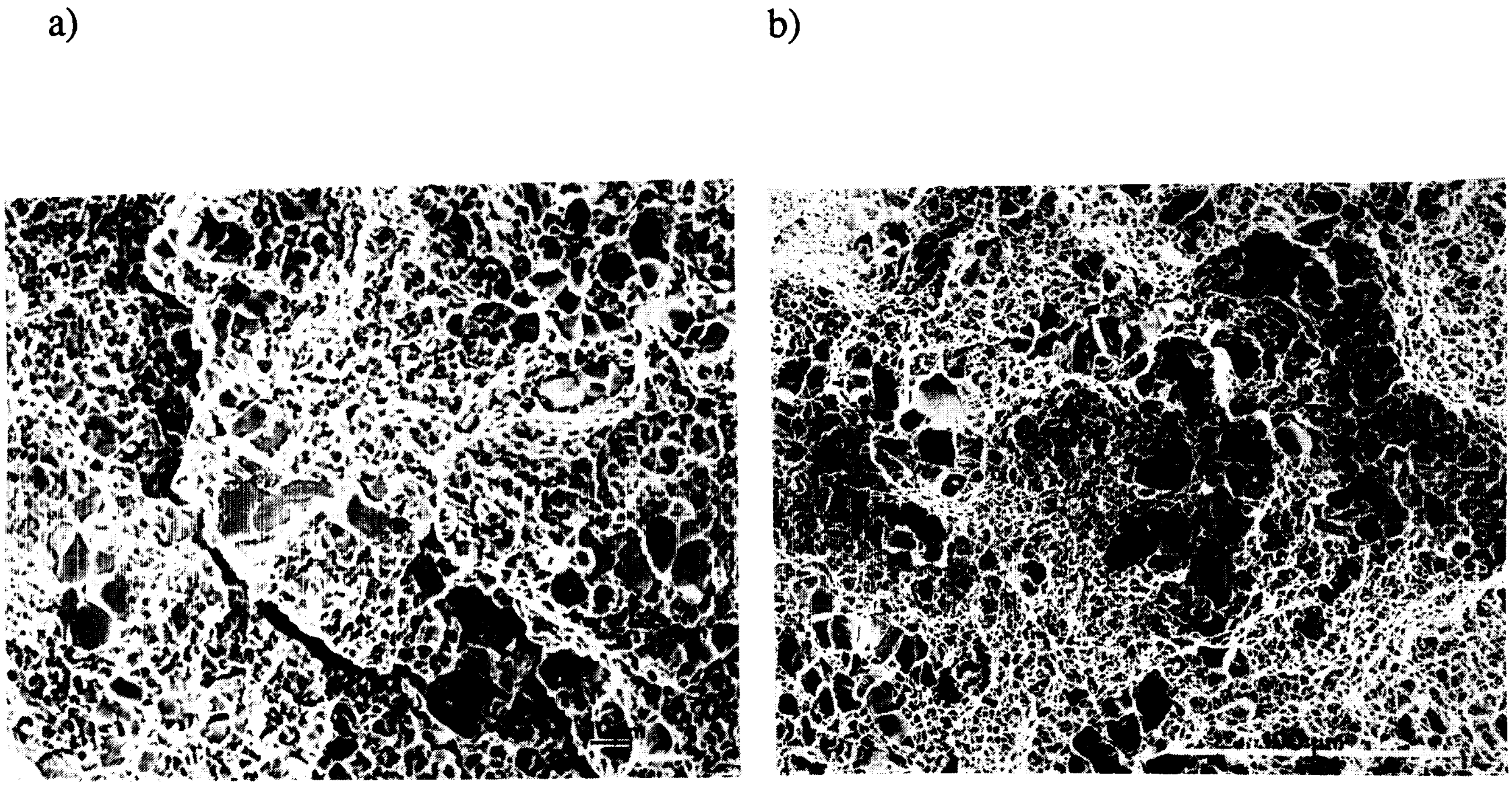

Figure 5.19 Fracture surfaces of the double-extruded multi-phase alloy Ni-20Al-30Fe in (a) 500°C-annealed state (b) 750°C-annealed state (c) 1300°C-annealed state (see fractograph in as-extruded state fig.4.3.2). Note that the fracture mode is similar in all cases and consists of transgranular cleavage in the pro-eutectic β' phase and dimple fracture in the eutectic.

ORIGINAL PAGE
BLACK AND WHITE PHOTOGRAPH

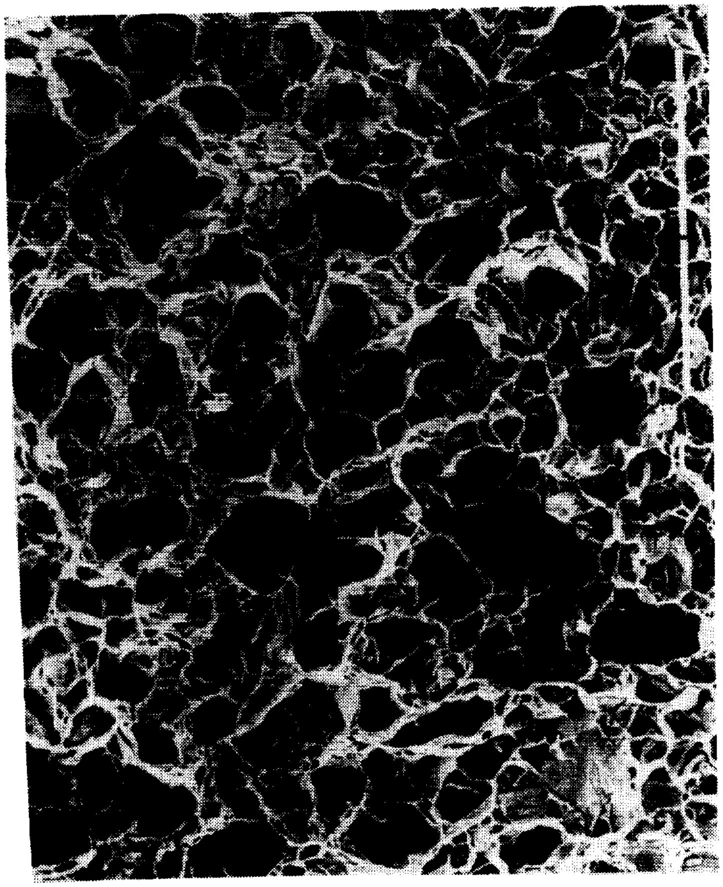

c)

Figure 5.19 continued.

ORIGINAL PAGE
BLACK AND WHITE PHOTOGRAPH

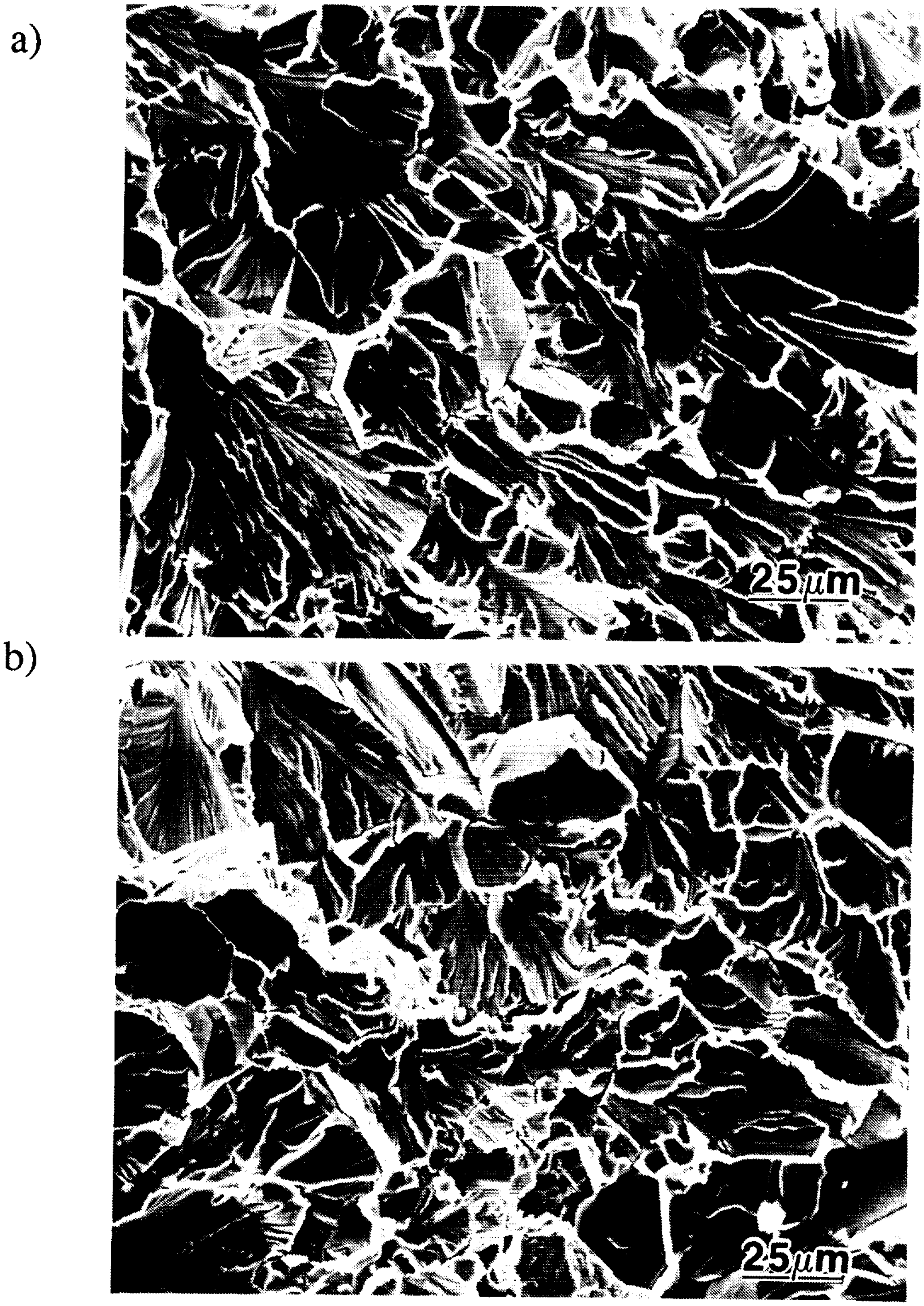

Figure 5.20 Fracture surfaces of the double-extruded β' alloy Ni-30Al-20Fe in: (a) 500°C-annealed state (b) 750°C-annealed state (see as-extruded fractograph in Fig 4.3.2). Fracture mode is similar in all cases and consists of both intergranular and (predominantly) transgranular cleavage failure.

ORIGINAL PAGE
BLACK AND WHITE PHOTOGRAPH

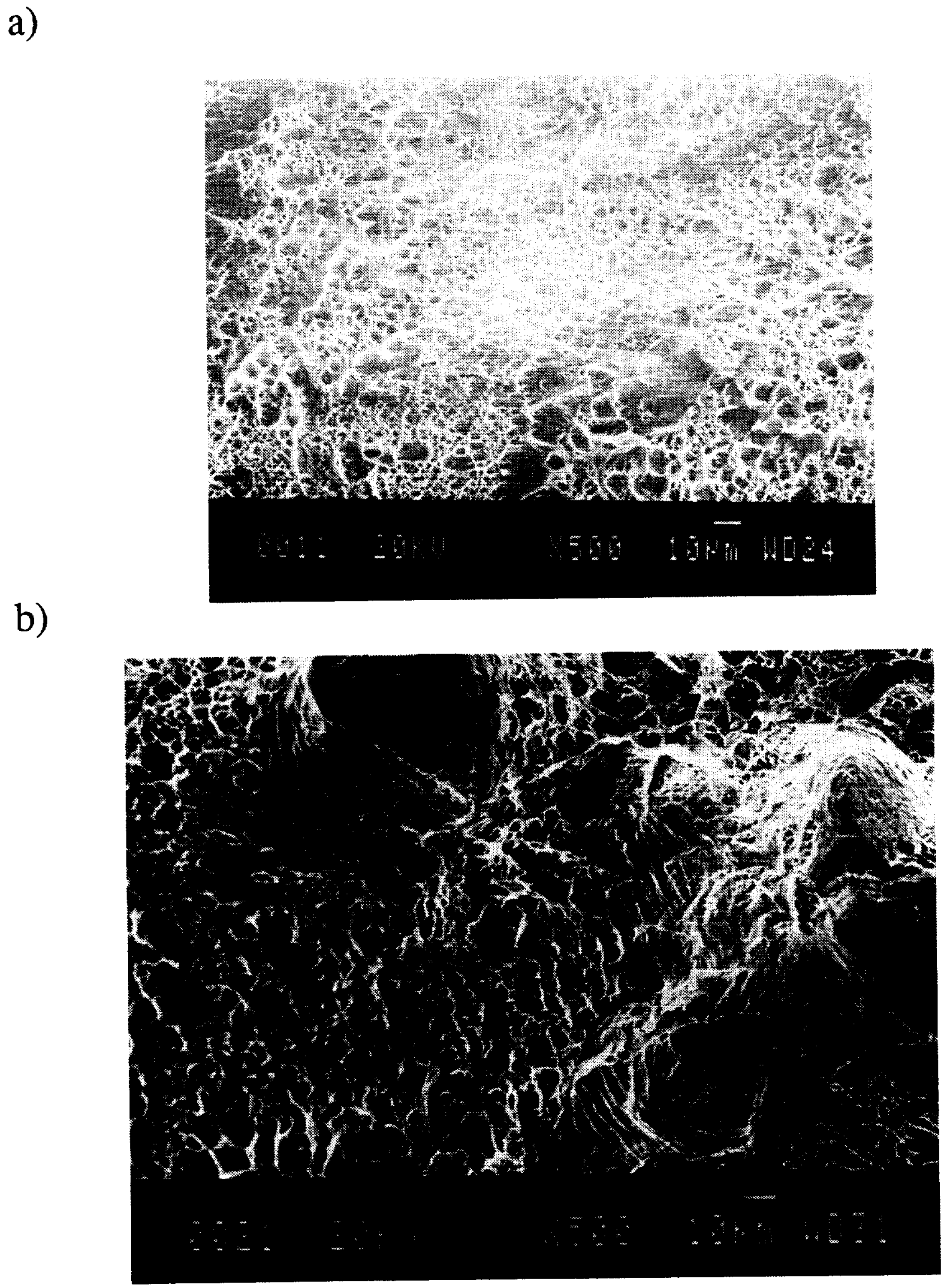

Figure 5.21 Fracture surfaces of the single-extruded γ/γ' alloy Ni-12Al-40Fe in: (a) 500°C-annealed state (b) 750°C-annealed state (see as-extruded fractograph in fig. 4.3.2). The alloy fails by dimple fracture irrespective of heat treatment.

ORIGINAL PAGE
BLACK AND WHITE PHOTOGRAPH

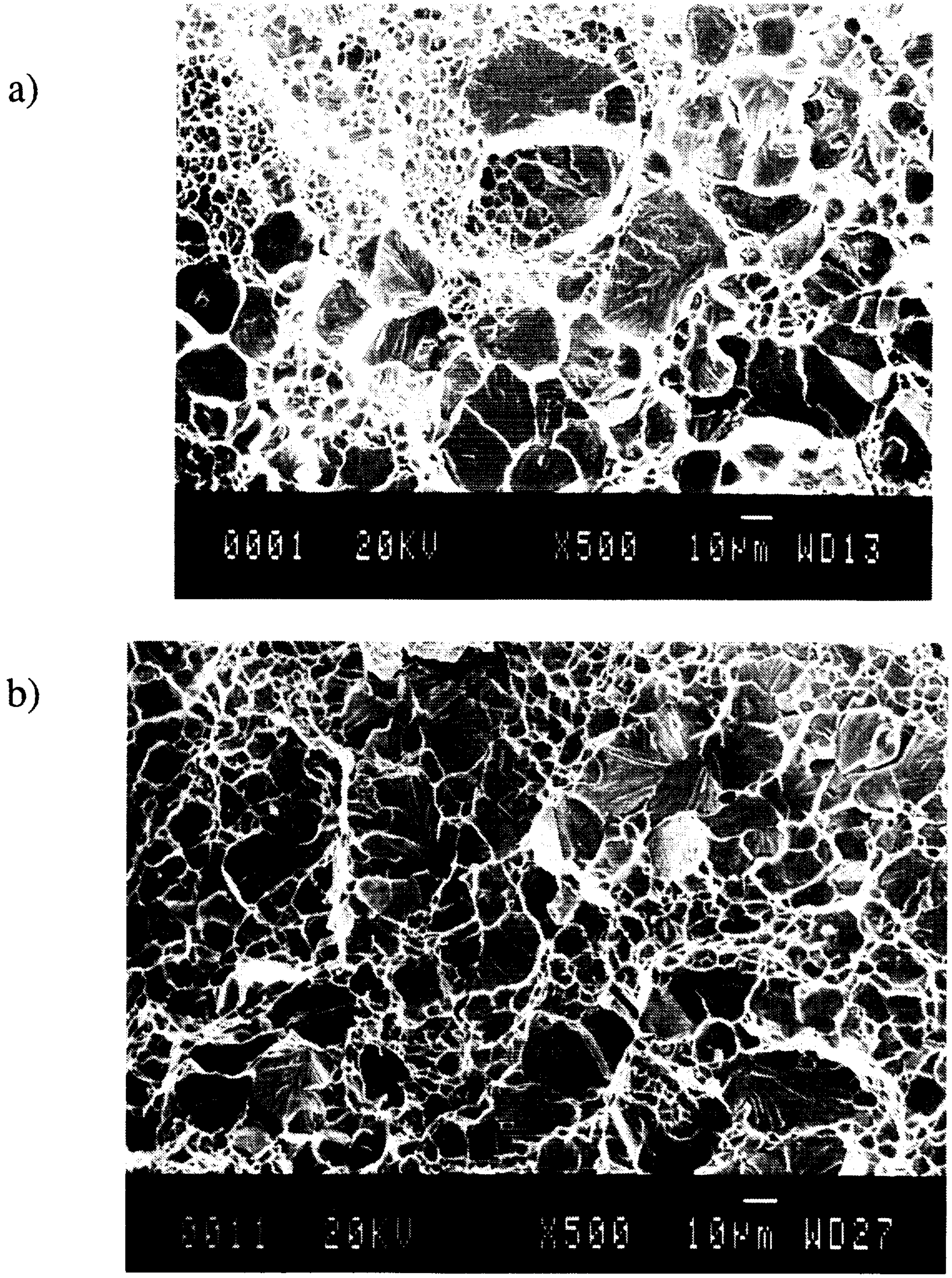
a)
0001 20KV X500 10μm WD13
b)
0011 20KV X500 10μm WD27

Figure 5.22 Fracture surfaces of the single-extruded boron-doped multi-phase alloys in: (a) as-extruded state (b) after annealing at 500°C (c) after annealing at 750°C (d) magnified image of the dimpled fracture surface in (c). Like the undoped multi-phase alloys, fracture consists of dimple failure in the eutectic and transgranular cleavage in the pro-eutectic (with the exception of 750°C annealing treatment).

ORIGINAL PAGE
BLACK AND WHITE PHOTOGRAPH

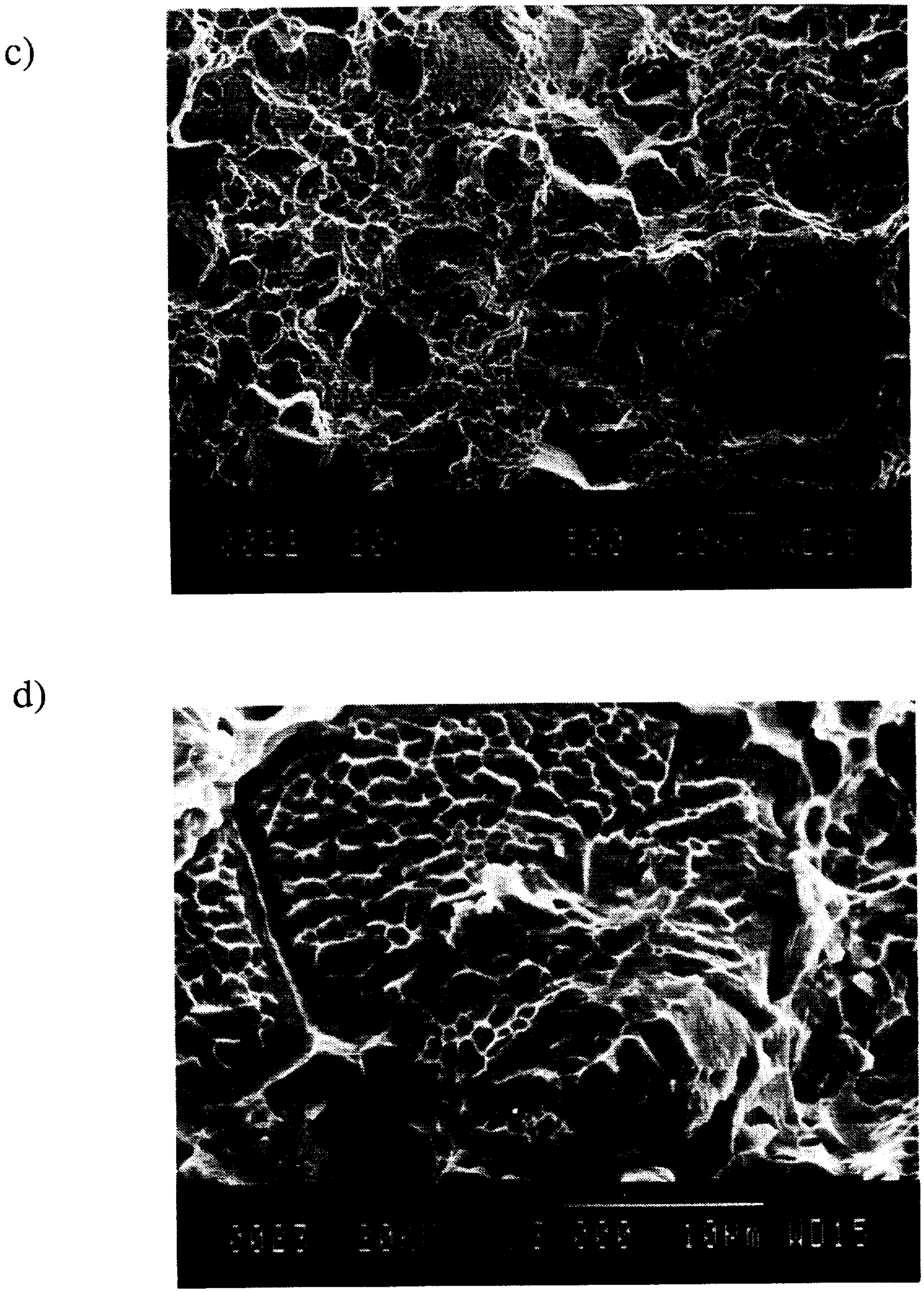
c)
d)
10μm WD15

Figure 5.22 continued

ORIGINAL PAGE
BLACK AND WHITE PHOTOGRAPH

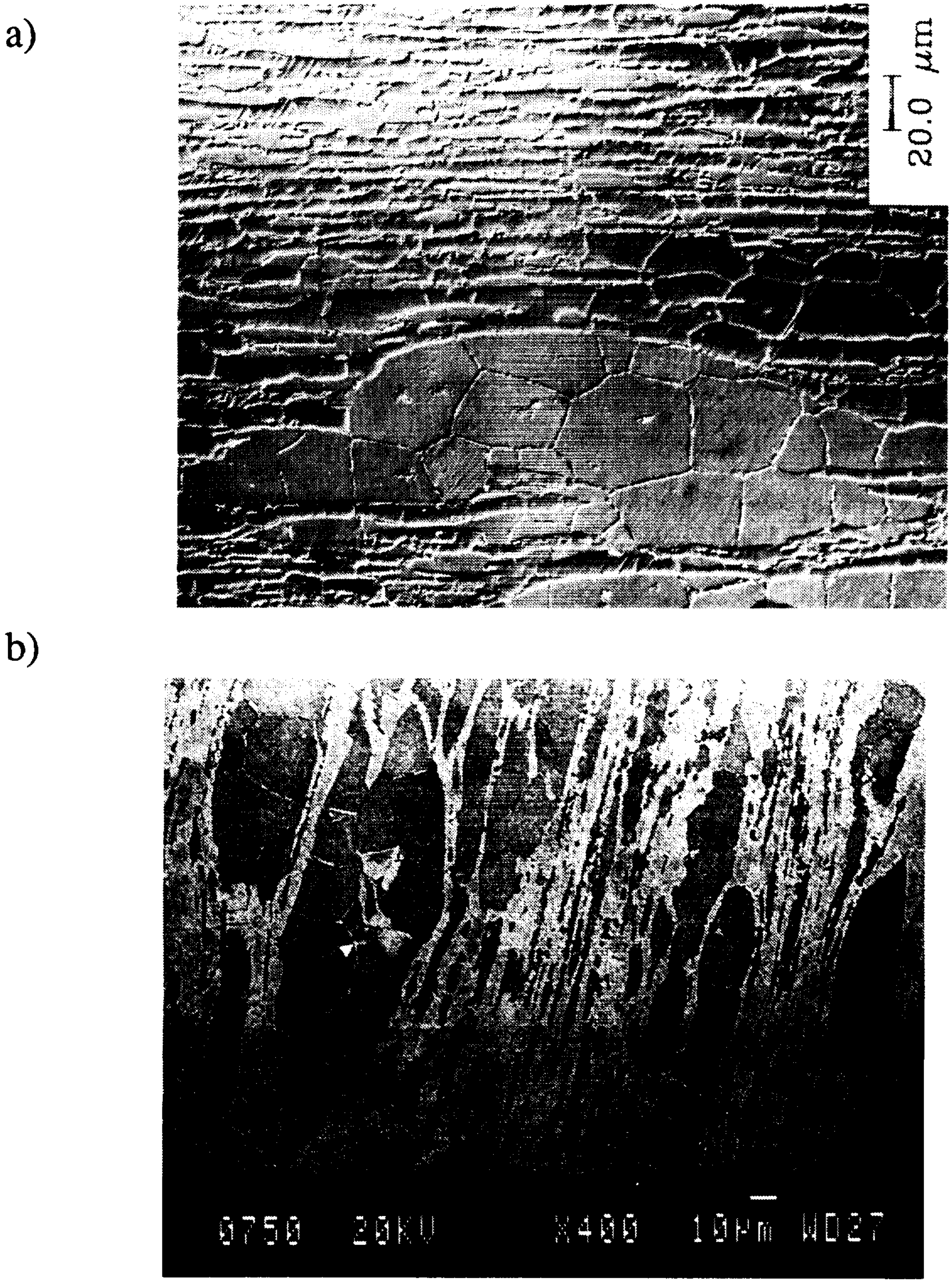

Figure 5.23 Examination of polished longitudinal sections of boron-doped multi-phase alloys annealed at 750°C by (a) optical microscopy (DIC contrast) and (b) backscattered electron imaging indicates the presence of a grain boundary phase which may be responsible for the dimpled fracture surface appearance.

For multi-phase alloy samples microalloyed with boron (fig. 5.22), the fracture surfaces exhibited similar characteristics to the undoped multi-phase alloys with one exception; when annealed at 750°C, many pro-eutectic phase particles exhibited a dimple rather than cleavage pattern (see fig. 5.22d). Examination of polished longitudinal sections of the boron-doped multi-phase alloy using both optical microscopy (DIC, fig. 5.23a) and SEM (backscattered image, fig. 5.23b) indicated the presence of a grain boundary phase. It was not clear, however, if the dimple fracture in the pro-eutectic phase was due to the intrinsic character of the boron-doped multi-phase β' phase or related to this grain boundary phase. A subsequent careful examination of the fracture surfaces of the pro-eutectic phase in the undoped multi-phase alloy samples, however, also revealed a few grains that exhibited such a dimpled pattern. Interestingly, no such grains could be detected for alloy samples annealed at 500°C. A qualitative analysis of comparing EDS peak counts of Ni K_α and Fe K_α x-rays in the SEM from regions exhibiting cleavage and dimple fracture indicated an iron-enrichment for pro-eutectic grains exhibiting dimpled fracture. Such an iron enrichment (in dimpled regions) is consistent with the AES data [102] on intergranular fracture surfaces of the β' alloy and is probably related to the thin, iron-rich grain boundary disordered phase referred to earlier (section 4.2). Thus, the dimple fracture is probably the result of intergranular separation in the pro-eutectic β' phase. An interesting (although qualitative) observation is the increased incidence of such dimpled fracture regions in the boron-doped alloys which suggest that boron stabilizes the disordered grain boundary phase.

5.3 Summary

The effect of heat treatment on the room temperature mechanical properties of the multi-phase alloy is the combined response to annealing of its constituent β' and γ/γ' phases. While its increased strength when annealed at 500°C is related to the annealing characteristic of the β' phase, the decrease in strength for annealing temperatures higher than 700°C is related to its γ/γ' constituent.

For the γ/γ' alloy, the decreased strength for annealing temperatures higher than 700°C is related to the coarsening of the γ' precipitates and the eventual dissolution/disordering of the ordered precipitates into the disordered γ matrix. The small increase in strength and decrease in tensile elongation observed for annealing temperatures up to 750°C is thought to be related (microstructurally) to the precipitation of β' precipitates at the γ/γ' grain boundaries; the increase of γ' precipitate size from ~10nm in the as-extruded state to ~20nm in the 750°C-annealed state is thought not to be significant with respect to their influence on mechanical properties. Similarly, the volume fraction of γ' precipitates in γ appear to be similar in the as-extruded and annealed states; the direct measurement of volume fraction of γ' precipitates is difficult due to their small size.

For the β' alloy, the increased strength in the 500°C-annealed state than that in the as-extruded or 750°C-annealed state is attributable to the dispersion of β (α-Fe) in β' matrix. The observed room temperature ductility in the as-extruded and 750°C-annealed state is attributable to its thin (~10nm), disordered grain boundary phase although (as discussed later), the influence of a <111> texture on ductility cannot be ruled out based on the experimental evidence presented here. The embrittlement at 500°C is attributable to one or both of the following reasons: (1) lack of a disordered grain boundary phase (2) dispersion of β (α-Fe) in β' which possibly decreases dislocation mobility by its pinning action.

CHAPTER 6

Room Temperature Mechanical Behavior of Ni-40Al-30Fe

This chapter presents the room temperature mechanical behavior of another β' alloy Ni-40Al-30Fe, including the effect of annealing on the mechanical properties. Some limited high temperature strength data (hot hardness tests) are also presented.

Microstructure

According to figure 2.3b, which is a section of the Ni-Fe-Al phase diagram for slowly (10°C/hr) cooled alloys, the alloy Ni-40Al-30Fe (marked with a 'x') lies in a single phase (β') region at room temperature. At 750°C, however, the alloy lies in a two-phase β'+β (where β' and β represent ordered and disordered b.c.c respectively) region. At higher temperatures, the two-phase field is observed to shrink, see for example figure 2.3d-e. Consequently, the alloy Ni-40Al-30Fe should be single phase again at temperatures greater than 900°C.

The as-extruded (double extruded) microstructure consisted of equiaxed grains with a grain size ~10μm. The absence of cracking around microhardness indentations indicated the not-so-brittle nature of the alloy, see figure 6.1a. Polished transverse and longitudinal sections of the as-extruded alloy (figure 6.1b-c) indicated a similar microstructure although bands of dark (from etching) areas were observed in the longitudinal sections (fig. 6.1c), indicative of a partially recrystallized microstructure. The partially recrystallized nature of the microstructure was confirmed by TEM. For example, figure 6.1d is a TEM micrograph of the double-extruded alloy showing two adjacent grains, one fully recrystallized and the other partially, the sub-boundaries in the partially recrystallized grain can be clearly seen. The sub-boundaries were observed to persist even after an annealing treatment of 200 min.

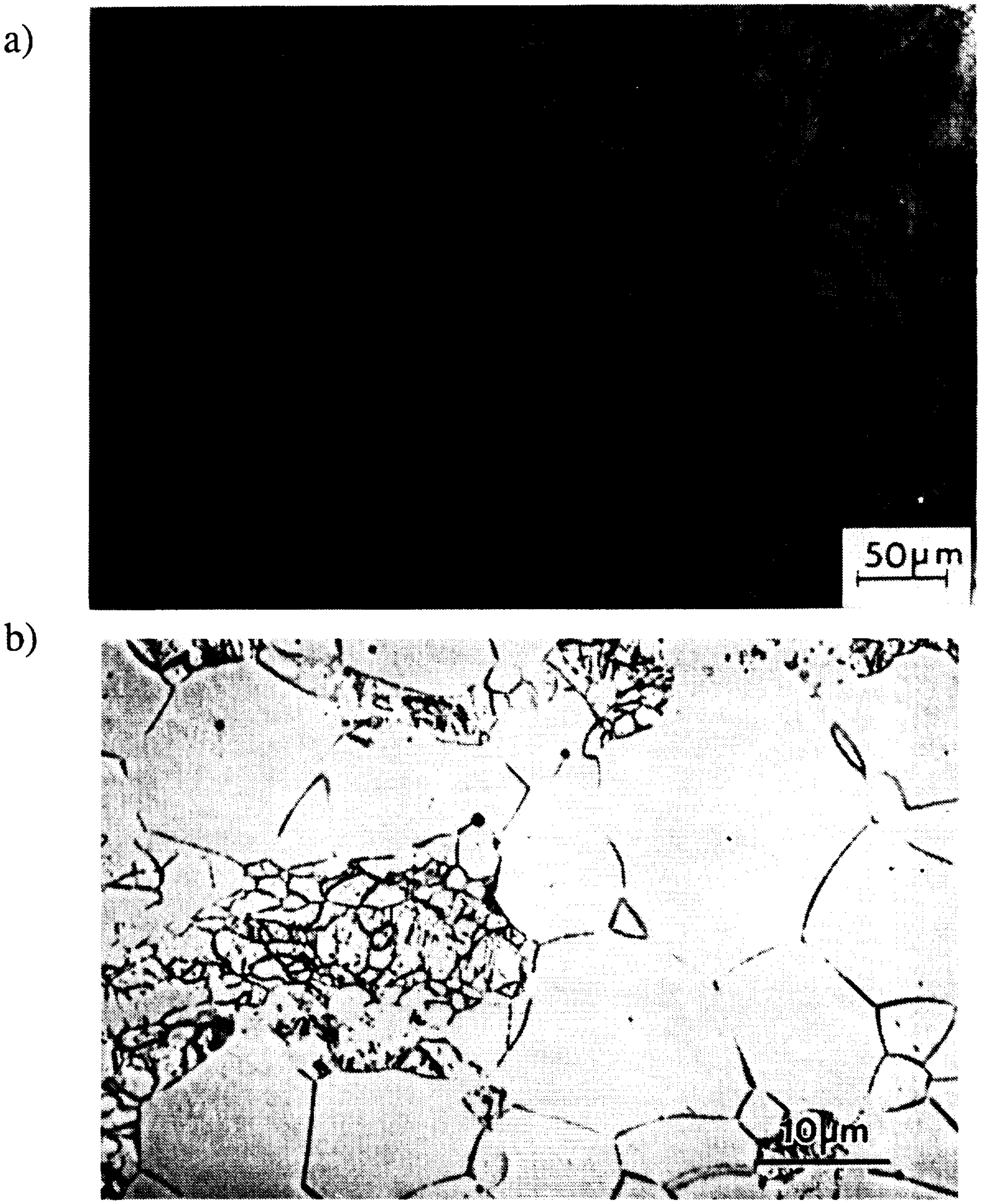

Figure 6.1 As-extruded Ni-40Al-30Fe: (a) Microhardness indentations indicate lack of cracking around indentations (b) polished transverse section indicates a grain size of ~10μm (c) polished longitudinal sections indicate bands of dark etched areas indicative of a partially recrystallized microstructure (d) bright-field TEM micrographs indicate a partially recrystallized microstructure; note the sub-boundaries in the partially recrystallized grain.

ORIGINAL PAGE
BLACK AND WHITE PHOTOGRAPH

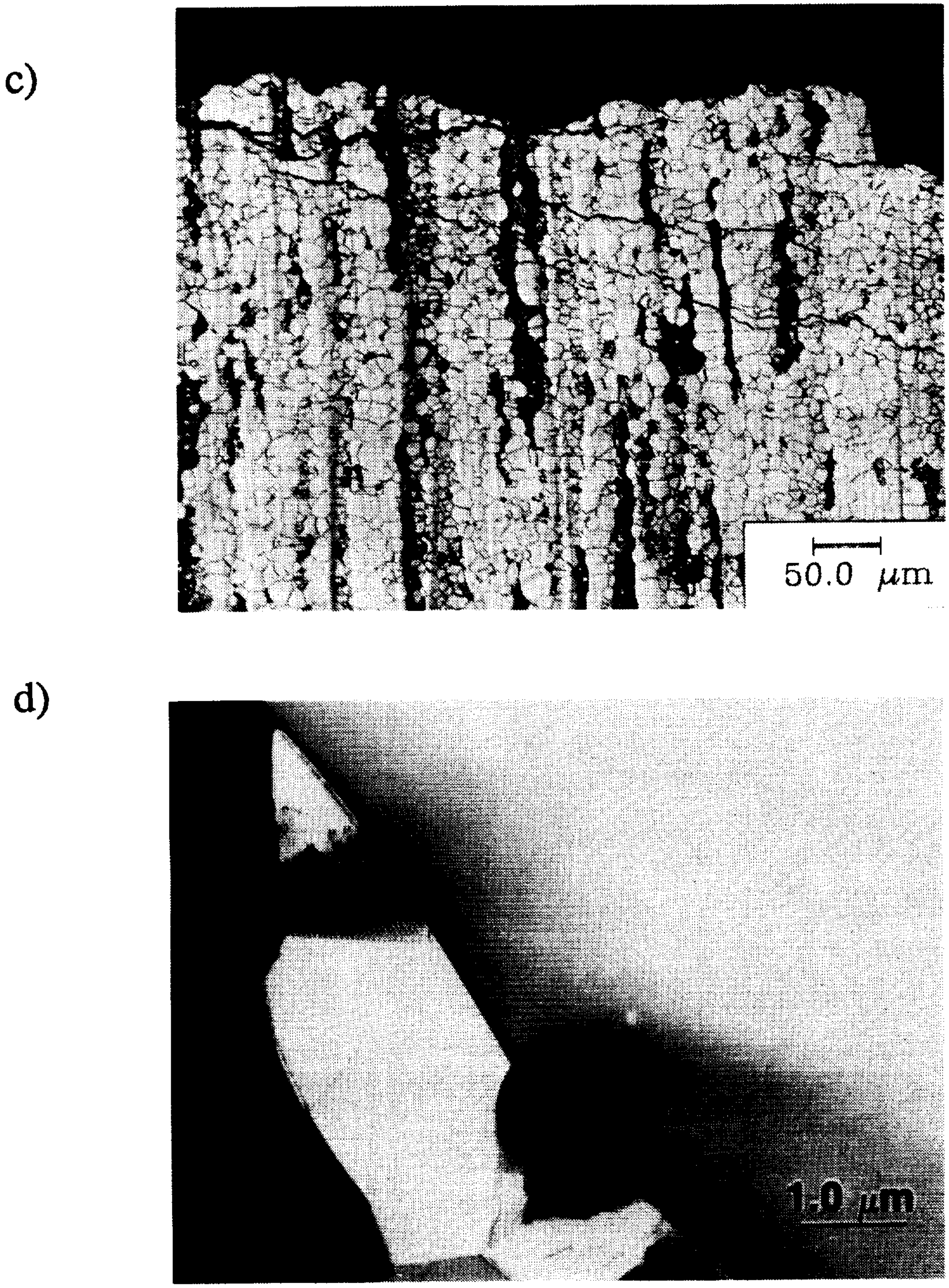
c)
50.0 μm
d)
1.0 μm

Figure 6.1 continued.

ORIGINAL PAGE
BLACK AND WHITE PHOTOGRAPH

at 750°C (followed by water quenching), see figure 6.2. The dislocations in the sub-boundaries were analyzed to be <100> dislocations which represent the deformation mode at high temperatures (the extrusion temperature of 1000°C).

Figure 6.3 is a pair of bright-field and superlattice dark field (SDF) images for the alloy annealed at 750°C. The bright field image shows approximately spherical precipitates ~40nm in diameter. The precipitates appear dark in SDF images representing disordered precipitates in an ordered (bright under SDF imaging). The magnetic nature of the specimen combined with the small sizes of the precipitates precluded structure determination through CBED. Selected area diffraction patterns indicated an ordered b.c.c superlattice which is indicative of the the disordered precipitates also being b.c.c (rather than f.c.c since no extra reflections were observed). Thus, the microstructure of the alloy Ni-40Al-30Fe was judged to be β'+β which was consistent with the 750°C Ni-Fe-Al isotherms. Interestingly, superlattice dark field imaging of the as-extruded alloy also indicates a similar β'+β microstructure, although the disordered precipitates were only ~10nm in diameter (fig. 6.4).

Though the as-extruded microstructure was expected to be single-phase from the phase diagrams for slowly cooled alloys (fig. 2.3b), the experimentally observed microstructure consisting of β precipitates in a β' matrix was inconsistent with the expected phase relationships since only a β' microstructure was be expected. The β+β' microstructure, by contrast, was similar to the 750°C isotherm which is indicative of a non-equilibrium structure being retained during post-extrusion cooling from 1000°C.

Mechanical Properties

Isochronal annealing experiments, similar to those described in the previous chapter, indicated a behavior which was similar to the β' Ni-30Al-20Fe; a small peak in Rockwell hardness was observed upon annealing at 500°C while the hardness in the as-

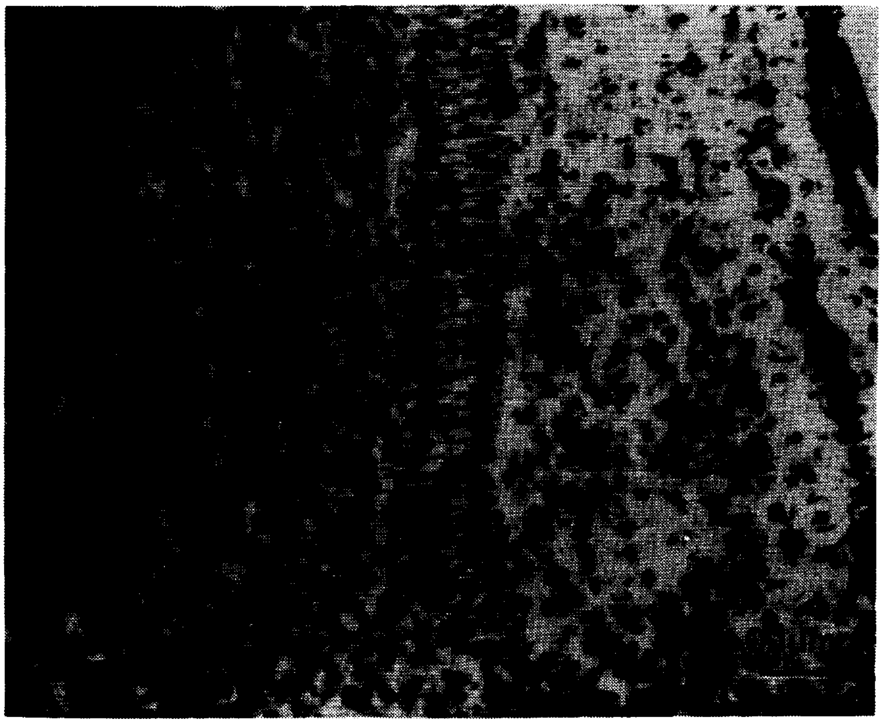

Figure 6.2 Bright field TEM micrograph of 750°C-annealed Ni-40Al-30Fe alloy, strained 0.5% in tension. Note the sub-boundary which indicates a partially recrystallized microstructure and consists of discrete <100> dislocations. Also, no discrete dislocations can be observed within the strained matrix due to strain field around the precipitates.

ORIGINAL PAGE
BLACK AND WHITE PHOTOGRAPH

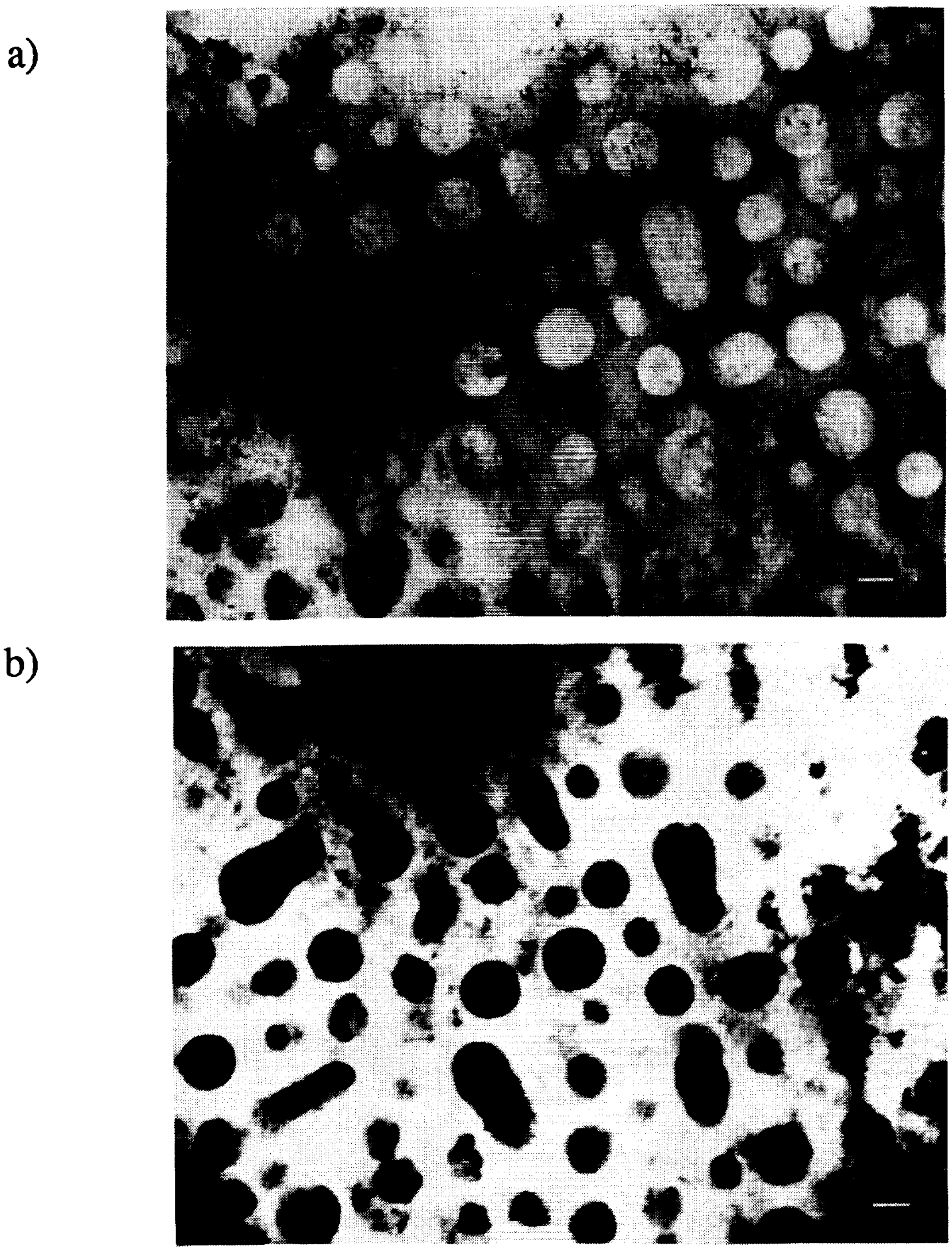

Figure 6.3a-b (a) Bright field (b) Superlattice dark field images of 750°C-annealed Ni-40Al-30Fe alloys. The dark spots in (b) represent disordered (α-Fe or β) precipitates in an ordered (bright) β' matrix. The size of β precipitates is ~40 nm.

ORIGINAL PAGE
BLACK AND WHITE PHOTOGRAPH

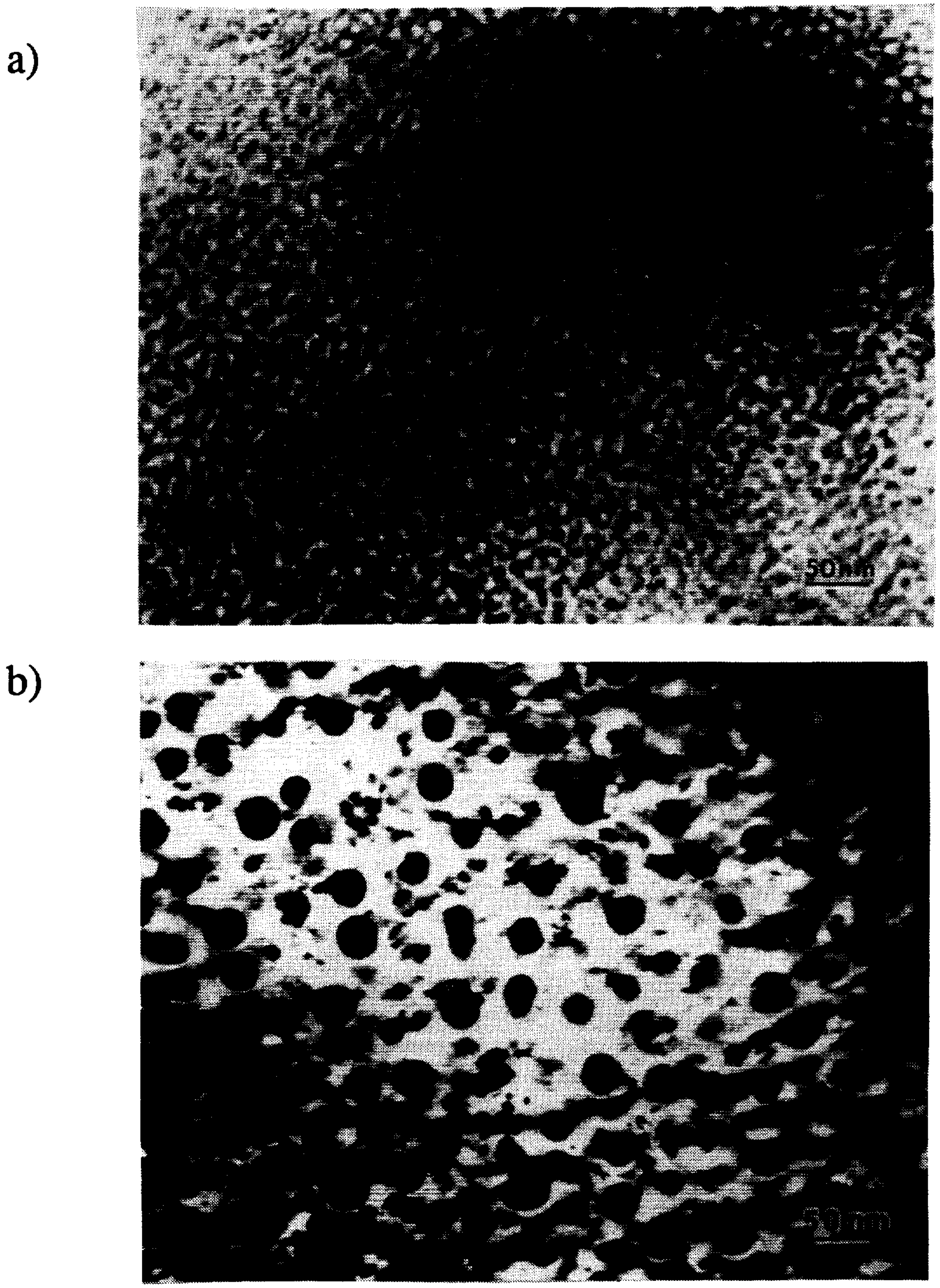

Figure 6.4 Superlattice dark-field images of Ni-40Al-30Fe in (a) as-extruded (b) 750°C-annealed state. The dark spots represent α-Fe dispersions within the β' matrix. Note the change in dispersoid size with annealing.

ORIGINAL PAGE
BLACK AND WHITE PHOTOGRAPH

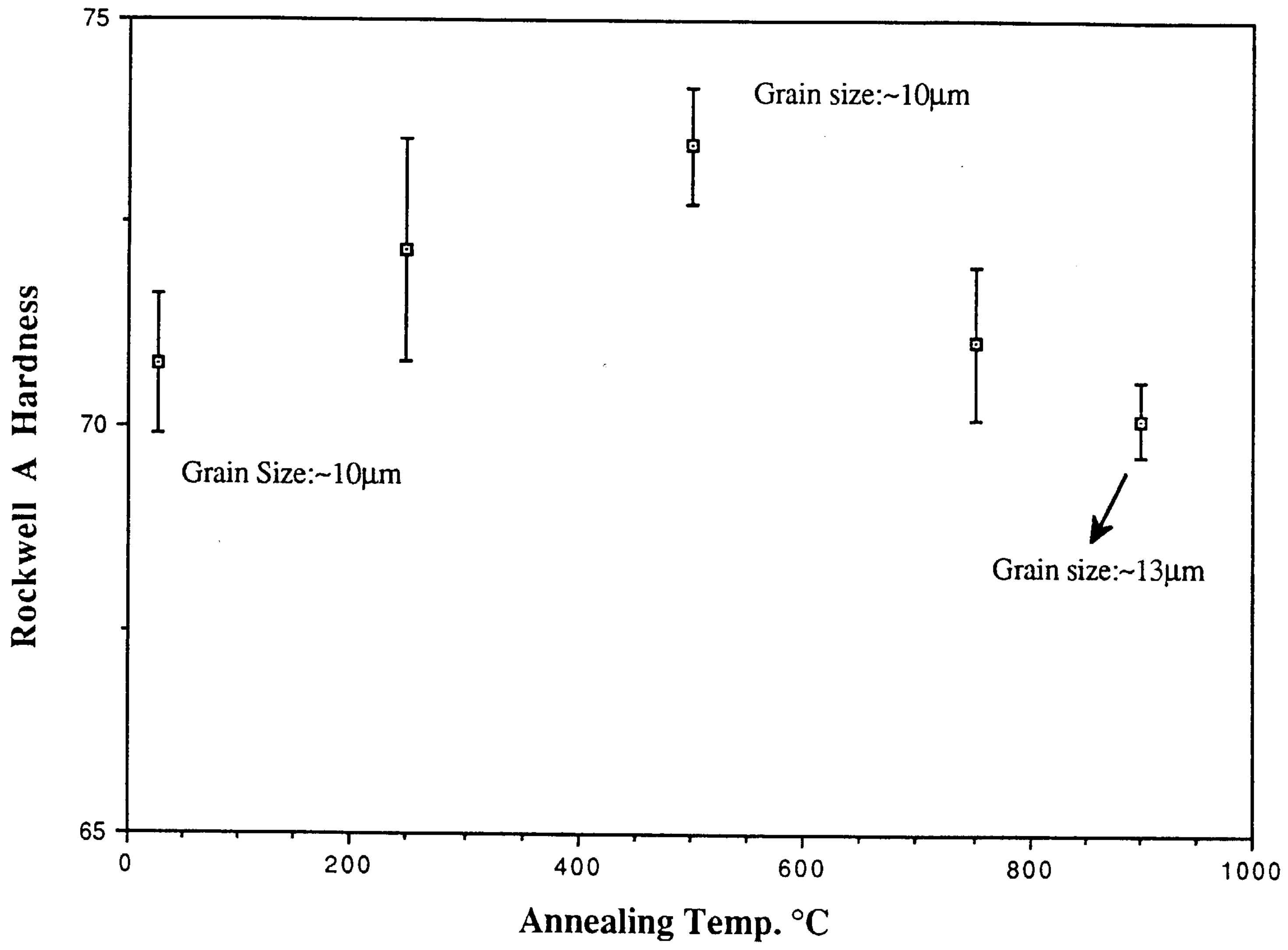

Figure 6.5 The variation of room temperature hardness after isochronal annealing at different temperatures; a small increase (within error bar limits) is observed at 500°C.

extruded and 750°C annealed state were similar (see fig. 6.5). The increased hardness after 500°C anneal was outside the 95% confidence interval limits and hence, is considered significant.

Room temperature tensile tests were performed on specimens from the as-extruded alloy and on samples annealed at 750°C. The stress strain graphs are shown in figure 6.6. When tested in air at room temperature, the as-extruded alloy exhibited a high (~900 MPa) fracture stress but no plastic elongation. By contrast, the when annealed at 750°C, the alloy exhibited a high yield stress (~950 MPa) and limited (0.5%) plastic elongation. An upper yield point phenomenon was observed.

Recently, Liu et al.[118] have reported increased plastic elongation for Fe-Al intermetallics when tested in vacuum. The embrittlement in ambient atmosphere was ascribed (without any proof) to hydrogen (from dissociation of water molecules) assisted embrittlement at the crack tips. To determine if a similar effect of increased ductility in vacuum could be obtained for Ni-40Al-30Fe (that is, the absence of water molecules), the as-extruded and 750°C annealed specimens were tensile tested in high vacuum (7×10^{-7} Torr), figure 6.6 shows the stress-strain curves. It is clear that no additional benefit was derived from vacuum testing.

The fracture surfaces (both air and vacuum tests) of as-extruded alloys and those annealed at 750°C were examined in a SEM. Figure 6.7 shows the fracture surfaces for as-extruded specimens (which is similar to the 750°C annealed specimens) tested in air. Failure occurs by transgranular cleavage in both cases. The fracture surfaces for alloys tested in vacuum were similar to those shown in fig. 6.7.

It is interesting to compare the room temperature mechanical behavior of the two β' alloys Ni-30Al-20Fe and Ni-40Al-30Fe. Both the alloys deform by <100> dislocations (see later). The former alloy, in its as-extruded state, exhibits a β' microstructure with a ~10 nm thick, discontinuous, Fe-rich γ grain boundary phase; the alloy exhibits up to 6% tensile elongation. However, when annealed at 500°C, no γ grain boundary phases are

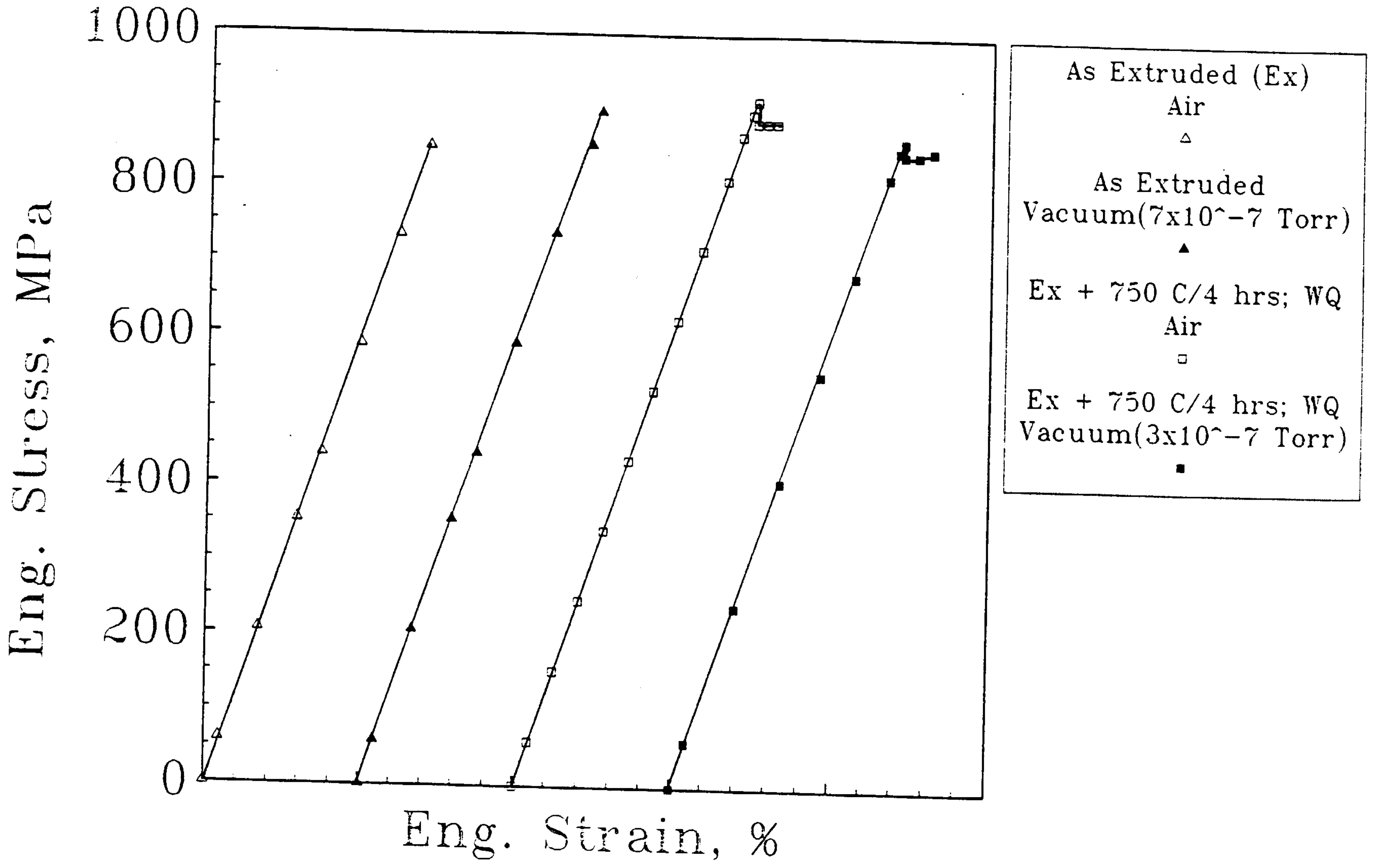

Figure 6.6 Stress-strain curves of as-extruded and 750°C-annealed Ni-40Al-30Fe, tested in air and vacuum.

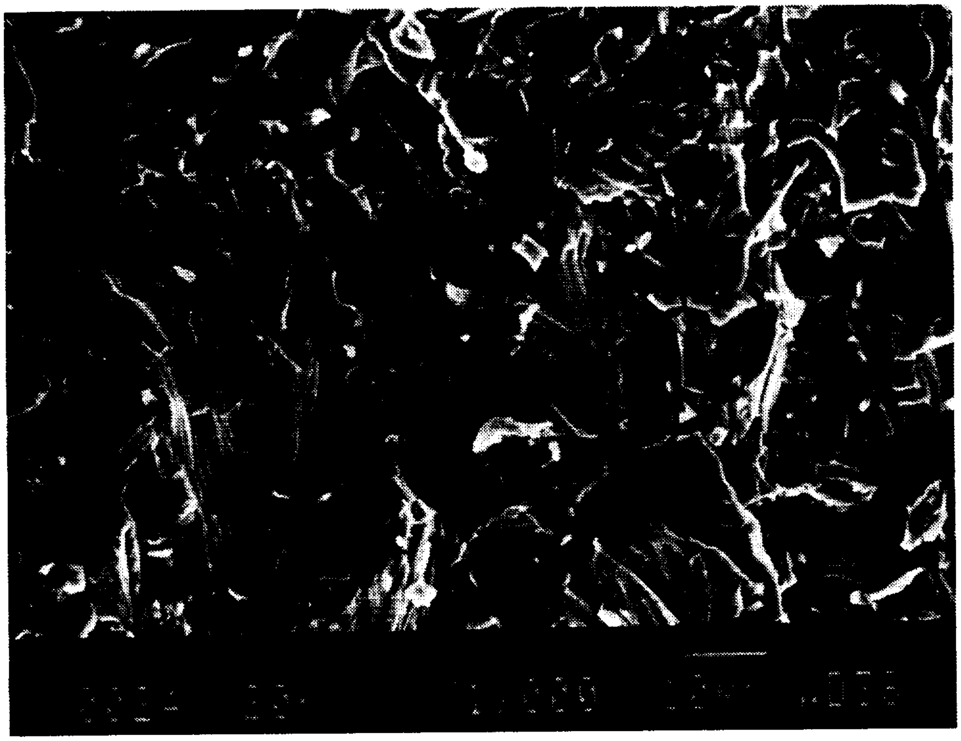

Figure 6.7 Fracture surface of as-extruded Ni-40Al-30Fe, tested in air, shows the failure mode to be transgranular cleavage.

ORIGINAL PAGE
BLACK AND WHITE PHOTOGRAPH

observed; rather, the alloy exhibits a microstructure consisting of β (α-Fe) precipitate dispersions in the β' ordered matrix, which is similar to the microstructure of the as-extruded Ni-40Al-30Fe. Not surprisingly, both the alloys (as-extruded Ni-40Al-30Fe and 500°C-annealed Ni-30Al-20Fe) exhibit high yield strengths (900 MPa and 1000 MPa respectively) and are brittle in tension. Interestingly, however, a coarsening of the dispersion strengthened microstructure for Ni-40Al-30Fe imparts slight tensile ductility to the alloy, suggesting that such coarsening may also be effective for the alloy Ni-30Al-20Fe. Long time annealing (250 hours) at 500°C, however, did not produce such a coarsened microstructure for Ni-30Al-20Fe (see chapter 4), presumably due to the slow kinetics of coarsening at 500°C.

The elevated temperature mechanical properties of Ni-40Al-30Fe were determined only by Vickers microhardness indentations. The trend in hardness (fig. 6.8) was similar to that observed for the β' alloy Ni-30Al-20Fe, although the critical temperature 'T_C' beyond which the hardness decreases sharply, was observed to be slightly higher for the alloy Ni-40Al-30Fe than the alloy Ni-30Al-20Fe, presumably due to the higher melting point of the former alloy. No elevated temperature tensile tests were performed.

Deformation Mechanisms

The analysis of deformation mechanism in Ni-40Al-30Fe by TEM examination of thin foils of the 750°C-annealed alloy, deformed ~2% in compression, was not successful due to the magnetic nature of the specimen and the difficulty in identifying discrete dislocations; the strain field resulting from the interaction of dislocations in the ordered matrix with the disordered precipitates made identification of individual dislocations difficult. As noted earlier, dislocations in the sub-boundaries in the partially recrystallized extruded microstructure were found to possess a <100> Burgers' vector which is indicative of the deformation mechanism at the extrusion temperature being <100> dislocations. This

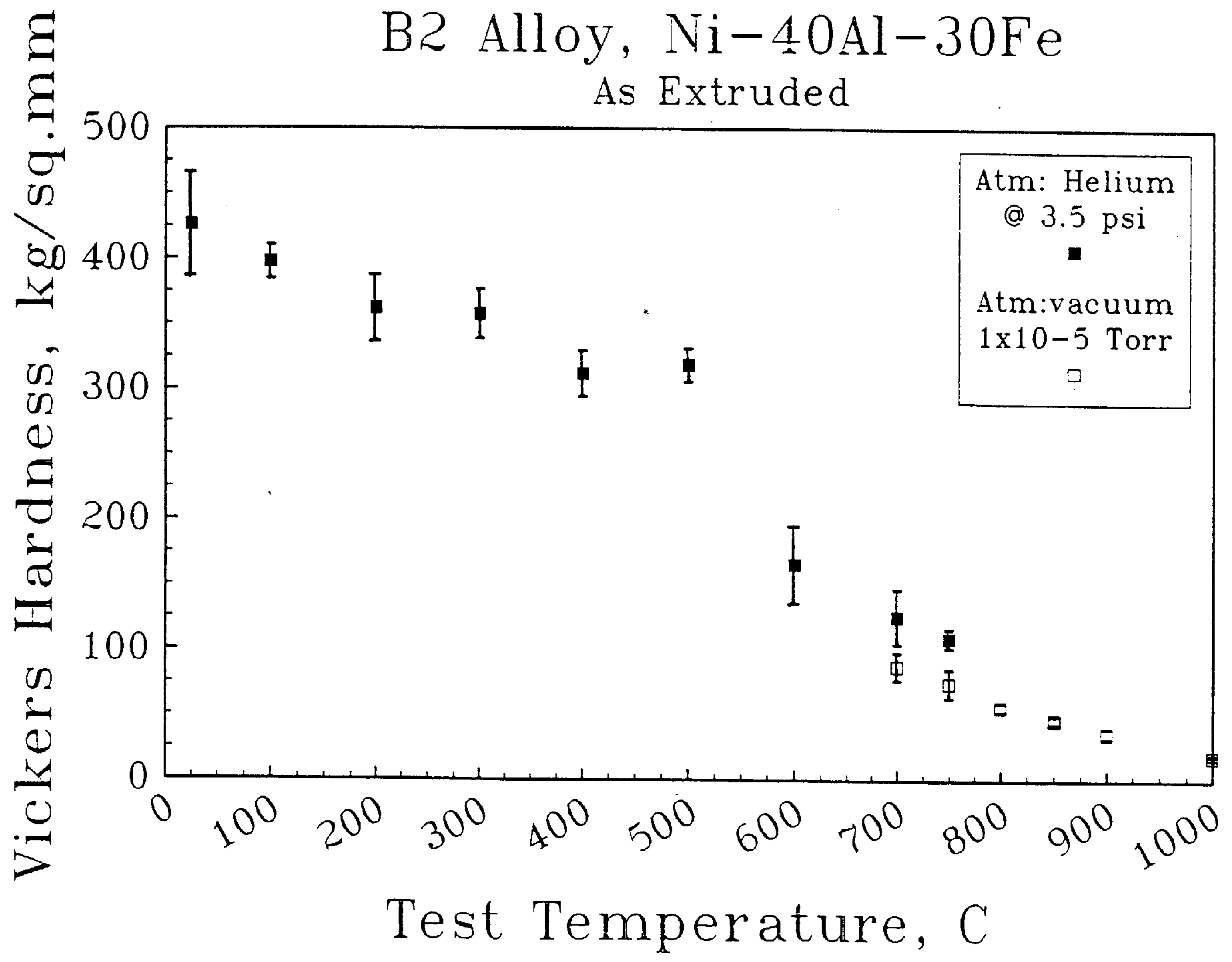

Figure 6.8 Elevated temperature strength properties as determined through Vickers hot hardness tests.

is consistent with the observations by Keith-Patrick et al. [119] who also reported <100> dislocations in Ni-40Al-30Fe alloys deformed at room temperature; alloys which deform by <100> dislocations at room temperature generally also deform by the same mechanism at high temperatures (although non-<100> dislocations may also arise from the collision of <100> dislocations). While the processing route adopted by Keith-Patrick et al.[119] is not clear (that is, whether the alloys were cast or powder processed), it is worthwhile noting that no β+β' microstructure was reported by them which is in contrast to the findings in the present work. Such microstructural differences may indicate why, while individual dislocations could not be identified clearly after 0.5% tensile strain due to the strain field around precipitates, such dislocations were clearly identified by Keith-Patrick et al.[119] after 0.5% compressive strain. The microstructural difference can be related to differences in annealing conditions; while the alloys in the present investigation were annealed at 750°C where such a β+β' microstructure is expected, those examined by Keith-Patrick et al.[119] were annealed at 1200°C where only a β' microstructure will be expected (see isotherms in Chapter 2).

In summary, the alloy Ni-40Al-30Fe, in its extruded state, exhibited a microstructure consisting of disordered precipitates in an ordered matrix. The as-extruded alloy was brittle in tension. Annealing at 750°C coarsened the β+β' microstructure and imparted limited (~0.5%) tensile ductility to the alloy. The alloy was found to be insensitive to the environment. The elevated temperature strength characteristic of the alloy was similar to those commonly observed for β' alloys.

CHAPTER 7

Annealed Microstructures In Multi-phase Ni-36Al

This chapter presents the results of the limited investigation into the microstructure and mechanical behavior of undoped and boron-doped multi-phase alloy Ni-36at.%Al in the as-extruded and heat treated state (the heat treatment being similar to those examined by Russell and Edington [20]).

Microstructures

The extrusions of the undoped and boron-doped multi-phase Ni-36Al were flawed, with casting pipes being observed at the center of extrusions. Figure 7.1 is a fractograph of the undoped alloy showing a casting pipe which was not healed by the extrusion process.

Figure 7.2a is an optical micrograph of Ni-36Al in its as-extruded state. The as-extruded (double extruded and air cooled) microstructure is martensitic which is indicative of rapid post-extrusion cooling rates. The microstructure consists of equiaxed grains ~100μm in diameter. The microstructure also shows evidence of extensive intergranular and transgranular cracking, presumably the result of brittle martensitic microstructure. There was no evidence of any additional phases at the grain boundaries.

As reported earlier, Russell and Edington [20] studied the mechanical properties of the alloy in a heat treated state and reported improved room temperature impact toughness and elevated temperature strength retention for alloys with a NiAl+Ni_3Al microstructure. The quasi-static mechanical properties were examined only by compression tests. To determine the effect of minor variations in heat treatment on the resulting microstructures and the effect of such heat treatments on the tensile ductility of Ni-36Al, different heat

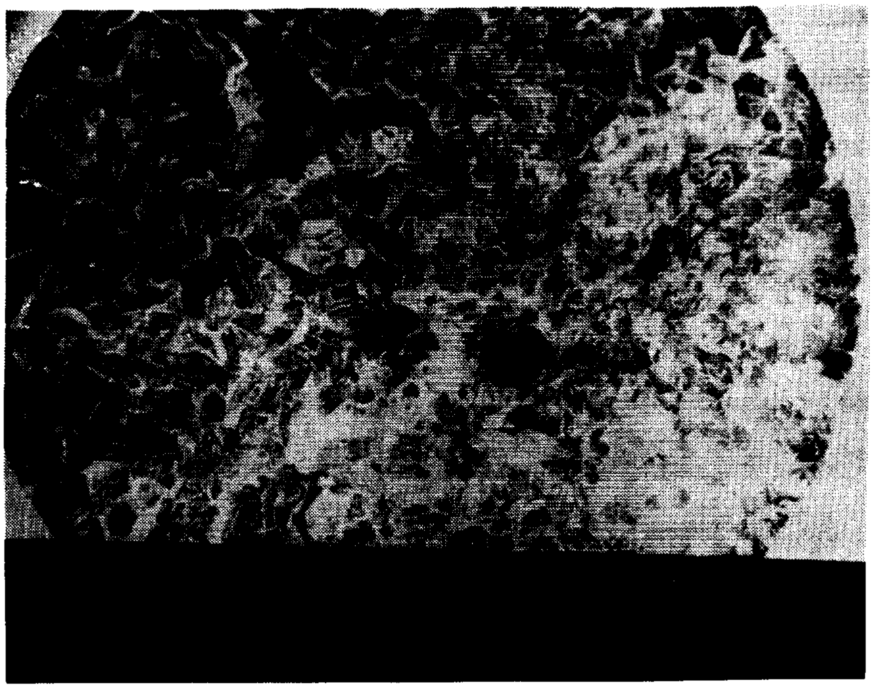

Figure 7.1 Fracture surface of as-extruded Ni-36Al alloy showing a casting pipe at the center which was not healed by the extrusion process.

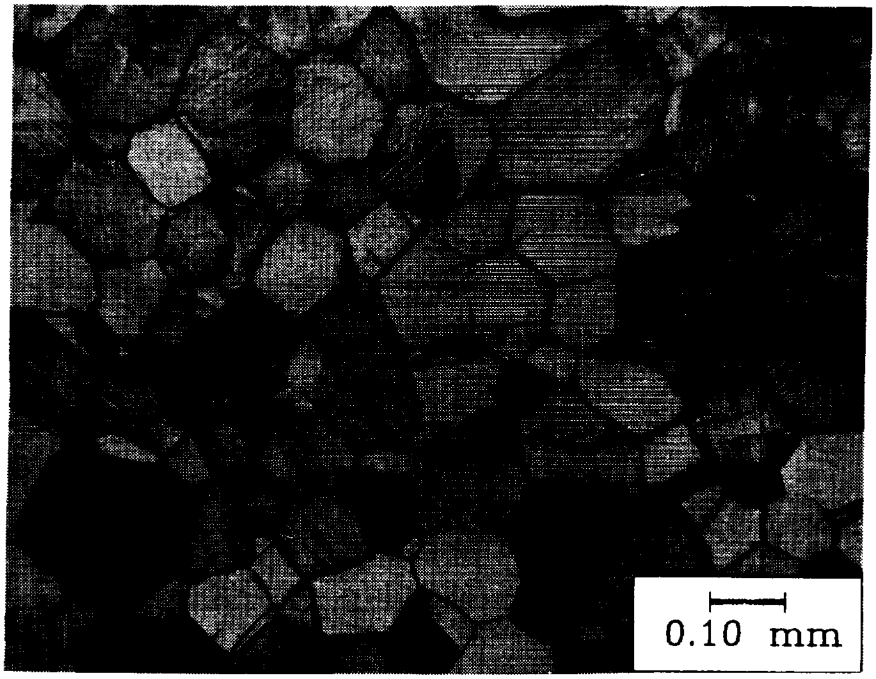

Figure 7.2 Optical micrograph of as-extruded Ni-36Al showing equiaxed grains, ~100μm in diameter. Note the intergranular and transgranular cracks in the polished microstructure which is indicative of its brittle nature.

ORIGINAL PAGE
BLACK AND WHITE PHOTOGRAPH

treatments schemes were examined to reproduce microstructures similar to those examined by Russell and Edinmgton [20].

When annealed at 1200°C for 1.5 hrs and water quenched, the microstructure was similar to the as-extruded microstructure. Following the solution anneal at 1200°C, some samples were water quenched and then held at the ageing temperatures, while others were quenched to 430°C and up-quenched to the aging temperature, similar to the heat treatment scheme adopted by Russell and Edington [20]. Two different aging temperatures (700°C and 800°C) and varying aging times (from 2.5 to 15 hours) were used.

For samples quenched from the solution anneal temperature to 430°C and up-quenched to 700°C, the aged microstructures exhibited additional phases both at the grain boundaries and within the grain interiors. While the grain boundary phase was continuous, the precipitates within the grain interiors were acicular (~1μm in width and ~20μm long), see fig. 7.3. That the precipitation within the grain interiors was along certain crystallographic directions is evident from figure 7.3a. Russell and Edington [20] determined that the precipitates at both the grain boundaries and within the grains were Ni_3Al. Further, the acicular precipitates in the grains were determined to be aligned with the <110> crystallographic direction of the matrix. Longer ageing times resulted in a higher density of acicular precipitates along with some coarsening of the precipitates (width increasing to ~2.5μm), see fig. 7.3b. Similarly, the grain boundary phase thickness was also observed to increase with increasing ageing time (from 2.5 μm for an ageing time of 2.5 hrs. to 5μm for an ageing time of 15 hrs.). Interestingly, a precipitate free zone (arrowed in fig. 7.3) is observed for both short and long ageing times and is believed to occur due to dissolution of Ni_3Al precipitates adjacent to the boundary and transport of the constituent elements to the grain boundary Ni_3Al phase; the principal reason for the formation of such zones is believed to be the difference in lattice parameters between the precipitates (Ni_3Al) and matrix (NiAl).

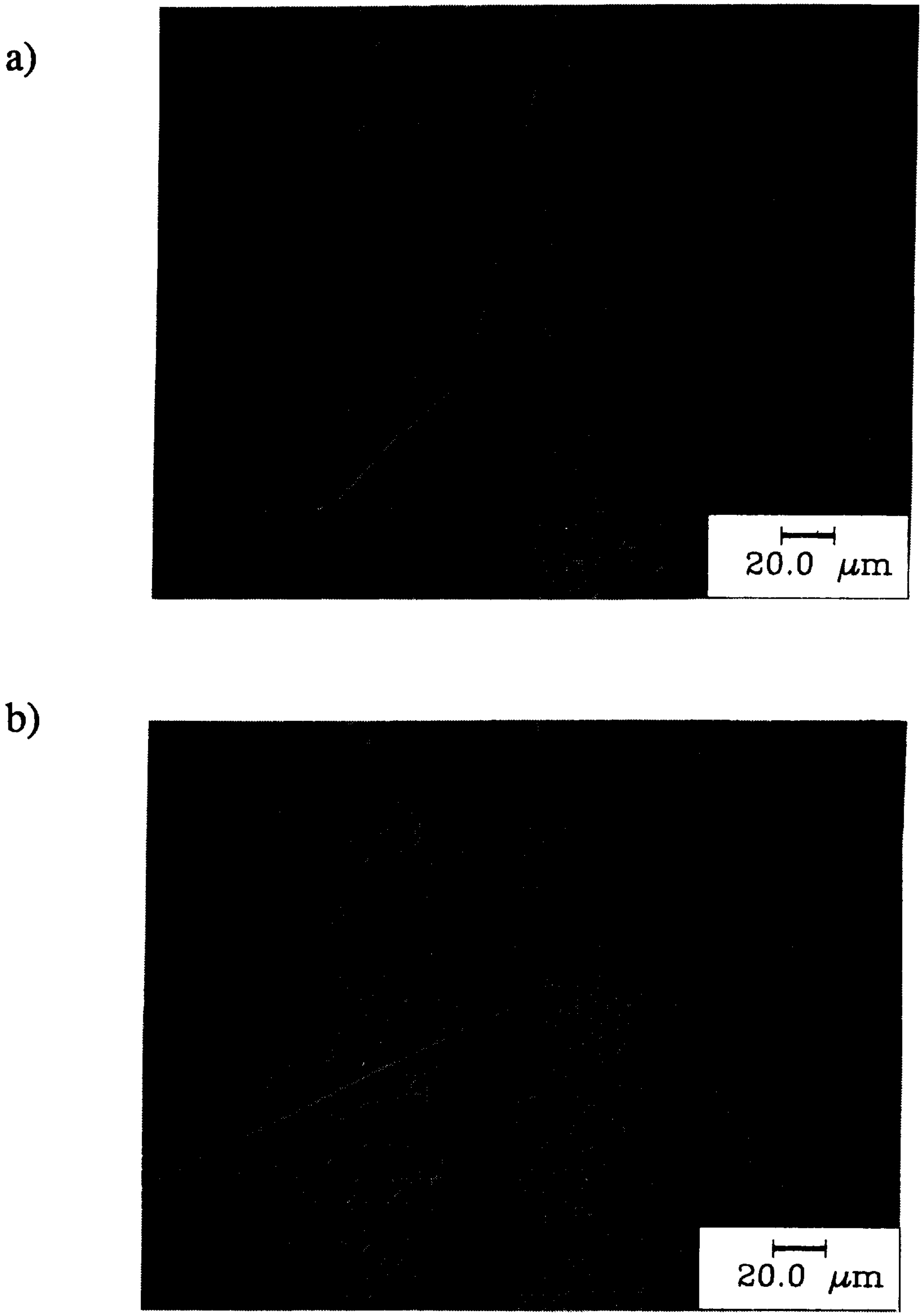

Figure 7.3 Optical micrographs of Ni-36Al, solution annealed at 1200°C for 1.5 hrs and quenched to 430°C and up-quenched to the ageing temperature of 700°C for (a) 2.5 hrs (b) 15 hrs.

When aged at 800°C (quenched from solution anneal temperature to 430°C and up-quenched to the ageing temperature) for 2.5 hrs., a precipitate free zone was also observed, see figure 7.4a. The density of precipitates in the 800°C-aged samples was higher than those when aged at 700°C for similar aging times, presumably due to increased thermal activation for transformation of the microstructure from single-phase NiAl to multi-phase NiAl+Ni_3Al. While the acicular precipitates were approximately of similar dimensions to those for samples aged at the lower temperature, the grain boundary phase was, however, considerably thicker (~5μm) which is again indicative of higher rate of diffusion of material to the grain boundary with increasing ageing temperatures. Interestingly, between the precipitate free zone and the region of acicular precipitation, a band of fine non-acicular precipitates were also observed (arrowed in figure 7.4). Longer annealing times (15 hrs) resulted in an essentially similar microstructure, see figure 7.4b.

While the acicular shape of precipitates is presumably due to the supersaturation being relieved through precipitation of the Ni_3Al phase on prior martensitic laths, similar to the Widmanstatten precipitation, the reasons behind the nucleation of spherical precipitates near the precipitate free zone are not well understood. The precipitate free zone itself is probably the result of diffusion of matter to the grain boundary to form the grain boundary precipitates.

Interestingly, for samples water quenched from the solution anneal temperature followed by annealing at 700°C (figure 7.5a-b), shorter annealing times resulted in a low density of acicular precipitates within the grain interior and a thin (~1μm) continuous grain boundary phase (Ni_3Al); longer annealing times resulted in an increased density of acicular-phase precipitation within the grain interior and an unchanged grain boundary phase thickness; no precipitate free zone was observed even after 15 hrs of annealing. For samples aged at 800°C (figure 7.6a-b), the precipitation density of acicular phase within the grain interior for similar aging times (~2.5 hrs) was higher, presumably due to the increased thermal activation for transformation; no precipitate free zone was observed.

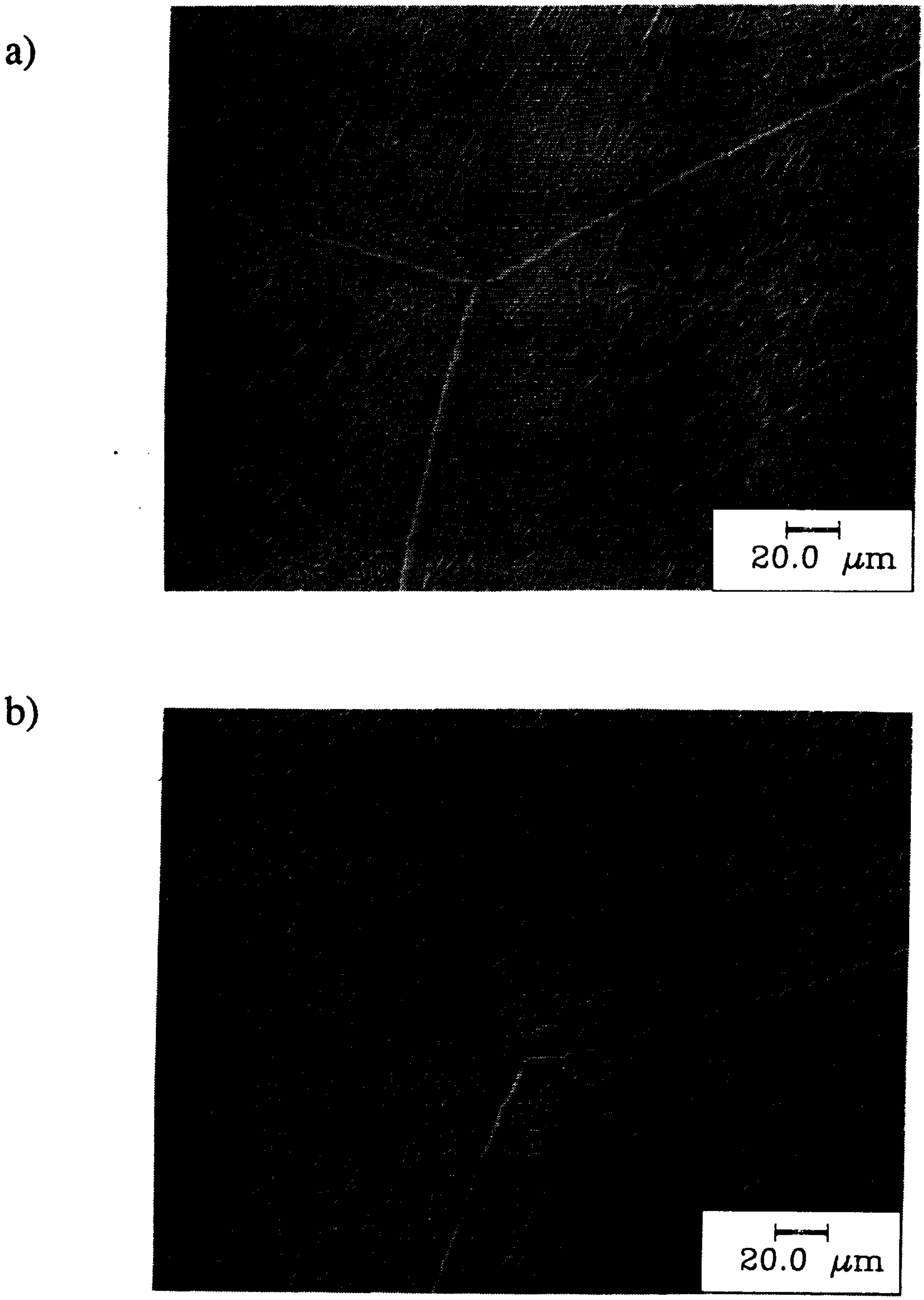

Figure 7.4 Optical micrographs of Ni-36Al, solution annealed at 1200°C for 1.5 hrs and quenched to 430°C and up-quenched to the ageing temperature of 800°C for (a) 2.5 hrs (b) 15 hrs.

ORIGINAL PAGE
BLACK AND WHITE PHOTOGRAPH

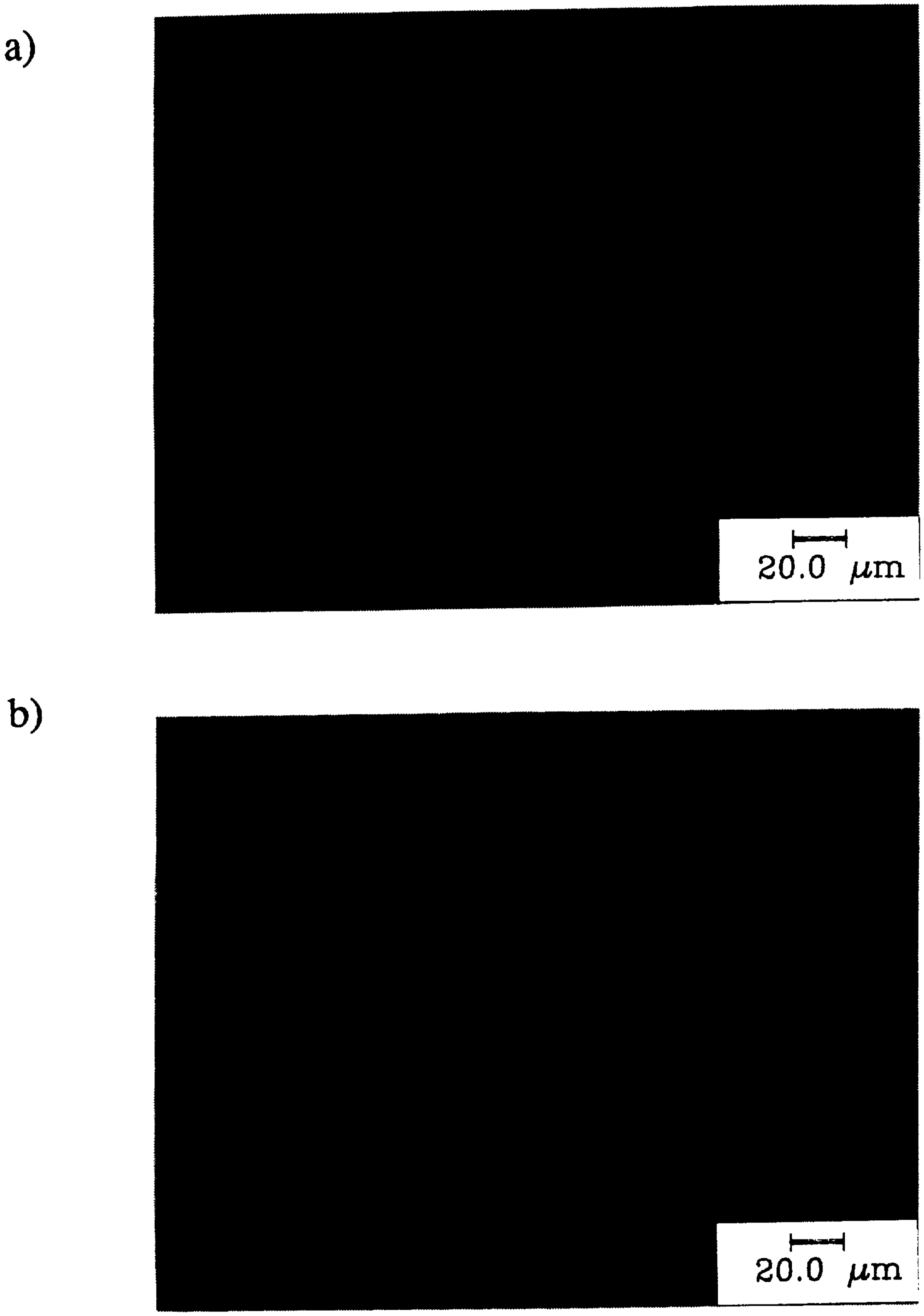

Figure 7.5 Optical micrographs of Ni-36Al, solution annealed at 1200°C for 1.5 hrs, water quenched and aged at the temperature of 700°C for (a) 2.5 hrs (b) 15 hrs.

ORIGINAL PAGE
BLACK AND WHITE PHOTOGRAPH

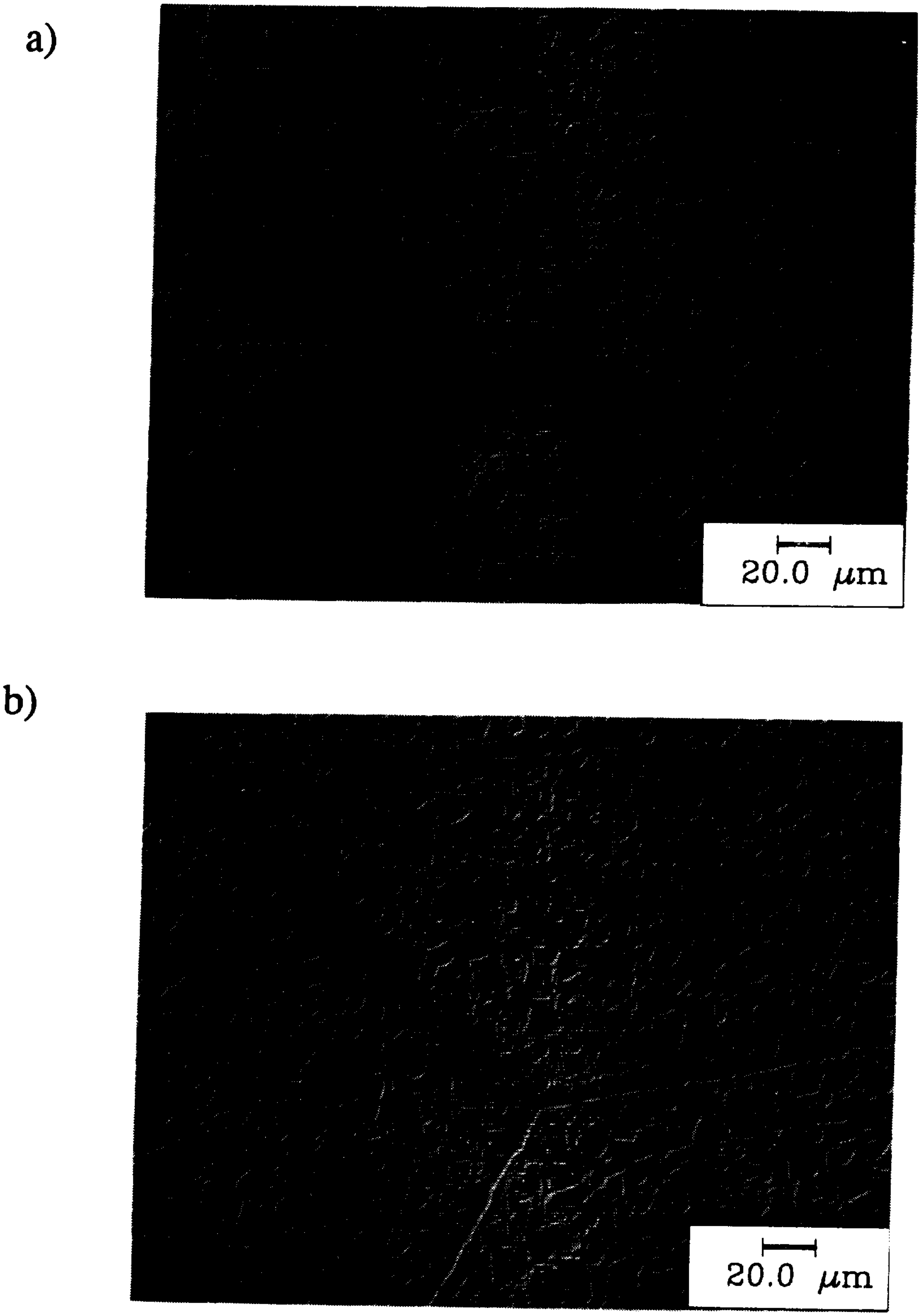

Figure 7.6 Optical micrographs of Ni-36Al, solution annealed at 1200°C for 1.5 hrs, water quenched and aged at the temperature of 800°C for (a) 2.5 hrs (b) 15 hrs.

Instead, the PFZ was replaced by a zone of fine, non-acicular precipitates, similar to although more extensive than in figure 7.4a. Also, long acicular precipitates emanating from the grain boundary into the grains (only on one side of the grain boundary which is indicative of precipitation being on certain preferred planes), similar to Widmanstatten precipitates, were observed. Longer annealing times only resulted in a coarsened grain boundary phase and acicular prcipitates (fig. 7.6b). In spite of similar ageing times of 2.5 hrs, the directly aged (water quenched from solution anneal temperature and then raised to the ageing temperature) microstructure exhibited a lower density of acicular precipitates than when up-quenched from the intermediate (430°C) hold temperature, presumably due to a higher nucleation rate at the intermediate temperature than in a water-quenched state. The thickness of the grain boundary phase, by contrast, is smaller (~2.5μm) than that when up-quenched from 430°C, presumably due to the absence of the PFZ in the former case.

Microstructures of the boron-doped alloy were similar to those for the undoped alloy presented here. Also, the microstructures following ageing at 700°C or 800°C were largely similar to those observed by Russell and Edington [20].

Mechanical Testing

In view of the flawed nature of extrusions for both boron-doped and undoped Ni-36Al alloys, the measured tensile properties were judged not to be representative of those of the alloy itself and hence tensile testing was not emphasized. Rather, the elevated temperature strength was characterized through hot hardness tests. Only one room temperature tensile test was performed in an as-extruded state for the alloy Ni-36Al; the alloy failed in a brittle manner at a low fracture stress of ~100 MPa.

Hot Hardness

The elevated temperature strength of as-extruded, boron-doped multi-phase Ni-36Al and both as-extruded and annealed, undoped alloy Ni-36Al was characterized by hot hardness indentations, similar to those discussed for ternary multi-phase alloys. Again, an average of seven indentations are reported and the error bars indicate a 95% confidence interval. From Figure 7.7a-d, it is clear that the room temperature hardness of both boron-doped and undoped binary multi-phase alloy is considerably (about 50%) higher than the ternary multi-phase alloy Ni-20Al-30Fe. Furthermore, the heat-treated microstructure (note that fig. 7.5b and 7.6b represent the microstructures after the heat treatments as outlined in figs. 7.7b-c, respectively) exhibits increased low temperature hardness although the hardness at higher temperatures is almost similar to those of the cast and extruded alloy. Also, unlike the ternary multi-phase alloy which exhibits a plateau in strength up to 400°C followed by rapid loss of strength at higher temperatures, the alloy Ni-36Al (both boron-doped and undoped) retains its strength upto ~700°C beyond which the strength decreases sharply. The dependence of hardness on temperature is reminiscent of the anomalous strengthening behavior of the γ' constituent phase in the alloy, Ni_3Al. This indicates that $\beta'+\gamma'$ alloys are capable of exhibiting good strength at intermediate temperatures which is consistent with the high temperature compressive yield strength data of Russell and Edington [20].

Fractography

The tensile fracture surface of the as-extruded alloy is shown in figure 7.8a. The as extruded alloy exhibits mixed mode (intergranular plus transgranular) fracture; note the martensitic laths across grain interiors. Figure 7.8b is a fracture surface of the binary alloy (undoped) after aging at 800°C. Again, the fracture type is mixed mode and the fractured grain boundary facets exhibit a rippled surface, presumably the result of acicular Ni_3Al precipitates within the NiAl grains. Russell and Edington [20] attributed the increased

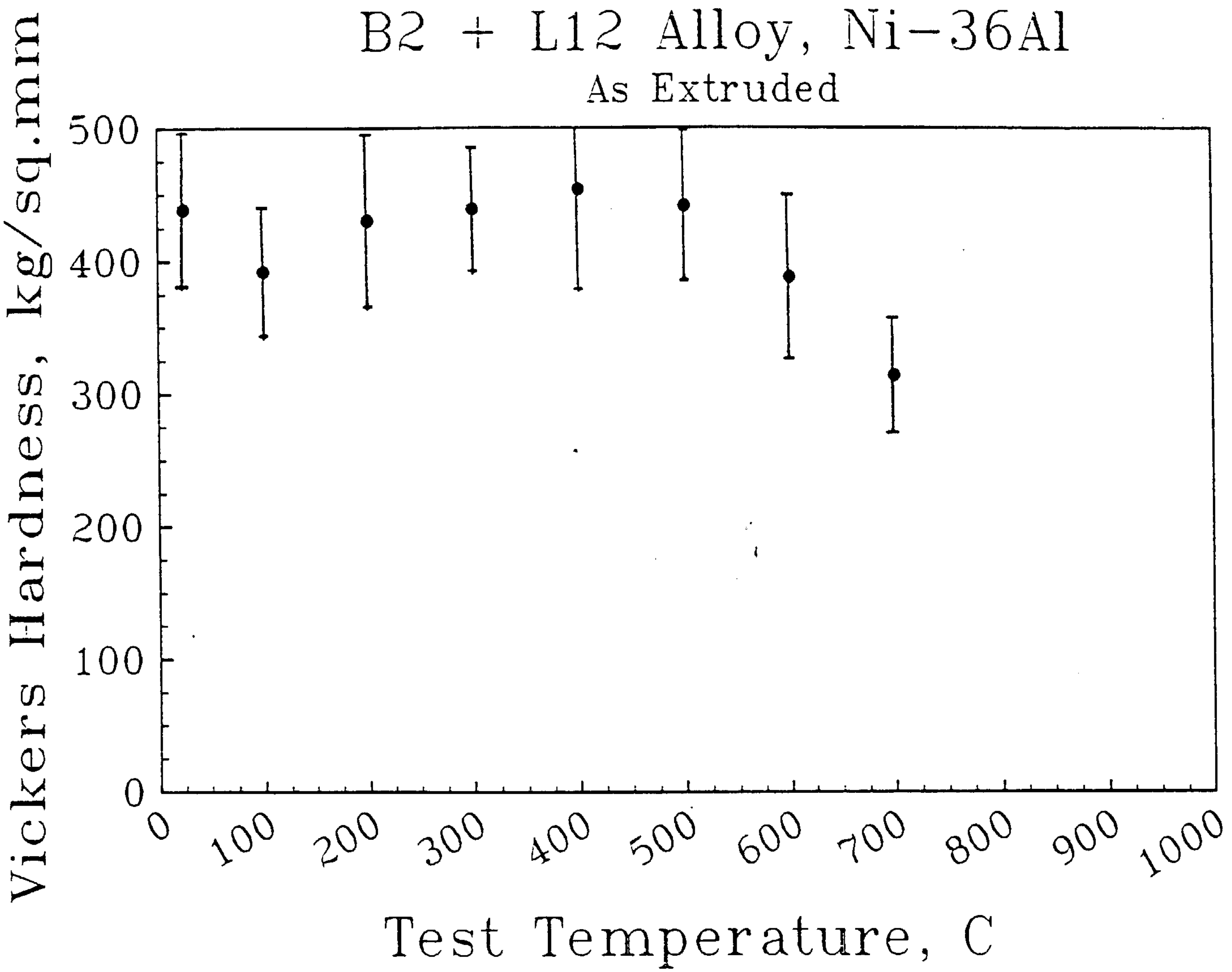

Figure 7.7a

Figure 7.7 Elevated temperature strength characteristics as measured by Vickers hot hardness indentation tests for (a) as-extruded Ni-36Al (b) heat-treated (aged at 700°C for 15 hrs) Ni-36Al (c) aged at 800°C for 15 hrs (d) as-extruded boron-doped Ni-36Al.

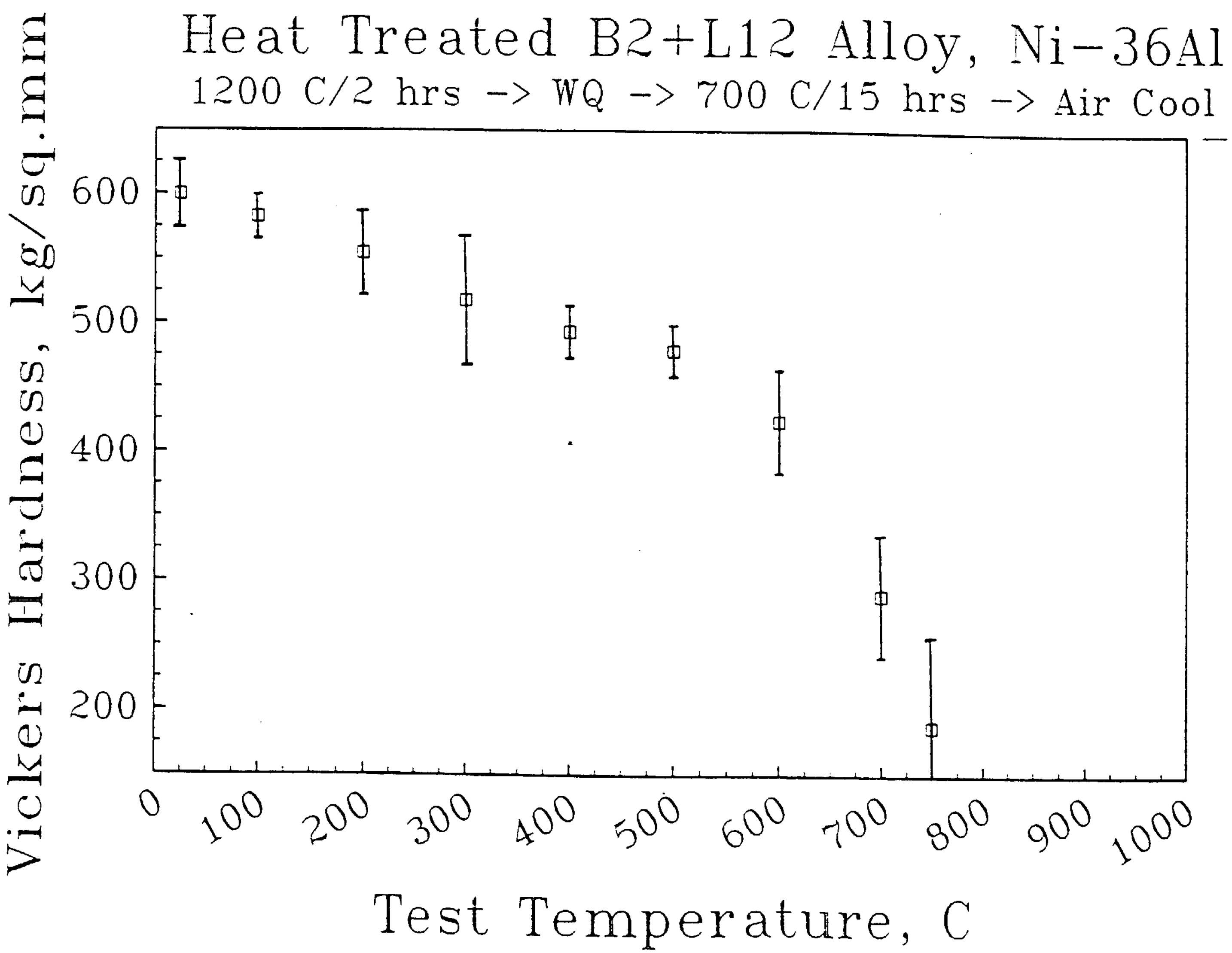

Figure 7.7b

Figure 7.7 continued.

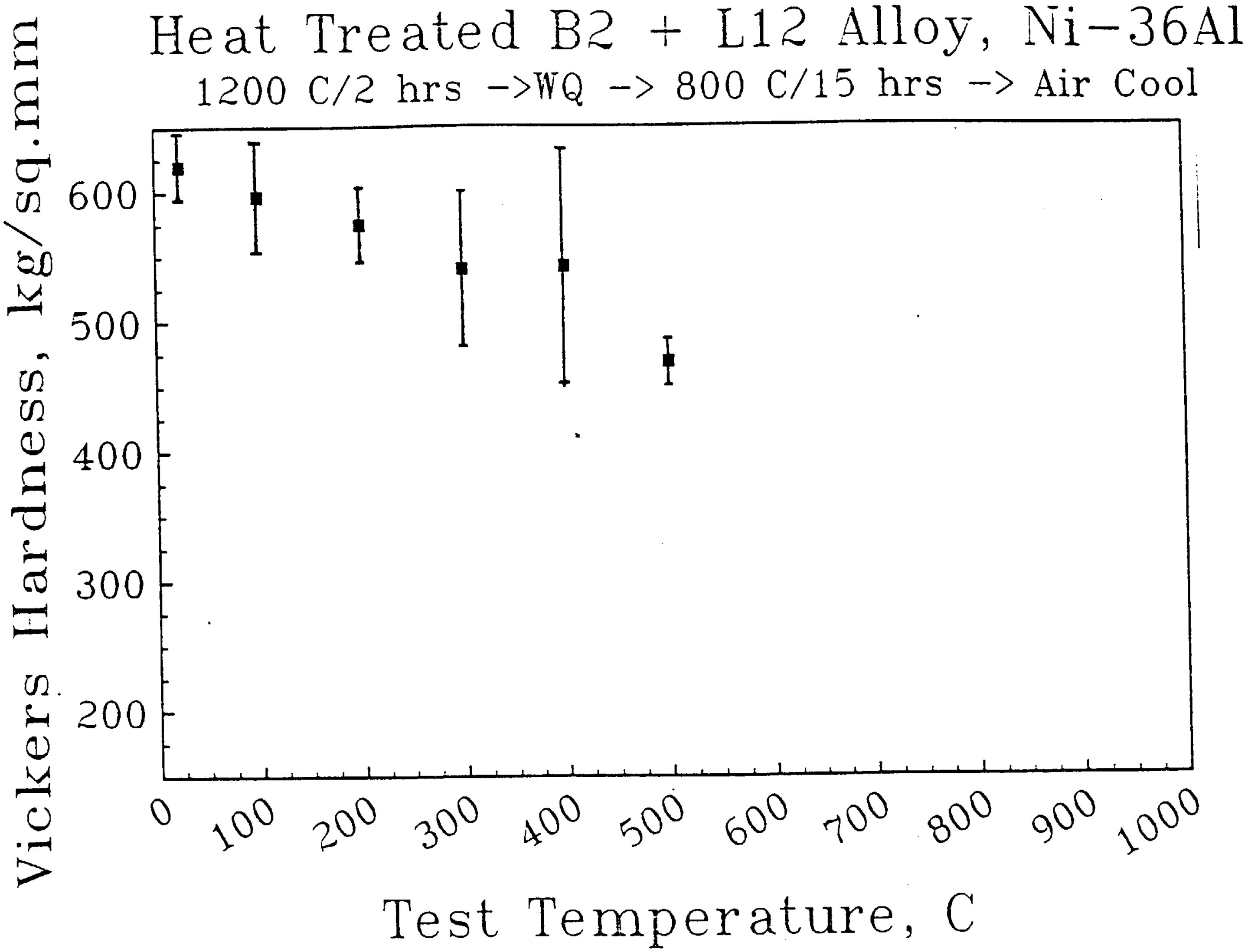

Figure 7.7c

Figure 7.7 continued.

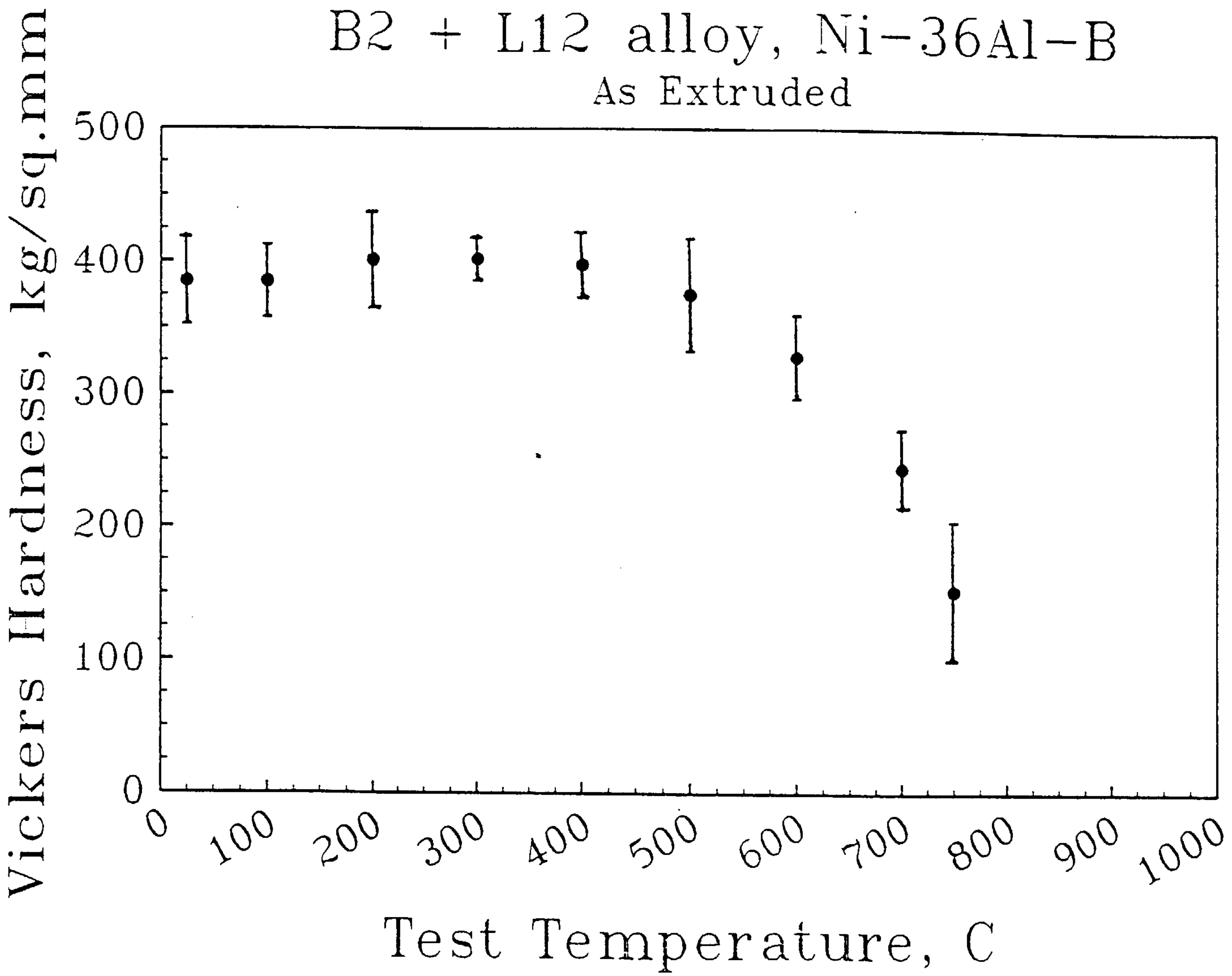

Figure 7.7d

Figure 7.7 continued.

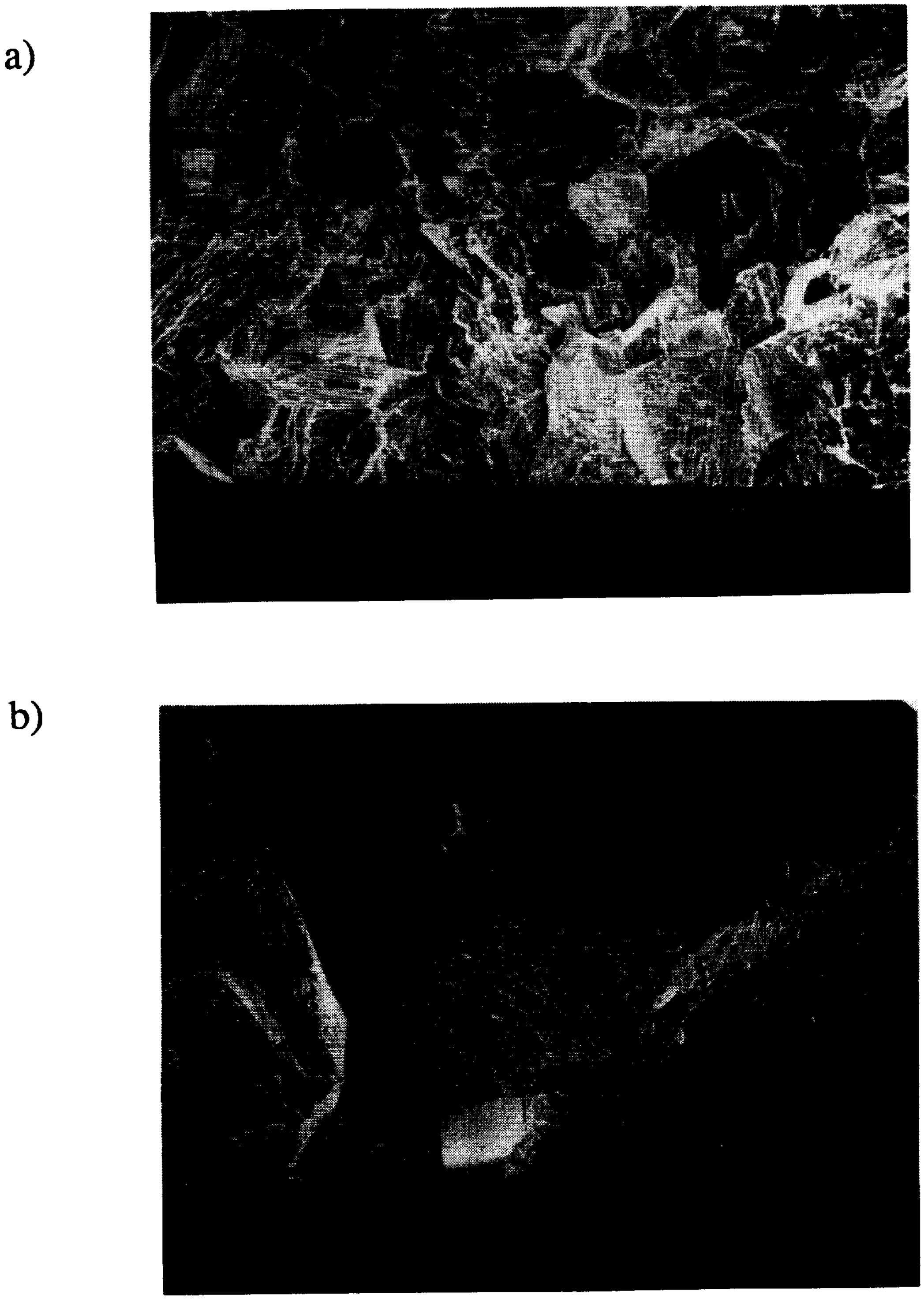

Figure 7.8 Fracture surfaces of (a) as-extruded Ni-36Al (b) heat-treated Ni-36Al aged at 800°C. The fracture mode is mixed (intergranular plus transgranular) for both conditions. Note the martensitic laths in (a) and the surface roughness of grains due to acicular precipitates in (b).

ORIGINAL PAGE
BLACK AND WHITE PHOTOGRAPH

fracture resistance that they observed of the heat treated microstructure to the acicular Ni_3Al precipitates.

In summary, the microstructures of both boron-doped and undoped binary multi-phase alloy Ni-36Al were similar. Ageing at 700°C or 800°C after a solution anneal at 1200°C resulted in microstructures largely similar to those observed by Russell and Edington [20]. The alloy is brittle in tension. Also, the elevated temperature strength retention is good which is consitent with the compressive yield strength data of Russell and Edington [20].

CHAPTER 8

Further Discussion

This chapter discusses the room and elevated temperature mechanical properties, deformation mechanisms and effect of processing (cooling rates during extrusion) of the multi-phase alloy Ni-20Al-30Fe in terms of those of its constituent phases and compares the present results with those on similar alloys investigated by others.

Ni-20Al-30Fe

Prior to this investigation, the only investigation into mechanical behavior of Ni-Fe-Al multi-phase alloys was due to Inoue et al.[28] although since then, concurrent with this investigation, there have been several reports on the mechanical behavior of such multi-phase alloys [97, 108, 113]. Inoue et al.[28] studied the alloy Ni-20Al-30Fe (along with a few other compositions) in a wire form made by 'in-rotating-water' rapid solidification technique. The microstructure was reported to consist of γ' $(Ni,Fe)_3(Fe,Al)$ plus β' (Ni,Fe)(Fe,Al) phases of 0.2μm grain size. Field et al.[97], by contrast, reported a duplex microstructure consisting of a β' phase and a fcc phase containing fine precipitates of γ' in rapidly solidified Ni-20Al-30Fe, with an orientation relationship between the β' and fcc phases, predominantly of the Kurdjumov-Sachs type. The presence of this orientation relationship was confirmed in the present work. By contrast, Larsen[113] reported a lamellar (~4μm diameter) morphology for the constituent phases in directionally solidified (DS) Ni-20Al-30Fe which is consistent with the pro-eutectic plus eutectic microstructure observed in the cast-and-extruded alloy examined here, the pro-eutectic phase probably resulted from the non-equilibrium cooling rates during casting. In contrast, pro-eutectic phase formation was suppressed in the rapidly solidified alloy [28,97], presumably due to the high undercooling. The differences in the scale of the eutectic (4μm for DS vs. 0.5μm for the cast and extruded alloy) are possibly due to the smaller undercooling and higher solidification growth rate associated with the directional solidification process compared with conventional casting, the interlamellar spacing being inversely proportional to the degree of undercooling and directly proportional to the growth rate. The duplex microstructure, as observed by Inoue et al.[28] and Field et al.[97], thus seems limited to the rapid solidification processing route.

Concerning the β'/γ interface, Larsen[113] reported the observation of misfit dislocations at the interphase interface, indicative of a semi-coherent boundary. While no misfit dislocations were observed in the extruded multi-phase Ni-20Al-30Fe, it is possible that any semi-coherent boundaries could have been eliminated during the extrusion and subsequent recrystallization processes and replaced by incoherent boundaries, characteristic of interfaces between phases exhibiting the Kurdjumov-Sachs relationship.

While Inoue et al.[28] and Huang et al.[108] examined the alloy in a rapidly solidified state, Inoue et al.[28] reported higher ductility (17%) than that reported by Huang et al.[108] (~10% ductility for rapidly solidified and annealed ribbons); the three reasons cited by Inoue et al.[28] for the good low temperature ductility were grain size refinement, suppression of ordering and suppression of grain boundary segregation. The data presented on melt-spun and annealed ribbons [108] and the extruded material here indicate that the high yield strength and plastic elongation are intrinsic properties of the alloy and not attributable only to rapid solidification processing.

Ni-30Al-20Fe

Inoue et al.[28] also reported the room temperature tensile behavior of rapidly solidified wires of the β' alloy Ni-30Al-20Fe and reported a yield strength of 400 MPa, a fracture stress of 600 MPa and 5% elongation. The fracture mode of the alloy was reported to be a mixture of dimple and intergranular fracture. Like the multi-phase alloy discussed above, the good ductility was again attributed to the rapid solidification process. By contrast, the alloy Ni-30Al-20Fe processed here through a casting and double-extrusion route (and air-cooled following extrusion) exhibited up to 6% room temperature elongation while exhibiting a yield strength of ~800 MPa, a fracture stress of ~925MPa and transgranular cleavage fracture. Although the elongation values in both investigations were similar, it is interesting to note that the yield strength for the cast and extruded alloy is almost twice that of the rapidly-solidified alloy. The microstructure of the cast-and-extruded alloy consisted of fully recrystallized β' grains of 25μm size with a thin (~10nm), discontinuous grain boundary γ phase which is in contrast to the single phase β' structure of 4μm grain size reported for the rapidly solidified wires[28]. It is not clear why, despite the smaller grain size (and hence the higher expected yield strength according to Hall-Petch relationships), the rapidly solidified wires exhibit a lower yield strength.

Recently, Raj et al.[118] have also reported the room temperature tensile behavior of Ni-30Al-20Fe microalloyed with 500 ppm Zr and processed through a powder extrusion route. Although no room temperature elongation was observed, the reported yield strength of 710 MPa was similar to the value for the cast-and-extruded alloy; the fracture mode was also observed to be of transgranular cleavage type. Interestingly, the microstructure was also reported to be single phase β' (as determined by x-ray diffraction) with a 26μm grain size. However, no grain boundary phases were reported in the powder extruded alloys. It is not clear why, despite similar grain size, the powder processed alloy is brittle while the cast and extruded alloy exhibits up to 6% room temperature elongation (although the lack of a grain boundary phase in the powder extruded alloy is a possible reason). The cooling rates of cast and extruded alloys and powder extruded alloys are expected to be similar. These results are conflicting and suggest that the observed room temperature mechanical properties of the β' alloy are highly dependent upon the processing route.

The influence of processing on room temperature ductility of Ni-30Al-20Fe is reminiscent of the influence of processing on room temperature ductility of isostructural Ni-50Al where ~2% elongation observed in a cast-and-extruded state is in contrast to the brittle behavior observed in a powder processed state. Note that the cast-and-extruded NiAl exhibited a <111> texture. Interestingly, a <111> texture is also observed for cast-and-extruded Ni-30Al-20Fe. Unlike NiAl, however, a thin, disordered grain boundary film is also observed for the ternary β' alloy. Baker and Schulson [119] have suggested the possibility of increasing the room temperature ductility of nominally brittle intermetallics by thin, disordered grain boundary phases. Such a suggestion appears to predict the ductility improvement in both Ni-24Al-0.02B [107] and Ni-30Al-20Fe. Interestingly, upon annealing at 500°C (~200 min.), while the <111> texture is still retained, the grain boundary phase is no longer observed. The annealed alloy is brittle which would be indicative of the validity of Baker and Schulsons hypothesis, that is, the ductility is enhanced by grain boundary phases rather than by a <111> texture. Unfortunately, the precipitation of fine (~10nm) α-Fe precipitates in the β' matrix (in the annealed state) precludes ascribing the embrittlement exclusively to the lack of a grain boundary disordered phase. Interestingly, for extruded stoichiometric Ni-50Al where there is no grain boundary phase but also exhibits limited tensile elongation despite its {100}<100> slip system, Vedula et al.[120] have indicated the possibility of room temperature tensile ductility being related to its <111> texture. Baker and Schulson [121], however, pointed out that for materials that deform by <100> slip, even a crystallographic texture will not alleviate the problem of lack of sufficient number of independent slip systems. By contrast, Chang et al. [122], working with NiAl single crystals, have reported that the fracture toughness is minimum along {110} planes and suggested that a crystallographic texture may possibly reduce the stress intensity factor along the weakest planes thereby delaying the onset of fracture. (Note that {110} planes were also identified as the cleavage planes in NiAl single crystals by Pascoe and Newey [9]). Hence, based on the results of the present investigation, it is not possible to determine either texture or grain boundary phases as a ductility enhancing microstructural feature. Rather, it is suggested that both texture and grain boundary phases appear conducive to good room temperature ductility.

27°C Mechanical Properties of Multi-phase alloy: Single extruded vs Double-extruded

Room temperature tensile tests of alloys similar to the constituent phases of the multi-phase alloy suggest that the large ductility of the γ/γ' phase is primarily responsible for the observed good room temperature ductility in the multi-phase alloy while the high strength is attributable to the strength of the β' phase. Some differences were, however, observed between the room temperature mechanical properties of single and double-extruded multi-phase and β' alloys. For the multi-phase alloys, the differences between the room temperature behavior of the single and double-extruded alloys, however, cannot simply be attributed to microstructural refinement following a second extrusion since the double-extruded alloy, coarsened by annealing at 1300°C (and air-cooled) still exhibits higher elongation than the single-extruded alloy. Hence, the effect of annealing on the room temperature mechanical behavior of the constituent phases need to be considered. Isochronal annealing experiments on β' and γ/γ' phases have shown that the β' phase exhibits hardening and embrittlement with a 500°C anneal while the properties of the γ/γ' alloy are generally unaffected (for annealing temperatures up to ~800°C). Like the β' alloy, the multi-phase alloy also exhibits hardening and loss (by almost 50%) of ductility when annealed at 500°C. Since the single-extruded alloys (both multi-phase Ni-20Al-30Fe and β' Ni-30Al-20Fe) were sand-cooled following extrusion while the double-extruded alloys were air-cooled, the slower rate of cooling from extrusion temperature for the single-extruded alloys probably resulted in a microstructural state similar to the 500°C annealed state for the double-extruded alloys. Hence, like the 500°C annealed double-extruded alloys, the single-extruded alloy would also be expected to be stronger and less ductile than the double-extruded (not annealed) alloys. This expectation is indeed correct for both the β' and the multi-phase alloy indicating that room temperature mechanical properties are considerably affected by post-processing cooling rates.

Elevated Temperature Mechanical Behavior of the Multi-phase Alloy

The hot-hardness and elevated temperature tensile test data indicate that while the the strength of the β' alloy decreases with increasing temperature, the γ/γ' retains its strength up to 700°C: unlike many γ'-based alloys, no anomalous strengthening was observed for the γ/γ' alloy. The multi-phase alloy exhibits a behavior intermediate between that of its constituent phases. Thus, at room temperature its yield strength (~760 MPa) is similar to that of the β' phase (~800 MPa) rather than that of the γ/γ' phase (yield strength ~500 MPa), while at 627°C, where the β' phase exhibits poorer strength (~200 MPa), its strength (~310 MPa) is similar to that of the γ/γ' phase (~345 MPa). Similarly, while the room temperature elongation of 20% is similar to that of the γ/γ' phase (which exhibits ~28% elongation), at higher temperatures, where the γ/γ' phase is brittle ($\varepsilon_f < 1\%$), the ductility of the multi-phase alloy (34 and 100% at 627°C and 827°C respectively) is similar to that of the β' phase (27 and 97%). This indicates that over the temperature range 300-827°C, the multi-phase alloy avoids the problems associated with each of its constituent phases at any particular temperature. The poor elevated temperature strength of the multi-phase alloy can be ascribed to both the poor elevated temperature strength of the β' constituent phase as well as the dissolution / disordering of γ' particles into γ and the lack of anomalous strengthening of the γ/γ' phase. The variation of the yield strength with temperature for the β' alloy Ni-30Al-20Fe is similar to that of both stoichiometric and off-stoichiometric NiAl alloys [4,5], although the transition temperatures (T_t) are different due to differences in solidus temperatures [1,7]. Interestingly, powder processed Ni-30Al-20Fe microalloyed with 500 ppm Zr [118], while exhibiting similar high temperature strength characteristics to the undoped Ni-30Al-20Fe, also exhibited a higher brittle-to-ductile transition temperature than the undoped Ni-30Al-20Fe processed through a cast-and-extrusion route.

Recently, the yield strength of DS Ni-20Al-30Fe was measured in compression over the temperature range 100-627°C [123]. The room temperature microstructure of the DS alloy has been discussed above. The phases observed at room temperature were similar to those observed in the present investigation (material processed through a casting and extrusion route) and those of Huang et al. [108], who studied rapidly solidified ribbons. While the elevated temperature behavior for the DS alloy was similar to that reported in this study, the room temperature yield strength (500 MPa) and tensile elongation (10%) were lower than the yield strength (760 MPa) and tensile elongation (~20%) reported here. The differences in room temperature mechanical behavior are probably related to differences in the scale of the microstructure (0.5μm lamellae width for cast and extruded Ni-20Al-30Fe compared to ~4μm lamellae wdith for the DS alloy).

γ/γ' Alloy Ni-12Al-40Fe

While the elevated temperature mechanical behavior of the β' phase examined here is typical of B2 alloys, the mechanical behavior of the γ/γ' alloy is worth further comment. Horton et al.[90] studied the elevated temperature mechanical behavior of some Ni-Fe-Al γ'-based alloys containing up to 20 at.% iron and reported a positive temperature dependence of the yield strength in each case. The degree of anomalous strengthening (i.e. difference in strength between 600°C and room temperature) was approximately constant for up to 10 at.% iron but decreased for alloys with higher iron concentrations. For example, the alloy Ni-15Al-20Fe exhibited nearly the same yield strength at 27°C and 600°C. If the trend is assumed to continue for higher iron concentrations, the lack of any positive temperature dependence of yield strength for the γ/γ' alloy Ni-12Al-40Fe is not surprising. Beardmore et al.[98] have shown that for Ni-Cr-Al γ/γ' alloys the degree of anomalous strengthening is sensitive to volume fraction of γ' precipitates, and increases with increasing volume fraction of precipitates. The observed behavior of γ/γ' Ni-12Al-40Fe is similar to the low (about 10-20%) γ' volume fraction alloys of Beardmore et al.[98]. However, the volume fraction of γ' precipitates in Ni-12Al-40Fe is much higher (see chapter 4), thus the observed lack of anomalous strengthening probably reflects the intrinsic behavior of the alloy. Between room temperature and 850°C, Horton et al.[90] also noted an increase in yield strength with increasing iron concentration. The room temperature strength of Ni-15Al-20Fe (637 MPa) they examined was higher than that of Ni-12Al-40Fe (507 MPa) examined here, indicating the deleterious effect of high iron concentration on the strength of γ' phases. The ductility drop at elevated temperature for the γ/γ' alloy Ni-12Al-40Fe was also observed in the alloys studied by Horton et al.[90]. While the effect has often been ascribed to dynamic embrittlement by oxygen [72], the observation of voids limited to only the γ/γ' phase in the interior of the multi-phase alloy, where it could be assumed to be shielded from ambient oxygen by the β' phase, indicates the possibility that the brittle behavior is intrinsic to the alloy at intermediate temperatures. For alloys containing up to 20 at.% iron, Horton et al.[90] observed the embrittlement to be most severe at 850°C, while for the Ni-12Al-40Fe studied here the corresponding temperature was ~627°C, indicating that the embrittlement temperature may be composition dependent.

Deformation Behavior of Multi-phase alloy

Turning now to the deformation modes, Field et al.[97] have reported the presence of a few <111> dislocations in the β' phase, although the majority of the dislocations had a <100> Burgers' vector. By contrast, only <100> dislocations were observed in the pro-eutectic β' phase of Ni-20Al-30Fe and in the cast and extruded β' alloy Ni-30Al-20Fe. The difference could be related to the fact that while the thin foils examined by Field et al.[97] were strained ~10%, those examined in the present work were strained ~2%, thus the stress in the former case presumably reached a level sufficient for activation of <111> slip. The activation of <111> slip in the β' phase at higher stress levels may provide additional deformation modes. It is emphasized, however, that <001> slip is the predominant deformation mode in the β' phase of the multi-phase aggregate, which is consistent with the observation that <001> slip occurs in the β'-structured alloy Ni-30Al-20Fe until fracture. Further, the primary deformation mechanism for β' phase, namely glide of <100> dislocations, does not change between 27°C and 827°C, although <110> dislocations arising from the interaction of <100> dislocations may contribute to the deformation of β' phase at higher temperatures. Similar observations of <110> dislocations in β' NiAl deformed at elevated temperatures has been noted by Lloyd and Loretto[124], Zaluzec and Fraser[125], Lasalmonie[126] and Baker and Schulson[121]. Mobile segments of <110> dislocations may alleviate the grain boundary incompatabilities resulting from only three independent slip systems provided by <001> slip [12] by providing additional slip systems. By contrast, Ball and Smallman [127] have suggested that elevated temperature deformation occurs through climb and cross slip of <100> dislocations. Such a suggestion would also be difficult to rule out in view of the dependence of T_t on melting point noted earlier. It is possible that both the above mechanisms are active in the elevated temperature deformation of β' alloys. For the γ/γ' phase deformation occurs by the motion of <110> dislocations at low temperature but 1/2<110> dislocations at elevated temperatures when disordering has occurred.

Returning to room temperature deformation, Field et al.[97], Larsen[113] and Huang et al.[108] have reported observations which they suggest indicate slip transfer between the β' and γ/γ' grains, and which thus are the reason for ductility in Ni-20Al-30Fe. Larsen[113] suggested that the production and emission of dislocations at the interphase interface, arising from the need to maintain plastic continuity between the phases, was the reason for ductility in Ni-20Al-30Fe. Field et al.[97] and Huang et al.[108] also reported ledges at the interphase interface which align with the {111} planes of the fcc phase and suggested that those arose from the deformation process, and facilitate the transmittal of dislocations across the interface, thereby imparting ductility top the alloy. While the transmittal of deformation across the interface was indeed confirmed by TEM in-situ experiments, it should be emphasized that deformation transfer did not necessarily imply transfer of slip dislocations. The evidence presented indicates that while slip transfer, as suggested by Huang et al.[108], does occur for specially aligned β'-γ/γ' grains, with the deformation indeed resulting in ledges which align with the {111} plane of γ/γ' phase, the majority of the grains are related by a Kurdjumov-Sachs relationship where such slip transfer is not observed (see section on in-situ straining in chapter 4). Rather, the predominant mode of deformation transfer appears to be the stress-assisted nucleation of slip in adjacent grains. Deformation transmittal occurs both from β' to γ/γ' phases and vice versa.

TEM in-situ experiment observations may also explain the lower (~10%) ductility observed by Field et al.[97] in their rapidly solidified ribbons compared to 17% in rapidly solidified wires and 22% in cast-and-extruded state; the difference may be related to differences in geometry of test specimens. As observed during in-situ straining, the γ/γ' phase in thin foils are more likely to generate cracks along slip bands which are transferred to the more brittle β' phase, hence the multi-phase aggregate is more likely to fail prematurely in a thin-foil (ribbon) form than as a wire or a dumb-bell shaped tensile specimen.

Multi-phase Alloy Design

This study of deformation behavior points to an interesting alloy-design philosophy. While NiAl-based β' alloys are attractive due to their low density and good oxidation resistance, their ambient temperature brittleness and poor yield strength and creep resistance at elevated temperatures are disadvantageous. By contrast, while Ni_3Al-based γ' alloys exhibit good high temperature strength (due to anomalous strengthening) and better creep properties (than β' alloys) along with good room temperature ductility (at least for boron doped nickel-rich alloys), they can exhibit brittle behavior at elevated temperatures (600°C-800°C) in air. Furthermore, the density and oxidation resistance properties of the γ' alloys are worse than β' alloys due to their lower aluminum content. The $\beta'+\gamma'$ (or $\beta' + \gamma/\gamma'$) multi-phase alloys, however, may offer a compromise in ductility and strength, both at room temperature and at elevated temperatures, with each phase alleviating the problems associated with the other constituent phase at any temperature. Also, since γ/γ' alloys are more creep resistant than γ' alloys, the addition of some suitably chosen γ/γ' alloy (which exhibits anomalous strengthening, see ref. 90) may offer the additional advantage of improved creep strength. Interestingly, Russell and Edington [20] reported high yield strength (700 MPa), independent of temperature up to 700°C, for a heat-treated $\beta'+\gamma'$ alloy, Ni-36Al. Hot hardness tests on Ni-36Al (chapter 7), processed similar to the multi-phase alloy, indicated high strength up to 700°C thereby confirming the behavior observed by Russell and Edington. Note that the γ' phase in Ni-36Al is Ni_3Al which exhibits anomalous strength behavior at high temperatures and remains ordered up to its melting point. Thus, improved high temperature strength in multi-phase ($\beta' + \gamma/\gamma'$) Ni-Fe-Al alloys could be obtained by the addition of some suitably chosen $(Ni\text{-}Fe)_3(Fe,Al)$ phase which exhibits anomalous strength behavior and remains ordered up to its melting point.

SUMMARY OF MAJOR RESULTS

Mechanical testing, fractography, optical and scanning electron microscopy of polished longitudinal sections and transmission electron microscopy of thin foils from both undeformed and deformed samples (deformed at both room and elevated temperatures) of the cast and extruded multi-phase alloy Ni-20Al-30Fe and alloys similar to its constituent phases have shown that:

1. The microstructure of Ni-20Al-30Fe consists of a pro-eutectic β' phase (of approx. composition Ni-30Al-20Fe) in a multi-phase eutectic. The eutectic also consisted of a β' phase (of composition Ni-32Al-17Fe); the microstructure of the other eutectic phase (of composition Ni-12Al-40Fe) was concluded to be γ/γ' (i.e. γ' precipitates in a f.c.c matrix).

2. The double-extruded multi-phase alloy exhibited a room temperature yield strength of 760 MPa and about 20% elongation. By contrast, the β' alloy exhibited up to 6% elongation while the γ/γ' Ni-12Al-40Fe exhibited a lower yield strength of 507 MPa and higher elongation (up to 37%).

3. When annealed at 500°C, a fine precipitation of α-Fe in the β' matrix was observed. In this annealed state, the β' alloy Ni-30Al-20Fe was brittle and the yield strength increased to 1000 MPa. The multi-phase alloy also exhibited a reduction in ductility (measured at 10%) and increase in yield strength (850 MPa) after a similar anneal. The γ/γ' alloy was essentially unaffected by this heat treatment.

4. When annealed at 750°C, instead of α-Fe dispersion in the β' matrix, a grain boundary γ phase was observed in the β' alloy Ni-30Al-20Fe. After this anneal, the β' alloy was ductile (2%) while the strength decreased to 700 MPa. By contrast, the precipitation of a β' grain boundary phase was observed in the γ/γ' alloy Ni-12Al-40Fe which led to a decrease in ductility and slight increase in yield strength. The mechanical properties of the multi-phase alloy after annealing at 750°C were essentially similar to those in the as-extruded state.

5. The elevated temperature strength of the β' alloy Ni-30Al-20Fe is typical of a B2 compound *viz.*, a yield strength plateau (at ~800 MPa) up to ~425°C after which the strength decreased rapidly while the ductility increased (from ~2% elongation at room temperature) with increasing temperature.

6. The γ/γ' alloy exhibited a gradual decrease in strength (from 507 MPa at room temperature) with increasing temperature to 625°C, above which the strength decreased more rapidly due to the coarsening and eventual dissolution of the γ' precipitates into the γ matrix. The failure strain was high at low temperatures (37% elongation at room temperature) but a ductility drop occurred at elevated temperature (to < 1% elongation), a feature observed in several related alloys [90].

7. The yield strength of the multi-phase alloy decreased slowly from 760 MPa at room temperature to 310 MPa at 625°C, after which it fell rapidly. The behavior was similar to that of its constituent phases. In contrast, the alloy exhibited good ductility at all temperatures, indicating that the arrangement of the constituent phases could ameliorate the inherent brittleness of the individual phases.

8. Slip was by <100> dislocations in the β' phase at all temperatures. Slip in the γ/γ' phase was by paired 1/2<110> dislocations at low temperature but by single 1/2<110> dislocations at elevated temperatures where the γ' precipitates had dissolved.

9. The ductile behavior of the multi-phase alloy Ni-20Al-30Fe at room temperature is related to the ductility of the constituent γ/γ' phase, Ni-12Al-40Fe. While failure occurred by the catastrophic propagation of cracks nucleated in the β' phase, one way the γ/γ' phase improves the ductility of the multi-phase polycrystalline aggregate is by inhibiting the crack propagation process.

10. During in-situ straining of multi-phase alloy samples at room temperature, transfer of deformation across the β'-γ/γ' interface was observed which indicates that besides inhibition of crack propagation process, the γ/γ' phase also improves ductility by easing the transmittal of deformation across grains (phases) in the polycrystalline aggregate.

11. The creep behavior of the double-extruded multiphase alloy at 827°C is similar to that of its constituent β' phase; by contrast, the γ/γ' phase is more creep resistant. Coarsening of the microstructure improved creep resistance indicating that interfacial sliding contributes significantly to the creep deformation of the multi-phase alloy.

12. Microalloying with boron did not significantly influence either the room temperature or the high temperature mechanical behavior of the multi-phase alloy Ni-20Al-30Fe.

CONCLUSIONS

From the present study, it is concluded that:

1. Macroalloying NiAl with Fe indeed results in improved room temperature ductility and yield strength although the deformation mechanism (slip vector) remains unchanged.

2. <100> slip does not necessarily result in brittle behavior for β' alloys; other microstructural features like disordered grain boundary phases and texture are also important.

3. Multi-phase approach to alloy design appears to be promising for intermetallics since the deficiencies in mechanical properties of any one phase may be alleviated by the addition of a suitably chosen second (or multiple) phases.

4. The extensive room temperature ductility of the multi-phase alloy is attributed to deformation transfer across interphase interfaces and crack stopping by the more ductile (γ/γ') constituent phase.

SUGGESTIONS FOR FUTURE WORK

The effect of texture on the mechanical properties of ordered alloys, especially those limited by the number of independent slip systems (e.g B2, $D0_{19}$ alloys) or those limited by the number of operative slip systems (e.g. $L1_0$ alloys), needs a closer examination. Chang's suggestions of different fracture toughness of single crystal intermetallics depending upon the orientation needs to be examined in case of other alloys like TiAl, Ti_3Al, $MoSi_2$ etc. It may be possible to improve the mechanical properties of such intermetallics by some suitable texture to the polycrystalline aggregate.

Similarly, the effect of disordered grain boundary phases on the room temperature mechanical behavior, especially ductility, needs to be determined in some other intermetallic systems like TiAl. Note that for TiAl, at Al deficient compositions (in the composition range 50-52 at.%Al and sufficiently high temperatures, a disordered β phase lies adjacent to the γ TiAl phase field. It may be possible that the observed trend of increasing ductility with decreasing Al contents (closer to the two-phase field) may be due to the retention of a thin (of the order of nm) disordered grain boundary film, possibly similar to Ni_3Al, during cooling of the microstructure from high temperatures. Although no such disordered grain boundary phases have been reported in the literature, a careful examination of the grain boundaries is warranted before the suggestion may be ruled out.

In view of the strong interest in B2 alloys, it is expected that further Ni-Fe-Al B2 alloys will be examined for their room temperature mechanical behavior. The observed room temperature ductility of ~6% for cast and extruded Ni-30Al-20Fe is interesting, especially since other investigators have failed to reproduce the property for the same alloy composition through powder processing. This indicates that powder processed intermetallics alloys which have been reported to be brittle in the past should be re-examined after processing through a casting and extrusion approach.

Finally, although the multi-phase alloy itself exhibited some interesting propertites both at room temperature and elevated temperatures, further development of such a class of alloys based on a three-phase $\gamma'+\beta'+\beta''$ or even four-phase $\gamma/\gamma' + \beta' + \beta''$ microstructures is required (β'' being the Heusler phase). Some efforts in this direction (on Ni-Al-Ti alloys) are already under way at the University of Cambridge under the leadership of Prof.R.W. Cahn. Although no such Heusler phases are observed in the Ni-Fe-Al system, the available ternary phase diagrams indicate that such systems are possible in Fe-Ti-Al, Co-Ti-Al etc. For Ni-Fe-Al alloys, the most promising results, however, are the observed room temperature ductility in B2 alloys. It should also be noted that Dr. R. Darolia (General Electric- Aircraft Engines) has recently indicated that microalloying NiAl single crystals with iron dramatically improves the tensile ductility. A better understanding of the effect of Fe additions at the ppm level on the room temperature tensile ductility is required.

REFERENCES

1. "Materials for Aerospace", Morris A. Steinberg, Scientific American, 1986, 67.
2. "The plane of the future", P. Grier, Govt. Executive, Sept. 1989, 19.
3. "The challenges of the orient express", John Vaccari, American Machinist, Jan. 1990, 55.
4. "Materials pace aerospace technology", J.J. De Luccia, R.E. Trabocco, J. Waldman and J.F. Collins, Advanced Materials and Processes, May 1989, 39.
5. "NASA's Hitemp program: build it or buy it", Materials Engineering, Jan. 1990, 51.
6. M.F. Singleton, J.L. Murray, and P. Nash, in Binary Alloy Phase Diagrams I, eds.T.B. Massalski, (ASM Metals Park, OH, 1986) 142.
7. J.K. Doychack, T.E. Mitchell, and J.L. Smialek, "High Temperature Oxidation of Beta-NiAl" in High Temperature Ordered Intermetallic Alloys, eds. C.C. Koch, C.T. Liu, and N.S. Stoloff, (Pittsburgh, PA, Materials Research Society, 1985), 3.
8. R.T. Pascoe and C.W.A. Newey, Metal Sci., 5 (1971) 50.
9. R.T. Pascoe and C.W.A. Newey, Metal Sci., 2 (1968) 138.
10. A. Ball and R.E. Smallman, Electron Microscopy, 1 (1964) 273.
11. G.W. Groves and A. Kelly, Phil. Mag., 8 (1963) 877.
12. R. von Mises, Z. agnew. Math. Mech., 8 (1928) 161.
13. E.M. Schulson, Res. Mech. Letters, 1, (1981) 111.
14. E.M. Schulson and D.R Barker, Scripta Metall., 17 (1983) 519.
15. R.B. Graham, M.E. Thesis, Dartmouth College, 1984.
16. J.D. Whittenberger, Mat. Sci. Eng., 57, (1983) 77.
17. A.U. Seybolt, Trans. ASM, 59 (1966) 860.
18. K. Aoki and O. Izumi, J. Japan Inst. Met., 43 (1979) 1190.
19. I. Baker and E.M. Schulson, Phys. Stat. Solidi (a), 85, (1985) 163.
20. K.C. Russell and J.W. Edington, Met. Sci. J., 6 (1972) 20.

21. R. Moskovic, J. Mat. Sci., 13, (1978) 1901.

22. C.T. Liu and H. Inouye, Met. Trans., 10A, (1979) 1515.

23. Y. Umakoshi and M. Yamaguchi, Phil. Mag. A, 4, (1980) 573.

24. M.G. Mendiratta, H.K. Kim and H.A. Lipsitt, Met. Trans., 15A, (1984) 395.

25. G. Sainfort, P. Mouturat, P. Pepin, G. Cabane and M. Salesse, Mem. Sci. Rev. Met., 60, (1963) 125.

26. C.C. Law and M.J. Blackburn, in Rapidly Solidified Lightweight Disk Material, Interim Report no. FR-18674-4, (1985).

27. P.S. Khadkikar, K. Vedula and B.S. Shabel, High Temperature Ordered Intermetallic Alloys - II, eds. N.S. Stoloff, C.C. Koch, C.T. Liu and O. Izumi, (Pittsburgh, PA, Materials Research Society, 1987) 157.

28. A. Inoue, T. Masumoto and H. Tomioka, J. Mat. Sci., 19, (1984) 3097.

29. A. Inoue, H. Tomioka and T. Masumoto, Met. Trans., 14A, (1983) 1367.

30. S. Furukawa, A. Inoue and T. Masumoto, Mat. Sci. Eng., 98 (1988) 515.

31. N. Ridley, J. Inst. Metals, 94 (1966) 255.

32. M.J. Cooper, Phil. Mag., 8 (1963) 805.

33. P. Delavignette, H, Richel and Amelinkx, Phys. Stat. Sol. (a), 13 (1972) 545.

34. R.J. Wasilewski, S.R. Butler and J.E. Hanlon, J. Appl. Phys., 39 (1968) 4234.

35. A.T. Donaldson and R.D. Rawlings, Acta Metall., 24 (1976) 811.

36. R.J. Wasilewski, J. Phys. Chem. Solids, 29 (1968) 39.

37. R. J. Wasilewski, J. Phys. Chem. Solids, 29 (1968) 51.

38. R. Meyer, E. Waschete and V. Gerold, Z. Metallk.,67 (1976) 97.

39. D. Paris and P. Lesbats, J. Nucl. Mater., 69/70 (1978) 628.

40. T. Hughes, E.P. Lautenschlager, J.B. Cohen and J.O. Brittain, J. Appl. Phys., 42, (1971) 3705.

41. R. Moskovic, J. Mat. Sci., 12 (1977) 489.

42. R.T. Pascoe and C.W.A. Newey, Phys. Stat. Sol., 29 (1968) 357.

43. S. Rosen and J.A. Goebel, Trans. TMS-AIME, 242 (1968) 722.

44. W.A. Maxwell and E.M. Grala, NACA TN3259 (1954) 39.

45. A. Ball, Met. Sci. J., 1 (1967) 47.

46. K. Enami, S. Nenno and K. Shimizu, Trans. Japan Inst. Metals, 14 (1973) 161.

47. J. Smialek and R. Hehemann, NASA TM X-2654 (1972).

48. K. Enami and S. Nenno, Met. Trans., 2 (1971) 1487.

49. I.M. Robertson and C.M. Wayman, Metallography, 17 (1984) 43.

50. I.E. Locci, P.S. Khadkikar, R.D. Noebe and K. Vedula, Proc. XII International Congress for Electron Microscopy, (1990).

51. A.G. Rozner and R.J. Wasilewski, J. Inst. Met., 94 (1966) 169.

52. E.M. Grala, "Mechanical Properties of Intermetallic Compounds", (1960).

53. K.H. Hahn and K. Vedula, Scripta Met., 23 (1989) 7.

54. A. Ball and R.E. Smallman, Acta Met., 14 (1966) 1349.

55. R.J. Wasilewski, S.R. Butler and J.E. Hanlon, Trans. Met. Soc. AIME, 239 (1967) 1357.

56. S.M. Copley, ibid., 8 (1963) p. 1599.

57. K. Aoki and O. Izumi, J. Mat. Sci., 14, (1979) 1800.

58. T. Takasugi, E.P. George, D.P. Pope and O. Izumi, Scripta Metall., 19 (1985) 551.

59. C.T. Liu, C.L. White and J.A. Horton, Acta Metall., 33 (1985) p. 213.

60. T.P. Weihs, V. Zinoviev, D.V. Viens and E.M. Schulson, Acta Metall., 35 (1987) 1109.

61. B.H. Kear and M.F. Hornbecker, Trans. Am. Soc. Met., 59, (1966) 155.

62. C.C. Koch, J.A. Horton, C.T. Liu, O.B. Gavin and J.O. Scarbrough in Rapid Solidification Processing, (Washington, Natl. Bur. Stds., 1983) 264.

63. A. Choudhury, C.L. White and C.R. Brooks, Scripta Met.,20 (1986) 1061.

64. A.I. Taub, S.C. Huang and K.M. Chang, Met. Trans., 42A, (1984) 399.

65. I. Baker, E.M. Schulson and J.R. Michael, Phil. Mag. B, 57 (1988) 379.

66. E.M. Schulson, T.P. Weihs, I. Baker, H.J. Frost, and J.A. Horton, Acta Metall., 34 (1986) 1395.

67. E.M. Schulson, Y. Xu, P. Munroe, S. Guha and I. Baker, Acta Metall., in press.

68. R.A.D. MacKenzie and S.L. Sass, Scripta Metall., 22 (1988) 1807.

69. I. Baker, E.M. Schulson and J.R. Michael, Phil. Mag. B, 57 (1988) 379.

70. J.A. Horton and M.K. Miller, Acta Metall., 35 (1987) 133.

71. M. Takeyama and C.T. Liu, Acta Metall., 36 (1988) 1241.

72. C.T. Liu in 'High Temperature Ordered Intermetallic Alloys II' (eds. N.S. Stoloff et al.) MRS Symposia Pittsburgh, Mat. Res. Soc. (1987) 355.

73. N.S. Stoloff and R.G. Davies, Prog. Mat. Sci., 13, (1966) 3.

74. V. Paidar, D.P. Pope and V. Vitek, Acta Metall., 32, (1984) 435.

75. J.A. Horton and C.T. Liu, Acta Metall., 33, (1985) 2191.

76. A.E. Staton-Beran and R.D. Rowlings, Phys. Stat. Solidi, 29, (1975) 613.

77. W. Köster, Arch. Eisenhüttenw, 7, (1934) 257.

78. A.J. Bradley and A. Taylor, Proc. Royal Soc. London A, 166, (1938) 353.

79. A.J. Bradley, J. Iron Steel Inst., 163, (1949) 19.

80. A.J. Bradley, J. Iron Steel Inst., 168, (1951) 233.

81. V.G. Rivlin and G.V. Raynor, Int. Met. Rev., 25, (1980) 79.

82. S. Kiuti, Rep. Aero. Res. Inst., Tokyo Imp. Univ., 13 (17), (1938) 553.

83. S. Kiuti, Rep. Aero. Res. Inst., Tokyo Imp. Univ., 15 (7), (1940) 601.

84. S. Kiuti, Rep. Aero. Res. Inst., Tokyo Imp. Univ., 16 (4), (1941) 167.

85. G. Sauthoff, Z. Metallkde.,Bd.77, H 10, (1986) 654.

86. H. Lipson and A. Taylor, Proc. Royal Soc. London, Ser. A, 173, (1939) 232.

87. M. Rudy and G. Sauthoff, Mat. Sc. Eng., 81, (1986) 525.

88. M. Rudy and G. Sauthoff in 'High Temperature Ordered Intermetallic Alloys I' (eds. C.C. Koch et al.) MRS Symposia Pittsburgh, Mat. Res. Soc. (1985) 327.

89. O.D. Sherby and P.M. Burke, Prog. Mat. Sci., 13 (1968) 325.

90. J.A. Horton, C.T. Liu and M.L. Santella, Met. Trans., 18A, (1987) 1265.

91. R.W. Cahn, P.A. Siemers, J.E. Gieger and P. Bardhan, Acta Metall., 35, (1987) 2737.

92. J.A. Horton, C.T. Liu and C.C. Koch, Proc. Symp. High Temperature Alloys: Theory and Design, ed. J.O. Stiegler, Met. Soc. of AIME, (1984) 309.

93. M.V. Nathal, private communication.

94. P.R. Munroe and I. Baker, Proc. 47th EMSA, (1989) 676.

95. I.M. Robertson and C.M. Wayman, Phil. Mag. A, 48, (1983) 421.

96. I.M. Robertson and C.M. Wayman, Phil. Mag. A, 48, (1983) 433.

97. R.D. Field, D.D. Krueger and S.C. Huang, Proc. MRS, 133, (1989) 567.

98. P. Beardmore, R.G. Davies and T.L. Johnston, Trans. AIME, 245, (1969) 1537.

99. D.A. Grose and G.S. Ansell, Met. Trans. A, 12A, (1981) 1631.

100. C.R. Brooks, J.E. Spruiell, and E.E. Stansbury, Int. Met. Rev., 29, (1984) 210.

101. S. Guha, I. Baker, P.R. Munroe and J.R. Michael, to be presented at ASM 1991 International Conference on High Temperature Aluminides and Intermetallics and published in Mat. Sci. Eng.

102. I. Baker, P.R. Munroe and S. Guha, unpublished research.

103. I. Baker and P.R. Munroe, High Temperature Aluminides and Intermetallics, Proc. 119th TMS Fall Meeting, (1989) 425.

104. W. Bell, W.R. Roser and G. Thomas, Acta Metall., 12 (1964) 1247.

105. M.H. Yoo, J.A. Horton and C.T. Liu, Acta Metall., 36 (1988) 2935.

106. J.A. Horton, I. Baker and M.H. Yoo, Phil Mag. A, 63, (1991) 319.

107. I. Baker, J.A. Horton and E.M. Schulson, Phil. Mag. Letters, 57 (1987) 17.

108. S.C.Huang, R.D. Field and D.D. Krueger, Met Trans. A, 21, (1990) 959.

109. M.V. Nathal, J.O. Diaz and R.V. Miner, Proc. MRS, 133, (1989) 269.

110. J. Klöwer, Doctoral Thesis, Tech. Univ. Aachen, Germany, (1989) 45.

111. R.R. Vandervoort, A.K. Mukherjee and J.E. Dorn, Trans. ASM, 59, (1966) 930.

112. W. Yang and R.A. Dodd, Met. Sci., 7, (1973) 41.

113. M. Larsen, Proc. 47th EMSA, (1989) 320.

114. I. Jung, M. Rudy and G. Sauthoff, Proc. MRS, 81 (1987) 263.

115. L.M. Brown and R. Ham, "Strengthening Methods in Crystals", ed. A. Kelly and R.B. Nicholson, Amsterdam (Elsevier), Chp. 2, (1971).

116. N.S. Stoloff and R.G. Davies, Acta Metall., 12 (1964) 473.

117. A.C. Arko and Y.H. Liu, Met. Trans. A, 2 (1971) 1875.

118. C.T. Liu and R.A. McKamey, "High Temperature Aluminides and Intermetallics", eds. S.H. Whang, C.T. Liu, D.P. Pope, J.P. Steigler, TMS, Indianapolis IN, (1990) 133.

119. D. Keith Patrick, K.M. Chang, D.B. Miracle and H.A. Lipsitt, "High Temperature Intermetallics and Ordered Alloys", vol. 213, (1991) 267.

118. S.V. Raj, R.D. Noebe and I.E. Locci, ibid, 673.

119. I. Baker and E.M. Schulson, Scripta Metall., 23, (1989) 345.

120. P.S. Khadkikar, K. Vedula and G. Michal, Met. Trans. A, 21, (1990) 279.

121. I. Baker and E.M. Schulson, Met. Trans., 15A, (1984) 1129.

122. K.M. Chang, R. Darolia and H.A. Lipsitt, "High Temperature Intermetallics and Ordered Alloys", vol. 213, MRS, (1991) 597.

123. R.D. Noebe, R.R. Bowman, J.T. Kim, M. Larsen and R. Gibala, "High Temperature Aluminides and Intermetallics", eds. S.H. Whang, C.T. Liu, D.P. Pope, J.P. Steigler, TMS, Indianapolis IN, (1990) 271.

124. C.H. Lloyd and M.H. Loretto, Phys. Stat. Sol., 39 (1970) 163.

125. N.J. Zaluzec and H.L. Fraser, Scripta Met., 8, (1974) 1049.

126. A. Lasalmonie, J. Mat. Sci., 17, (1982) 2419.

127. A. Ball and R.E. Smallman, Acta. Metall., 14 (1966) 1517.

APPENDIX I

In this section, the processing parameters for the second extrusion of the alloys, which were carried out at NASA Lewis Research Center, are enclosed for possible future reference. The extrusion data sheets for the first extrusion of each alloys, which were carried out at Oak Ridge National Laboratory, were not available. The following is a brief summary of the extrusion parameters from the enclosed sheets:

Alloy	Reduction Ratio	Extrusion Temp., °C	Break thru Pressure, ksi	Running Press.,ksi	Punch Speed
Ni-20Al-30Fe	6:1	1000	147.1	122.6	5.5
(Batch #1)	6:1	1000	177.8	131.8	5
Ni-20Al-30Fe	6:1	1100	105.9	86.9	2.7
(Batch #2)	6:1	1000	108.6	95	2.5
Ni-12Al-40Fe	16:1	1200	132.7	90.5	-
Ni-30Al-20Fe	6:1	1000	159.4	122.6	5.5
	6:1	1000	92.4	74	7.3
Ni-40Al-30Fe	6:1	1000	156.3	128.7	5
	6:1	1000	104	73.5	6.9
Ni-36Al	16:1	1200	129	80	6.1
Ni-35.9Al-0.2B	16:1	1200	132	89	6.1
Ni-20Al-30Fe-0.2B	16:1	1200	110	73.5	6.9

HOT EXTRUSION DATA SHEET
(PFS-HotExtDS)

Date Submitted: 88/04
Date Completed: 88/04

Engineer's Name: GAYDOSH
Eng's ID: ~~ORANGE/GREEN~~ Yellow / Red
Charge Number: YOG-2272

General Type of Material: INTERMETALLIC

Nominal Composition: NI-20AL-30FE

Type of Billet: CANNED SOLID (PREVIOSLY EXTRUDED AT 7:1, 1100 C)
Size of Billet (inches) Diameter: 2 Length: 5.5

Proposed Extrusion Conditions
Temperature (F): 1832
Reduction Ratio: 6:1
Type of Die: ROUND
Punch Speed (inch/min): MAX
Special Conditions:

Safety Checks
Leak Test: NA Date:
Heat Test (2h 1500F): NA Date:

Actual Extrusion Conditions
Date: 22Apr88
Ext. ID: L-2401
Crew:
Temperature: 1832
Reduction Ratio: 6:1
Type of Die Round: X Sh Bar: Other: Angle: 90
Special Conditions:

Valve Selection (X to specify) 1/8: 7/16: 3.5: X
Preset Punch Speed:
Valve Opening:

Side Ram: X Pressure (psi): 3150 Max Tonnage: 340
Main Ram: Pressure (psi): Max Tonnage:
Comb Ram: Pressure (psi): Max Tonnage:

Lubricant Container: Dylon
Die: Formkote
Graphite Paper: X

Dummy Thickness:
Carbon Thickness:
Container Mat:
Cont Temp (F):
Times Used: 1
Stem Material:
Stem ID:
Times Used: 1

Time at Temperature (h): 2.4
Transfer Time (s): 8.6

Post Test Analysis of Extrusion
Sucessful: X Unsucessful:
Comment:

Shooter: Butt left in Die:
Sticker:
Break thru Pressure (ksi): 147.1
Punch Speed: 5.5
Running Pressure (ksi): 122.6
Time to Ext: 1
Condition of Extrusion:

Length of Ext: 20.5
Nominal Cross Section: .87" di
Condition of Die:

General Comments:

HOT EXTRUSION DATA SHEET
(PFS-HotExtDS)

Engineer's Name: GAYDOSH
Eng's ID: ~~BLUE/GREEN~~ Red / Yellow
Charge Number: YOG-2272
Date Submitted: 88/04/
Date Completed: 88/04/

General Type of Material: INTERMETALLIC

Nominal Composition: ~~NI-36AL~~ Ni-20Al-30Fe

Type of Billet: CANNED SOLID (PREVIOSLY EXTRUDED AT 7:1, 1100 C)
Size of Billet (inches) Diameter: 2 Length: 5.5

Proposed Extrusion Conditions
Temperature (F): 1832 Reduction Ratio: 6:1
Type of Die: ROUND
Punch Speed (inch/min): MAX
Special Conditions:

Safety Checks
Leak Test: NA Date:
Heat Test (2h 1500F): NA Date:

Actual Extrusion Conditions
Date: 22Apr88 Ext. ID: L-2400
Crew:
Temperature: 1832 Reduction Ratio: 6:1
Type of Die Round: X Sh Bar: Other: Angle: 90
Special Conditions:

Valve Selection (X to specify) 1/8: 7/16: 3.5: X
Preset Punch Speed: Valve Opening:

Side Ram: X Pressure (psi): 3150 Max Tonnage: 340
Main Ram: Pressure (psi): Max Tonnage:
Comb Ram: Pressure (psi): Max Tonnage:

Lubricant Container: Dylon Graphite Paper: X
Die: Formkote
Dummy Thickness: Carbon Thickness:
Container Mat: Cont Temp (F): Times Used: 184
Stem Material: Stem ID: Times Used: 184

Time at Temperature (h): 2.2 Transfer Time (s): 12.1

Post Test Analysis of Extrusion
Sucessful: X Unsucessful:
Comment:

Shooter: Butt left in Die: Sticker:
Break thru Pressure (ksi): 177.8 Punch Speed: 5 "/s
Running Pressure (ksi): 131.8 Time to Ext: 1.1
Condition of Extrusion:

Length of Ext: 21.8 Nominal Cross Section: .87" dia
Condition of Die:

General Comments:

Sumit

HOT EXTRUSION DATA SHEET
(PFS-HotExtDS)

Engineer's Name: Whittenberger
Eng's ID: Sumit-99
Charge Number: YOG1265
Date Submitted: 90/06/
Date Completed: 90/06/

General Type of Material:

Nominal Composition: Ni- 20Al- 30Fe

Type of Billet: Solid
Size of Billet (inches) Diameter: 3 Length: 6

Proposed Extrusion Conditions
Temperature (F): 2012
Reduction Ratio: 6:1
Type of Die: Round
Punch Speed (inch/min): Max
Special Conditions:

Safety Checks
Leak Test: NA Date:
Heat Test (2h 1500F): NA Date:

Actual Extrusion Conditions
Date: 90/06/08 Ext. ID: L-2698 ✓
Crew:
Temperature: 2012 Reduction Ratio: 6:1
Type of Die Round: X Sh Bar: Other: Angle: X
Special Conditions:

Valve Selection (X to specify) 1/8: 7/16: 3.5: X
Preset Punch Speed:
Valve Opening:

Side Ram: Pressure (psi): Max Tonnage:
Main Ram: X Pressure (psi): 3350 Max Tonnage: 640
Comb Ram: Pressure (psi): Max Tonnage:

Lubricant Container: Dylon Graphite Paper: X
Die: Formkote
Dummy Thickness: 2 Carbon Thickness: 1.5
Container Mat: NU DIE V Cont Temp (F): 600 Times Used: 497
Stem Material: NASA 218 Stem ID: NASA #1 Times Used: 477

Time at Temperature (h): 3.1 Transfer Time (s): 7.5

Post Test Analysis of Extrusion
Sucessful: X Unsucessful:
Comment:

Shooter: Butt left in Die: Sticker:
Break thru Pressure (ksi): 105.9 Punch Speed: 2.7 "/
Running Pressure (ksi): 86.9 Time to Ext: 2.2 s
Condition of Extrusion:

Length of Ext: 30.3 Nominal Cross Section: 1.26
Condition of Die:

General Comments:

HOT EXTRUSION DATA SHEET
(PFS-HotExtDS)

Sumit

ngineer's Name: Whittenberger
ng's ID: Re:sumit-99 Charge Number: YOG1265
Date Submitted: 90/06/08
Date Completed: 90/06/08

eneral Type of Material: Re-extrusion of piece from L-2698

ominal Composition: Ni-20Al-30Fe

ype of Billet: Solid
ize of Billet (inches) Diameter: 3 Length: 6

roposed Extrusion Conditions
Temperature (F): 1832 Reduction Ratio: 6:1
Type of Die: Round
Punch Speed (inch/min): Max
Special Conditions:

afety Checks
Leak Test: NA Date:
Heat Test (2h 1500F): Na Date:

Not Shipped

ctual Extrusion Conditions
Date: 90/06/22 Ext. ID: L-2703
Crew:
Temperature: 1832 Reduction Ratio: 6:1
Type of Die Round: X Sh Bar: Other: Angle: 90
Special Conditions:

Valve Selection (X to specify) 1/8: 7/16: 3.5: X
Preset Punch Speed: Valve Opening:

Side Ram: Pressure (psi): Max Tonnage:
Main Ram: X Pressure (psi): 3350 Max Tonnage: 680
Comb Ram: Pressure (psi): Max Tonnage:

Lubricant Container: Dylon Graphite Paper: X
Die: Formkote
Dummy Thickness: 2 Carbon Thickness: 1.5
Container Mat: Nu Die V Cont Temp (F): 600 Times Used: 502
Stem Material: NASA 218 Stem ID: NASA #1 Times Used: 482

Time at Temperature (h): 2.5 Transfer Time (s): 6

ost Test Analysis of Extrusion
Sucessful: X Unsucessful:
Comment:

Shooter: Butt left in Die: Sticker:
Break thru Pressure (ksi): 108.6 Punch Speed: 2.5 "/s
Running Pressure (ksi): 95 Time to Ext: 2.4 s
Condition of Extrusion:

Length of Ext: 32.5 Nominal Cross Section: 1.283
Condition of Die:

General Comments:

HOT EXTRUSION DATA SHEET
(PFS-HotExtDS)

Engineer's Name: GAYDOSH
Eng's ID: 2 (SUMIT2)(NO STEM)Charge Number: YOG-2272
Date Submitted: 88/10
Date Completed: 88/10

General Type of Material: INTERMETALLIC

Nominal Composition: NI-40FE-12AL

Type of Billet: CANNED CASTING
Size of Billet (inches) Diameter: 2 Length: 5.5

Proposed Extrusion Conditions
Temperature (F): 2192 F
Reduction Ratio: 16:1
Type of Die: ROUND
Punch Speed (inch/min): MAX
Special Conditions:

Safety Checks
Leak Test: NA Date:
Heat Test (2h 1500F): NA Date:

Actual Extrusion Conditions
Date: 88/10/21 Ext. ID: L-2429
Crew:
Temperature: 2192 F Reduction Ratio: 16:1
Type of Die Round: X Sh Bar: Other: Angle: 90
Special Conditions:

Valve Selection (X to specify) 1/8: 7/16: Preset Punch Speed:
3.5: X Valve Opening:

Side Ram: X Pressure (psi): 3150 Max Tonnage: 340
Main Ram: Pressure (psi): Max Tonnage:
Comb Ram: Pressure (psi): Max Tonnage:

Lubricant Container: FORMKOTE Graphite Paper: X
Die: DYLON
Dummy Thickness: 2 Carbon Thickness: 1.5
Container Mat: NU DIE V'Cont Temp (F): 600 Times Used: 21
Stem Material: ? Stem ID: NEW Times Used: 21

Time at Temperature (h): 1.5 Transfer Time (s): <10

Post Test Analysis of Extrusion
Sucessful: X Unsucessful:
Comment:

Shooter: Butt left in Die: Sticker:
Break thru Pressure (ksi): 132.7 Punch Speed:
Running Pressure (ksi): 90.5 Time to Ext:
Condition of Extrusion:

Length of Ext: 57 Nominal Cross Section: 0.56
Condition of Die:

General Comments: NO CHART PAPER; STRESSES ESTIMATED FROM GAGE PRESSURE READINGS

HOT EXTRUSION DATA SHEET
(PFS-HotExtDS)

Engineer's Name: GAYDOSH
Eng's ID: ~~ORANGE~~/WHITE
Pink
Charge Number: YOG-2272
Date Submitted: 88/04/
Date Completed: 88/04/

General Type of Material: INTERMETALLIC

Nominal Composition: NI-30AL-20FE

Type of Billet: CANNED SOLID (PREVIOSLY EXTRUDED AT 7:1, 1100 C)
Size of Billet (inches) Diameter: 2 Length: 5.5

Proposed Extrusion Conditions
Temperature (F): 1832
Reduction Ratio: 6:1
Type of Die: ROUND
Punch Speed (inch/min): MAX
Special Conditions:

Safety Checks
Leak Test: NA Date:
Heat Test (2h 1500F): NA Date:

Actual Extrusion Conditions
Date: 22Apr88
Ext. ID: L-2402
Crew:
Temperature: 1832
Reduction Ratio: 6:1
Type of Die Round: X Sh Bar: Other: Angle: 90
Special Conditions:

Valve Selection (X to specify) 1/8: 7/16: 3.5: X
Preset Punch Speed:
Valve Opening:

Side Ram: X Pressure (psi): 3150 Max Tonnage: 340
Main Ram: Pressure (psi): Max Tonnage:
Comb Ram: Pressure (psi): Max Tonnage:

Lubricant Container: Dylon
Die: Formkote
Graphite Paper: X
Dummy Thickness:
Carbon Thickness:
Container Mat: Cont Temp (F): Times Used: 186
Stem Material: Stem ID: Times Used: 186

Time at Temperature (h): 2.5
Transfer Time (s): 11.3

Post Test Analysis of Extrusion
Sucessful: X Unsucessful:
Comment:

Shooter: Butt left in Die: Sticker:
Break thru Pressure (ksi): 159.4
Punch Speed: 5.5 "/
Running Pressure (ksi): 122.6
Time to Ext: 1
Condition of Extrusion:

Length of Ext: 21.5
Nominal Cross Section: .87" DIA
Condition of Die:

General Comments:

HOT EXTRUSION DATA SHEET
(PFS-HotExtDS)

Engineer's Name: GAYDOSH
Eng's ID: PINK/WHITE
Charge Number: YOG-1265
Date Submitted: 89/01/
Date Completed: 89/03/

General Type of Material: INTERMETALLIC

Nominal Composition: NI-30AL-20FE

Type of Billet: CANNED SOLID (PREVIOUSLY EXTRUDED)
Size of Billet (inches) Diameter: 2 Length: 5.5

Proposed Extrusion Conditions
Temperature (F): 1832 F
Reduction Ratio: 6:1
Type of Die: ROUND
Punch Speed (inch/min): MAX
Special Conditions:

Safety Checks
Leak Test: NA Date:
Heat Test (2h 1500F): NA Date:

Actual Extrusion Conditions
Date: 89/03/03
Ext. ID: L-2477
Crew:
Temperature: 1832 F
Reduction Ratio: 6:1
Type of Die Round: X Sh Bar: Other: Angle: 90
Special Conditions:

Valve Selection (X to specify) 1/8: 7/16: 3.5: X
Preset Punch Speed:
Valve Opening:

Side Ram: X Pressure (psi): 3150 Max Tonnage: 340
Main Ram: Pressure (psi): Max Tonnage:
Comb Ram: Pressure (psi): Max Tonnage:

Lubricant Container: DYLON
Die: FORMKOTE
Graphite Paper: X
Dummy Thickness: 2
Carbon Thickness: 1.5
Container Mat: NU DIE V'Cont Temp (F): 600 Times Used: 26
Stem Material: ? Stem ID: NEW Times Used: 26

Time at Temperature (h): 1.3
Transfer Time (s): 9.2

Post Test Analysis of Extrusion
Sucessful: X Unsucessful:
Comment:

Shooter: Butt left in Die:
Sticker:
Break thru Pressure (ksi): 92.4
Punch Speed: 7.3 "
Running Pressure (ksi): 74
Time to Ext: .75 s
Condition of Extrusion:

Length of Ext: 19"
Nominal Cross Section: .873 " d
Condition of Die:

General Comments:

HOT EXTRUSION DATA SHEET
(PFS-HotExtDS)

Engineer's Name: GAYDOSH
Eng's ID: ~~RED/YELLOW~~ orange/green
Charge Number: YOG-2272
Date Submitted: 88/04/
Date Completed: 88/04/

General Type of Material: INTERMETALLIC

Nominal Composition: NI-40AL-30FE

Type of Billet: CANNED SOLID (PREVIOSLY EXTRUDED AT 7:1, 1100 C)
Size of Billet (inches) Diameter: 2 Length: 5.5

Proposed Extrusion Conditions
Temperature (F): 1832 Reduction Ratio: 6:1
Type of Die: ROUND
Punch Speed (inch/min): MAX
Special Conditions:

Safety Checks
Leak Test: NA Date:
Heat Test (2h 1500F): NA Date:

Actual Extrusion Conditions
Date: 22Apr88 Ext. ID: L-2403
Crew:
Temperature: 1832 Reduction Ratio: 6:1
Type of Die Round: X Sh Bar: Other: Angle: 90
Special Conditions:

Valve Selection (X to specify) 1/8: 7/16: 3.5: X
Preset Punch Speed:
Valve Opening:

Side Ram: X Pressure (psi): 3150 Max Tonnage: 340
Main Ram: Pressure (psi): Max Tonnage:
Comb Ram: Pressure (psi): Max Tonnage:

Lubricant Container: Dylon Graphite Paper: X
Die: Formkote
Dummy Thickness: Carbon Thickness:
Container Mat: Cont Temp (F): Times Used: 187
Stem Material: Stem ID: Times Used: 187

Time at Temperature (h): 2.6 Transfer Time (s): 9

Post Test Analysis of Extrusion
Sucessful: X Unsucessful:
Comment:

Shooter: Butt left in Die: Sticker:
Break thru Pressure (ksi): 156.3 Punch Speed: 5 "/s
Running Pressure (ksi): 128.7 Time to Ext: 1.1
Condition of Extrusion:

Length of Ext: 21.8 Nominal Cross Section: .87" dia
Condition of Die:

General Comments:

HOT EXTRUSION DATA SHEET
(PFS-HotExtDS)

Date Submitted: 89/01
Date Completed: 89/03

Engineer's Name: GAYDOSH
Eng's ID: ORANGE/GREEN
Charge Number: YOG-1265

General Type of Material: INTERMETALLIC

Nominal Composition: NI-40AL-30FE

Type of Billet: CANNED SOLID (PREVIOUSLY EXTRUDED)
Size of Billet (inches) Diameter: 2 Length: 5.5

Proposed Extrusion Conditions
Temperature (F): 1832 F
Reduction Ratio: 6:1
Type of Die: ROUND
Punch Speed (inch/min): MAX
Special Conditions:

Safety Checks
Leak Test: NA Date:
Heat Test (2h 1500F): NA Date:

Actual Extrusion Conditions
Date: 89/03/03 Ext. ID: L-2476
Crew:
Temperature: 1832 F Reduction Ratio: 6:1
Type of Die Round: X Sh Bar: Other: Angle: 90
Special Conditions:

Valve Selection (X to specify) 1/8: 7/16: 3.5: X
Preset Punch Speed:
Valve Opening:

Side Ram: X Pressure (psi): 3150 Max Tonnage: 340
Main Ram: Pressure (psi): Max Tonnage:
Comb Ram: Pressure (psi): Max Tonnage:

Lubricant Container: DYLON Graphite Paper: X
Die: FORMKOTE
Dummy Thickness: 2 Carbon Thickness: 1.5
Container Mat: NU DIE V'Cont Temp (F): 600 Times Used: 26
Stem Material: ? Stem ID: NEW Times Used: 26

Time at Temperature (h): 1 Transfer Time (s): 8.3

Post Test Analysis of Extrusion
Sucessful: X Unsucessful:
Comment:

Shooter: Butt left in Die: Sticker:
Break thru Pressure (ksi): 104 Punch Speed: 6.9 "
Running Pressure (ksi): 73.5 Time to Ext: .8 s
Condition of Extrusion:

Length of Ext: 20.1 Nominal Cross Section: .864 " c
Condition of Die:

General Comments:

HOT EXTRUSION DATA SHEET
(PFS-HotExtDS)

ngineer's Name: GAYDOSH Date Submitted: 89/01/3
ng's ID: (SUMIT) A Charge Number: YOG-1265 Date Completed: 89/03/0

eneral Type of Material: INTERMETALLIC

ominal Composition: NI-36AL

ype of Billet: CANNED CASTING
ize of Billet (inches) Diameter: 2 Length: 5.5

roposed Extrusion Conditions
Temperature (F): 2192 F Reduction Ratio: 16:1
Type of Die: ROUND
Punch Speed (inch/min): MAX
Special Conditions:

afety Checks
Leak Test: NA Date:
Heat Test (2h 1500F): NA Date:

ctual Extrusion Conditions
Date: 89/03/08 Ext. ID: L-2484
Crew:
Temperature: 2192 F Reduction Ratio: 16:1
Type of Die Round: X Sh Bar: Other: Angle: 90
Special Conditions:

Valve Selection 1/8: 7/16: Preset Punch Speed:
(X to specify) 3.5: X Valve Opening:

Side Ram: X Pressure (psi): 3150 Max Tonnage: 340
Main Ram: Pressure (psi): Max Tonnage:
Comb Ram: Pressure (psi): Max Tonnage:

Lubricant Container: DYLON Graphite Paper: X
Die: FORMKOTE
Dummy Thickness: 2 Carbon Thickness: 1.5
Container Mat: NU DIE V'Cont Temp (F): 600 Times Used: 269
Stem Material: ? Stem ID: NEW Times Used: 269

Time at Temperature (h): 1.2 Transfer Time (s): 7.5

ost Test Analysis of Extrusion
Sucessful: X Unsucessful:
Comment:

Shooter: Butt left in Die: Sticker:
Break thru Pressure (ksi): 129 Punch Speed: 6.1 "/s
Running Pressure (ksi): 80 Time to Ext: .9 s
Condition of Extrusion:

Length of Ext: 54.5 " Nominal Cross Section: .56 " dia
Condition of Die:

General Comments:

HOT EXTRUSION DATA SHEET
(PFS-HotExtDS)

Engineer's Name: GAYDOSH Date Submitted: 89/01
Eng's ID: (SUMIT) B Charge Number: YOG-1265 Date Completed: 89/03

General Type of Material: INTERMETALLIC

Nominal Composition: NI-35.9AL-0.2B

Type of Billet: CANNED CASTING
Size of Billet (inches) Diameter: 2 Length: 5.5

Proposed Extrusion Conditions Temperature (F): 2192 F Reduction Ratio: 16:1
Type of Die: ROUND
Punch Speed (inch/min): MAX
Special Conditions:

Safety Checks Leak Test: NA Date:
Heat Test (2h 1500F): NA Date:

Actual Extrusion Conditions Date: 89/03/08 Ext. ID: L-2485
Crew:
Temperature: 2192 F Reduction Ratio: 16:1
Type of Die Round: X Sh Bar: Other: Angle: 90
Special Conditions:

Valve Selection 1/8: 7/16: Preset Punch Speed:
(X to specify) 3.5: X Valve Opening:

Side Ram: X Pressure (psi): 3150 Max Tonnage: 340
Main Ram: Pressure (psi): Max Tonnage:
Comb Ram: Pressure (psi): Max Tonnage:

Lubricant Container: DYLON Graphite Paper: X
Die: FORMKOTE
Dummy Thickness: 2 Carbon Thickness: 1.5
Container Mat: NU DIE V'Cont Temp (F): 600 Times Used: 27
Stem Material: ? Stem ID: NEW Times Used: 27

Time at Temperature (h): 1.25 Transfer Time (s): 8.1

Post Test Analysis of Extrusion Sucessful: X Unsucessful:
Comment:

Shooter: Butt left in Die: Sticker:
Break thru Pressure (ksi): 132 Punch Speed: 6.1 "
Running Pressure (ksi): 89 Time to Ext: 0.9 s
Condition of Extrusion:

Length of Ext: 57 " Nominal Cross Section: .57 " di
Condition of Die:

General Comments:

HOT EXTRUSION DATA SHEET
(PFS-HotExtDS)

Engineer's Name: GAYDOSH   Date Submitted: 89/01/3
Eng's ID: (SUMIT) C   Charge Number: YOG-1265   Date Completed: 89/03/0

General Type of Material: INTERMETALLIC

Nominal Composition: NI-29.9FE-20.1AL-0.2B

Type of Billet: CANNED CASTING
Size of Billet (inches)   Diameter: 2   Length: 5.5

Proposed Extrusion Conditions
Temperature (F): 2192 F   Reduction Ratio: 16:1
Type of Die: ROUND
Punch Speed (inch/min): MAX
Special Conditions:

Safety Checks
Leak Test: NA   Date:
Heat Test (2h 1500F): NA   Date:

Actual Extrusion Conditions
Date: 89/03/08   Ext. ID: L-2486
Crew:
Temperature: 2192 F   Reduction Ratio: 16:1
Type of Die   Round: X   Sh Bar: Other: Angle: 90
Special Conditions:

Valve Selection   1/8:   7/16:   Preset Punch Speed:
(X to specify)   3.5: X   Valve Opening:

Side Ram: X   Pressure (psi): 3150   Max Tonnage: 340
Main Ram: Pressure (psi):   Max Tonnage:
Comb Ram: Pressure (psi):   Max Tonnage:

Lubricant   Container: DYLON   Graphite Paper: X
Die: FORMKOTE
Dummy Thickness: 2   Carbon Thickness: 1.5
Container Mat: NU DIE V'Cont Temp (F): 600   Times Used: 271
Stem Material: ?   Stem ID: NEW   Times Used: 271

Time at Temperature (h): 1.4   Transfer Time (s): 6.9

Post Test Analysis of Extrusion
Sucessful: X   Unsucessful:
Comment:

Shooter: Butt left in Die: Sticker:
Break thru Pressure (ksi): 110   Punch Speed: 6.9 "/s
Running Pressure (ksi): 73.5   Time to Ext: .8 s
Condition of Extrusion:

Length of Ext: 63.5   Nominal Cross Section: .53 " dia
Condition of Die:

General Comments:

APPENDIX II

Preliminary experiments in comparing the long range order (LRO) of Ni-30Al-20Fe in the as-extruded and annealed state by comparing the integrated intensities of {100} and {200} reflections were unsuccessful, primarily due to the difficulty in synthesizing strain free powder from the extrusions. Due to the high compressive ductility of these alloys, the powders synthesized by filing the extrusions were strained; x-ray diffraction of these powders indicated peak broadening. By contrast, when annealed at 500°C, x-ray diffraction indicated that the powders were relatively-strain free. It was difficult to compare the LRO of powders that were strained in one case and strain free in the other. To circumvent this difficulty, rapidly solidifed powders of the alloy were obtained from NASA Lewis Research Center. These powders were examined in both as-received state and after annealing at 500°C for 200 min. The intensities were measured using a long counting time (50-200s) and a small step size (0.032°), the latter corresponding to the slit size (0.2mm) used at the detector. Repeat experiments were conducted to determine the average ratio of intensities of the {100} superlattice to {200} fundamental peaks. The experiments were also conducted using both CuK_α and CuK_β radiation. The results are summarized below:

Radiation	Ratio of {100} to {200} peaks	
	CuK_α	CuK_β
As-received powder	0.34	0.316
	0.27	0.268
	0.36	0.313
	0.323±0.047	0.299±0.027
500°C-annealed powder	0.33	0.29
	0.33	
	0.32	
	0.327±0.006	

The results indicate that the ratio of superlattice to fundamental peaks are independent of the annealing treatment. Since any changes in LRO should result in a change in the ratio of superlattice to fundamental peak intensities, the results also indicate that the LRO of Ni-30Al-20Fe does not change significantly upon annealing at 500°C.

Example intensity-2theta plots of as-received Ni-30Al-20Fe powder and those annealed at 500°C are presented in this section (radiation used being CuK_{α}). Note that, in both cases, the {100} peaks are plotted in the angular range 29.5-32.5° while the fundamental {200} peak is plotted in the angular range 63.0-66.0°. Interestingly, for the powder annealed at 500°C, the {200} peak shows evidence of peak splitting, which is absent in the as-received powder. Since the microstructure of the alloy after 500°C-anneal is known to be $\beta+\beta'$, the two peaks could be ascribed one each to the β' (ordered b.c.c) and β (b.c.c) phases. Also, the {100} peak shows no evidence of peak splitting since no {100} peak is expected from a β phase.

It should also be noted that for a given powder, the ratio of integrated intensities is dependent upon the radiation used. This is not surprising since the scattering factors of atoms are dependent upon the radiation used. For a given radiation, the closer the radiation is to the K absorption edge of a constituent element, the weaker the scattering from that particular atom for that particular radiation. Interestingly, the ratios of {100} to {200} peaks obtained using CuK_{β} radiation also indicate that no significant differences in LRO exist between the two states.

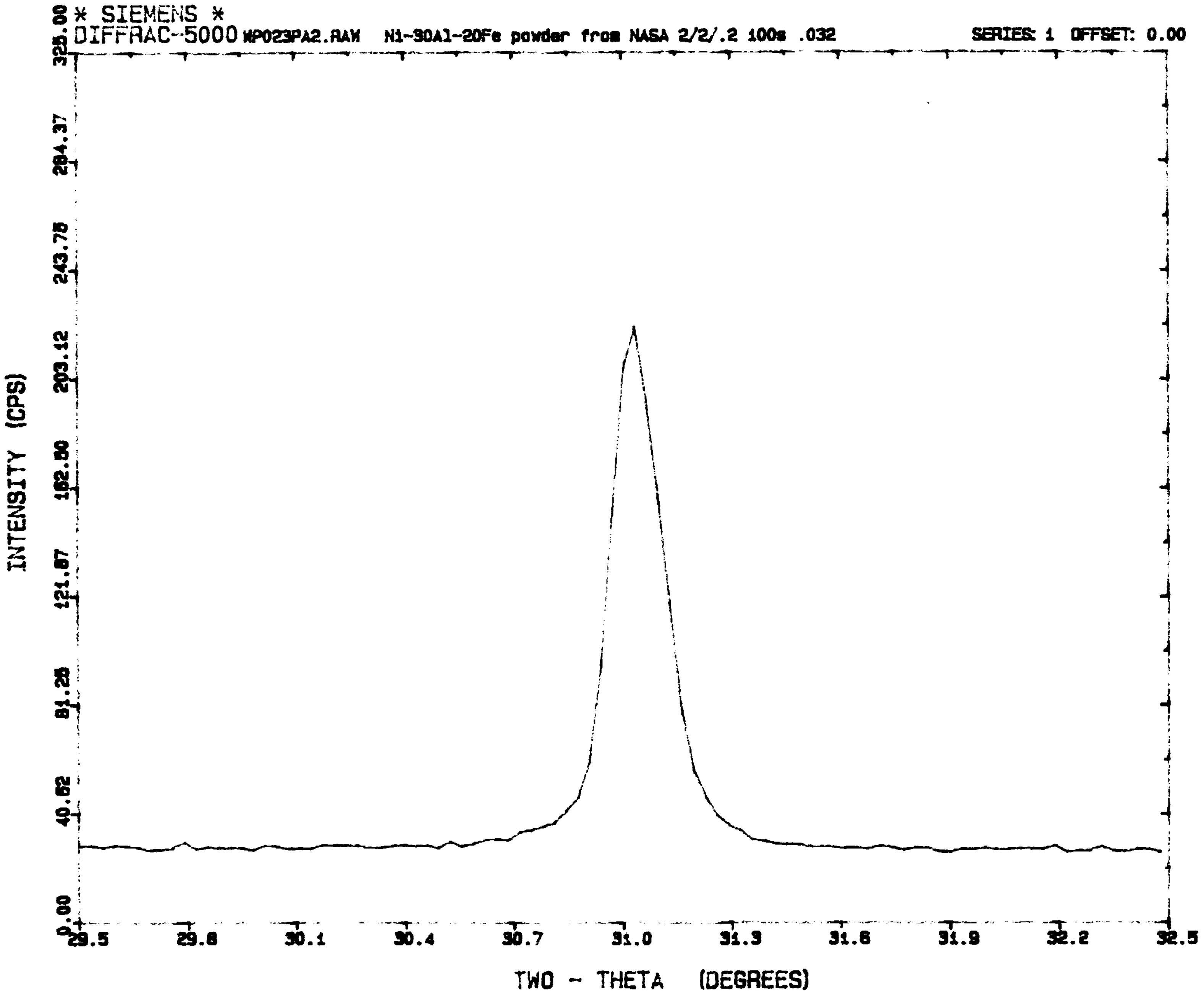
* SIEMENS *
DIFFRAC-5000 WP023PA2.RAW   Ni-30Al-20Fe powder from NASA 2/2/.2 100s .032
SERIES: 1 OFFSET: 0.00
INTENSITY (CPS)
325.00
284.37
243.75
203.12
162.50
121.87
81.25
40.62
0.00
29.5
29.8
30.1
30.4
30.7
31.0
31.3
31.6
31.9
32.2
32.5
TWO - THETA (DEGREES)

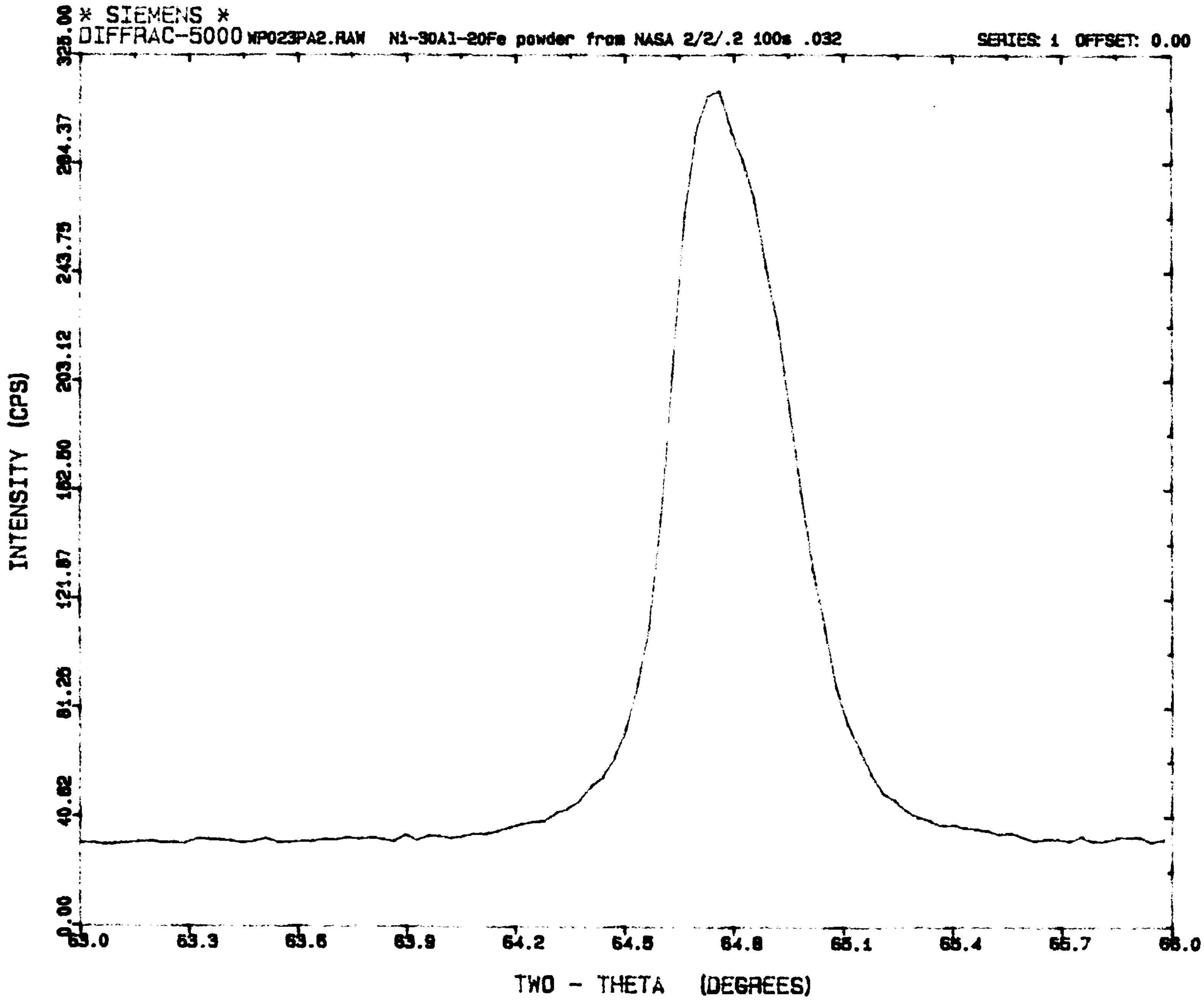
* SIEMENS *
DIFFRAC-5000 WP023PA2.RAW N1-30A1-20Fe powder from NASA 2/2/.2 100s .032
SERIES: 1 OFFSET: 0.00
INTENSITY (CPS)
325.00
284.37
243.75
203.12
162.50
121.87
81.25
40.62
0.00
63.0
63.3
63.6
63.9
64.2
64.5
64.8
65.1
65.4
65.7
66.0
TWO - THETA (DEGREES)

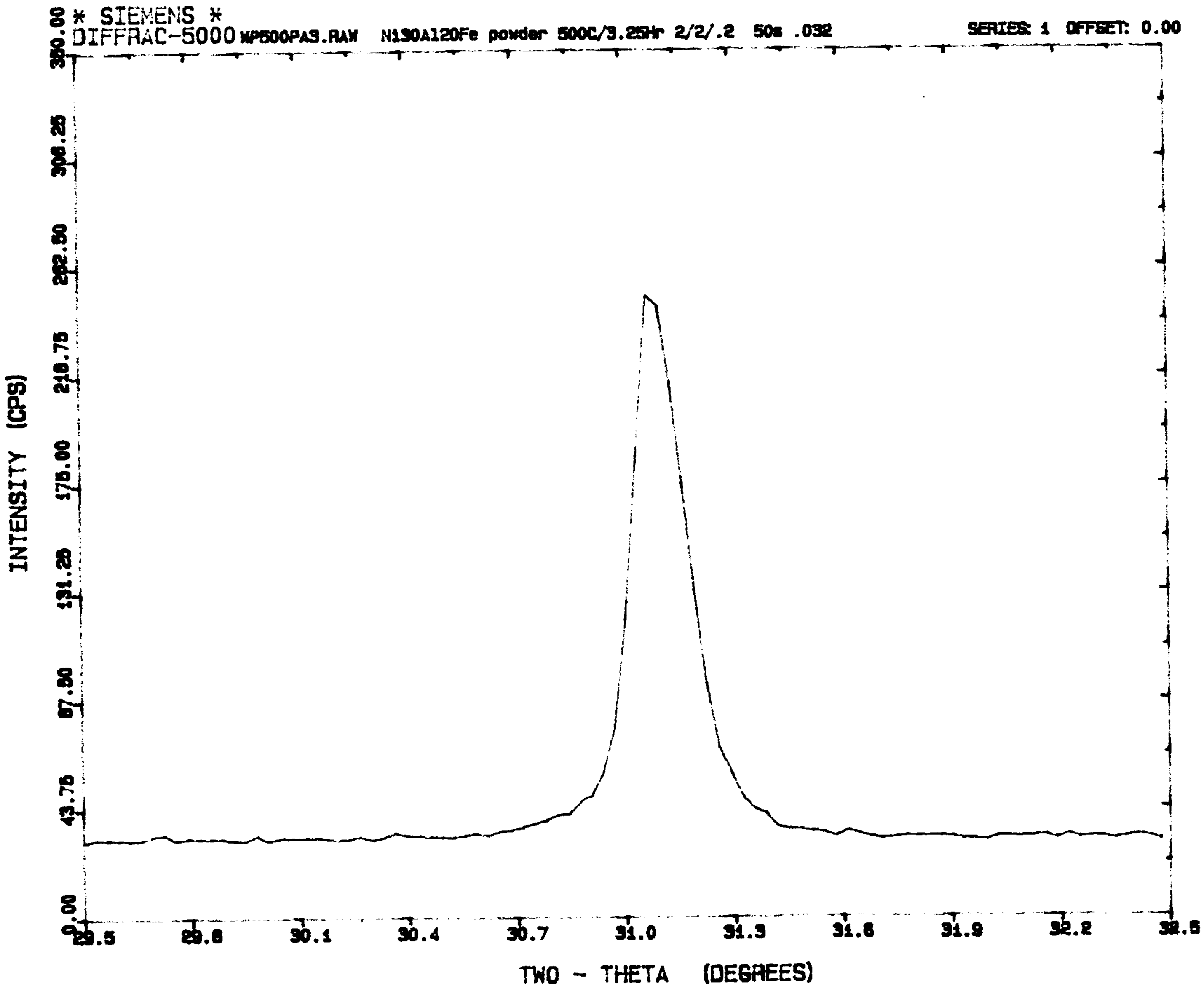
* SIEMENS *
DIFFRAC-5000 WP500PAS.RAW N130A120Fe powder 500C/3.25Hr 2/2/.2 50s .032
SERIES: 1 OFFSET: 0.00
INTENSITY (CPS)
0.00
43.75
87.50
131.25
175.00
218.75
262.50
306.25
350.00
29.5
29.8
30.1
30.4
30.7
31.0
31.3
31.6
31.9
32.2
32.5
TWO - THETA (DEGREES)

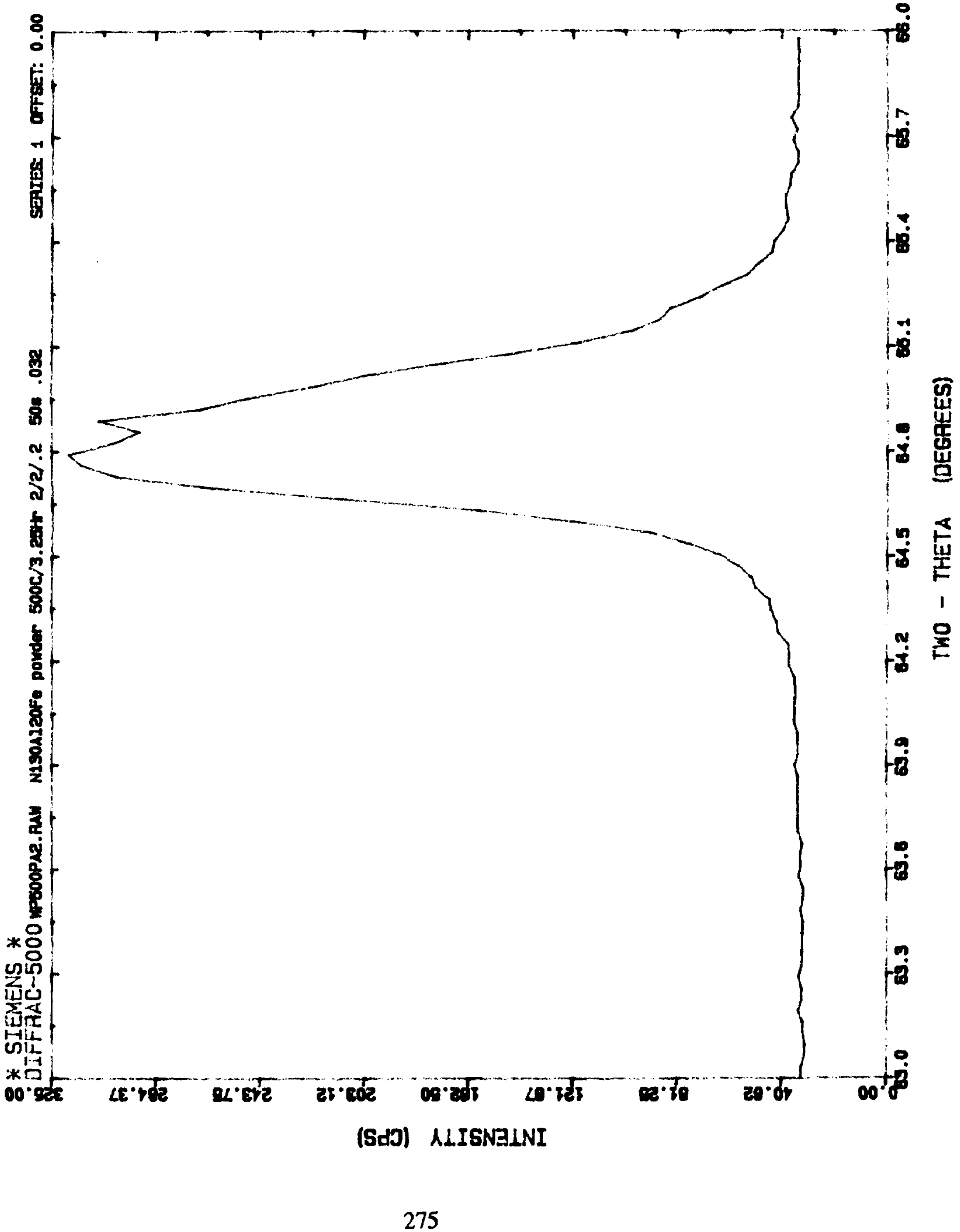
* SIEMENS *
DIFFRAC-5000
NP500PA2.RAW Ni30Al20Fe powder 500C/3.25Hr 2/2/.2 50s .032
SERIES 1 OFFSET: 0.00
INTENSITY (CPS)
325.00
284.37
243.75
203.12
162.50
121.87
81.25
40.62
0.00
TWO - THETA (DEGREES)
63.0
63.3
63.6
63.9
64.2
64.5
64.8
65.1
65.4
65.7
66.0

REPORT DOCUMENTATION PAGE	*Form Approved* *OMB No. 0704-0188*

Public reporting burden for this collection of information is estimated to average 1 hour per response, including the time for reviewing instructions, searching existing data sources, gathering and maintaining the data needed, and completing and reviewing the collection of information. Send comments regarding this burden estimate or any other aspect of this collection of information, including suggestions for reducing this burden, to Washington Headquarters Services, Directorate for information Operations and Reports, 1215 Jefferson Davis Highway, Suite 1204, Arlington, VA 22202-4302, and to the Office of Management and Budget, Paperwork Reduction Project (0704-0188), Washington, DC 20503.

1. AGENCY USE ONLY (*Leave blank*)	**2. REPORT DATE** 1992	**3. REPORT TYPE AND DATES COVERED** Final Contractor Report

4. TITLE AND SUBTITLE

Improving the Low Temperature Ductility of NiAl

5. FUNDING NUMBERS

WU-505-90-01

6. AUTHOR(S)

Sumit Guha

7. PERFORMING ORGANIZATION NAME(S) AND ADDRESS(ES)

Dartmouth College
Thayer School of Engineering
Hanover, New Hampshire

8. PERFORMING ORGANIZATION REPORT NUMBER

None

9. SPONSORING/MONITORING AGENCY NAMES(S) AND ADDRESS(ES)

National Aeronautics and Space Administration
Lewis Research Center
Cleveland, Ohio 44135-3191

10. SPONSORING/MONITORING AGENCY REPORT NUMBER

NASA CR-189211

11. SUPPLEMENTARY NOTES

Prepared as a thesis in partial fulfillment of the requirements for the degree of Doctor of Philosophy, Dartmouth College, Thayer School of Engineering, Hanover, New Hampshire (funded by NASA Grant NAG3-775). Responsible person, Michael V. Nathal, NASA Lewis Research Center, (216) 433-9516.

12a. DISTRIBUTION/AVAILABILITY STATEMENT

Unclassified - Unlimited
Subject Category 26

12b. DISTRIBUTION CODE

13. ABSTRACT *(Maximum 200 words)*

The intermetallic NiAl, by virtue of its high melting point, relatively low density (compared to the Ni-base superalloys) and excellent high temperature oxidation resistance, exhibits excellent potential as a structural material for application in air-breathing and single-stage-to-orbit engines. Unfortunately, like most intermetallics, NiAl is brittle at ambient temperatures. This brittleness has been partly attributed to the lack of five independent slip systems as required by von Mises criterion for uniform, volume conserving deformation since the operative <100> slip offers only three independent slip systems. Isostructural FeAl, however, deforms by <111> slip at room temperature which provides five independent slip systems. Thus, it was decided to macroalloy NiAl with Fe to promote <111> slip thereby possibly improving the ductility. An alternative approach was multi-phase alloys based on NiAl. The results indicated that up to 6% tensile elongation combined with high yield strength (~800 MPa) could be obtained for an alloy Ni-30 at.% Al-20 At.% Fe with an essentially ordered b.c.c. microstructure. These results compare favorably with those of stoichiometric (Ni-50 at.%Al) where 2% tensile elongation and ~250 MPa yield strength is observed. Interestingly, like Ni-50Al, this alloy also deforms by <100> slip at room temperature. The multi-phase alloy approach proved even more successful with ductilities of ~20%, yield strength of 760-850 MPa (depending upon heat treatment) and high fracture strength (1200-1400 MPa) being observed for an alloy Ni-20 at.%Al-30 at.%Fe. The room temperature and elevated temperature microstructure, mechanical properties and deformation behavior of the multi-phase alloy Ni-20Al-30Fe and alloys similar to its constituent phases has been examined here. The high room temperature ductility of the multi-phase alloy was attributed to deformation transfer across interphase boundaries and the crack stopping action of the constituent γ/γ' phase. At elevated temperatures, it was observed that while the constituent γ/γ' phase became increasingly brittle with increasing temperatures, the β' phase became more ductile. Thus, the multi-phase alloy did not exhibit any elevated temperature embrittlement. Similarly, while the β' phase became weak at high temperatures, the γ/γ' phase exhibited better strength retention leading to the improved elevated temperature strength of the multi-phase alloy. Thus, the multi-phase alloy benefits from both its constituent phases, with each phase alleviating the disadvantages associated with the other phase over any temperature range. The multi-phase alloy approach is suggested as a possible approach to designing intermetallic-based alloys.

14. SUBJECT TERMS

B2 compounds; Ductile phase toughening; Intermetallics; Nickel aluminide

15. NUMBER OF PAGES

276

16. PRICE CODE

A13

17. SECURITY CLASSIFICATION OF REPORT	**18. SECURITY CLASSIFICATION OF THIS PAGE**	**19. SECURITY CLASSIFICATION OF ABSTRACT**	**20. LIMITATION OF ABSTRACT**
Unclassified	Unclassified	Unclassified	

NSN 7540-01-280-5500

Standard Form 298 (Rev. 2-89)
Prescribed by ANSI Std. Z39-18
298-102